TECHNISCHE UNIVERSITÄT MÜNCHEN

TUM School of Computation, Information and Technology

# Development and Implementation of a Generalized Multi-Ion Transport Model in Plasma Edge Fluid Codes

**Sergei Olegovich Makarov**

Vollständiger Abdruck der von der TUM School of Computation, Information and Technology der Technischen Universität München zur Erlangung des akademischen Grades eines

**Doktors der Naturwissenschaften**
**(Dr. rer. nat.)**

genehmigten Dissertation.

| | |
|---|---|
| Vorsitz: | Prof. Dr. Eric Sonnendrücker |
| Prüfer*innen der Dissertation: | 1. Hon.-Prof. Dr. Frank Jenko |
| | 2. Prof. Dr. Mathias Groth, Aalto-Universität, Espoo, Finnland |

Die Dissertation wurde am 24.07.2023 bei der Technischen Universität München eingereicht und durch die TUM School of Computation, Information and Technology am 16.12.2023 angenommen.

MAX-PLANCK-INSTITUT FÜR PLASMAPHYSIK

TECHNISCHE UNIVERSITÄT MÜNCHEN

# Development and Implementation of a Generalized Multi-Ion Transport Model in Plasma Edge Fluid Codes

**Sergei Olegovich Makarov**

Dissertation

**Doctor Rerum Naturalium**

Academic Supervisor: Hon.-Prof. Dr. Frank Jenko

Scientific Supervisors: Dr. David Coster
Dr. Andreas Stegmeir

To my family.

# Abstract

Fusion energy is a promising candidate for clean energy transition. Understanding plasma parameters at the edge of magnetic fusion devices is crucial for optimizing reactor performance. Investigating the plasma edge is challenging due to numerous complex phenomena, including impurity radiation, plasma-surface interactions, and plasma-atom/molecule interactions. Nevertheless, the plasma in the edge region is typically highly collisional, allowing for simplification of the problem by leveraging the close-to-equilibrium distribution functions of electrons and ion species. This property enables the application of moment methods to find small perturbations in the distribution functions compared to the Maxwell-Boltzmann equilibrium. While the well-known Braginskii closure method can be used for single-ion plasmas, fusion plasma mixtures consist of multiple ion species in non-trace concentrations (e.g., deuterium, tritium, helium, and impurities). For the multi-ion problem, a more general method of solving the kinetic equation is required, such as the Zhdanov closure.

This thesis focuses on improving the Zhdanov closure and applying it to multi-ion models in edge fluid codes like SOLPS-ITER and GRILLIX. The improvements include deriving heat stresses that contribute to the radial electric field in the Pfirsch-Schlüter regime and obtaining improved versions of the Zhdanov-Yushmanov expressions. The improved analytical method accounts for the mass dependence of different ions, providing superior solutions for kinetic coefficients of middle-mass impurities (up to helium) in deuterium plasmas compared to the Zhdanov-Yushmanov formulae. Furthermore, the thesis establishes the connection between the commonly used Braginskii equations and the Zhdanov coefficients, ensuring momentum and energy conservation in collisions.

The Zhdanov-Grad module has been fully integrated into the SOLPS-ITER code, and test simulations have been conducted to demonstrate the new capabilities of the code. The main accomplishment of the thesis lies in the example simulations of the deuterium-tritium mixture in a JET-like tokamak. The previous 3.0.7 SOLPS-ITER code was only suitable for modeling a single hydrogen species with heavy impurities. The thesis analyzes the effect of thermal force on isotope separation in the scrape-off layer and investigates the improved contributions of thermal and friction forces to helium transport in the ITER divertor. The applicability of collisional theory in the tokamak edge is also discussed.

For the GRILLIX code, multi-ion equations with polarisation drift are formulated, and the multi-species infrastructure of the code has been developed through integration tests following a continuous integration continuous delivery approach in code development.

# Zusammenfassung

Kernfusion ist ein vielversprechender Kandidat für den Wechsel zu grüner Energie. Das Verständnis der Plasmaparameter am Rand magnetischer Fusionsreaktoren ist entscheidend für die Optimierung der Reaktorleistung. Die Untersuchung des Plasmarands ist aufgrund zahlreicher komplexer Phänomene eine Herausforderung, darunter Strahlung durch Verunreinigungen, Wechselwirkungen von Plasma mit Oberflächen und Wechselwirkungen von Plasma mit Atomen/Molekülen. Dennoch ist das Plasma in der Randregion in der Regel stark kollisionsbehaftet, was eine Vereinfachung des Problems ermöglicht, indem die nahezu im Gleichgewicht befindlichen Verteilungsfunktionen von Elektronen und Ionenarten genutzt werden. Diese Eigenschaft ermöglicht die Anwendung von Momentmethoden zur Bestimmung kleiner Störungen in den Verteilungsfunktionen im Vergleich zum Maxwell-Boltzmann-Gleichgewicht. Während das bekannte Braginski-Schließungsverfahren für Einzelionenplasmen verwendet werden kann, bestehen Fusionsplasmamischungen aus mehreren Ionenarten in nicht-spurenhaften Konzentrationen (bspw. Deuterium, Tritium, Helium und Verunreinigungen). Für das Mehr-Ionen-Problem ist eine allgemeinere Methode zur Lösung der kinetischen Gleichung erforderlich, wie z. B. die Zhdanov-Schließung.

Diese Arbeit konzentriert sich auf die Verbesserung der Zhdanov-Schließung und deren Anwendung auf Mehr-Ionen-Modelle in Rand-Fluidcodes wie SOLPS-ITER und GRILLIX. Die Verbesserungen umfassen die Ableitung von Wärmespannungen, die zum radialen elektrischen Feld im Pfirsch-Schlüter-Regime beitragen, sowie verbesserte Versionen der Zhdanov-Yushmanov-Ausdrücke. Diese verbesserte analytische Methode berücksichtigt die Massenabhängigkeit verschiedener Ionen und stellt eine bessere Lösung für die kinetischen Koeffizienten mittelschwerer Verunreinigungen (bis hin zu Helium) in Deuteriumplasmen im Vergleich zu den Zhdanov-Yushmanov-Formeln dar. Darüber hinaus stellt diese Arbeit eine Verbindung zwischen den häufig verwendeten Braginski-Gleichungen und den Zhdanov-Koeffizienten her, um die Impuls- und Energieerhaltung bei Kollisionen sicherzustellen.

Das Zhdanov-Grad-Modul wurde vollständig in den SOLPS-ITER-Code integriert, und Testsimulationen wurden durchgeführt, um die neuen Fähigkeiten des Codes zu demonstrieren. Die Hauptleistung der Arbeit liegt in den Beispiel-Simulationen der Deuterium-Tritium-Mischung in einem JET-ähnlichen Tokamak. Der bisherige SOLPS-ITER-Code 3.0.7 war nur für die Modellierung einer einzigen Wasserstoffart mit schweren Verunreinigungen geeignet. Die Arbeit analysiert die Auswirkungen der thermischen Kraft auf die Isotopentrennung in dem Scrape-Off Layer und untersucht die verbesserten Beiträge der thermischen und Reibungskräfte zum Heliumtransport im ITER-Divertor. Die Anwendbarkeit der kollisionsbasierten Theorie im Tokamak-Randbereich wird ebenfalls diskutiert.

*Zusammenfassung*

Für den GRILLIX-Code werden Mehr-Ionen-Gleichungen mit Polarisationsdrift formuliert, und die Mehrspezies-Infrastruktur des Codes wurde durch Integrationsprüfungen entwickelt, die einem kontinuierlichen Integrations-/Auslieferungsansatz im Code-Entwicklungsprozess folgen.

# Contents

**Abstract** vii

**Zusammenfassung** ix

**Contents** xi

**List of Figures** xv

**List of Tables** xxi

**Acronyms** xxiii

**1 Introduction** 1
- 1.1 Climate change and global de-carbonization strategy . . . 1
- 1.2 Fusion reactor as a clean and save energy source . . . 2
- 1.3 Progress in fusion development . . . 6
- 1.4 Tokamak configurations: limiter and divertor . . . 11
- 1.5 H-mode . . . 13
- 1.6 Plasma edge in a tokamak . . . 14
- 1.7 Multi-ion collisonal plasma . . . 15
- 1.8 Scope of the thesis . . . 16

**2 Multi-species collisional theory** 19
- 2.1 Zhdanov and Braginskii approaches . . . 19
- 2.2 Microscopic level: collisional operator for the kinetic equation . . . 20
- 2.3 Macroscopic level: solid spheres vs Coulomb collisions effect on the gas behavior . . . 25
  - 2.3.1 Heat and momentum exchange in the quasihydrodynamic approximation . . . 25
  - 2.3.2 Thermal force . . . 28
- 2.4 Zhdanov closure . . . 32
  - 2.4.1 General form of the moment equations . . . 32
  - 2.4.2 Distribution function approximation with irreducible tensorial Hermite polynomials $H^{mn}_{r_1..r_n}(\gamma^{1/2}_{\alpha Z}\mathbf{c}_{\alpha Z})$ . . . 34
  - 2.4.3 21N-moment closure for the fully-ionized plasma . . . 37
  - 2.4.4 Zhdanov-Yushmanov analytical expressions . . . 42

**3 Transport and turbulent edge and scrape-off layer codes** **47**
3.1 Classical, neoclassical and turbulent cross-field transport . . . . . 47
3.2 Transport along magnetic field . . . . . 49
3.3 SOLPS-ITER 2D transport code . . . . . 50
3.3.1 General information . . . . . 50
3.3.2 Continuity equations . . . . . 52
3.3.3 Parallel momentum conservation equations . . . . . 53
3.3.4 Electron heat equation . . . . . 57
3.3.5 Ion heat equation . . . . . 58
3.3.6 Charge conservation equation . . . . . 59
3.3.7 Focus of the thesis for the model improvement . . . . . 62
3.4 GRILLIX 3D turbulent code . . . . . 63
3.4.1 General information . . . . . 63
3.4.2 Electron continuity equation . . . . . 64
3.4.3 Vorticity equation (charge conservation equation) . . . . . 65
3.4.4 Parallel momentum equation . . . . . 66
3.4.5 Ohm's law . . . . . 66
3.4.6 Faraday's law . . . . . 66
3.4.7 Electron temperature equation . . . . . 66
3.4.8 Ion temperature equation . . . . . 67
3.4.9 Focus of the thesis for the model improvement . . . . . 67

**4 New steps in the Zhdanov closure** **69**
4.1 Multi-species fluid equations . . . . . 69
4.2 Heat stresses . . . . . 73
4.3 Parallel transport coefficients . . . . . 76
4.3.1 Heat flux . . . . . 76
4.3.1.1 System of rank-1 equations . . . . . 76
4.3.1.2 Averaged over charge states heat flux . . . . . 76
4.3.1.3 Charge states corrections for the heat flux . . . . . 78
4.3.2 Additional vector moment . . . . . 78
4.3.2.1 Averaged over charge states additional vector moment . . 78
4.3.2.2 Charge states corrections for the additional vector moment 79
4.3.3 Thermal and Friction forces . . . . . 79
4.3.3.1 Useful relations for the friction term . . . . . 79
4.3.3.2 Summed over charge states thermal force . . . . . 79
4.3.3.3 Charge states corrections for the thermal force . . . . . 80
4.3.3.4 Summed over charge states friction force . . . . . 80
4.3.3.5 Charge states corrections for the friction force . . . . . 81
4.3.4 Viscous-stress tensor . . . . . 81
4.3.4.1 System of rank-2 equations . . . . . 81
4.3.4.2 Summed over charge states viscous-stress tensor . . . . . 82
4.3.4.3 Charge states corrections for the viscous-stress tensor . . 83

4.4 Improved analytical expressions . . . 84
4.4.1 Matrix coefficients analysis . . . 84
4.4.2 Heat flux . . . 87
4.4.3 Thermal and friction forces . . . 92
4.4.3.1 Thermal force . . . 92
4.4.3.2 Friction force . . . 94
4.4.4 Viscous-stress tensor . . . 97
4.5 Conclusions according to the improvements of the Zhdanov closure . . . 100

**5 Multi-ion closure for the fluid codes 103**
5.1 SOLPS-ITER . . . 103
5.1.1 General remarks . . . 103
5.1.2 Ion parallel heat flux . . . 103
5.1.3 Ion thermal and friction forces . . . 105
5.1.4 Ion viscous-stress tensor divergence . . . 106
5.2 GRILLIX . . . 109
5.2.1 General remarks . . . 109
5.2.2 Multi-species drift reduction . . . 109
5.2.3 Multi-ion continuity equations . . . 111
5.2.4 Vorticity equation in the multi-ion case . . . 112
5.2.5 Ohm's law . . . 113
5.2.6 Electron temperature equation . . . 113
5.2.7 MPI multi-species infrastructure and MMS tests . . . 114
5.3 Conclusions according to the improvements of the SOLPS-ITER and GRILLIX models . . . 116

**6 SOLPS-ITER simulations with the Zhdanov-Grad module 119**
6.1 ITER modeling with D+He+Ne mixture . . . 119
6.1.1 Main plasma parameters . . . 119
6.1.2 Helium transport in deuterium plasmas . . . 120
6.1.3 Ion distribution functions . . . 121
6.2 JET-like modeling with D+T+Ne mixture . . . 124
6.2.1 Modeling setup . . . 124
6.2.2 Collisional theory applicability . . . 126
6.2.3 Difference in the hydrogen isotope transport in the SOL . . . 128
6.2.4 Thermal force and poloidal flows . . . 130
6.3 Conclusions according to the SOLPS-ITER modeling results with Zhdanov-Grad module . . . 134

**7 Conclusion & Outlook 135**
7.1 Summary . . . 135
7.2 Outlook . . . 137

**Bibliography 139**

**A Mistake corrections in the Zhdanov monograph** **157**

**B G-objects, Z-varibles and S-coefficients** **159**

**C Heat flux derivation** **163**
C.1 Averaged over charge states . . . 163
C.2 Charge state corrections . . . 166

**D Additional vector moment derivation** **169**
D.1 Averaged over charge states . . . 169
D.2 Charge state corrections . . . 170

**E Thermal force derivation** **173**
E.1 Summed over charge states . . . 173
E.2 Charge state corrections . . . 174

**F Friction force derivation** **177**
F.1 Summed over charge states . . . 177
F.2 Charge state corrections . . . 180

**G Viscous-stress tensor derivation** **183**
G.1 Averaged over charge states . . . 183
G.2 Charge state corrections . . . 185

**H Improved analytical method for the additional vector moment, the thermal and friction forces** **187**
H.1 Additional vector moment . . . 187
H.2 Thermal and Friction forces . . . 188

**I Improved analytical method for the viscous-stress tensor** **191**

**J Zhdanov closure for SOLPS-ITER (additional content)** **193**
J.1 Electron transport coefficients . . . 193
J.2 Electron and ion heat sources . . . 193
J.3 Viscous-stress tensor divergence . . . 194
J.4 Viscous-drift currents . . . 196

**K Acknowledgments** **199**

# List of Figures

1.1 Climate change evidences. (a) Global surface temperature time evolution, which is measured over the past 2000 years: reconstructed from tree rings, corals, and ice cores in blue [1] and directly observed data is in black [2, 3, 4]. (b) $CO_2$ atmospheric concentration over 800 thousand years. Reconstruction from ice cores and current direct measurements [5]. Adapted from [6]. . . . . 1

1.2 (a) Comparison of fusion reactions rates as a functions of the fuel (present in ion state) temperature for different reactants [7]. For the near-future reactors (ion temperatures: 10-20keV) D + T reaction has the largest fusion reaction rate. (b) Abundance (atom fraction) of the chemical elements in Earth's upper continental crust as a function of atomic number [8]. Important for fusion Li, Be, Pb and W are not rare elements. Pb and W are major industrial metals [8]. . . . . 3

1.3 (a) Reactor wall temperature evolution after shutdown of the fusion reactor due to the decay heat in case of LOCA for the different reactor concepts described in [9] (adapted from FusionEP talk of Andrey Litnovsky `https://www.youtube.com/watch?v=3D4YoHB6G38&ab_channel=FusionEPtalks`). (b) Comparison of the potential ingestion radiotoxicity of three power sources, a fission reactor (gray solid), a fusion reactor (light green area) and a coal-fired power plant (black dashed), all of the same electrical power output, plotted as a function of time after the end of operation. Adapted from [10]. . . . . 5

1.4 (a) Progress over 60 years: the triple products for different fusion concepts ($n_{i0}T_{i0}\tau_E$ for $MCF$ and $n\langle T_i\rangle_n\tau$ for $ICF$). A horizontal lines represent $Q$ for different $n_{i0}T_{i0}\tau_E$ for $MCF$. Adapted from [7] (b) A tokamak configuration. "Twisted" magneic lines are formed by magnetic field induced by currents in coils and plasma. Adapeted from [11]. . . . . 7

1.5 (a) Main plasma parameters time-traces in the non-inductive plasma discharge in the EAST tokamak. $I_p$ is kept on the $330kA$ level, while the induced loop voltage is close to zero. Adapted from [12, 13] (b) Fusion power generated in D-T reactions in JET tokamak. DTE1 campaign (1997): $P_{fus} = 16MW$ in a transient and $P_{fus} = 4MW$ in a flat-top regimes. DTE2 campaign (2021): a flat-top $P_{fus} = 10MW$ in 15/85 D-T mixture (red) and $P_{fus} = 7MW$ in 50/50 (reactor-like) D-T mixture (blue). Adapted from [14, 15]. . . . . 8

1.6 The limiter (left) and divertor (right) tokamak configurations in the poloidal plane. In the limiter configuration, plasma is limited by the limiter surface. In the divertor configuration, plasma is limited by the separatrix surface, which is created by the $B_p$, induced by both $I_p$ and $I_c$ (current in the poloidal field coil). The X-point is formed at the location, where $B_p$ from $I_p$ is exactly compencated by $B_p$ from $I_c$. Dotted arrows represent plasma flows in the SOL (an accrual flux structure is more complex). The figure is inspired by [16]. . . . . 12

1.7 Schematic illustration of the difference between the plasma pressure radial OMP profile in the L- and H-mode. The r coordinate is normalised (r/a) to the distance between the magnetic axis and the LCFS in the OMP (here a is slightly different from the typical minor radius definition). . . . 13

1.8 Examples of the SOLPS-ITER code (discussed in details in section 3.3) simulation results. High main ion collisionality is observed in the SOL of ASDEX Upgrade plasmas: (a) D with impurities (b) He with impurities. He plasmas also exhibit high collisionality in the plasma edge, because the ion collisionallity scales as $Z^3$ (Z - ion charge number) for the similar $T_i$ and electron density ($n_e$) [17]. . . . . 15

2.1 The elastic collision ($g = g'$) of a particle type $\alpha Z$ with a particle type $\beta\zeta$. The reference point "0" is attached to the particle $\beta\zeta$. The figure is adapted from [18]. . . . . 20

2.2 (a) An example of the hyporbolic trajectories in the attractive potential ($sign(Z) \neq sign(\zeta)$) for the small $g$ (blue) and the large $g$ (red) and the same $b$ (red and blue). There is a larger $\chi$ for a smaller $g$. (b) Hyperbolic trajectories of the two only known interstellar objects passing though the Solar system 1I/'Oumuamua and 2I/Borisov. Adapted from [19] . . . . . 23

2.3 Schematic interpretation of the particle trajectories with (a) the solid sphere collisions and (b) the Coulomb collisions. . . . . 24

2.4 Particle $\alpha Z$ from the mono-energetic beam propagates through the scattering centers $\beta\zeta$ with the effective cross-section $Q^{(1)}_{\alpha Z\beta\zeta}$. . . . . 27

2.5 The distribution functions along the axis "1", which are contracted over axis "2" and "3" and normalized to the $v^{th}_{\alpha Z}$, for the light species $\alpha Z$ and the heavy species $\beta\zeta$ are plotted in the case of the temperature gradients occur along the the axis "1". Solid lines represent 13N-moment approximation of the distribution functions $f_{\alpha Z/\beta\zeta}$, whereas dashed lines represent local Maxwell distribution functions $f^0_{\alpha Z/\beta\zeta}$. Zero net particle fluxes in the positive or negative dirrections $\mathbf{u}_{\alpha Z} = \mathbf{u}_{\beta\zeta} = 0$. Also, for illustrative purposes: $\mathbf{h}^T_{\alpha Z}/n_{\alpha Z} = \mathbf{h}^T_{\beta\zeta}/n_{\beta\zeta}$. . . . . 29

3.1 The SOLPS-ITER computational mesh for the ASDEX Upgrade tokamak, as example, in physical space (left) and the so-called rectangular representation of the B2.5 domain (right). Directions of curvilinear coordinates x, y and z are shown. The location of divertor targets, location of gas puff and pumps are plotted. The locations of different zones (core, SOL, PFR) and boundaries are shown on both the physical and rectangular meshes with color coding. Letters 'W', 'N', 'E', 'S' stand for 'western', 'northern', 'eastern' and 'southern' sides of the rectangular mesh correspondingly. Adapted from [20]. . . . . 51

3.2 The GRILLIX computational mesh using FCI approach in tokamak geometry. Adapted from [21]. . . . . 64

4.1 (a) The heat conductivity transport coefficient for deuterium, using the EMIM, the ZY expression and the IAM, for the D + C + another impurity case with equal distribution between charge states. The additional impurity is varied along the horizontal axis. The dash-dotted line shows the case where: $\widetilde{\nabla_\parallel T_\beta} = 2 \times \nabla_\parallel T_D : \beta \neq D$. The number in parentheses at the top of the figure gives normalised impurity density ($= \overline{Z_\beta^2} n_\beta / n_D : \beta \neq D$) and is kept constant. (b) The velocity dependent part of the heat flux transport coefficient for the deuterium due to D/impurity velocity difference $c^{(h_w^A)}_{imp\ D}$ (solid) and for another impurity due to impurity/D velocity difference $c^{(h_w^A)}_{D\ imp}$ (dashed), using the EMIM, the ZY expression and the IAM, for D + C + another impurity. . . . . 91

4.2 (a) The TF transport coefficient for another impurity (solid) and for carbon (dashed) using EMIM, the ZY expressions and the IAM for D+C+another impurity. Dash-dotted (another impurity) and dotted (carbon) lines are plotted for the case where $\widetilde{\nabla_\parallel T_\beta} = 2 \times \nabla_\parallel T_D : \beta \neq D$. (See the caption to figure 4.1a for additional information). (b) Zoom of the dotted box in (a). . . . . 93

4.3 (a) The FR transport coefficient for another impurity/D (solid), for C/D (dashed) and for another impurity/C (dotted) using the EMIM, the ZY experssions, the IAM and the IAM (MDF) for the D + C + another impurity case. (See the caption to figure 4.1a for additional information). (b) Zoom of the dotted box in (a). . . . . 96

4.4 (a) The effective strain viscosity coefficient for D (solid) and for another impurity (dashed) using the EMIM, the ZY experssions and the IAM for the D + C + another impurity case. (b) The effective heat stress coefficient D (solid) and for another impurity (dashed) using the EMIM and the IAM for the D + C + another impurity case. (See the caption to figure 4.1a for additional information). . . . . 99

5.1 The ratio between the total ion heat conductivities, the total ion viscosity coefficients (velocity and heat flux dependent viscous-stress tensors), which are calculate using EMIM $c^{eff}_{Calc}$, and which are calcuated using 3.0.7 SOLPS-ITER formulation $c^{eff}_{SOLPS}$, for the D + C + another impurity case. (See the caption to figure 4.1a for additional information). . . . 105

5.2 An example of initial profiles of electrons (rank 0), $D^+$ (rank 1), $T^+$ (rank 2), $He^{+2}$ (rank 3) in the circular geometry in the multi-ion GRILLIX mode.115

5.3 Numerical error of MMS verification procedure. The sup- and L2-norms (nrm) for $D^+$, $T^+$, $He^{+2}$ densities (normalized to the npol=8 values) for the slab (a) and circular (b) geometries. The 3 order convergence, which should be reached asymptotically, is plotted. Starting from 8 the number of planes is doubled together with the perpendicular grid resolution and the time-step. . . . . 116

6.1 ITER outer target profiles for the Standard SOLPS-ITER 3.0.7 model and the Zhdanov-Grad module activated. (a) Electron temperature. (b) Total surface power loads, which includes the energy flux of ions and electrons, ion recombination loads, energy flux from recycled neutrals (which return a portion of the incoming energy back to the plasma volume), radiation loads, and other interactions involving neutrals and the plasma-facing surface. . . . . 120

6.2 The flow velocity difference between the $He^{+2}$ ion species and $D^+$ ion species, normalized to the $D^+$ velocity $|u_{\parallel He^{+2}} - u_{\parallel D^+}|/\sqrt{T_i/m_D}$ using (a) the Standard SOLPS-ITER model, which is based on the ZY expressions, and (b) the ZG module in the IAM mode. Blue circles define spatial points where ion distribution functions are studied in figures 6.3a and 6.3b.121

6.3 Distribution functions of the $D^+$, $He^{+2}$ and $Ne^{+6}$ ion species (the most populated charge states of the particular species type in the chosen divertor locations) at the (a) HFS and (b) LFS in the divertor region (at the spatial points marked by blue circles in figure 6.2b). $f^0$ is the non-modified Maxwell function. . . . . 122

6.4 (a) JET-like modeling geometry including plasma fluid (purple) and kinetic neutral (orange) numerical grids. Beryllium wall - green. Tungsten wall - red. Core boundary - yellow. Puffing surface - cyan. Pumping surfaces - black. Blue surfaces indicate neutral pressure measurements surfaces. Green dashed lines indicate OMP and IMP. (b) Anomalous transport coefficients at the OMP. . . . . 125

6.5 Plasma profiles at the OMP. (a) Left axis: electron density ($n_e$) (red), D ion density ($n_D$) (blue), T ion density ($n_T$) (magenta), total hydrogen isotope ion density (black); right axis: $Z_{eff}$ (dashed yellow). (b) Electron temperature ($T_e$) (red), ion temperature ($T_i$) (blue). . . . . 126

6.6 (a) $n_e$ 2D profile in the divertor. (b) $T_e$ 2D profile in the divertor. . . . . 127

6.7 (a) The Knudsen number according to the $\nabla_{\|} T_i$ scale (b) The normalized D parallel heat flux (before flux limiting application) $|h_{\|D^+}/(\sqrt{T_i/m_D} \cdot p_{D^+})|$. The colour bar is on a logarithmic scale and the white region is below the scale. . . . . 128
6.8 The T and D ion density ratio $n_T/n_D$ as a result artificial adjustment of the isotope mass ratio $m_T/m_D$ for the TF and FR kinetic coefficients calculation. (a) a realistic ion mass is used: $m_T/m_D = 1.5$; (b) T mass is factored by 2/3: $m_T/m_D = 1$; (c) T mass is factored by 5: $m_T/m_D = 7.5$, Ne mass is factored by 10 (to keep Ne heavier than both hydrogen isotopes). Black numbers represent poloidal cell numbers in the reference flux tube (number 7 from the separatrix), where the TF effect is analysed (figures 6.10a and 6.10a). In the poloidal cell number 17, the ion distribution functions analysis is performed in figure 6.11. . . . . 129
6.9 (a) Schematic of the main fluxes in the SOL. Blue arrow - poloidal ion flow in SOL from the LFS towards the HFS. Blue circle - approximate stagnation point of poloidal flows. Magenta arrows - poloidal ion fluxes in the divertor region. Green arrows - neutral fueling from the PFR to the SOL below X-point. Red arrow - neutral fueling of the confined region. (b) Ratio T to D ion density in the SOL for the "realistic ion mass" case (the same as in figure 6.8a) plotted on the numerical rectangular SOLPS-ITER mesh: vertical scale - numerical magnetic flux tube number, beginning from the separatrix and ending at the computational boundary in the far-SOL; horizontal scale - poloidal cell number from the inner target (IT) to the outer target (OT). Dark blue dash-dotted horizontal line - the reference flux tube, where the TF effect is analysed (figures 6.10a and 6.10a); black dashed vertical line - divertor entrance; green dotted vertical line - IMP poloidal location; magenta dotted vertical line - OMP location. 131
6.10 (a) The TF (red) and FR (blue), which act on the T species due to the D-T interactions (due to the D-T flow velocity difference for FR), in the inner (solid) and outer (dashed) divertor in the reference flux tube shown in figure 6.9b (poloidal distance from the corresponding target is marked along the horizontal axis). Numbers correspond to the poloidal numerical cells (horizontal axis in figure 6.9b). (b) Solid lines: ratio of T vs D ion densities (red), ion parallel velocities (blue) and ion parallel fluxes (yellow) in the inner divertor in the reference flux tube (left vertical scale). Dashed line: $T_i$ (right vertical scale). . . . . 132
6.11 Distribution functions of the $D^+$, $T^+$ and $Ne^{+6}$ ion species at the HFS in the reference flux tube number 7 from the separatrix and poloidal cell number 17 (see figures 6.8a and 6.9b). $f^0$ is the non-modified Maxwell function. . . . . 133

# List of Tables

1.1 Tokamak's pressures and triple products. An illustration of those relations to confinement times and auxiliary heating power density. . . . . 10

6.1 Main simulation parameters for the D+T+Ne mixture in the JET-like configuration . . . . . 124

# Acronyms

| | |
|---|---|
| $B_p$ | poloidal magnetic field. |
| $B_t$ | toroidal magnetic field. |
| $E_r$ | radial electric field. |
| $I_p$ | plasma current. |
| $P_h$ | auxiliary heating power. |
| $P_{ext}$ | external heating power. |
| $P_{fus}$ | fusion power. |
| $T_e$ | electron temperature. |
| $T_i$ | ion temperature. |
| $T_{\alpha Z}$ | temperature of the species $\alpha Z$. |
| $T_{av}$ | average temperature of the mixture. |
| $V$ | plasma volume. |
| $W_{rs}$ | total strain tensor. |
| $Z_\alpha^{max}$ | maximal charge number of the species type $\alpha$. |
| $Z_{eff}$ | effective plasma charge. |
| $\Psi_p$ | poloidal magnetic flux. |
| $\alpha^{max}$ | total number of different species types in the mixture. |
| $\lambda_{\alpha Z}^{mfp}$ | mean free-path of the species $\alpha Z$. |
| $\lambda_q$ | scrape-off layer power fall-off length. |
| $\ln \Lambda$ | Coulomb logarithm. |
| $\mu_{\alpha\beta}$ | reduced mass. |
| $\omega_{\alpha Z}$ | cyclotron frequency of the species $\alpha Z$. |
| $\pi_{\alpha Z rs}$ | viscous-stress tensor of the species $\alpha Z$. |
| $\pi_{rs}$ | total viscous-stress tensor. |
| $\rho_{\alpha Z}^s$ | sound Larmor radius of the species $\alpha Z$. |
| $\sigma_{\alpha Z rs}$ | additional tensor moment of the species $\alpha Z$. |
| $\tau_E$ | energy confinement time. |
| $\mathbf{E}$ | electric field. |
| $\mathbf{h}_{\alpha Z}$ | heat flux of the species $\alpha Z$. |
| $\mathbf{r}_{\alpha Z}$ | additional vector moment of the species $\alpha Z$. |
| $\mathbf{w}_{\alpha Z}$ | diffusive velocity of the species $\alpha Z$. |
| $\mathbf{B}$ | magnetic field. |
| $\mathbf{u}$ | mass-average flow velocity. |
| $\mathbf{u}_{\alpha Z}$ | flow velocity of the species $\alpha Z$. |
| $\varepsilon_0$ | vacuum permittivity. |
| $\varphi$ | electrostatic potential. |

| | |
|---|---|
| $e$ | electron charge. |
| $e_{slm}$ | Levi-Civita symbol. |
| $f^0_{\alpha Z}$ | zero-order approximation of the distribution function for species $\alpha Z$. |
| $m_\alpha$ | mass of the species. |
| $n_e$ | electron density. |
| $n_i$ | ion density. |
| $n_i T_i \tau_E$ | triple product. |
| $n_s$ | total number of different fluid species in the mixture (different charge states, are treated as a separate fluid). |
| $n_{\alpha Z}$ | density of the species $\alpha Z$. |
| $p$ | total pressure. |
| $p_{\alpha Z}$ | partial pressure of the species $\alpha Z$. |
| $r_D$ | Debye radius. |
| $v^{th}_{\alpha Z}$ | thermal velocity of the species $\alpha Z$. |
| Be | beryllium. |
| C | carbon. |
| CFS | Commonwealth Fusion Systems. |
| CGS | Centimetre–gram–second system of units. |
| CI/CD | continuous integration/continuous delivery. |
| D | deuterium. |
| ELM | edge localized modes. |
| EMIM | explicit matrix inversion method. |
| ETB | edge transport barrier. |
| FCI | flux-coordinate independent. |
| FR | friction force. |
| H | hydrogen. |
| H-mode | high confinement mode. |
| He | helium. |
| HFS | high field side. |
| HTS | high-temperature superconductor. |
| IAM | improved analytical method. |
| IAM (MDF) | improved analytical method, where the $c^{(h^A_w)}_{\beta\alpha}$ and $c^{(r^A_w)}_{\beta\alpha} : m_\beta < m_\alpha$ are set to zero. |
| ICF | inertial confinement fusion. |

| | |
|---|---|
| ICRH | ion cyclotron resonance heating. |
| IMAS | ITER integrated modeling analysis suite. |
| IMP | inner mid-plane. |
| JET | Joint European Torus. |
| L-mode | low confinement mode. |
| l.h.s. | left hand side. |
| LCFS | last closed flux surface. |
| LFS | low field side. |
| Li | lithium. |
| LOCA | loss-of-coolant accident. |
| MCF | magnetic confinement fusion. |
| MHD | magnetohydrodynamics. |
| MMS | method of manufactured solutions. |
| MPI | message passing interface. |
| N | nitrogen. |
| NBI | neutral beam injection. |
| Ne | neon. |
| NIF | National Ignition Facility. |
| OMP | outer mid-plane. |
| Pb | lead. |
| PFM | plasma-facing material. |
| PFR | private flux region. |
| Q | fusion energy gain factor. |
| r.h.s. | right hand side. |
| RMP | resonant magnetic perturbations. |
| SI | International System of Units. |
| SOL | scrape-off layer. |
| T | tritium. |
| TF | thermal force. |
| W | tungsten. |
| Z | charge number of the species. |
| ZG | Zhdanov-Grad. |

| | |
|---|---|
| ZY | Zhdanov-Yushmanov. |

# 1 Introduction

## 1.1 Climate change and global de-carbonization strategy

Over the past 50 years Earth has experienced the climate change, which has happened neither in the last 2000 years (figure 1.1a) nor in the last 800.000 years (figure 1.1b). There is a consensus in the science community about the anthropogenic cause of this change. The climate change is the result of the emission of greenhouse gases ($CO_2$, $CH_4$, etc) due to human activity. The largest, but not the only, contribution to greenhouse gas production comes from the energy industry, which includes electrical power, transportation, heating/cooling, industry. The greenhouse gases are the products of the combustion of fossil (coal, oil, gas) and bio (wood, ethanol, etc) fuels, which are used during the primary energy consumption. There is no fundamental barrier to redistribute most of the energy consumption in transportation, heating/cooling, industry sectors from fuels towards usage of secondary energy carries, such as electricity. In some areas it is even economically viable in case of modern technology application. A good example is a transition from the gasoline to the electrical vehicles, which was accelerated significantly in the last decade. Thus, the crucial challenge is the reduction of the greenhouse gas production during the primary energy consumption, i.e. reduce a fossil and bio fuel combustion.

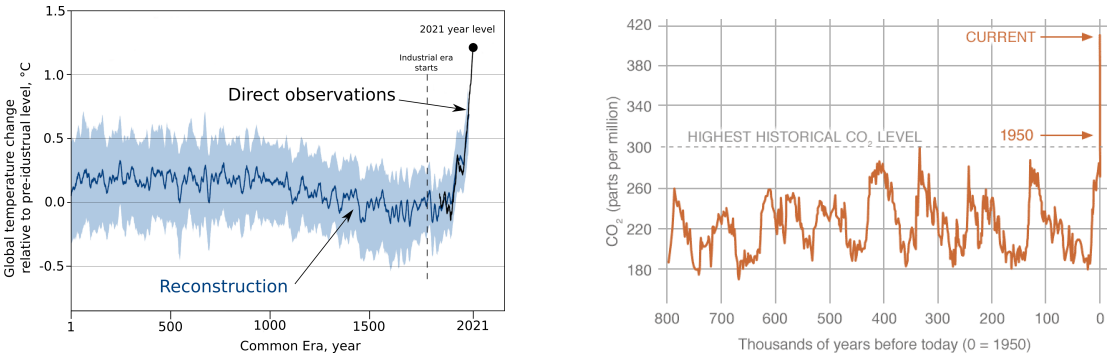


**Figure 1.1:** Climate change evidences. (a) Global surface temperature time evolution, which is measured over the past 2000 years: reconstructed from tree rings, corals, and ice cores in blue [1] and directly observed data is in black [2, 3, 4]. (b) $CO_2$ atmospheric concentration over 800 thousand years. Reconstruction from ice cores and current direct measurements [5]. Adapted from [6].

In 2021, 82% of world total primary energy consumption consisted of carbon-based fossil fuels [22], which includes oil (31%), coal (27%) and gas (24%). Different scenarios are under consideration to prevent global climate change [23]. All of them include a rapid transition to low-/no-emission energy sources. Wind and solar energy, which covers currently around 5% of the world primary energy, are considered as the main candidates to replace current energy sources. However, it is an open question at what extent this transition can be performed based on solar and wind energy, since such types of energy have the following disadvantages and corresponding risks. 1) Weather, season and daily energy production fluctuation, which requires energy storage or/and electricity redistribution using long-range international grids of high capacity to compensate this fluctuation. An organization of such systems is a significant and challenging part of the clean energy transition via weather-dependent sources. Apart from the technical difficulties, political aspects plays a big role. International electricity transmission of such scale supposes mutual dependence of the participants, which in case of complicating relations threatens national energetic stability. 2) Location dependence. There are a lot of places on Earth, which are not well suited for either wind or solar efficient energy production, where at the same time, high energy consumption needs take place, i.e. highly populated areas with the poor average solar radiation and wind strength. Potential solution as long-range electric power transmission has political and technical constrains, similar to the previous point. 3) Low power density of the solar and wind energy is also a significant drawback. Gigawatt-class solar and offshore wind power plants spread over dozens and hundreds of $km^2$ correspondingly. 4) The solar- and wind-based transition requires significant amount of cobalt mineral, which is mined mainly in Democratic Republic of the Congo (D.R.C.) [22]. The solar/wind industry suffers greatly from the cobalt supply crisis [24]. A strategy of the low-/no-emission transition should include a diversification of these risks, i.e. development of the zero-emission energy source, which avoids these limitations.

## 1.2 Fusion reactor as a clean and save energy source

Fusion energy is a perfect candidate of the future zero-emission energy source. It is based on the nuclear fusion of light nuclei, which releases large amount of energy due to mass difference between reactants and products according to the famous Einstein equation $E = mc^2$. Consequently, a fusion reactor does not produce $CO_2$ or any other greenhouse gas. The most promising reaction for the near-future reactors is a fusion of deuterium (D) and tritium (T) nucleus (figure 1.2a) resulting in a neutron and an alpha-particle together with $17.6 MeV$ energy:

$$ {}^{2}_{1}D + {}^{3}_{1}T \rightarrow {}^{4}_{2}He\ (3.5\ MeV) + {}^{1}_{0}n\ (14.1\ MeV) \tag{1.1} $$

Similar processes of hydrogen isotopes fusion occur in the center of a star. Planets, like our Earth, receive energy, which originates from fusion reactions in the center of a parent star and consequently transferred via photon radiation emitted from the star's

photosphere. Solar and wind energies are different ways to collect this energy, which Earth surface receives from the Sun. Alternatively, fusion reactions can be carried out *in situ*, which naturally leads to avoidance of the drawbacks of solar and wind energies, which are described in section 1.1.

Fusion reactors are independent of weather fluctuations, as well as climatic conditions of the specific location. A fusion reactor is a stable energy supplier, which does not require additional energy storage or international electricity transfers. It can be integrated in existing electricity grid infrastructure, where most of the produced energy is simultaneously used by a local consumer. Density of the energy production with respect to occupied area in fusion reactors is much larger than in solar and wind power plants. A gigawatt-class EU-DEMO reactor [25] is planned to be located on an area of hundreds $m^2$. The fusion power plant site with all needed facilities will require area of several $km^2$. Additionally, several reactors can share common infrastructure, like present fission reactors, increasing the produced power density.

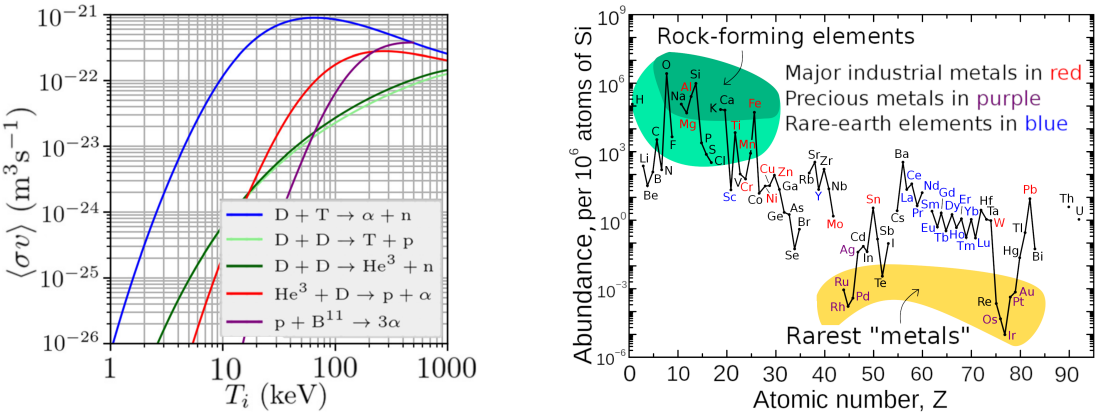


**(a)** **(b)**

**Figure 1.2:** (a) Comparison of fusion reactions rates as a functions of the fuel (present in ion state) temperature for different reactants [7]. For the near-future reactors (ion temperatures: 10-20keV) D + T reaction has the largest fusion reaction rate. (b) Abundance (atom fraction) of the chemical elements in Earth's upper continental crust as a function of atomic number [8]. Important for fusion Li, Be, Pb and W are not rare elements. Pb and W are major industrial metals [8].

It is important to consider what resources are crucial to build and operate a fusion reactor. First reactant - D is presented in the sea water in practically unlimited amounts and can be extracted by many countries, which have an access to the shore. Second reactant - T is not a stable isotope and occur in nature only in trace amounts. For self-sufficient power plant operation, T is needed to be produced inside the reactor "blanket": thick tile, a part of the reactor wall, which surrounds a location of fusion reactions and protects other reactor components from neutron radiation [26]. The T production, so called "breeding", based on a nuclear reactions, which are initiated by the neutron product in (1.1), which impacts into the reactor wall. This process requires

two addititonal initial components: lithium (Li), specifically ${}^{6}_{3}Li$ isotope (${}^{7}_{3}Li$ isotope in some designs), as a breeding reactant and beryllium (Be) (lead (Pb) in some designs), as a neutron multiplier [26](needed to produce more T per initial neutron appeared in (1.1)):

$$ {}^{6}_{3}Li + {}^{1}_{0}n \rightarrow {}^{4}_{2}He\ (2.05\ MeV) + {}^{3}_{1}T\ (2.75\ MeV) \tag{1.2} $$

$$ {}^{9}_{4}Be + {}^{1}_{0}n \rightarrow 2\,{}^{4}_{2}He + 2\,{}^{1}_{0}n\ (-1.67\ MeV) \tag{1.3} $$

A consumption of D, Li and Be during breeding and fusion is relatively small. Simple estimations from (1.2) and (1.3) shows that several thousands tons of Li and Be are needed for one thousand tons of T production, which together with 700 tones of D release in fusion around 560 Exajoules of energy (1.1). It is close to annual global primary energy consumption [22], so a consumption of initial reactants is practically negligible. However, during 40 years cycle a gigawatt-scale reactor will produce maximum 2 Exajoule of energy and consume, as a result, only ∼7 tons or ∼14% of 50 tons of Li stored in the blanket [27, 26]. Also, around 400 tons of Be will be initially placed into the EU-DEMO reactor (this number can be changed during the design update) [27]. Thus, the larger challenge is an initial usage of materials, which are required during the reactor construction. Also, around 200 tons of tungsten (W) will be used as plasma-facing material (PFM) in EU-DEMO reactor [27, 28].

${}^{6}_{3}Li$ appears in nature as a small fraction of total Li, with natural abundance of 4.85 %. World Li reserves and resources are over 26,000,000 and 98,000,000 tons correspondingly [29]. The world's identified resources of Be have been estimated to be more than 100,000 tons [30]. As alternative, another possible neutron multiplier, Pb has world reserves around 2 billion tons [31]. World W reserves are 3,400,000 tons [32]. In general, no rare elements are necessary for fusion energy production (figure 1.2b). Thus, the needed resources are available to cover significant part of the future world energy supplies with fusion reactors. Estimations [33] show that reserves of enriched ${}^{6}_{3}Li$ will be enough to cover ∼3500 years of the future energy demand according to known resources and 23 million years of the future energy demand, if Li extracted from sea water is taken into account. Although, the considered resources are not evenly distributed among the countries, due to the small consumption during the fusion power plant operation energy supplies are protected from perturbation global political climate to the certain extant. Unlike, the climate change problem (discussed in section 1.1), resources availability is a mid-/long-term issue. Fusion reactors have a large advantage in this time-scale compare to the fossil fuels, which resources are restricted by large dozens or small hundreds years.

Since a fusion reactor is a nuclear device, it is necessary to briefly discuss the nuclear safety, nuclear waste production and connection to the military technology of the fusion energy. Fusion reactors are intrinsically safe, i.e. fusion reactions require extreme conditions of matter: high temperature plasma with low energy losses (more details in section 1.3), which is truly difficult to achieve and sustain. As a result, if any control system fails, these specific conditions are not satisfied and fusion reactions stop immediately,

as well as the associated breeding process. In contrast to fission reactions, which are based on a chain-process and can be sustained and increased even without the will and control of a human. It can lead to severe nuclear disaster, for example, the Chernobyl disaster [34]. Moreover, a nuclear fission reactor shutdown does not guarantee nuclear safety. In case of loss-of-coolant accident (LOCA) the decay heat and zirconium-water reaction leads to dangerous temperature increases causing a rector core meltdown, which can lead to accidents like the Fukushima nuclear disaster [35] and the Three Mile Island accident [36]. The decay heat on a fission plant is 6-7% of a full power [37]. The decay heat accompanied with zirconium-water reaction leads to increase up to the dangerous melting temperatures (around 2800°$C$) within hours or even minutes in case of LOCA [35, 36].

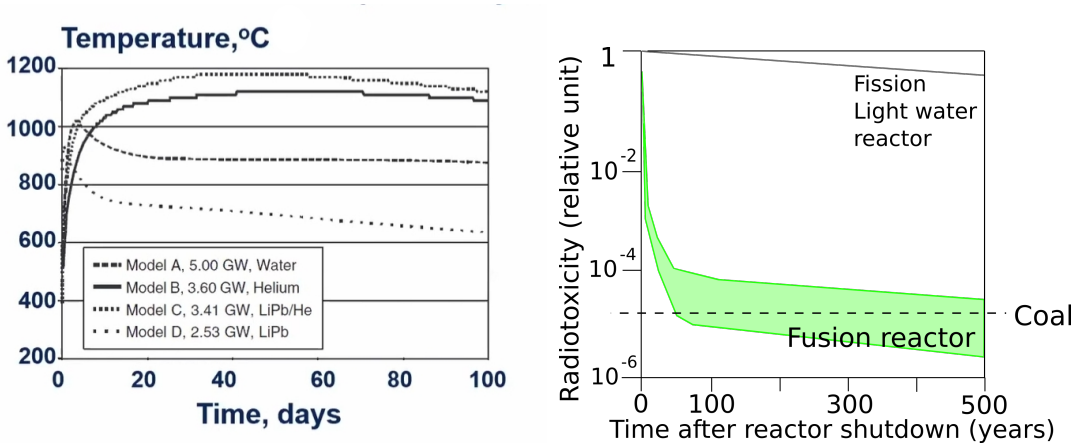


(a) (b)

**Figure 1.3:** (a) Reactor wall temperature evolution after shutdown of the fusion reactor due to the decay heat in case of LOCA for the different reactor concepts described in [9] (adapted from FusionEP talk of Andrey Litnovsky `https://www.youtube.com/watch?v=3D4YoHB6G38&ab_channel=FusionEPtalks`). (b) Comparison of the potential ingestion radiotoxicity of three power sources, a fission reactor (gray solid), a fusion reactor (light green area) and a coal-fired power plant (black dashed), all of the same electrical power output, plotted as a function of time after the end of operation. Adapted from [10].

To some extent, similar issues can arise in a fusion reactor. Fusion neutrons activate reactor materials, which leads to a decay heating after the reactor shutdown. For the ITER reactor decay heating is not a safety issue [38]. The EU-DEMO blanket decay heating is 10-20MW (or 1-2% of a total power) during the first hour after shutdown and drops to several MW during the first day after shutdown [27]. Different fusion reactor models investigating LOCA, show around 5-10 days before temperature reach 1000°$C$ (figure 1.3a), when W, in case of contact with atmosphere due to a leak, can form volatile oxides (to prevent this, special "SMART" W-alloys are under development) [39]. The components of a fusion reactor wall: W, Be, lithium orthosilicate and stainless steel melting temperatures will not be reached in fusion reactor after shutdown (figure 1.3a).

As stated in [40], if required, additional efforts will be made to provide cooling by passive means. Thus, a fusion power plant can and must be design passively resilient to any type of accidents, to be a reliable future energy source.

A fusion reactor produces several times less radiotoxic waste than a typical fission reactor for the same electrical output (figure 1.3b). However, it is even more important to emphasize that a fusion reactor does not produce long-lived radioactive material. After 50-100 years the radiotoxicity of the fusion power plant operation products drops down to the coal ash level. A long term radiotoxic storage is not required for the fusion reactor. It is a big advantage with respect to fission nuclear energy. Another advantage is that most of the perspective fusion reactor concepts, i.e. magnetically confinement fusion, are not related to nuclear military technologies. Fusion energy does not conflict with The Treaty on Non-Proliferation of Nuclear Weapons, so has no related obstacles which are present with fission energy. Besides, scientific publications on fusion topics are open and can be distributed widely. It is important for the efficient scientific communication. Summarising the section, it can be stated that fusion energy has many advantages among other energy sources and will have good chances in the upcoming decarbonization race.

## 1.3 Progress in fusion development

Fusion energy is challenging to achieve. Sixty years have passed since the first serious attempts to make fusion reactions happen was made in the 1960-s. However, the energy, which is delivered to the D-T fuel, have been smaller than the energy, which is gained in the fusion reactions (1.1), in fusion machines, which have been developed during this decades. Recently, a significant break-through in the fusion development was achieved. First in a mankind history, scientific energy breakeven was accomplished, i.e. fusion energy gain factor (Q) was achieved grater than unity. The $Q = P_{fus}/P_{ext}$, where fusion power ($P_{fus}$) is the power produced in a controlled fusion reactions, and external heating power ($P_{ext}$) is the external power delivered inside the reactor wall. On 5 December 2022, at National Ignition Facility (NIF) 3.15 MJ of fusion energy were produced after delivering 2.05 MJ of laser energy to the fuel target [41], for an equivalent of steady-state Q of 1.54. The NIF is based on the inertial confinement fusion (ICF) concept. Unfortunately, petawatt-class laser drivers needed for the ICF are extremely inefficient. The NIF lasers have around 1% wall-plug efficiency, which means around 322 MJ of electrical power were consumed to conduct this historical experiment. Even if, 20% wall-plug efficiency lasers, which are discussed in [42], for power plant are developed, Q around 100 is needed. Thus, this fusion concept is still far from the practical application.

It is worth to consider different fusion concepts, which avoid ICF disadvantages. In [7] overview, most of the fusion approaches (ICF, magnetic confinement fusion (MCF) or those combinations), which were published in the peer-reviewed papers, are collected. A triple product ($n_i T_i \tau_E$), which is a product of the fusion reactants density, temperature and the energy confinement time, i.e. the characteristic time of thermal energy dissipation in a specific fusion machine, is chosen to compare different approaches. It is related to the Q at the fusion temperatures (10-20 $keV$) and includes physically relevant

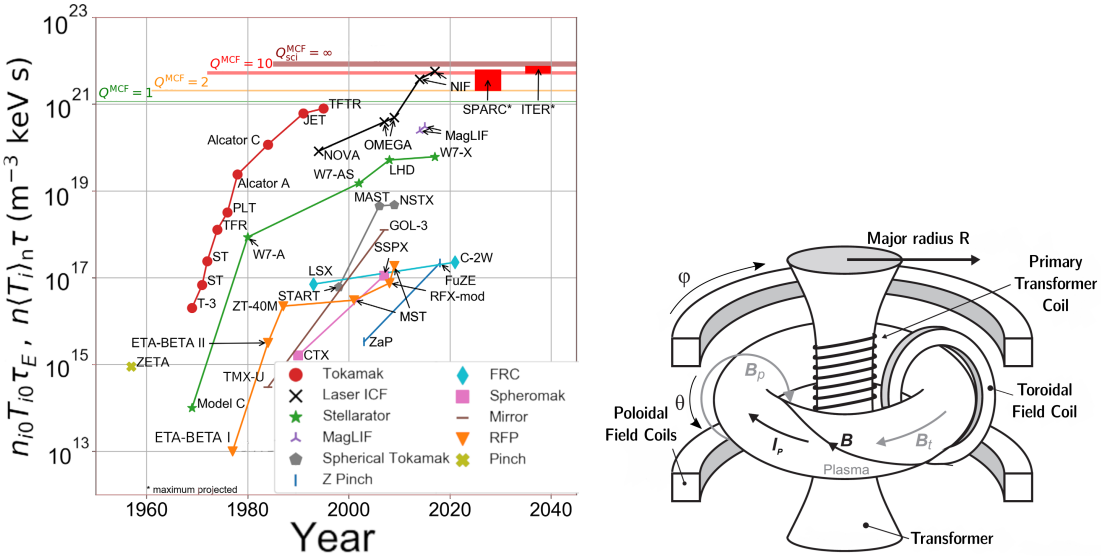


(a) (b)

**Figure 1.4:** (a) Progress over 60 years: the triple products for different fusion concepts ($n_{i0}T_{i0}\tau_E$ for $MCF$ and $n\langle T_i\rangle_n\tau$ for $ICF$). A horizontal lines represent $Q$ for different $n_{i0}T_{i0}\tau_E$ for $MCF$. Adapted from [7] (b) A tokamak configuration. "Twisted" magneic lines are formed by magnetic field induced by currents in coils and plasma. Adapeted from [11].

parameters. The exact relation to the Q depends on a particular approach. However, the $n_iT_i\tau_E$ is an order of magnitude accuracy parameter to compare various fusion devises. Figure 1.4a represents progress in a fusion machine's "zoo" in the last 60 years together with planed machines. Despite the relatively high values of $n_iT_i\tau_E$ in MagLIF device, it is not discussed herein, because of the similarity to ICF laser efficiency issue. Besides, approaches, which have demonstrated low triple products, are not in a focus of present research.

Comparable to laser ICF $n_iT_i\tau_E$ were achieved in tokamaks, which are MCF devices. For the similar temperatures, MCF device trades the large density, which is presented in ICF, (in tokamaks the density is 10 orders of magnitude smaler than in NIF) for the larger energy confinement time (in tokamaks it is 10 orders of magnitude larger than in ICF) [7], which is accomplished with a use of externally/internally generated magnetic field (**B**). At the temperature of dozens of keV the mater is present in the plasma state, i.e. consist of electrons and ions. **B** is used to confine charged particles, which reduces the particle and energy loss in the device.

A tokamak is a toroidal MCF device, which was developed in the Kurchatov Institute in the Soviet Union in the 1960s. It is based on a "twisted" **B** configuration, which is a result of a combination of the toroidal magnetic field ($B_t$) and poloidal magnetic field ($B_p$) (figure 1.4b). In the tokamak, the $B_t$ is generated by the extarnal toroidal field coil, and the $B_p$ is generated by the plasma current ($I_p$), which is conducted in plasma

in the toroidal direction (figure 1.4b). Additionally, a part of $B_p$ is formed by poloidal coils to control the shape and position of the plasma.

The $I_p$ can be generated by a transformer, where the **B** is rising in time. A transformer has fundamentally limited amount of volt-seconds, which are needed to drive current in the tokamak plasma, because the **B** cannot be raised infinitely long and restricted by ∼10-20 T [43]. Most of the tokamak-reactor concepts involve a steady-state (or long-term) operation. Therefore, other methods of a current drive are developed for the long (theoretically infinitely long) operation [44]. Organization of the special advanced scenario, i.e. the optimization of the self-generated non-inductive current by the bootstrap mechanism above 50% [45], is preferable. The rest fraction of the $I_p$ is planned to generate by various non-inductive current drive systems [45, 44]. Non-inductive tokamak operation has been demonstrated in many machines [46]. However, the most impressive results were achieved in EAST tokamak in China on 30 December 2021, where the D plasma of high central temperature electron temperature ($T_e$) 6 $keV$ was successfully confined for 1056s (figure 1.5a) [12]. However, important for $n_i T_i \tau_E$ quantities were far from the breakeven parameters: central ion temperature ($T_i$) $\sim 0.7$ $keV$, central $n_e$ $\sim 2 \cdot 10^{19}$ $m^{-3}$ (close to ion density ($n_i$)) and energy confinement time ($\tau_E$) $\sim 0.07$ $s$ [12]

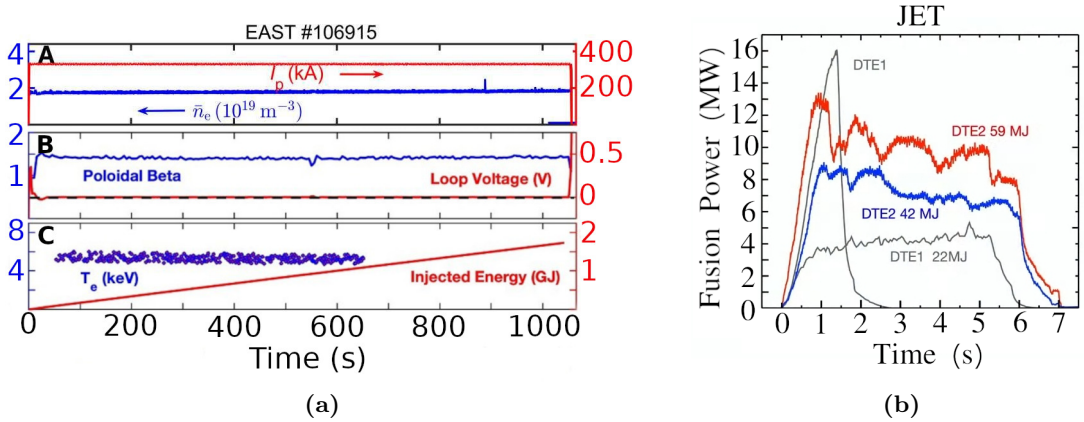


**(a)** **(b)**

**Figure 1.5:** (a) Main plasma parameters time-traces in the non-inductive plasma discharge in the EAST tokamak. $I_p$ is kept on the $330kA$ level, while the induced loop voltage is close to zero. Adapted from [12, 13] (b) Fusion power generated in D-T reactions in JET tokamak. DTE1 campaign (1997): $P_{fus} = 16MW$ in a transient and $P_{fus} = 4MW$ in a flat-top regimes. DTE2 campaign (2021): a flat-top $P_{fus} = 10MW$ in 15/85 D-T mixture (red) and $P_{fus} = 7MW$ in 50/50 (reactor-like) D-T mixture (blue). Adapted from [14, 15].

Scientific energy breakeven was not achieved in tokamaks to date. Tokamaks have demonstrated $Q = 0.3$ in a flat-top and $Q = 0.7$ in a transient regimes (figure 1.5b). On 21 December 2021 in Joint European Torus (JET) ∼10 $MW$ of fusion power were generated in 5s flat-top D-T plasma (figure 1.5b) with ∼30 $MW$ as an input by neutral beam injection (NBI) and ion cyclotron resonance heating (ICRH) [47]. The JT-60U tokamak

in Japan is the $n_i T_i \tau_E$ record holder among tokamaks with a value $1.53 \cdot 10^{21}\ m^{-3} keV s$ in the D plasma [48].

Two tokamak-reactors are currently under construction: ITER [49] and SPARC [50]. ITER and SPARC suppose to achieve high $n_i T_i \tau_E$ and demonstrate scientific breakeven in the D-T mixture (figure 1.4a). ITER is an international state-funded project, which is located in southern France. Conceptual and engineering designs were carried out in the 1990s. On 24 October 2007 the ITER organization was officially established by the seven members - China, the European Union, India, Japan, Korea, Russia and the United States. ITER plans to demonstrate Q > 10 in 2035. Besides, ITER plans to achived Q > 5 in a non-inductive steady-state regime [51]. The SPARC project was announced in 2018 by the privately-funded company Commonwealth Fusion Systems (CFS), Cambridge, Massachusetts, US. Q > 2 according to the conservative estimations and Q > 11 according to the optimistic estimations is expected to be achieved in SPARC [52]. SPARC construction is supposed to be finished by the end of 2025 [53].

Superconductors are essential for the tokamak-reactor design. The coil heating due to the electrical resistivity leads to large wall-plug electricity demands and conductor overheating in the non-superconducting tokamak, which makes copper based reactor design not feasible. Therefore, all planned tokamak-reactors use superconductors. The ITER design is based on conventional superconductors. A critical **B**, at which the conductor loses the superconductivity, limits $B_t$ in the plasma around 6T. Tokamak operational limits and the energy confinement [54] for the given $B_t$ suggest that $n_i T_i \tau_E$ can be increased by increasing the $\tau_E$. For the given **B** $\tau_E$ can be increased by increasing the size of the machine (together with the $I_p$ (1.5)). Using the multi-machine $\tau_E^{98,y2}$ scaling for $H_{98,y2} = 1.0$ [55]:

$$\tau_E = H_{98,y2} \cdot \tau_E^{98,y2}, \quad \tau_E^{98,y2} = 0.05621 \cdot I_p^{0.93} \cdot B_t^{0.15} \cdot \overline{n}_e^{0.41} \cdot P_h^{-0.69} \cdot R^{1.97} \cdot \kappa^{0.78} \cdot \varepsilon^{0.58} \cdot M^{0.19} \tag{1.4}$$

where $H_{98,y2}$ is a multiplicative pre-factor, which represents the specific regime $\tau_E$ difference with respect to the predicted $\tau_E^{98,y2}$ for the high confinement mode (H-mode) (section 1.5), $\overline{n}_e$ is the volume-averaged density, M is the averaged mass number, R is the tokamak major radius, $\varepsilon$ is the inverse aspect ratio, $\kappa$ is an elongation. The units are (s, MA, T, MW, $10^{19}\ m^{-3}$ , AMU, m). It defines large scales of ITER [54].

High-temperature superconductor (HTS) coils, which have been recently developed, have larger critical **B** (also critical temperature and critical current density) than conventional superconductors. On 5 September 2021, using full-scale HTS coil the **B** of 20T was achieved [53]. HTS magnets potentially can be game-changers in the fusion technology, because plasma $B_t$ can be increased up to $\approx 12\ T$ via HTS application. Larger **B** extends tokamak operational limits, i.e. larger pressure $n_{i0} T_{i0}$ can be reached, because the beta limit is not violated in a high-field tokamak [50]. Also, larger $B_t$ allows to establish a larger $I_p$. Consequently, an increased $I_p$ leads to the broadening of a $n_e$ limit. According to the $I_p$ [56] and $n_e$ [57, 58] limits:

$$I_p^{max} = \frac{5a\varepsilon B_t}{q_{95}^{lim}} f_{corr}^{Uckan}, \quad n_e^{GW} = \frac{I_p}{\pi a^2}, \tag{1.5}$$

where $f_{corr}^{Uckan}$ is a geometrical factor from [59], $a$ is a minor tokamak radius, $q_{95}^{lim} \approx 3$ is a minimal safety factor needed for stable tokamak operation ($q_{95}^{min} > 2$ is a hard limit: an external kink mode is destabilized). Subsequently, larger $I_p$, $B_t$, $n_e$ lead to the $\tau_E$ increase (1.4) without changing the device size. Thus, the $\tau_E$ can be increased up to the JET values in AUG/DIII-D/EAST/KSTAR size machine in $H_{98,y2} = 1.0$ regime [52].

**Table 1.1:** Tokamak's pressures and triple products. An illustration of those relations to confinement times and auxiliary heating power density.

| | JET 42976* | SPARC | ITER |
|---|---|---|---|
| $\tau_E$, $s$ [60, 7] | 0.9 | 0.77 | 3.7 |
| $T_{i0}$, $keV$ [60, 7] | 28 | 20 | 20 |
| $n_{i0}$, $10^{19}m^{-3}$ [60, 7] | 3.3 | 40 | 10 |
| $P_h$, $MW$ [60, 52, 51] | 25.7 | 25 | 73 |
| $V$, $m^3$ [52] | 80 | 16 | 800 |
| $P_h/V$, $MW/m^3$ | 0.32 | 1.6 | 0.09 |
| $P_h\tau_E/V$, $MPa$ | 0.28 | 1.23 | 0.33 |
| $n_{i0}T_{i0}$, $keV10^{20}m^{-3}$ | 9.2 | 80 | 20 |
| , $MPa$ | 0.15 | 1.28 | 0.32 |
| $n_{i0}T_{i0}\tau_E$, $keV10^{20}m^{-3}s$ | 8.3 | 62 | 74 |

*one of the high fusion power discharges [60]. Other high fusion power discharges have different parameters, but a similar $n_{i0}T_{i0}\tau_E$.

The steady-state 0-D energy balance suggests:

$$\frac{3n_iT_iV}{\tau_E} \approx P_h \tag{1.6}$$

where plasma volume ($V$) and auxiliary heating power ($P_h$). Here for simplicity, $n_e \approx n_i$ and $T_e \approx T_i$, and the fusion and the bremsstrahlung power were neglected (the net heating power at high-Q is found similar to the chosen $P_h$ [61, 52]). Therefore, for the JET-like $P_h$ and $\tau_E$, but smaller $V$ in a compact device, the average ion pressure $n_iT_i$, as well as a central ion pressure $n_{i0}T_{i0}$ can be achieved larger than in JET (Table 1.1). High $n_iT_i$ was demonstrated in small high-field high-current tomkamk Alcator C-Mod [62]. Thus, in SPARC it is possible to achieve ITER-like $n_iT_i\tau_E$ [7] for a JET-like $\tau_E$ (Table 1.1). Note, the ITER and JET $n_{i0}T_{i0}$ are smaller than for SPARC due to

$P_h\tau_E/V$ difference (together with operational limits, which does not allow high pressures in ITER [54]).

Describing tokamaks, it is valuable to mention about one of the main threat of the tokamak stable operation, i.e. plasma disruptions [63]. They lead to the high first-wall loads, which can cause PFM melting, high currents and high mechanical stresses, which can also lead to the severe damages. An intensive development of the disruption prediction [64], mitigation [65] and resilience [66] for reactor-type tokamaks are underway. However, it is not clear to date, if these technologies can be sufficiently reliable for a stable reactor operation. If this issue is not solved, stellarators are the best next candidates as fusion reactor approach, since they have demonstrated decent $n_iT_i\tau_E$ (figure 1.4a) and does not significantly suffer from the plasma disruptions due to the absence of the $I_p$ [67]. Also, current drive systems, which consume additional power for the $I_p$ generation, are not needed in stellarators. Further discussion is devoted to the physics in tokamaks, in spite of this, theoretical results, which are obtained in the thesis, can be applied (with the required modifications) for stellartors or for any other fully-ionized plasma applications within the theory applicability area.

## 1.4 Tokamak configurations: limiter and divertor

In a tokamak, a "twisted" magnetic lines form, so called, magnetic surfaces (figure 1.4b). The magnetic surfaces form a set of nested toroids. We consider the toroidally-symmetric case, where the toroidal angle ($\varphi$) is defined identically as an angular coordinate in a cylindrical coordinate system. Each for the surface can be uniquely defined by the set of points with the same poloidal magnetic flux ($\Psi_p$), i.e the magnetic flux, which passes through the surface, which is bounded by the ring, which is formed by the set of points with different $\varphi$. In the poloidal plane, i.e. plane, which is perpendicular to the toroidal direction, we define a radial ($r$) and a poloidal ($\theta$) coordinates (figure 1.6). The $\theta$ coordinate is along the flux surfaces in the poloidal plane. The $r$ coordinate is a normal to the flux surfaces.

Due to the Lorenz force in $\mathbf{B}$, charged particles move along Larmor orbits (figure 1.6) instead of freely escaping the high pressure region, which is needed for fusion to occur. It prevents the energy and particle transport across $\mathbf{B}$. Due to $B_p$ all points of the flux surface are connected along $\mathbf{B}$. As a result, an electrostatic potential, caused by the difference in the drift motion for electrons and ions [68], is equalised via parallel electrical conductivity. A tokamak concept is built around this idea, since in case of small $B_p$, the electrical charge accumulation at the different points of the flux surface leads to the fast plasma loss [68]. Also, in a zero-order approximation, $n_e$ ($n_i$), $T_e$, $T_i$ can be assumed equal on the each flux surface, due to the efficient transport along $\mathbf{B}$. However, the plasma is not perfectly confined in the tokamak. Namely, there is a perpendicular, with respect to $\mathbf{B}$, energy and particles loss (perpendicular loss). This loss occur in the radial direction, mainly due to the drift-driven microscopic turbulence [69]. Therefore, the $P_h$, which is delivered to the center of the flux surfaces are transported outwards in the radial direction with a characteristic time $\tau_E$. Consequently, plasma extends into

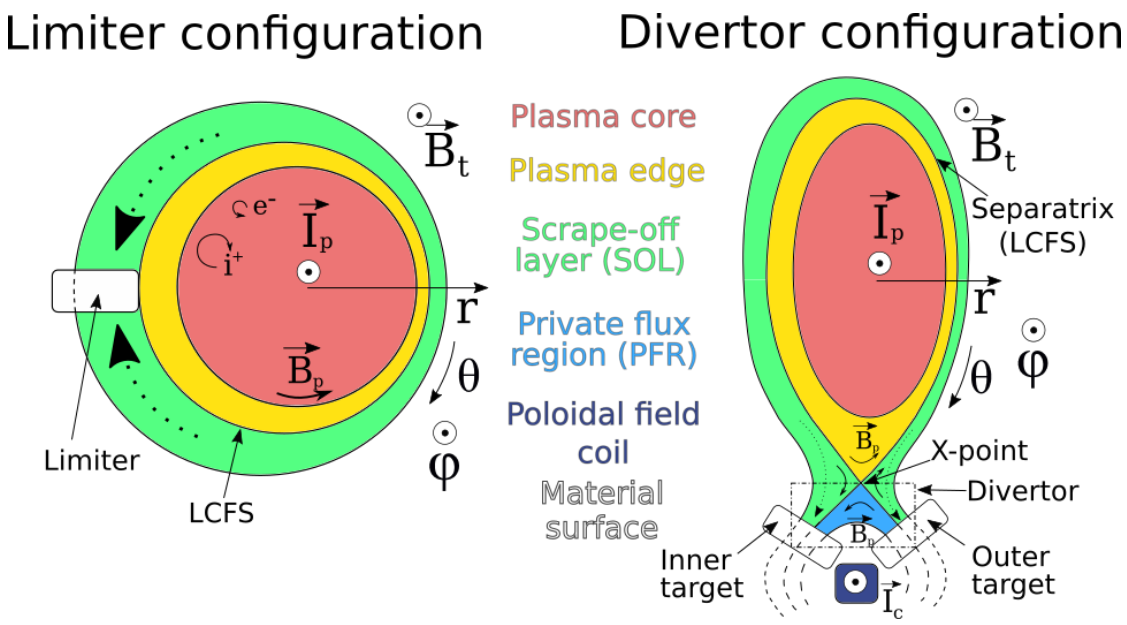


**Figure 1.6:** The limiter (left) and divertor (right) tokamak configurations in the poloidal plane. In the limiter configuration, plasma is limited by the limiter surface. In the divertor configuration, plasma is limited by the separatrix surface, which is created by the $B_p$, induced by both $I_p$ and $I_c$ (current in the poloidal field coil). The X-point is formed at the location, where $B_p$ from $I_p$ is exactly compencated by $B_p$ from $I_c$. Dotted arrows represent plasma flows in the SOL (an accrual flux structure is more complex). The figure is inspired by [16].

the outer flux surfaces, until this propagation is not stopped by a some barrier. One of the tokamak configurations uses a part of the wall to "limit" the plasma. In this limiter configuration, in the steady-state case (1.6), plasma fills all the flux surfaces from the center to the limiter (figure 1.6). In this case, an additional type of loss, i.e. the parallel, with respect to **B**, energy and particles loss (parallel loss), occur. After crossing the last closed flux surface (LCFS), i.e. the next flux surface after this intersects with the limiter, the plasma is efficiently transported in the parallel direction to the limiter surface, where it is cooled down and recombined, i.e. become a neutral gas [70]. The region outside the LCFS is called the scrape-off layer (SOL) (figure 1.6). The region inside the LCFS and close to the LCFS, where the processes due to the vicinity of the LCFS plays important role, is called plasma edge (figure 1.6). The region deep inside the LCFS, where the prosseses independent from the edge and SOL processes, is called plasma core (figure 1.6). The exact border between the core and the edge depends on the definition for a particular application.

It is required to separate the plasma inside the LCFS (confined region) from the region, where the plasma particles impact the surface. Interaction with the surface leads to the impurity (W, if it is used as a PFM) production due to the sputtering. The impurity source should be located remotely from the confined region, to avoid fusion

plasma dilution by impurities, which leads to the additional radiation energy and fusion efficiency losses. Moreover, the increased area between the confined region and the material surface can be used to dissipate energy into the wider area to prevent melting of the PFM, which can occur at the plasma-surface interaction location. Driven by these ideas the, so-called, divertor tokamak configuration (figure 1.6) was developed [70]. In this configuration the plasma is limited by the separatrix surface, which is formed by using an additional poloidal field coil, in the bottom and/or top of the tokamak. Thus, flux surfaces which are outside the separtrix go around this poloidal field coil and eventually intersect with the surface. The region, where the plasma is transported in the parallel direction through the SOL after crossing the separatrix, and where it interacts with the surface (target), is called divertor (figure 1.6).

Instead of the coordinated system, which depends on the **B** configuration, it is sometimes convenient to define an ordinary polar coordinates ($r^*$,$\theta^*$) in each poloidal plane. Only 0 point is defined by **B** in this case. Together with $\varphi$ they form an orthogonal curvilinear coordinate system ($r^*$,$\theta^*$,$\varphi$). For example, one can define the surface for the $\theta^* = 0$, which is called outer mid-plane (OMP), and the surface for the $\theta^* = \pi$, which is called inner mid-plane (IMP). The OMP and IMP can be also described in ($r$,$\theta$,$\varphi$) using corresponding coordinate transform ($r^*$,$\theta^*$,$\varphi$) $\rightarrow$ ($r$,$\theta$,$\varphi$).

## 1.5 H-mode

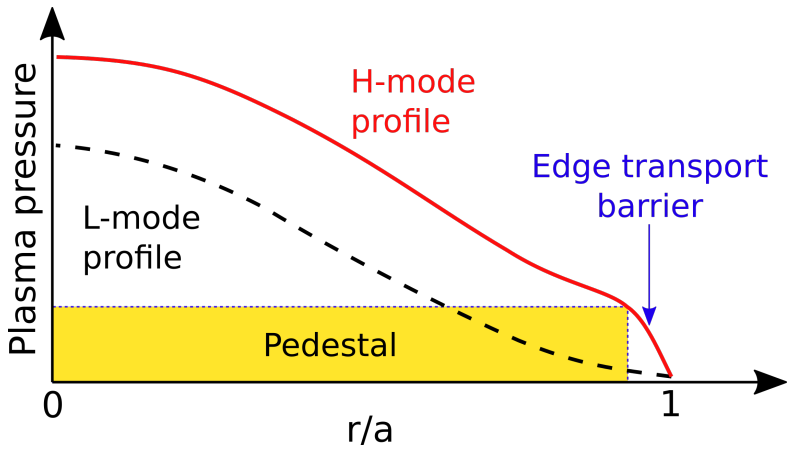


**Figure 1.7:** Schematic illustration of the difference between the plasma pressure radial OMP profile in the L- and H-mode. The r coordinate is normalised (r/a) to the distance between the magnetic axis and the LCFS in the OMP (here a is slightly different from the typical minor radius definition).

At low values of the $P_h$ the plasma remains in the low confinement mode (L-mode) with $H_{98,y2} \approx 0.5$. This regime exhibits high radial transport caused by turbulence (section 3.1) is observed. On 4th February 1982, the H-mode was experimentally achieved for the first time in human history on the ASDEX tokamak in Garching, Germany [71]. The

H-mode is characterized by a sudden improvement in confinement compared to the L-mode with $H_{98,y2} \approx 1.0$. This breakthrough was unexpected, and its underlying physical mechanism was unclear at the time, remaining incomplete even today.

However, there are commonly accepted features of the H-mode. In the plasma edge, a strong radial electric field ($E_r$) peaking leads the zonal $E \times B$ flows that reduce radial turbulent transport. This reduction in turbulence results in the formation of an edge transport barrier (ETB) for the energy and particles. Consequently, the pressure gradient drastically increases in the edge region, as depicted in figure 1.7. The H-mode pressure profile is elevated compared to theL-mode pressure profile at the so-called H-mode pedestal (figure 1.7).Furthermore, in addition to the improvement in $\tau_E$, the increase in $n_i T_i$ is also beneficial for the $n_i T_i \tau_E$ (section 1.3). It is not surprising that practically all modern tokamak-reactor designs rely on establishing an H-mode.

However, there are special magnetohydrodynamics (MHD) instabilities that occur at the edge in typical H-mode scenarios.These instabilities, known as edge localized modes (ELM)s, cause periodic relaxation of pressure gradients in short time periods.They release a large amount of energy into the SOL, which can damage PFM of the divertor or the first wall. Consequently, ELMs should be avoided in reactor machines. Several methods for active ELM suppression or mitigation exist, such as the resonant magnetic perturbations (RMP) system [72, 63]. Moreover, intrinsically ELM-free regimes are currently being actively developed [73].

## 1.6 Plasma edge in a tokamak

Recently it has been understood that the edge and SOL plasma behavior affects significantly the total plasma performance, and the studies in this area has been accelerated. However, edge and SOL physics is complicated (also in ELM-free regimes). First-of all, in contrast to the core, plasma parameters changes significantly, while plasma is transported from the core-edge boundary to the wall. For example, in the ITER baseline partially detached scenario [74, 75] plasma parameters changes from $T_e = 2\ keV$, $n_e = 9 \cdot 10^{19}\ m^{-3}$ at the core-edge boundary, through $T_e = 200\ eV$, $n_e = 3 \cdot 10^{19}\ m^{-3}$ at the sepatratrix, towards $T_e = 2\ eV$, $n_e = 3 \cdot 10^{21}\ m^{-3}$, when plasma reaches the divetror target. At the each location different processes play those major roles. Second, the interaction with the surface includes a complex plasma-sheath and neutral-recycling processes, i.e. atom/molecular multiple reflections from the surface after plasma recombination on it and following ionisation in the plasma volume, accompanied with the material surface sputtering [70]. Third, neutral and impurity radiation provides significant heat sinks, which significantly change plasma behaviour. Fourth, plasma-neutral and neutral-neutral interactions, including molecular chemistry, play major roles in the tokamak performance, acting in the SOL and especially divertor. Fifth, a divertor configuration (figure 1.6) requires complex 3D-geometry treatment, which in some cases can be reduced to a 2D-problem by exploiting toroidal symmetry. Sixth, in contrast to the core physics in the edge and SOL turbulent transport is usually performed via large-

scale non-local structures, i.e. filaments [76]. It is limiting the flux-tube local turbulence simulations applicability.

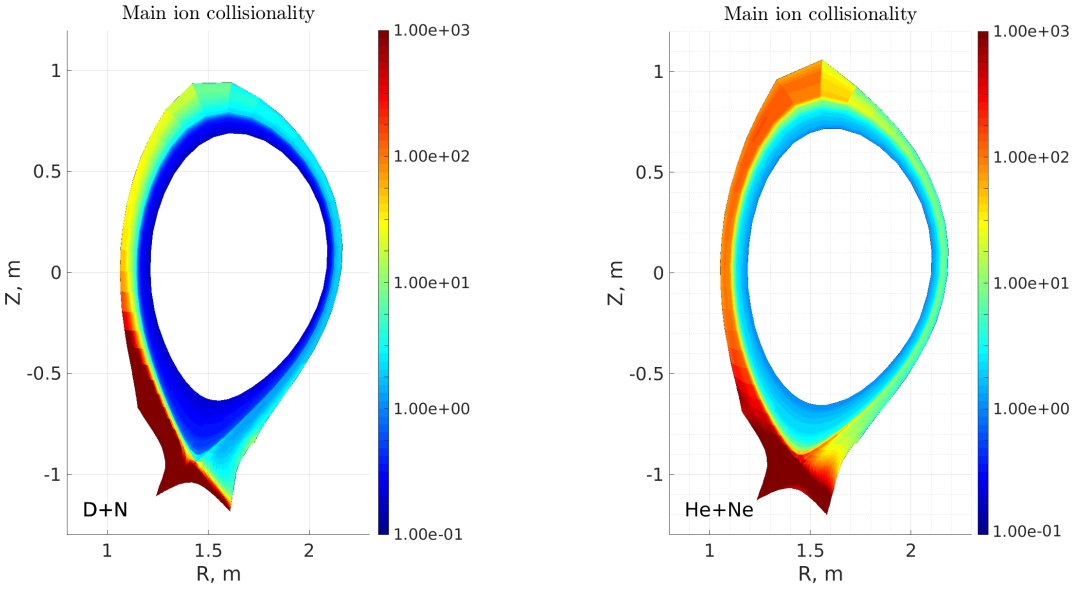


**(a)** **(b)**

**Figure 1.8:** Examples of the SOLPS-ITER code (discussed in details in section 3.3) simulation results. High main ion collisionality is observed in the SOL of ASDEX Upgrade plasmas: (a) D with impurities (b) He with impurities. He plasmas also exhibit high collisionality in the plasma edge, because the ion collisionallity scales as $Z^3$ (Z - ion charge number) for the similar $T_i$ and $n_e$ [17].

However, one of the properties can be exploited for the edge and SOL models reasonable simplification. The SOL (and in some cases edge) plasmas are highly collisional (figure 1.8a), by which it is meant that macroscopic parameters change slowly on parallel (perpendicular) length scales of the mean free path (gyroradius) and time scales between collisions (gyromotion period). For the highly collisional plasmas, so-called, a collisional closure can be used. It allows to solve a set of 3-D fluid equations instead of 6-D kinetic equitation in phase space. The analytical contraction of the velocity space leads to the great economy of computational resources by avoiding numerical velocity space integration with a high resolution, in a wide range of the temperatures from $T_e = 2\ keV$ in the edge to $T_e = 2\ eV$ in the divertor.

## 1.7 Multi-ion collisonal plasma

For the highly collisional plasmas a closure method such as the one proposed by Braginskii [17] can be applied to the moments of the distribution function. The kinetic effects are taken into account in the fluid equations by means of transport coefficients,

such as the heat conductivity, the dynamic viscosity, the friction and the thermal force kinetic coefficients, which are obtained by closure. However, the Braginskii approach is applicable to the single-ion species case and assumes only trace levels of impurities. There are many different ion species in non-trace amounts in fusion plasmas. First, the fraction of the two fuel components D and T should be controlled at the level close to 50/50 in the plasma core, by the puffing, pellet injection and pumping, for the most efficient fusion reactions. Second, helium (He) is a product of fusion reactions, which should be efficiently removed from the reactor by the pumping system. Third, a radiative impurity, for example neon (Ne), is seeded into the divertor region for the target heat loads control. Radiative impurity transport studies are essential for reactor operation. The machine should be designed, to compress impurities in the divetor, i.e. increase the amount of impurity in the divertor for the sufficient impurity radiation at this location and decrease the amount of impurity in the core to prevents its dilution. Forth, the divertor plasma mixture and plasma parameters should be controlled to reduce W sputtering from the target. All of these challenges can be effectively addressed through the utilization of multi-species edge and SOL models. For the multicomponent case, Grad method [77, 78] can be applied. This method is based on the tensorial Hermite polynomials finite expansion approximation of the distribution function with a local Maxwellian distribution function as the zeroth-order approximation. Grad method allows treatment of arbitrary plasma mixtures, i.e. species in the mixture can have both close and very different masses and/or densities. The Zhdanov closure, which is based on Grad method, is discussed in detail in [18, 79]. Transport equations for multicomponent fully ionized plasmas consisting multiple charged species were obtained in the 21N-moment approximation by Zhdanov and Yushmanov [79]. The more complete set of moment equations, including equations for the partial viscous-stress tensors, is presented in [18]. The Grad-Zhdanov method includes numerical explicit matrix inversion method (EMIM). Thus, the transport coefficients, which are calculated using closure, cannot be written via some analytical expressions. However, under assumption of the large mass difference between main ions and impurities the Zhdanov-Yushmanov (ZY) analytical expressions were developed to close the system of the moment equations. Based on ZY analytical expressions the Braginskii closure were extended for the light single main ion species with multiple heavy impurity species case [80]. Also, the single-ion heat stress tensor, which plays its major role in the $E_r$ formation [81], which defines the radial turbulent transport [82](and references therein), is used for the Braginskii closure extension for the fluid equations [83]. However, for the fusion reactor $D + T + impurities$ mixture simulations a complete Grad-Zhdanov closure including the heat-stress tensor should be implemented together with self-consistent Braginskii equations multi-ion generalization.

## 1.8 Scope of the thesis

The first part of the thesis, which is presented in chapter 4, is devoted to the improvement and extension of the 21N-moment Zhdanov closure [18]. Using the general expression for the moment equation (A1.8) in [18], which were obtained by Zhdanov, the parallel-

parallel component (along **B**) of the viscous-stress tensor, which is depend on the the parallel and diamagnetic heat fluxes, is derived [84]. Besides, the improved versions of the ZY analytical expressions are developed taking into account species masses dependence. This allows to extend applicability of analytical transport coefficients for the middle mass impurities [84], such as He and Ne, whereas the ZY analytical expressions show different impurity transport behaviour [85]. For D-T mixtures the improved analytical method (IAM) provides qualitatively correct results, but for the accurate transport coefficients calculation the EMIM is required [84].

In the second part of the thesis (chapter 5), the fluid equations for the 2D transport and 3D turbulent models are discussed. Significant non-Maxwellian part of the distribution function is present along **B** in collisional magnetized plasma [18, 17]. This affects the parallel transport coefficients, which control the plasma dynamics along **B**. The parallel transport in SOL and private flux region (PFR) plays an important role in transferring energy, momentum and particles from the plasma towards targets, between targets and from the targets towards plasma. Besides, the plasma dynamics along **B** affects plasma transport across **B**. First of all, in the confinement region, the stationary **B** and electric field (**E**) leads to the diamagnetic and $E \times B$ mean-field drifts, which are balanced by the parallel flows. In the toroidal geometry, the result of the interplay between the cross-field and parallel stationary transport is the perturbations of the plasma parameters (species densities, temperatures and electrostatic potential) on the magnetic surface, which leads to the neoclassical energy, momentum and ion (main and impurity) transport across the flux surfaces [81, 86]. Thus, a correct implementation of the collisional parallel transport into the fluid 2D transport SOLPS-ITER code [87], which is discussed in details in section 3.3, allows to take these effects into account [88, 83]. Second of all, the parallel plasma dynamics characterizes the microscopic turbulence behavior [69]. The collisonal parallel dynamics based on Braginskii transport coefficients is the key part of the fluid 3D turbulent GRILLIX code [89, 90], which is discussed in details in section 3.4. Multi-ion generalized fluid equations for the SOLPS-ITER and GRILLIX models are obtained in the thesis.

The third part of the thesis is dedicated to the SOLPS-ITER modeling results. Those are discussed in chapter 6. First, the difference in the middle mass impurity SOL transport due to the mass contribution in the IAM friction and thermal force kinetic coefficients in the ITER baseline scenario simulations is discussed [85]. Second, the first SOLPS-ITER $D + T + Ne$ simulations in JET-like configuration are carried out [91]. The difference in the hydrogen isotope behaviour in SOL due to the Zhdanov thermal force and neutral physics is analyzed. However, before the new advances of this thesis are outlined, it is worth to describe the basis and the current state of the multi-species collisional theory (chapter 2). Also, a brief overview of the SOLPS-ITER and GRILLIX models is performed in chapter 3.

# 2 Multi-species collisional theory

In this chapter the connection between microcopic phenomenon, i.e. binary collisions between particles, with the statistical behavior of plasma, i.e. plasma kinentics, and consequently, with the macroscopic plasma dynamics, i.e. fluid equations is discussed. This is performed via the multi-species collisional closure theory, which was developed by Zhdanov and Yushmanov [18], which is based on Grad method [77, 78]. Also, the inconsistency in the Zhdanov monograph [18], which is resolved in [92], is taken into account.

## 2.1 Zhdanov and Braginskii approaches

The Zhdanov and Braginskii closures can be applied to collisional plasmas. The differences between these approaches should be emphasized.

The Zhdanov closure approach relies on the Grad moment method for solving the kinetic equation. This method assumes that, for a given set of moment equations of the $k$-th order, the distribution function of each species in the mixture can be approximated using a series, where coefficients higher than the $k$-th order are set to zero. In the Zhdanov method, the linearization procedure is applied to both the left hand side (l.h.s.) and the collisional right hand side (r.h.s.) of the moment equations, while considering the complete kinetic equation with the Boltzmann collisional operator.

In contrast, the Braginskii closure [17] is based on Chapman–Enskog method, where the distribution function is expanded in a series using a small parameter $\varepsilon$. The $\varepsilon \approx \lambda/L$, where $\lambda$ is a mean-free path of the corresponding species, and $L$ is a characteristic length scale of the problem, represents the well-known Knudsen number. By employing $\varepsilon$-ordering, the linearization procedure is directly applied to the kinetic equation prior to integration through the moment method.

The Braginskii closure specifically applies to single-ion plasma mixtures, utilizing the ordering of the small electron-to-ion mass ratio ($m_e/m_i$) to simplify the collisional operator in the kinetic equations. This simplification allows for the separate solution of electron and ion equations by neglecting terms on the order of $m_e/m_i$. In contrast, the Zhdanov closure can be applied to mixtures of species with arbitrary masses, including multi-ion plasmas.

It is important to note that, as described in paragraphs 4.6 and 4.7 of the Zhdanov monograph [18], the Grad method, when linearized with respect to $\varepsilon$, is equivalent to the linear Chapman-Enskog method. This equivalence justifies the truncation of the expansion at a certain order $k$ to approximate the distribution function. Additionally, for single-ion plasmas, the $m_e/m_i$ ordering can be applied in the final step of the Zhdanov

closure (paragraph 8.2 in [18]), reproducing the well-known Braginskii results for electron and ion transport coefficients.

Lastly, it should be highlighted that the Braginskii closure employs the Landau collisional operator, which limits its applicability to Coulomb collisions only. On the other hand, the Zhdanov closure is based on the Boltzmann collisional operator, allowing for the inclusion of various types of elastic collisions with known differential cross-sections, such as those involving neutral atoms and charged particles (ions and electrons). The subsequent sections of this thesis discuss the introduction of multi-species collisional theory.

## 2.2 Microscopic level: collisional operator for the kinetic equation

The behavior of particles during binary collisions can be effectively described by considering scattering in a central field. This approach allows us to understand the trajectories and interactions of particles in collision processes, providing valuable insights into their dynamics and behavior.

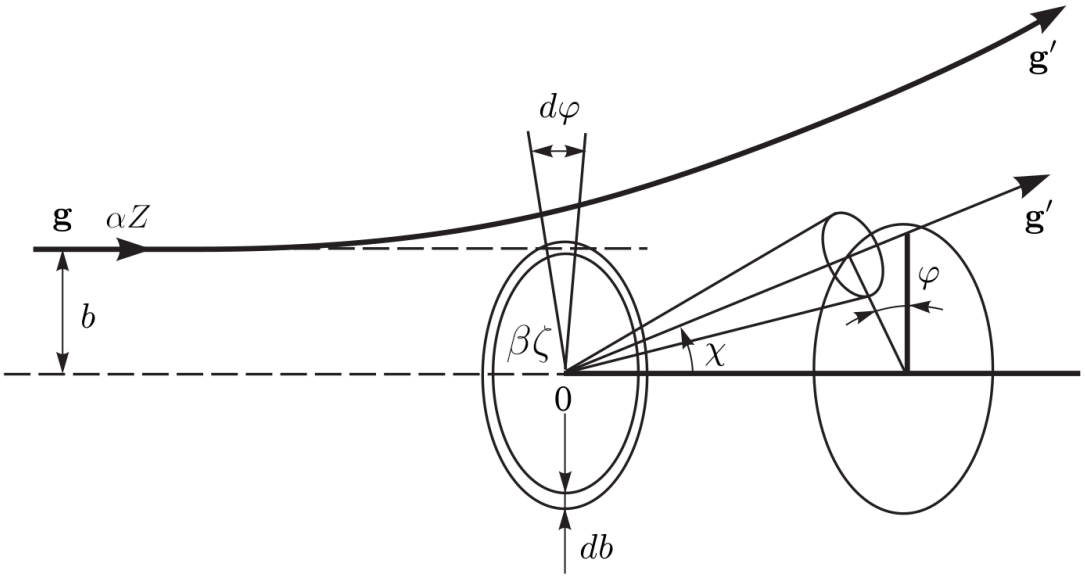


**Figure 2.1:** The elastic collision ($g = g'$) of a particle type $\alpha Z$ with a particle type $\beta\zeta$. The reference point "0" is attached to the particle $\beta\zeta$. The figure is adapted from [18].

Following Zhdanov notation from chapter 8th in [18], the subscripts $\alpha Z$ are used in the thesis to define species-dependent variables where the first subscript defines a species type $\alpha$ with mass $m_\alpha$, and the second subscript defines the a charge number $Z$. In plasma the movement of the species $\alpha Z$ is described with the kintetic equation with the collisional operator $C_{\alpha Z}$:

$$\frac{\partial f_{\alpha Z}}{\partial t} + \mathbf{v} \cdot \frac{\partial f_{\alpha Z}}{\partial \mathbf{r}} + \frac{\mathbf{F}_{\alpha Z}}{m_\alpha} \cdot \frac{\partial f_{\alpha Z}}{\partial \mathbf{v}} = C_{\alpha Z} \tag{2.1}$$

The distribution function $f_{\alpha Z}(\mathbf{r}, \mathbf{v}, t)$ defines the amount of particles in the 6-D phase-space volume $d\mathbf{r}d\mathbf{v}$, where the $\mathbf{r}$ is a radius-vector and the $\mathbf{v}$ is a velocity space. The $\mathbf{F}_{\alpha Z}$ is an extarnal force, i.e , which acts on the species $\alpha Z$. The Boltzmann collisional operator for the species $\alpha Z$ with species $\beta\zeta$ describes the sources and sinks of the species $\alpha Z$ in the $d\mathbf{r}d\mathbf{v}$ per $dt$:

$$C_{\alpha Z} = \sum_{\beta\zeta} C_{\alpha Z \beta\zeta}, \qquad \boxed{C_{\alpha Z \beta\zeta} = \iint (f'_{\alpha Z} f'_{1\beta\zeta} - f_{\alpha Z} f_{1\beta\zeta}) g \sigma_{\alpha Z \beta\zeta}(g, \chi) d\Omega d\mathbf{v}_{1\beta\zeta},} \tag{2.2}$$

where the $f'_{\alpha Z} \overset{\text{def}}{=} f_{\alpha Z}(\mathbf{r}, \mathbf{v}'_{\alpha Z}, t)$, the $\mathbf{v}'_{\alpha Z}$ is a velocity after collision, the subscript "1" is used to distinguish projectile and target particles, when $\alpha Z = \beta\zeta$, the relative velocity before the collision: $\mathbf{g} = \mathbf{v}_{\alpha Z} - \mathbf{v}_{1\beta\zeta}$ and the relative velocity after the collision: $\mathbf{g}' = \mathbf{v}'_{\alpha Z} - \mathbf{v}'_{1\beta\zeta}$ (figure 2.1). The $\chi$ and $\varphi$ are the polar and azimuthal angles, respectively. The particle $\alpha Z$ has the $b$ impact parameter. The $d\Omega$ is the solid angle element, in which the particle $\alpha Z$, which come from the element $b\,db\,d\varphi$ of surface perpendicular to $\mathbf{g}$, is scattered.

Here and further in the thesis the species summation convention is used:

$$\sum_{\alpha Z} \equiv \sum_{\alpha=1}^{\alpha^{max}} \sum_{Z=0}^{Z_\alpha^{max}}, \quad \sum_{\alpha} \equiv \sum_{\alpha=1}^{\alpha^{max}}, \quad \sum_{j=j_1..j_2} \equiv \sum_{j=j_1}^{j_2}, \tag{2.3}$$

where we define the total number of different species types in the mixture ($\alpha^{max}$), and the maximal charge number of the species type $\alpha$ ($Z_\alpha^{max}$) The $j_1$ and $j_2$ are natural numbers, which can be different from 1 and $\alpha^{max}$. The separation of the summation over the charge states and over the species types (2.3) is the key feature, which is used in the subsections 4.3.1.2 and 4.3.4.2. This is the reason of the double subscript $\alpha Z$ notation in the thesis, despite it makes all the equations lengthy. When $Z_\alpha^{max} = 0 : \forall\alpha$ (neutral gases), the second subscript is omitted.

The main parameter, which defines the particle behaviour in the collisions, is a differential scattering cross-section $\sigma_{\alpha Z \beta\zeta}(g, \Omega)$. For the particle flux $J_{\alpha Z}$ that scatters on the center $\alpha Z$, the amount of particles, which are scattered in the $d\Omega$ per second, is $J_{\alpha Z}\sigma_{\alpha Z \beta\zeta}(g, \Omega)d\Omega$. Based on our mechanical approach (figure 2.1) one can write:

$$J_{\alpha Z}\sigma_{\alpha Z \beta\zeta}(g, \Omega)d\Omega = J_{\alpha Z} b\,db\,d\varphi. \tag{2.4}$$

The Boltzmann collisional operator (2.2) for the elastic collisions can be obtained based on the following ideas. The particle $\alpha Z$ that moves with $g$ covers with the area $b\,db\,d\varphi$

the volume of a cylinder $gb\,db\,d\varphi\,dt$ during the time interval $dt$. Therefore, The $\alpha Z$ is scattered in $d\Omega$ (figure 2.1) on the $f_{\beta\zeta}gb\,db\,d\varphi d\mathbf{v}_{1\beta\zeta}\,dt$ amount of scattering centers $\beta\zeta$ in phase-volume $d\mathbf{v}_{1\beta\zeta}$. Thus, the total negative source due to collisions for the species $\alpha Z$ is:

$$C^{-}_{\alpha Z} = -\sum_{\beta\zeta}\iint f_{\alpha Z} f_{1\beta\zeta} g b\,db\,d\varphi d\mathbf{v}_{1\beta\zeta} = -\sum_{\beta\zeta}\iint f_{\alpha Z} f_{1\beta\zeta} g \sigma_{\alpha Z\beta\zeta}(g,\chi) d\Omega d\mathbf{v}_{1\beta\zeta}, \tag{2.5}$$

where (2.4) is used. The corresponding positive source from the elastic collisions with particles:

$$C^{+}_{\alpha Z} = \sum_{\beta\zeta}\iint f'_{\alpha Z} f'_{1\beta\zeta} g' \sigma_{\alpha Z\beta\zeta}(g',\chi) d\Omega d\mathbf{v}_{1\beta\zeta}. \tag{2.6}$$

The (2.6) is directly used further in the thesis. However, using reciprocity relation for direct and inverse elastic collisions and Jacobians equality [18]:

$$g\sigma_{\alpha Z\beta\zeta}(g,\chi) d\Omega d\mathbf{v}_{\alpha Z} d\mathbf{v}_{1\beta\zeta} = g'\sigma_{\alpha Z\beta\zeta}(g',\chi) d\Omega d\mathbf{v}'_{\alpha Z} d\mathbf{v}'_{1\beta\zeta}, \quad d\mathbf{v}_{\alpha Z} d\mathbf{v}_{1\beta\zeta} = d\mathbf{v}'_{\alpha Z} d\mathbf{v}'_{1\beta\zeta} \tag{2.7}$$

one can finally obtain equation (2.2).

The $\sigma_{\alpha Z\beta\zeta}(g,\chi)$ is different for the various types of collisions. This leads to the difference in macroscopic plasma behaviours according to the type of collisions that occur. The simplest model of the neutral-neutral collisions is as solid spheres collisions with a constant diameters $d_\alpha$ and $d_\beta$. The azimuthal angles angles:

$$\cos\frac{\chi}{2} = \frac{b}{d_{\alpha\beta}}, \quad b \le d_{\alpha\beta}, \quad d_{\alpha\beta} \stackrel{\text{def}}{=} \frac{d_\alpha + d_\beta}{2}, \tag{2.8}$$

as wall as, differential cross-sections:

$$\sigma_{\alpha\beta} = \frac{1}{4} d^2_{\alpha\beta}, \tag{2.9}$$

which are independent of $g$. This is in contrast to the collisions of changed pariticles, which are described by the Coulomb potential $U_{\alpha Z\beta\zeta} = Z\zeta e^2/(4\pi\varepsilon_0 r)$, where electron charge ($e$), vacuum permittivity ($\varepsilon_0$) are defined, also $r$ is radial coordinate in the spherical coordinate system (figure 2.1). The azimuthal scattering angle $\chi$ is smaller for the given $b$ and larger $g$ (figure 2.2a):

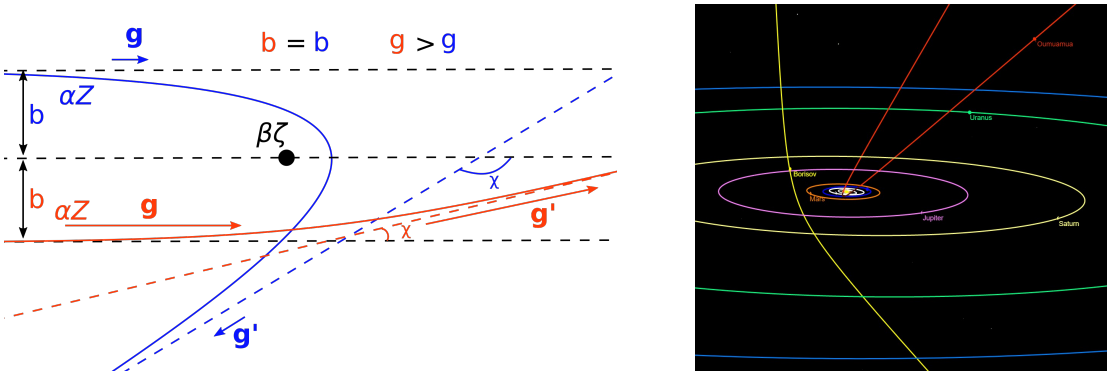


(a) (b)

**Figure 2.2:** (a) An example of the hyporbolic trajectories in the attractive potential ($sign(Z) \neq sign(\zeta)$) for the small $g$ (blue) and the large $g$ (red) and the same $b$ (red and blue). There is a larger $\chi$ for a smaller $g$. (b) Hyperbolic trajectories of the two only known interstellar objects passing though the Solar system 1I/'Oumuamua and 2I/Borisov. Adapted from [19]

$$\tan\frac{\chi}{2} = \frac{b_0}{b}, \quad b_0 \stackrel{\text{def}}{=} \frac{|Z\zeta|e^2}{4\pi\varepsilon_0\mu_{\alpha\beta}g^2}, \quad \mu_{\alpha\beta} \stackrel{\text{def}}{=} \frac{m_\alpha m_\beta}{m_\alpha + m_\beta}, \tag{2.10}$$

where reduced mass ($\mu_{\alpha\beta}$) and mass of the species ($m_\alpha$) are defined. In this case the differential cross-sections is described by the famous Rutherford formula:

$$\sigma_{\alpha Z\beta\zeta} = \frac{(b_0/2)^2}{\sin^4(\chi/2)} = \left(\frac{|Z\zeta|e^2}{8\pi\varepsilon_0\mu_{\alpha\beta}g^2}\right)^2 \frac{1}{\sin^4(\chi/2)}. \tag{2.11}$$

Thus, for the given flux $J_{\alpha Z}$, the amount particles, which are scattered into the $d\Omega$ per second, decreases with increasing $g$ according to (2.11).

This formula is derived based on a classical mechanics particle motion (figure 2.1). However, a similar formula can be obtained for quantum mechanical scattering (§20 in [93]). Therefore, our classical description is valid for Coulomb collisions in plasmas, which are considered in the thesis. In the frame of our model in a single collision the movement of the charged particle $\alpha Z$ with respect to the charged particle $\beta\zeta$ is performed along the hyperbolic trajectories like interstellar objects with respect to the Sun, for instance, an interstellar asteroid 1I/'Oumuamua, which was discovered by astronomer Robert Weryk in October 2017, and an interstellar comet 2I/Borisov, which was discovered by amateur astronomer Gennadiy Borisov in August 2019 (figure 2.2b).

The differential cross-sections contribute into the transport cross-sections of the form:

$$Q^{(l)}_{\alpha Z\beta\zeta}(g) \stackrel{\text{def}}{=} \int_{\Omega} \sigma_{\alpha Z\beta\zeta}(g,\chi)(1-\cos^{l}\chi)d\Omega \tag{2.12}$$

which appear in the collisional r.h.s. of the moment equations [18], which are discussed in the section 2.3.

For example, the corresponding transport cross-sections for $l = 1$ for the solid spheres ($SolSph$) and the Coulomb ($Coul$) collisions are [18]:

$$Q^{(1)\ SolSph}_{\alpha\beta}(g) = \pi d^2_{\alpha\beta}, \quad Q^{(1)\ Coul}_{\alpha Z\beta\zeta}(g) \approx 4\pi b_0^2 \ln\Lambda, \tag{2.13}$$

where $\ln\Lambda$ is the Coulomb logarithm ($\ln\Lambda$). In the thesis the $\ln\Lambda$ is assumed the same for all collisions, however it is possible to include different Coulomb logarithms for different combinations of colliding species following [18]. The $Q^{(1)\ Coul}_{\alpha Z\beta\zeta}(g)$ is derived by cutting integral (2.12) with $b_{max} = r_D$, as a standard Debye radius ($r_D$) shielding [17, 18]. Similarly to the differential cross-sections, the solid spheres transport cross-section is independent on the $g$, whereas the Coulomb transport cross-section decreases, when the $g$ increases. The meaning of the latter can be understood in the way: for the larger relative velocities the eccentricity of the hyperbolic trajectories in the binary collisions $\to \infty$ and the scattering angle $\chi \to 0$ (figure 2.2a). As a result, the relative velocities do not change significantly in the collisions $\mathbf{g} \to \mathbf{g'}$ and $\cos\chi \to 1$ in (2.12).

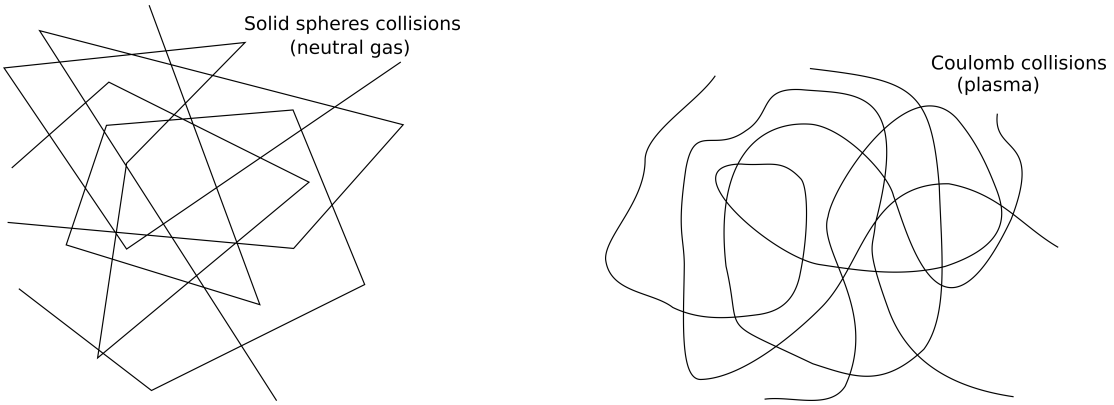


**Figure 2.3:** Schematic interpretation of the particle trajectories with (a) the solid sphere collisions and (b) the Coulomb collisions.

It is important to note that by analyzing the integral (2.13) (paragraph 1.3 in [18]) one can observe the distinction in particle trajectories between the neutral gas (figure 2.3a) and the plasma (figure 2.3b). A neutral particle moves freely and undergoes infrequent collision, resulting in large $\chi$ as illustrated in figure 2.3a. On the other hand, a charged

particle experiences frequent collisions with small $\chi$, as schematically represented in figure 2.3b. In section 2.3 the difference between neutral gas and plasma macroscopic phenomenon is discussed.

## 2.3 Macroscopic level: solid spheres vs Coulomb collisions effect on the gas behavior

Collisions play a crucial role in shaping the macroscopic dynamics of plasmas or gases. They significantly influence various transport processes, energy exchange, and momentum transfer within the system. Understanding collisional effects is essential for predicting the behavior of the plasma or gas in different scenarios and applications.

### 2.3.1 Heat and momentum exchange in the quasihydrodynamic approximation

Several important consequences for the macroscopic plasma and neutral gas behaviours due to the difference between solid spheres and Coulomb cross-sections (2.13) for the same kinetic equation (2.1) and Boltzmann collisional operator (2.2) are introduced to the reader. First, the momentum and the heat exchange between different species has different dependence on the temperature in case of the solid spheres and Coulomb collisions.

The distribution functions of each species are considered close to the local Maxwell distribution functions, with small perturbations introduced by a polynomial expansion (section 2.4). For example, in the Quasihydrodynamic approach, where the linear polynomials are taken into account, (based on the Eq. (3.1.10) and (3.1.11) from [18]) the corresponding r.h.s. terms can be written:

$$\mathbf{R}_{\alpha Z} \stackrel{\text{def}}{=} m_\alpha \iiint (\mathbf{v}-\mathbf{u}) C_{\alpha Z} d^3\mathbf{v}, \quad \mathbf{R}_{\alpha Z\beta\zeta} \stackrel{\text{def}}{=} m_\alpha \iiint (\mathbf{v}-\mathbf{u}) C_{\alpha Z\beta\zeta} d^3\mathbf{v}, \tag{2.14}$$

$$Q_{\alpha Z} \stackrel{\text{def}}{=} m_\alpha \iiint \frac{(\mathbf{v}-\mathbf{u})^2}{2} C_{\alpha Z} d^3\mathbf{v}, \quad Q_{\alpha Z\beta\zeta} \stackrel{\text{def}}{=} m_\alpha \iiint \frac{(\mathbf{v}-\mathbf{u})^2}{2} C_{\alpha Z\beta\zeta} d^3\mathbf{v}, \tag{2.15}$$

$$\mathbf{R}_{\alpha Z} = \sum_{\beta\zeta} \mathbf{R}_{\alpha Z\beta\zeta}, \quad Q_{\alpha Z} = \sum_{\beta\zeta} Q_{\alpha Z\beta\zeta}, \tag{2.16}$$

$$\mathbf{R}_{\alpha Z} = -\sum_{\beta\zeta} \frac{n_{\alpha Z}\mu_{\alpha\beta}}{\tau^{(Zh)}_{\alpha Z\beta\zeta}} (\mathbf{u}_{\alpha Z} - \mathbf{u}_{\beta\zeta}), \quad Q_{\alpha Z} = -3\sum_{\beta\zeta} \left(\frac{\mu_{\alpha\beta}}{m_\alpha + m_\beta}\right) \frac{n_{\alpha Z}}{\tau^{(Zh)}_{\alpha Z\beta\zeta}} (T_{\alpha Z} - T_{\beta\zeta}), \tag{2.17}$$

where we define moments of the distribution function: the density of the species $\alpha Z$ ($n_{\alpha Z}$), the flow velocity of the species $\alpha Z$ ($\mathbf{u}_{\alpha Z}$), the temperature of the species $\alpha Z$ ($T_{\alpha Z}$) and additionally the mass-average flow velocity ($\mathbf{u}$), the average temperature of the mixture ($T_{av}$), $n_i$ and $T_i$:

$$n_{\alpha Z} \stackrel{\text{def}}{=} \iiint f_{\alpha Z} d^3\mathbf{v}, \quad n_{\alpha Z} u_{\alpha Z k} \stackrel{\text{def}}{=} \iiint v_k f_{\alpha Z} d^3\mathbf{v}, \quad T_{\alpha Z} \stackrel{\text{def}}{=} \frac{2}{3}\frac{m_\alpha}{n_{\alpha Z}} \iiint \frac{(\mathbf{v}-\mathbf{u})^2}{2} f_{\alpha Z} d^3\mathbf{v},$$
$$\mathbf{u} \stackrel{\text{def}}{=} \frac{\sum_{\alpha Z} m_a n_{\alpha Z} \mathbf{u}_{\alpha Z}}{\sum_{\alpha Z} m_\alpha n_{\alpha Z}}, \quad T_{av} \stackrel{\text{def}}{=} \frac{\sum_{\alpha Z} n_{\alpha Z} T_{\alpha Z}}{\sum_{\alpha Z} n_{\alpha Z}}, \quad n_i \stackrel{\text{def}}{=} \sum_{\alpha Z \in ions} n_{\alpha Z}, \quad T_i \stackrel{\text{def}}{=} \frac{\sum_{\alpha Z \in ions} n_{\alpha Z} T_{\alpha Z}}{n_i}, \tag{2.18}$$

$n_e$ and $T_e$ are defined as for $\alpha$ and $Z$, which corresponds to the electrons. Using Eq. (3.1.15), (4.2.20) and (5.1.9) from [18] we define the collisional frequency:

$$1/\tau^{(Zh)}_{\alpha Z \beta \zeta} \stackrel{\text{def}}{=} \frac{16}{3} n_{\beta\zeta} \Omega^{11}_{\alpha Z \beta \zeta}, \tag{2.19}$$

$$\Omega^{lr}_{\alpha Z \beta \zeta} \stackrel{\text{def}}{=} \left(\frac{2\pi}{\gamma_{\alpha Z \beta \zeta}}\right)^{1/2} \int_0^\infty \int_0^\pi \tilde{g}^{2r+3} \exp(-\tilde{g}^2)(1-\cos^l\chi)\sigma_{\alpha Z \beta \zeta}(\tilde{g},\chi)\sin\chi d\chi d\tilde{g} =$$
$$\left(\frac{1}{2\pi\gamma_{\alpha Z \beta \zeta}}\right)^{1/2} \int_0^\infty \tilde{g}^{2r+3} \exp(-\tilde{g}^2) Q^{(l)}_{\alpha Z \beta \zeta}\left(\left(\frac{2}{\gamma_{\alpha Z \beta \zeta}}\right)^{1/2} \tilde{g}\right) d\tilde{g}, \tag{2.20}$$

$$\tilde{g} \stackrel{\text{def}}{=} \left(\frac{\gamma_{\alpha Z \beta \zeta}}{2}\right)^{1/2} g, \quad \gamma_{\alpha Z \beta \zeta} \stackrel{\text{def}}{=} \frac{\gamma_{\alpha Z}\gamma_{\beta\zeta}}{\gamma_{\alpha Z}+\gamma_{\beta\zeta}}. \quad \gamma_{\alpha Z} \stackrel{\text{def}}{=} \frac{m_\alpha}{T_{\alpha Z}}. \tag{2.21}$$

Certain simplification can be made, if the $T_{av}$ is used instead the $T_{\alpha Z}$ in: $\gamma_{\alpha Z \beta \zeta} = \mu_{\alpha\beta}/T_{av}$ (different temperatures have to be kept in $T_{\alpha Z} - T_{\beta\zeta}$, when the heat exchange source (2.17) is derived). In this case, the $\Omega^{lr}_{\alpha Z \beta \zeta}$ are well-known Chapman-Cowling integrals [94]. Thus:

$$1/\tau^{(Zh)}_{\alpha Z \beta \zeta} = \frac{16}{3} n_{\beta\zeta} \left(\frac{T_{av}}{2\pi\mu_{\alpha\beta}}\right)^{1/2} \int_0^\infty \tilde{g}^5 \exp(-\tilde{g}^2) Q^{(1)}_{\alpha Z \beta \zeta}\left(\left(\frac{2T_{av}}{\mu_{\alpha\beta}}\right)^{1/2} \tilde{g}\right) d\tilde{g}, \tag{2.22}$$

Here the contribution from the two distribution functions close to Maxwell ones is taken into account [18]. Thus, the transport cross-section is contracted with the $\tilde{g}^5$-weighted $\exp(-\tilde{g}^2)$. Qualitatively, our collisional frequency definition (2.19), (2.22) can be understood, if the motion of the mono-energetic beam with the velocity $v^{beam} = (T_{av}/\mu_{\alpha\beta})^{1/2}$ of particles $\alpha Z$ through the scattering centers $\beta\zeta$ is considered. Particle $\alpha Z$ covers with the area $Q^{(1)}_{\alpha Z \beta \zeta}\left(v^{beam}\right)$ the volume $v^{beam} Q^{(1)}_{\alpha Z \beta \zeta}\left(v^{beam}\right) dt$. The amount of scattering centers $\beta\zeta$, which are covered per unit of time, is

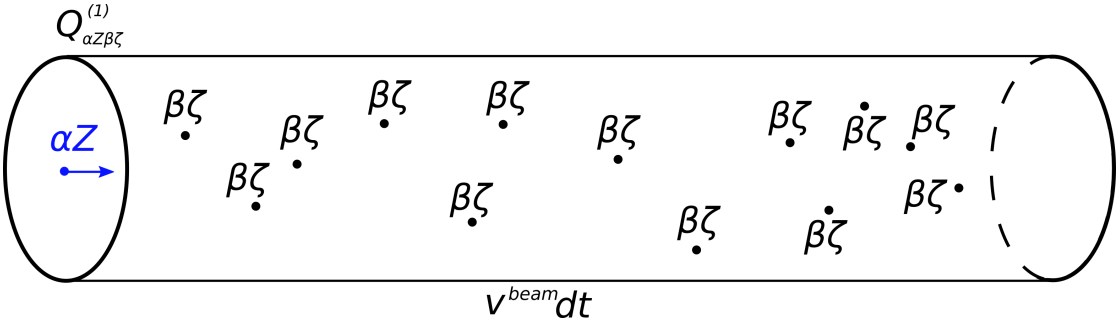


**Figure 2.4:** Particle $\alpha Z$ from the mono-energetic beam propagates through the scattering centers $\beta\zeta$ with the effective cross-section $Q^{(1)}_{\alpha Z\beta\zeta}$.

$n_{\beta\zeta}v^{beam}Q^{(1)}_{\alpha Z\beta\zeta}\left(v^{beam}\right) = A/\tau^{(Zh)}_{\alpha Z\beta\zeta}$ (figure 2.4). Therefore, the $\tau^{(Zh)}_{\alpha Z\beta\zeta}$ (up to a constant coefficient $A$) is characteristic time, when the particles $\alpha Z$ from the beam change those momentum along the beam direction due to the scattering, since $Q^{(1)}_{\alpha Z\beta\zeta}\left(v^{beam}\right) = \int_\Omega \sigma_{\alpha Z\beta\zeta}(v^{beam},\chi)(1-\cos\chi)d\Omega$ is an effective cross-section of velocity changing along a specific direction, whereas in each collision it is changed as $v^{beam}(1-\cos\chi)$. Thus, the $\tau^{(Zh)}_{\alpha Z\beta\zeta}$ is a characteristic time of the momentum exchange between two fluids along the given direction, where the constant coefficient $A$ comes from the distribution functions contribution in the integral (2.22) instead of simple beam treatment.

For arbitrary $l$ and $r$ the Chapman-Cowling $\Omega^{lr}_{\alpha Z\beta\zeta}$ integrals for solid spheres and Coulomb collisions can be found using Eq. (5.1.9) and (8.1.5) in [18] correspondingly:

$$\Omega^{lr\ SolSph}_{\alpha Z\beta\zeta} = \left(\frac{T_{av}}{2\pi\mu_{\alpha\beta}}\right)^{1/2}\frac{1}{2}(r+1)!\left[1-\frac{1}{2}\frac{1+(-1)^l}{l+1}\right]\pi d^2_{\alpha\beta}, \tag{2.23}$$

$$\Omega^{lr\ Coul}_{\alpha Z\beta\zeta} = \sqrt{\pi}l(r-1)!\left(\frac{|Z\zeta|e^2}{4\pi\varepsilon_0}\right)^2\frac{\ln\Lambda}{\mu^{1/2}_{\alpha\beta}(2T_{av})^{3/2}}, \tag{2.24}$$

The collsional time ($l=1$ and $r=1$) for solid spheres and Coulumb models can be obtained using (2.23) or (2.24) and (2.19):

$$1/\tau^{(Zh)\ SolSph}_{\alpha Z\beta\zeta} = \frac{16}{3}\sqrt{\frac{\pi}{2}}n_{\beta\zeta}d^2_{\alpha\beta}\left(\frac{T_{av}}{\mu_{\alpha\beta}}\right)^{1/2}, \tag{2.25}$$

$$1/\tau^{(Zh)\ Coul}_{\alpha Z\beta\zeta} = \frac{8}{3}\sqrt{\frac{\pi}{2}}n_{\beta\zeta}\left(\frac{|Z\zeta|e^2}{4\pi\varepsilon_0\mu_{\alpha\beta}}\right)^2\ln\Lambda\left(\frac{T_{av}}{\mu_{\alpha\beta}}\right)^{-3/2}, \tag{2.26}$$

The solid spheres collisional frequency (2.25) is increasing with temperature. This is the result of the coverage volume increases due to the constant transport cross-section $Q^{(1)\ SolSph}_{\alpha\beta}(g)$ and increasing $\alpha Z/\beta\zeta$ relative velocities (figure 2.4). For the Coulomb collisions, one can observe an opposite behaviour. The Coulomb collisional frequency decreases for the increasing temperature, because of the decrease of the coverage volume due to the faster shrinking of $Q^{(1)\ Coul}_{\alpha Z\beta\zeta}(g)$ (2.13) than the rise of the particle trajectory length with the $\alpha Z/\beta\zeta$ relative velocities (figure 2.4), according to hyperbolic scattering mechanism (figure 2.2a). Thus, we have obtained quite important result: the microscopic momentum and heat exchange between species $\alpha Z$ and $\beta\zeta$ increase in the solid spheres collisions and decrease in the Coulomb collisions for $T_{av} \uparrow$. At first glance it seems counter-intuitive, however it become clear after studying Rutherford scattering in Coulomb collisions, as it is performed above. The consequence of the momentum e-i exchange temperature dependence is a famous Spitzer resistivity $\propto T_e^{-3/2}$. Due to the inefficient e-i heat transfer in the high temperature plasmas in the magnetic fusion devices, the significant difference between $T_e$ and $T_i$ is usually observed in the plasma core (as example in stellarators [95]).

Using the higher order 13N-moment and 21N-moment Zhdanov approximations [18], the heat conductivity and dynamic viscosity can be obtained. For example, along $\mathbf{B}$ (or for $\mathbf{B} = 0$) both of them are $\propto n_{\alpha Z} T_{av} \tau^{(Zh)}_{\alpha Z\beta\zeta}$. Therefore, for the solid spheres and Coulomb models they are $\propto T_{av}^{1/2}$ and $\propto T_{av}^{5/2}$ correspondingly. The latter reproduces then well-known Braginskii results for the fully ionized simple plasma [17]. As a diffusive processes, the heat conductivity and the dynamic viscosity $\propto (\lambda^{mfp}_{\alpha Z})^2/\tau^{(Zh)}_{\alpha Z\beta\zeta} \sim \lambda^{mfp}_{\alpha Z} v^{th}_{\alpha Z}$, where we introduce the mean free-path of the species $\alpha Z$ ($\lambda^{mfp}_{\alpha Z}$) and the thermal velocity of the species $\alpha Z$ ($v^{th}_{\alpha Z}$):

$$v^{th}_{\alpha Z} \stackrel{\text{def}}{=} \sqrt{T_{\alpha Z}/m_\alpha}, \quad \lambda^{mfp}_{\alpha Z} \stackrel{\text{def}}{=} v^{th}_{\alpha Z} \overline{\tau}^{(Zh)}_{\alpha Z}, \quad 1/\overline{\tau}^{(Zh)}_{\alpha Z} \stackrel{\text{def}}{=} \sum_{\beta\zeta} \mu_{\alpha\beta}/(m_\alpha \tau^{(Zh)}_{\alpha Z\beta\zeta}) \tag{2.27}$$

Also, $\lambda^{mfp}_{\alpha Z} \propto 1/Q^{(1)}_{\alpha Z\beta\zeta}$ (here $\beta\zeta$ represents the species, which contributes the most into the sum in (2.27)). Therefore, the $\lambda^{mfp\ SolSph}_{\alpha Z}$ is independent of $T_{av}$, and the $\lambda^{mfp\ Coul}_{\alpha Z} \propto T_{av}^2$, which also leads to the corresponding heat conductivity and viscosity $T_{av}$-dependencies.

In the mixture of electrons and several ions the e-i mass difference can be exploited. In e-e and e-i collisions, relative velocities depends only on the electron distribution function. The calculation can be made more accurate, if $T_{av}$ is replaced with $T_e$ in (2.26) for e-e and e-i collisions. Correspondingly, $T_{av}$ can be replaced with $T_i$ in (2.26) for i-i collisions.

### 2.3.2 Thermal force

The second important consequence from the different particle behaviour in binary collisions is an opposite thermal force (TF) action in the neutral gas and the plasma.

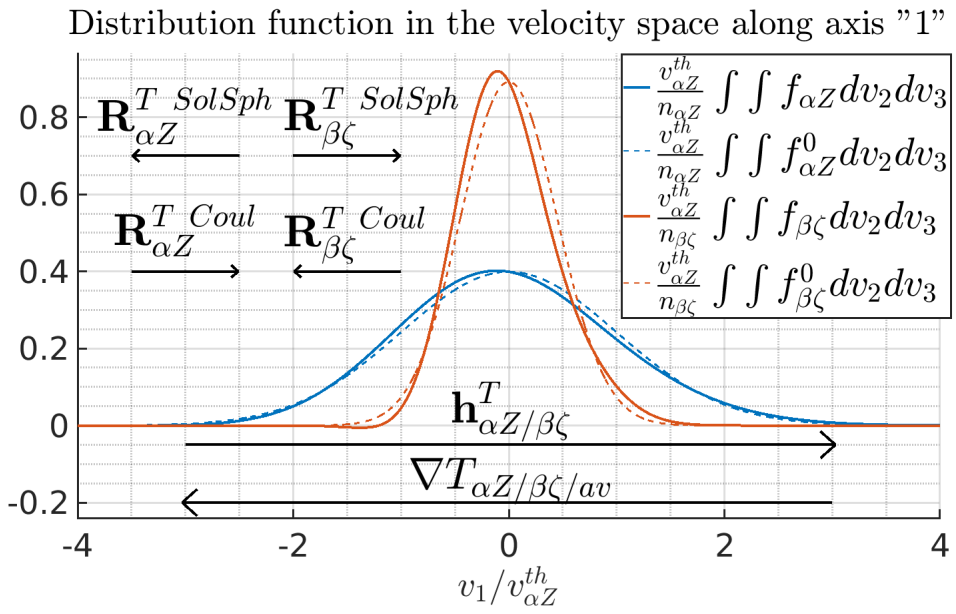


**Figure 2.5:** The distribution functions along the axis "1", which are contracted over axis "2" and "3" and normalized to the $v^{th}_{\alpha Z}$, for the light species $\alpha Z$ and the heavy species $\beta\zeta$ are plotted in the case of the temperature gradients occur along the the axis "1". Solid lines represent 13N-moment approximation of the distribution functions $f_{\alpha Z/\beta\zeta}$, whereas dashed lines represent local Maxwell distribution functions $f^0_{\alpha Z/\beta\zeta}$. Zero net particle fluxes in the positive or negative dirrections $\mathbf{u}_{\alpha Z} = \mathbf{u}_{\beta\zeta} = 0$. Also, for illustrative purposes: $\mathbf{h}^T_{\alpha Z}/n_{\alpha Z} = \mathbf{h}^T_{\beta\zeta}/n_{\beta\zeta}$.

The TF is a part of the momentum r.h.s. (2.14), which is proportional to the temperature gradient and appears in higher order approximations starting from 13N-moment, together with the heat conductivity, the viscosity and corrections to the flow velocity difference dependent part of the momentum r.h.s. (2.14), which is called friction force (FR) in the present work. The TF is a result of the hot-tail formation along the specific directions, i.e. an overpopulation of the phase-space at the large velocities $> Cv^{th}_{\alpha Z}$ in the one direction and at the small velocities $< Cv^{th}_{\alpha Z}$ in the opposite direction (constant $C \sim 1$) with respect to the Maxwell distribution function, due to the presence of the temperature gradient. To illustrate this, the example of 13N-moment approximation of the distribution functions of species $\alpha Z$ and $\beta\zeta$ for the case, where the temperature gradients are along the given "1" axis and $m_\beta = 5m_\alpha$, $T_{\alpha Z} = T_{\beta\zeta}$ and $\mathbf{u}_{\alpha Z} = \mathbf{u}_{\beta\zeta} = 0$ (also no spatial derivatives of the $u_{\alpha Z k}$ and $u_{\beta\zeta k}$), is shown in figure 2.5. Another example for 21N-moment approximation in the tokamak plasma simulations can be seen in figure 6.3 in the case, which is analyzed the subsection 6.1.3. In the 13N-moment approximation the hot-tail is introduced via 3-order vector moment - the heat flux of the species $\alpha Z$ ($\mathbf{h}_{\alpha Z}$):

$$h_{\alpha Zk} \stackrel{\text{def}}{=} \frac{m_\alpha}{2} \iiint \left( (\mathbf{v}-\mathbf{u})^2 - \frac{5T_{\alpha Z}}{m_\alpha} \right) (v_k - u_k) f_{\alpha Z} d^3\mathbf{v} \tag{2.28}$$

Then the hot-tail in the form of temperature gradient-dependent part of the heat flux $\mathbf{h}^T_{\alpha Z}$ contributes into the momentum r.h.s., and the TF can be obtained in this case [18]:

$$\mathbf{R}^T_{\alpha Z} = \sum_{\beta\zeta} \frac{\mu_{\alpha\beta}}{T_{av}} G^{(2)}_{\alpha Z \beta\zeta} \left( \frac{\mathbf{h}^T_{\alpha Z}}{m_\alpha n_{\alpha Z}} - \frac{\mathbf{h}^T_{\beta\zeta}}{m_\beta n_{\beta\zeta}} \right), \tag{2.29}$$

where $G^{(2)}_{\alpha Z\beta\zeta}$ is a kinetic coefficient, which depends on the collisions. In the Zhdanov moment approach the linearized Boltzmann collisonal operator is used, i.e. in (2.2) in the distribution functions multiplications $f_{\alpha Z} f_{1\beta\zeta}$ the second order terms of the perturbations with respect to the Maxwell distribution functions, like $\propto h^T_{\alpha Zk} h^T_{\beta\zeta l}$, are neglected. In other words, the collisions between hot-tails of distribution functions (solid blue with solid red in figure 2.5) are not taken into account, whereas the hot-tail interactions with the non-modified Maxwell distribution functions $f^0$ (solid blue with dashed red and solid red with dashed blue in figure 2.5) are included.

Note that for the equal masses $m_\alpha = m_\beta$ in case of equal normalized fluxes $\mathbf{h}^T_{\alpha Z}/n_{\alpha Z} = \mathbf{h}^T_{\beta\zeta}/n_{\beta\zeta}$ the hot-tails contributions from the species $\alpha Z$ and $\beta\zeta$ compensate each other. This happens, for example, if the one species is artificially split into two fluids. However, for the heavier species the contribution from its hot-tail become small. For the example in figure 2.5, solid-blue/dashed-red collisions contribute more into the TF than solid-red/dashed-blue collisions. This is because the light species distribution function affects relative velocities in the collisions more than the heavy distribution function. Thus, the TF appears due to the light species hot-tail with the reduction due to the residual heavy species hot-tail contribution. The connection between the heat fluxes and the temperature gradients is described by the heat conductivity tensor. In cases where non-diagonal components of heat conductivity tensor do not contribute, for example, the temperature gradient $\nabla T_{av}$ is along $\mathbf{B}$ (for this subsection for simplicity: $\forall \alpha Z : T_{\alpha Z} = T_{av}$), the $\mathbf{h}^T_{\alpha Z}$ is directed against the $\nabla T_{av}$. It is worth to mention that $\mathbf{h}^T_{\alpha Z}/n_{\alpha Z} \sim \mathbf{h}^T_{\beta\zeta}/n_{\beta\zeta}$ in the light main species and heavy trace-impurity species case ($n_{\alpha Z} \gg n_{\beta\zeta}$), if $\tau^{(Zh)}_{\beta\zeta\alpha Z} \sim \tau^{(Zh)}_{\alpha Z\alpha Z}$, because it can be shown that $\mathbf{h}^T_{\alpha Z} \propto -n_{\alpha Z} T_{av} \tau^{(Zh)}_{\alpha Z\alpha Z} \nabla T_{av}$ and $\mathbf{h}^T_{\beta\zeta} \propto -n_{\beta\zeta} T_{av} \tau^{(Zh)}_{\beta\zeta\alpha Z} \nabla T_{av}$. For $\tau^{(Zh)}_{\beta\zeta\alpha Z} < \tau^{(Zh)}_{\alpha Z\alpha Z}$ case (for example, high-Z impurity in H-plasma) the heavy species hot-tail is even smaller: $\mathbf{h}^T_{\alpha Z}/n_{\alpha Z} > \mathbf{h}^T_{\beta\zeta}/n_{\beta\zeta}$. Thus, figure 2.5 describes relatively realistic case.

The $\mathbf{h}^T_{\alpha Z/\beta\zeta}$ and $\nabla T_{av}$ are opposite, which is true for both solid spheres and Coulomb collisions (figure 2.5). However, the "size" of the hot-tail against the $\nabla T_{av}$ depends on the collisions type for the given mixture parameters, by means of the heat conductivity, which is mentioned in subsection 2.3.1. Also, in the higher order approximations, such

as 21N-moment approach, the "shape" of the hot-tail is different for the solid spheres and Coulomb collisions, which is represented by different responses of additional vector moments on the $\nabla T_{av}$. Thus, the direction of the $\mathbf{R}^T_{\alpha Z}$ with respect to the $\nabla T_{av}$ is controlled by the sign of $G^{(2)}_{\alpha Z\beta\zeta}$. Using Eq. (4.2.18) in [18] or (C15) in [92] it is derived:

$$G^{(2)}_{\alpha Z\beta\zeta} = -\frac{16}{3}\mu_{\alpha\beta}n_{\alpha Z}n_{\beta\zeta}\left(\frac{2}{5}\Omega^{12}_{\alpha Z\beta\zeta} - \Omega^{11}_{\alpha Z\beta\zeta}\right) = -\frac{n_{\alpha Z}\mu_{\alpha\beta}}{\tau^{(Zh)}_{\alpha Z\beta\zeta}}\left(\frac{2}{5}\frac{\Omega^{12}_{\alpha Z\beta\zeta}}{\Omega^{11}_{\alpha Z\beta\zeta}} - 1\right). \quad (2.30)$$

Using (2.23) and (2.24), one can get:

$$G^{(2)\ SolSph}_{\alpha Z\beta\zeta} = -\frac{1}{5}\frac{n_{\alpha Z}\mu_{\alpha\beta}}{\tau^{(Zh)}_{\alpha Z\beta\zeta}}, \quad (2.31)$$

$$G^{(2)\ Coul}_{\alpha Z\beta\zeta} = \frac{3}{5}\frac{n_{\alpha Z}\mu_{\alpha\beta}}{\tau^{(Zh)}_{\alpha Z\beta\zeta}}. \quad (2.32)$$

The difference in the response of the r.h.s. integrals (2.30) with the $Q^{(1)\ SolSph}_{\alpha\beta}$ and $Q^{(1)\ Coul}_{\alpha Z\beta\zeta}(g)$ on the hot-tail formation is expressed as a function from $r$ in (2.23) and (2.24), correspondingly. Thus, we have captured a very interesting physical phenomenon: in the neutral gas the light species transfers momentum to the heavy species *towards* the direction of the hot-tail and *against* the direction of the $\nabla T_{av}$, whereas in the fully-ionized plasma the light species transfers momentum to the heavy species *against* the direction of the hot-tail and *towards* the direction of the $\nabla T_{av}$ (figure 2.5). Why such difference occurs for the same models, where only differential cross-sections are chosen differently? Similar to the subsection 2.3.1 reasoning should be done to reveal this. The transport cross-section $Q^{(1)\ SolSph}_{\alpha\beta}$ is independent of the velocity. However, the overpopulated phase-space in the large velocity range towards the hot-tail leads to the efficient average momentum loss, because this population has large velocities (figure 2.5). In contrast, the $Q^{(1)\ Coul}_{\alpha Z\beta\zeta}(g)$ shrinks in the large velocity range because of the Rutherford mechanism of the scattering (figure 2.2a). Therefore, the efficient average momentum loss happens in the low velocity range in the direction against the hot-tail, resulting a momentum gain for the heavy particles towards the $\nabla T_{av}$ (figure 2.5).

This explanation is similar to the one done by Braginskii in the "§ 3. Kinetics of a Simple Plasma (Qualitative Description)" in [17]. This phenomenon is well-known. For example, the electron TF contributes into the thermal current [96], which is routinely measured between the cold inner and hot outer targets in the ASDEX Upgrade tokamak by shunts [97] and used to estimate the plasma temperatures in the outer divertor. Besides, the TF between the light main ions and heavy impurities plays its major role in the impurity leakage from the divertor towards upstream due to the parallel component of the ion temperature gradient [98].

## 2.4 Zhdanov closure

We introduce the essential steps of the Zhdanov closure using the Grad method in this section. The Grad method is a powerful technique that is based on the distribution function approximation for each species in the mixture through a irreducible tensorial Hermite series expansion.

### 2.4.1 General form of the moment equations

To begin the process, we construct a general equation for the moments of the distribution function. This equation serves as a foundation for our analysis and allows us to explore the behavior and characteristics of the system. By carefully examining the moments of the distribution function, we can gain valuable insights into the macroscopic properties and dynamics of the plasma.

The moment method is based on the integration of the kinetic equation (2.1) over velocity space with the weight functions $\psi_{\alpha Z}(\mathbf{v}_{\alpha Z}, \mathbf{r}, t)$:

$$\int \psi_{\alpha Z} \left( \frac{\partial f_{\alpha Z}}{\partial t} + \mathbf{v}_{\alpha Z} \cdot \frac{\partial f_{\alpha Z}}{\partial \mathbf{r}} + \frac{\mathbf{F}_{\alpha Z}}{m_\alpha} \cdot \frac{\partial f_{\alpha Z}}{\partial \mathbf{v}_{\alpha Z}} \right) d\mathbf{v}_{\alpha Z} = \int \psi_{\alpha Z} C_{\alpha Z} d\mathbf{v}_{\alpha Z} \tag{2.33}$$

Additionally we define the averaging of the function $\phi_{\alpha Z}$ and the relative velocity with respect to the $\mathbf{u}$:

$$n_{\alpha Z} \langle \phi_{\alpha Z} \rangle \stackrel{\text{def}}{=} \int \phi_{\alpha Z} f_{\alpha Z} d\mathbf{v}_{\alpha Z} = \int \phi_{\alpha Z} f_{\alpha Z} d\mathbf{c}_{\alpha Z}, \quad \mathbf{c}_{\alpha Z} \stackrel{\text{def}}{=} \mathbf{v}_{\alpha Z} - \mathbf{u} \tag{2.34}$$

In is convenient to substitute $\mathbf{v}_{\alpha Z}$ by $\mathbf{c}_{\alpha Z}$ (second "=" in (2.34)). As a result (see Eq.( 2.1.1-2.1.9) in [18]), (2.33) turns into a general form of moments equations:

$$\begin{aligned} &\frac{dn_{\alpha Z} \langle \psi_{\alpha Z} \rangle}{dt} + n_{\alpha Z} \langle \psi_{\alpha Z} \rangle \nabla \cdot \mathbf{u} + \nabla \cdot (n_{\alpha Z} \langle \psi_{\alpha Z} \mathbf{c}_{\alpha Z} \rangle) - n_{\alpha Z} \left[ \left\langle \frac{d\psi_{\alpha Z}}{dt} \right\rangle \right. \\ &\qquad \left. + \langle \mathbf{c}_{\alpha Z} \cdot \nabla \psi_{\alpha Z} \rangle + \frac{1}{m_\alpha} \langle \mathbf{F}^*_{\alpha Z} \cdot \nabla_c \psi_{\alpha Z} \rangle - \left\langle \mathbf{c}_{\alpha Z s} \frac{\partial \psi_{\alpha Z}}{\partial c_{\alpha Z r}} \right\rangle \frac{\partial u_r}{\partial x_s} \right] = R^{\psi}_{\alpha Z} \end{aligned} \tag{2.35}$$

Here and further in the thesis the Einstein summation notation is applied, and we define:

$$\nabla \stackrel{\text{def}}{=} \partial / \partial \mathbf{r}, \quad \nabla_c \stackrel{\text{def}}{=} \partial / \partial \mathbf{c}_{\alpha Z}, \quad d/dt \stackrel{\text{def}}{=} \partial / \partial t + \mathbf{u} \cdot \nabla, \tag{2.36}$$

$$n_{\alpha Z} \mathbf{F}^*_{\alpha Z} \stackrel{\text{def}}{=} n_{\alpha Z} \mathbf{F}_{\alpha Z} - \rho_{\alpha Z} \frac{d\mathbf{u}}{dt}, \quad \rho_{\alpha Z} \stackrel{\text{def}}{=} m_\alpha n_{\alpha Z}, \tag{2.37}$$

and the collsional r.h.s. of the moment equations is defined as:

$$R^{\psi}_{\alpha Z} \stackrel{\text{def}}{=} \int \psi_{\alpha Z} C_{\alpha Z} d\mathbf{c}_{\alpha Z}. \tag{2.38}$$

Thus using (2.6) we can derive a contribution from positive collisional source:

$$R^{\psi+}_{\alpha Z} = \int \psi_{\alpha Z} C^{+}_{\alpha Z} d\mathbf{c}_{\alpha Z} = \sum_{\beta\zeta} \iiint \psi_{\alpha Z} f'_{\alpha Z} f'_{1\beta\zeta} g' \sigma_{\alpha Z \beta\zeta}(g', \chi) d\Omega d\mathbf{c}_{\alpha Z} d\mathbf{c}_{1\beta\zeta}. \tag{2.39}$$

Using the Jacobians equality (2.7) the integration variables are substituted:

$$R^{\psi+}_{\alpha Z} = \sum_{\beta\zeta} \iiint \psi_{\alpha Z} f'_{\alpha Z} f'_{1\beta\zeta} g' \sigma_{\alpha Z \beta\zeta}(g', \chi) d\Omega d\mathbf{c}'_{\alpha Z} d\mathbf{c}'_{1\beta\zeta} \tag{2.40}$$

We can use the elastic collisions properties: for the particles from the primed phase-space the velocities after collisions are unprimed $\mathbf{c}_{1\beta\zeta}$ and $\mathbf{c}_{\alpha Z}$. Thus, $\psi_{\alpha Z}$ is the function of velocities after collisions $\mathbf{c}_{\alpha Z}$ for the particles from the primed phase-space. Now the primed and unprimed values can be replaced: $\mathbf{c}'_{\alpha Z} \to \mathbf{c}_{\alpha Z}$, $\mathbf{c}'_{1\beta\zeta} \to \mathbf{c}_{1\beta\zeta}$, $\mathbf{g}' \to \mathbf{g}$, $\psi_{\alpha Z} \to \psi'_{\alpha Z}$. In other words, the integration over the primed phase-space is equivalent to the integration over unprimed phase-space:

$$R^{\psi+}_{\alpha Z} = \sum_{\beta\zeta} \iiint \psi'_{\alpha Z} f_{\alpha Z} f_{1\beta\zeta} g \sigma_{\alpha Z \beta\zeta}(g, \chi) d\Omega d\mathbf{c}_{\alpha Z} d\mathbf{c}_{1\beta\zeta} \tag{2.41}$$

As a result, the collisional r.h.s. of the moment equations is significantly simplified by exploiting the elastic properties. The difference between positive $C^{+}_{\alpha Z}$ and negative $C^{-}_{\alpha Z}$ collision sources is represented only by the difference in the weight function before $\psi_{\alpha Z}$ and after $\psi'_{\alpha Z}$ collisions:

$$\boxed{R^{\psi}_{\alpha Z} = \sum_{\beta\zeta} \iiint (\psi'_{\alpha Z} - \psi_{\alpha Z}) f_{\alpha Z} f_{1\beta\zeta} g \sigma_{\alpha Z \beta\zeta}(g, \chi) d\Omega d\mathbf{c}_{\alpha Z} d\mathbf{c}_{1\beta\zeta}.} \tag{2.42}$$

Now it can be seen that the difference $(\psi'_{\alpha Z} - \psi_{\alpha Z})$ includes combinations in the form of $(1 - \cos^{l}\chi)$, because the $\cos\chi$ defines the angular relation between velocities before and after collisions needed for integration over $\Omega$. Therefore, the transport cross-sections $Q^{(l)}_{\alpha Z \beta\zeta}(g)$ (2.12) and the Chapman-Cowling $\Omega^{lr}_{\alpha Z \beta\zeta}$ integrals (2.20) appear in the collisional r.h.s. of the moment equations.

The general equation (2.35) for the moments of the distribution function leads to an infinite system of differential equations when the weight functions $\psi_{\alpha Z}$ are chosen to be equal to $1, \mathbf{c}_{\alpha Z}, c^2_{\alpha Z}$, and so on. This occurs because in equation (2.35), moments higher

polynomial degrees than $\psi_{\alpha Z}$ are included. Specifically, if the polynomial degree of $\psi_{\alpha Z}$ is $k$, equation (2.35) includes moments with polynomial degree $k+1$. In other words, the lower order moment equations includes higher order moments. The infinite system of equations has to be truncated for the specific $k$. In this case the closure of the system of moment equation has to be applied to relate the lower order moments to the higher order moments by means of transport coefficients. The essence of the Zhdanov closure, which is based on Grad method, is discussed in the subsection 2.4.2.

### 2.4.2 Distribution function approximation with irreducible tensorial Hermite polynomials $H^{mn}_{r_1..r_n}(\gamma^{1/2}_{\alpha Z}\mathbf{c}_{\alpha Z})$

The Zhdanov closure involves approximating the distribution function using reducible tensorial Hermite polynomials. In this subsection, we recapitulate the key steps from chapter 4, section 4.1, and Appendix A1 in [18], as well as insights from [92, 99]. By reproducing these crucial steps, we establish a solid foundation for our analysis and subsequent developments in the Zhdanov closure using the Hermite polynomials.

The type of the polynomials, which are taken for the distribution function approximation, are defined by the orthogonality properties with respect to the function $f^{(0)}$, which is chosen as a zero-order approximation of the distribution function for species $\alpha Z$ ($f^0_{\alpha Z}$). In Grad method, the local Maxwellian is considered as $f^0_{\alpha Z}$:

$$f^{(0)}_{\alpha Z} \stackrel{\text{def}}{=} n_{\alpha Z}\left(\frac{\gamma_{\alpha Z}}{2\pi}\right)^{3/2}\exp\left(-\frac{\xi^2_{\alpha Z}}{2}\right), \quad \boldsymbol{\xi}_{\alpha Z} \stackrel{\text{def}}{=} \gamma^{1/2}_{\alpha Z}\mathbf{c}_{\alpha Z}, \tag{2.43}$$

If the orthoganallisation procedure with weight function $(2\pi)^{-3/2}\exp\left(-\xi^2/2\right)$ is performed in the spherical coordinates, the irreducible tensorial Hermite polynomials are obtained [18, 78]:

$$H^{mn}_{r_1..r_m}(\boldsymbol{\xi}) \stackrel{\text{def}}{=} (-2)^n n! S^n_{m+1/2}(\xi^2/2)P^{(m)}(\boldsymbol{\xi}), \tag{2.44}$$

where $S^n_{m+1/2}$ are the Sonine polynomials (associated Laguerre polynomials) used in Chapman-Enskog-Burnett theory:

$$S^n_{m+1/2}(u^2) \stackrel{\text{def}}{=} \sum_{p=0}^{n}\frac{\left(-u^2\right)^p(m+n+1/2)!}{p!(n-p)!(m+p+1/2)!}, \tag{2.45}$$

$$S^0_{m+1/2}(u^2)=1, \quad S^1_{m+1/2}(u^2)=-u^2+m+3/2,$$
$$S^2_{m+1/2}(u^2)=\frac{1}{2}\left(u^4-2(m+5/2)u^2+(m+3/2)(m+5/2)\right), \tag{2.46}$$

the $P^{(m)}$ are the irreducible harmonic polynomials, which are defined in [78] (also written in Appendix A1 in [18]). Here we introduce a few first irreducible harmonic polynomials:

$$P^{(0)}(\boldsymbol{\xi}) = 1, \quad P_r^{(1)}(\boldsymbol{\xi}) = \xi_r, \quad P_{rs}^{(2)}(\boldsymbol{\xi}) = \xi_r\xi_s - \frac{1}{3}\delta_{rs}\xi^2 \tag{2.47}$$

where $\delta_{rs}$ is a Kronecker delta. The tensorial Hermite polynomials $H^n_{r_1..r_n}(\boldsymbol{\xi})$ are orthogonal with weight function $(2\pi)^{-3/2}\exp\left(-\xi^2/2\right)$ in the Cartesian system [77] and are the linear combination of $H^{mn}_{r_1..r_n}(\boldsymbol{\xi})$. Thus, for $H^{mn}_{r_1..r_n}(\boldsymbol{\xi})$ the orthogonality properties are kept also for the Cartesian system, as it should be. To relate Hermite polynomials to the moments it is convenient to use following combination:

$$G^{mn}_{\alpha Z\ r_1..r_m}(\boldsymbol{\xi}_{\alpha Z}, \gamma_{\alpha Z}) \stackrel{\text{def}}{=} 2^{-n} m_\alpha \gamma_{\alpha Z}^{-(n+m/2)} H^{mn}_{r_1..r_m}(\boldsymbol{\xi}_{\alpha Z}) = (-1)^n m_\alpha \gamma_{\alpha Z}^{-(n+m/2)} n! S^n_{m+1/2}(\xi^2/2) P^{(m)}(\boldsymbol{\xi}), \tag{2.48}$$

Further in the thesis, the subscripts $r_1..r_m$ are omitted. As a result, the distribution function is approximated in the following way:

$$f_{\alpha Z}(\mathbf{r}, \boldsymbol{\xi}_{\alpha Z}, t) = f^{(0)}_{\alpha Z}(\mathbf{r}, \boldsymbol{\xi}_{\alpha Z}, t) \sum_{m=0}^{\infty}\sum_{n=0}^{\infty} \tilde{b}^{mn}_{\alpha Z}(\mathbf{r}, t) G^{mn}_{\alpha Z}(\boldsymbol{\xi}_{\alpha Z}, \gamma_{\alpha Z}(\mathbf{r}, t)) \tag{2.49}$$

where coefficients of the expansion $\tilde{b}^{mn}_{\alpha Z}$ are obtained from the orthogonality condition for the Hermite polynomials:

$$\tilde{b}^{mn}_{\alpha Z}(\mathbf{r}, t) = 2^{2n} m_\alpha^{-2} \gamma_{\alpha Z}(\mathbf{r}, t)^{2n+m} \varrho_{mn} b^{mn}_{\alpha Z}(\mathbf{r}, t), \quad \varrho_{mn} \stackrel{\text{def}}{=} \frac{(2m+1)!\,(m+n)!}{n!(m!)^2(2m+2n+1)!}, \tag{2.50}$$

$$b^{mn}_{\alpha Z}(\mathbf{r}, t) \stackrel{\text{def}}{=} \int G^{mn}_{\alpha Z}(\boldsymbol{\xi}_{\alpha Z}, \gamma_{\alpha Z}(\mathbf{r}, t)) f_{\alpha Z}(\mathbf{r}, \boldsymbol{\xi}_{\alpha Z}, t) d\mathbf{c}_{\alpha Z}, \tag{2.51}$$

if (2.49) is substituted into (2.51), only $\tilde{b}^{mn}_{\alpha Z}$ coefficient survived due to Hermite polynomials orthogonality property and the relation (2.50) is, indeed, obtained [18]. The choice of combination (2.48) make $b^{mn}_{\alpha Z}(\mathbf{r}, t)$ equal to the corresponding moment of the distribution function $f_{\alpha Z}(\mathbf{r}, \boldsymbol{\xi}_{\alpha Z}, t)$. Thus, the orthogonality property is essential to find a relation between the moments of the distribution function for $\psi_{\alpha Z} = G^{mn}_{\alpha Z}$, for which the system of differential equations (2.35) is constructed, with the coefficients of the approximation (2.49).

In the collisional regime, i.e. macroscopic parameters change slowly on length scales along $\mathbf{B}$ (across $\mathbf{B}$) of the mean free path (gyroradius) and time scales between collisions (gyromotion period), it can be shown (4th chapter in [18]) that the distribution function

can be approximated by the finite amount of the polynomials in the expansion (2.49). The fast convergence of the expansion is explicitly shown, for example, in [99]. Therefore, we cut our series (2.49) for the specific $m^{max}$ and $n_m^{max}$ (e.g. 21N-moment approximation in subsection 2.4.3):

$$f_{\alpha Z}(\mathbf{r},\boldsymbol{\xi}_{\alpha Z},t) = f^{(0)}_{\alpha Z}(\mathbf{r},\boldsymbol{\xi}_{\alpha Z},t)\sum_{m=0}^{m^{max}}\sum_{n=0}^{n_m^{max}} 2^{2n} m_\alpha^{-2}\gamma_{\alpha Z}(\mathbf{r},t)^{2n+m}\varrho_{mn} b^{mn}_{\alpha Z}(\mathbf{r},t) G^{mn}_{\alpha Z}(\boldsymbol{\xi}_{\alpha Z},\gamma_{\alpha Z}(\mathbf{r},t)), \tag{2.52}$$

whereas the series is formed following the polynomial hierarchy. In this case, the coefficients $\tilde{b}^{mn}_{\alpha Z}(\mathbf{r},t) = 0$ for $m > m^{max}$ and $n > n_m^{max}$. Subsequently, all the moments $b^{mn}_{\alpha Z}(\mathbf{r},t) = 0$ for $m > m^{max}$ and $n > n_m^{max}$, and the finite closed system of moment equations (2.35) is formed and ready for practical applications, if the collisional r.h.s. are calculated. The distribution function (2.42) is substituted into the collisional sources (2.42) ($R^{mn}_{\alpha Z} = R^{\psi}_{\alpha Z}$ for $\psi_{\alpha Z} = G^{mn}_{\alpha Z}$). In fact, in appendix A1 [18] another method of collsional r.h.s. integration is performed with respect to the one suggested the section 4.2 in [18]. Therefore, to avoid inconstancy we follow [92] further. After linearization we get :

$$R^{mn}_{\alpha Z} = \sum_{\beta\zeta}\iiint (G^{mn\prime}_{\alpha Z} - G^{mn}_{\alpha Z}) f^{(0)}_{\alpha Z} f^{(0)}_{\beta\zeta}(1+\Phi_{\alpha Z}+\Phi_{\beta\zeta}) \times g\sigma_{\alpha Z\beta\zeta}(g,\chi) d\Omega d\mathbf{c}_{\alpha Z} d\mathbf{c}_{1\beta\zeta} \tag{2.53}$$

where the expansions without the first term are:

$$\Phi_{\alpha Z} = \sum_{k=0}^{m^{max}}\sum_{l=0}^{n_k^{max}} 2^{2l} m_\alpha^{-2}\gamma_{\alpha Z}^{2l+k}\varrho_{kl} b^{kl}_{\alpha Z} G^{kl}_{\alpha Z}(1-\delta_{k0}\delta_{l0}) \tag{2.54}$$

It can be shown that $k \neq m$ elements are zero (see appendix A1 in [18]), i.e. rank of the moments in the collisional r.h.s. $b^{kl}_{\alpha Z}$ is the same in l.h.s. $b^{mn}_{\alpha Z}$. This is a result of the orthogonality properties for polynomials of different ranks.

Finally we get:

$$R^{mn}_{\alpha Z} = \sum_{\beta\zeta} \iiint (G^{mn\prime}_{\alpha Z} - G^{mn}_{\alpha Z}) f^{(0)}_{\alpha Z} f^{(0)}_{\beta\zeta} \times \left(1 + \sum_{l=0}^{n^{max}_m} 2^{2l} \varrho_{ml} (1 - \delta_{m0}\delta_{l0}) \Big( m_\alpha^{-2} \gamma_{\alpha Z}^{2l+m} G^{ml}_{\alpha Z} b^{ml}_{\alpha Z} + m_\beta^{-2} \gamma_{\beta\zeta}^{2l+m} G^{ml}_{\beta\zeta} b^{ml}_{\beta\zeta} \Big) \right) \times g \sigma_{\alpha Z \beta\zeta}(g, \chi) d\Omega d\mathbf{c}_{\alpha Z} d\mathbf{c}_{1\beta\zeta}, \quad (2.55)$$

which, after accurate integration, provides the combinations of the Chapman-Cowling integrals (2.20) with the corresponding moments $b^{kl}_{\alpha Z}$ and $b^{kl}_{\beta\zeta}$, as it is discussed in end of the subsection 2.4.1. Following Zhdanov, to achieve this the same temperature in the coefficients $\forall \alpha Z : T_{\alpha Z} = T_{av}$ are assumed, whereas different temperatures are kept in the differences $T_{\alpha Z} - T_{\beta\zeta}$, which is necessary, for instance, for heat exchange source $R^{01}_{\alpha Z}$. This assumption is valid, if $|T_{\alpha Z} - T_{\beta\zeta}| \ll T_{av}$. Nonetheless, so far, we keep temperatures different: according to [92]:

$$R^{mn}_{\alpha Z} \stackrel{\text{def}}{=} \sum_{\beta\zeta} R^{ml}_{\alpha Z \beta\zeta} = \sum_{\beta\zeta} \sum_{l=0}^{n^{max}_m} R^{mnl}_{\alpha Z \beta\zeta} \quad (2.56)$$

$$R^{mnl}_{\alpha Z \beta\zeta} = (1 - \delta_{m0}\delta_{l0}) \Big( A^{mnl}_{\alpha Z \beta\zeta} b^{ml}_{\alpha Z} + B^{mnl}_{\alpha Z \beta\zeta} b^{ml}_{\beta\zeta} \Big) + \delta_{m0}\delta_{l0} C^{mnl}_{\alpha Z \beta\zeta}, \quad (2.57)$$

where the $A^{mnl}_{\alpha Z \beta\zeta}$, $B^{mnl}_{\alpha Z \beta\zeta}$, $C^{mnl}_{\alpha Z \beta\zeta}$ are obtained according Eq. (16) in [92], and the relation to the Chapman-Cowling integrals are taken according appendix A2 in [18].

Finally, we discuss different approximations by choice of the cut $m^{max}$ and $n^{max}_m$ in (2.52) [99, 18]. For $m^{max} = 1$, $n^{max}_0 = 1$ and $n^{max}_1 = 0$ the 5N-moment system (Quasihydrodynamic approach) is obtained. The phenomenon, which are discussed in subsection 2.3.1, can be studied. To obtain the TF (subsection 2.3.2), the heat flux and the viscous-stress tensor the 13N-moment approach is used: $m^{max} = 2$, $n^{max}_0 = 1$, $n^{max}_1 = 1$ and $n^{max}_2 = 0$. However, for the Coulomb collisions the 13N-moment is not converged. The accurate calculation for the transport coefficients for the FR, TF, the heat conductivity and the viscosity requires inclusion additional vector and tensor moments: $m^{max} = 2$, $n^{max}_0 = 1$, $n^{max}_1 = 2$ and $n^{max}_2 = 1$. In this case the 21N-moment system of moment equations is derived. The complete system of the Zhdanov equations for the fully-ionized plasma is shown in subsection 2.4.3.

### 2.4.3 21N-moment closure for the fully-ionized plasma

The 21N-moment system of moment equations is essential for describing the dynamics of fully-ionized collisional plasmas. This system was derived by Zhdanov in chapter 4 and chapter 8 of his work [18]. The 21N-moment equations provide a comprehensive framework to capture the complex interactions and transport phenomena in the

multi-companent plasma, allowing for a more accurate and detailed representation of its behavior.

The coefficient of approximation are truncated according to the rule: $m^{max} = 2$, $n_0^{max} = 1$, $n_1^{max} = 2$ and $n_2^{max} = 1$. The corresponding moments in this case are:

$$n_{\alpha Z} b^{00}_{\alpha Z} = \rho_{\alpha Z}, \quad n_{\alpha Z} b^{01}_{\alpha Z} = 0, \quad n_{\alpha Z} b^{10}_{\alpha Z r} = \rho_{\alpha Z} w_{\alpha Z r}, \quad n_{\alpha Z} b^{11}_{\alpha Z} = h_{\alpha Z r},$$
$$n_{\alpha Z} b^{12}_{\alpha Z} = r_{\alpha Z r}, \quad n_{\alpha Z} b^{20}_{\alpha Z} = \pi_{\alpha Z r s}, \quad n_{\alpha Z} b^{21}_{\alpha Z} = \sigma_{\alpha Z r s}, \quad (2.58)$$

and the distribution function is:

$$f_{\alpha Z}(\mathbf{c}) = n_{\alpha Z} \left(\frac{\gamma_{\alpha Z}}{2\pi}\right)^{3/2} \exp\left(-\frac{\gamma_{\alpha Z} c^2}{2}\right) \cdot$$
$$\left[1 + \gamma_{\alpha Z} \mathbf{w}_{\alpha Z} \cdot \mathbf{c} + \frac{1}{5}\gamma_{\alpha Z}^2 \frac{\mathbf{h}_{\alpha Z}}{p_{\alpha Z}} \cdot \mathbf{c} \left(c^2 - \frac{5}{\gamma_{\alpha Z}}\right) + \frac{1}{70}\gamma_{\alpha Z}^3 \frac{\mathbf{r}_{\alpha Z}\gamma_{\alpha Z}}{p_{\alpha Z}} \cdot \mathbf{c} \left(c^4 - \frac{14}{\gamma_{\alpha Z}} c^2 + \frac{35}{\gamma_{\alpha Z}^2}\right) + \right.$$
$$\left. \frac{1}{2}\gamma_{\alpha Z} \frac{\pi_{\alpha Z r s}}{p_{\alpha Z}} \left(c_r c_s - \frac{1}{3}\delta_{rs} c^2\right) + \frac{1}{14}\gamma_{\alpha Z}^2 \frac{\sigma_{\alpha Z r s}\gamma_{\alpha Z}}{p_{\alpha Z}} \left(c_r c_s - \frac{1}{3}\delta_{rs} c^2\right)\left(c^2 - \frac{7}{\gamma_{\alpha Z}}\right)\right] \quad (2.59)$$

where the first there moments are:

$$\rho_{\alpha Z} = m_\alpha \iiint f_{\alpha Z} d^3\mathbf{c}, \quad \rho_{\alpha Z}\mathbf{w}_{\alpha Z} \stackrel{\text{def}}{=} m_\alpha \iiint \mathbf{c} f_{\alpha Z} d^3\mathbf{c},$$
$$T_{\alpha Z} = \frac{1}{3}\frac{m_\alpha}{n_{\alpha Z}} \iiint c^2 f_{\alpha Z} d^3\mathbf{c}, \quad \rho_{\alpha Z}\mathbf{u}_{\alpha Z} = m_\alpha \iiint \mathbf{v} f_{\alpha Z} d^3\mathbf{c},$$
$$\mathbf{u} = \sum_{\alpha Z} \frac{\rho_{\alpha Z}}{\rho}\mathbf{u}_{\alpha Z}, \quad \rho \stackrel{\text{def}}{=} \sum_{\alpha Z} \rho_{\alpha Z} \quad \mathbf{c} = \mathbf{v} - \mathbf{u}, \quad \mathbf{w}_{\alpha Z} = \mathbf{u}_{\alpha Z} - \mathbf{u}, \quad n_{\alpha Z} = \frac{\rho_{\alpha Z}}{m_\alpha}, \quad (2.60)$$

and the higher order moments are:

$$\mathbf{h}_{\alpha Z} = \frac{m_\alpha}{2} \iiint \left(c^2 - \frac{5}{\gamma_{\alpha Z}}\right) \mathbf{c} f_{\alpha Z} d^3\mathbf{c}, \quad \mathbf{r}_{\alpha Z} \stackrel{\text{def}}{=} \frac{m_\alpha}{4} \iiint \left(c^4 - \frac{14}{\gamma_{\alpha Z}} c^2 + \frac{35}{\gamma_{\alpha Z}^2}\right) \mathbf{c} f_{\alpha Z} d^3\mathbf{c},$$
$$\pi_{\alpha Z r s} \stackrel{\text{def}}{=} m_\alpha \iiint \left(c_r c_s - \frac{1}{3}\delta_{rs} c^2\right) f_{\alpha Z} d^3\mathbf{c}, \quad p_{\alpha Z} \stackrel{\text{def}}{=} n_{\alpha Z} T_{\alpha Z},$$
$$\sigma_{\alpha Z r s} \stackrel{\text{def}}{=} \frac{m_\alpha}{2} \iiint \left(c_r c_s - \frac{1}{3}\delta_{rs} c^2\right)\left(c^2 - \frac{7}{\gamma_{\alpha Z}}\right) f_{\alpha Z} d^3\mathbf{c}, \quad \pi_{rs} \stackrel{\text{def}}{=} \sum_{\alpha Z} \pi_{\alpha Z r s}, \quad p \stackrel{\text{def}}{=} \sum_{\alpha Z} p_{\alpha Z}. \quad (2.61)$$

where we define the diffusive velocity of the species $\alpha Z$ ($\mathbf{w}_{\alpha Z}$), the viscous-stress tensor of the species $\alpha Z$ ($\pi_{\alpha Z rs}$), the partial pressure of the species $\alpha Z$ ($p_{\alpha Z}$), the total viscous-stress tensor ($\pi_{rs}$) and the total pressure ($p$). Also, the additional vector moment of the species $\alpha Z$ ($\mathbf{r}_{\alpha Z}$) and the additional tensor moment of the species $\alpha Z$ ($\sigma_{\alpha Z rs}$) with respect to the 13N-moment approximation are defined. The Zhdanov system of the moment equation is:

$$\frac{d\rho_{\alpha Z}}{dt} + \rho_{\alpha Z}\nabla\cdot\mathbf{u} + \nabla\cdot(\rho_{\alpha Z}\mathbf{w}_{\alpha Z}) = 0, \tag{2.62}$$

$$\rho\frac{d\mathbf{u}}{dt} + \nabla p + \nabla\cdot\overleftrightarrow{\pi} - \sum_{\alpha Z} n_{\alpha Z}\left\langle\mathbf{F}_{\alpha Z}\right\rangle = 0, \tag{2.63}$$

$$\frac{3}{2}\frac{dp_{\alpha Z}}{dt} + \frac{5}{2}p_{\alpha Z}\nabla\cdot\mathbf{u} + \nabla\cdot\left(\mathbf{h}_{\alpha Z} + \frac{5}{2}p_{\alpha Z}\mathbf{w}_{\alpha Z}\right) + \pi_{\alpha Z rs}\frac{\partial u_r}{\partial x_s} - n_{\alpha Z}\mathbf{w}_{\alpha Z}\left\langle\mathbf{F}^*_{\alpha Z}\right\rangle = R^{01}_{\alpha Z}, \tag{2.64}$$

$$-\rho_{\alpha Z}\omega_{\alpha Z}\mathbf{w}_{\alpha Z}\times\mathbf{b} + \nabla p_{\alpha Z} + \nabla\cdot\overleftrightarrow{\pi}_{\alpha Z} - \rho_{\alpha Z}\left\langle\mathbf{F}^*_{\alpha Z}\right\rangle = \mathbf{R}^{10}_{\alpha Z}, \tag{2.65}$$

$$-\rho_{\alpha Z}\omega_{\alpha Z}\mathbf{h}_{\alpha Z}\times\mathbf{b} + \frac{5}{2}\frac{p_{\alpha Z}}{m_\alpha}\nabla T_{\alpha Z} = \mathbf{R}^{11}_{\alpha Z}, \tag{2.66}$$

$$-\rho_{\alpha Z}\omega_{\alpha Z}\mathbf{r}_{\alpha Z}\times\mathbf{b} = \mathbf{R}^{12}_{\alpha Z}, \tag{2.67}$$

$$-\omega_{\alpha Z}\{\pi_{\alpha Z lr}e_{slm}b_m\} + p_{\alpha Z}W_{rs} = R^{20}_{\alpha Z rs}, \tag{2.68}$$

$$-\omega_{\alpha Z}\{\sigma_{\alpha Z lr}e_{slm}b_m\} = R^{21}_{\alpha Z rs}, \tag{2.69}$$

where the cyclotron frequency of the species $\alpha Z$ ($\omega_{\alpha Z}$) and the total strain tensor ($W_{rs}$):

$$\omega_{\alpha Z} \overset{\text{def}}{=} \frac{Ze|\mathbf{B}|}{m_\alpha}, \quad \mathbf{b} \overset{\text{def}}{=} \frac{\mathbf{B}}{B}, \quad W_{rs} \overset{\text{def}}{=} 2\left\{\frac{\partial u_r}{\partial x_s}\right\}, \quad \left\{K_r L_s\right\} \overset{\text{def}}{=} \frac{1}{2}\left(K_r L_s + L_r K_s\right) - \frac{1}{3}K_l L_l \delta_{rs} \tag{2.70}$$

are defined. Also, the Levi-Civita symbol ($e_{slm}$) is used.

Note, the time derivatives (2.65), (2.66), (2.67), (2.68) and (2.69) are neglected as small with respect to the collsional r.h.s. and the magnetised term $\propto \omega_{\alpha Z}$. This is valid when the time scales of the problem $\tau_\parallel$ along $\mathbf{B}$ is large than the time between collisions $\tau$, and time scales of the problem $\tau_\perp$ across $\mathbf{B}$ is larger than the cyclotron frequency $\omega$: $\tau/\tau_\parallel \ll 1$ and $1/(\omega\tau_\perp) \ll 1$. Besides the spatial derivatives of the order $(\lambda/L_\parallel)^2$ along $\mathbf{B}$ and $(\rho^s/L_\perp)^2$ across $\mathbf{B}$ are neglected, where $\lambda$ is a mean-free path, $\rho^s$ is a sound Larmour radius (sound Larmor radius of the species $\alpha Z$ ($\rho^s_{\alpha Z}$)), $L_\parallel$ and $L_\perp$ are spacial scales of the problem along $\mathbf{B}$ and across $\mathbf{B}$ correspondingly. This is applicable, when $\lambda/L_\parallel \ll 1$ and $\rho^s/(L_\perp) \ll 1$. For example, in (2.68) and (2.69) the terms $\left\{\partial h_r/\partial x_s\right\}$, which represent the heat stresses, are assumed small with respect to the strain tensor $pW_{rs}$ (in estimations here we omit species subscripts). Along $\mathbf{B}$ one can estimate:

$$\left\{\frac{\partial h_\parallel}{\partial x_\parallel}\right\} \sim \frac{nT\tau}{m}\frac{\Delta T}{L_\parallel^2} \sim n\left(\frac{\lambda}{L_\parallel}\right)\sqrt{\frac{T}{m}}\frac{\Delta T}{L_\parallel}, \quad pW_{\parallel\parallel} \sim n\frac{T\Delta V_\parallel}{L_\parallel} \tag{2.71}$$

If $\Delta T \sim T$ and $\Delta V_\parallel \sim \sqrt{T/m}$ the heat stresses are smaller than the strain stress by factor of $\lambda/L_\parallel$. However, in some cases $(\lambda/L_\parallel)\Delta T/m \sim \sqrt{T/m}\Delta V_\parallel$, and the heat stresses become of the same order of the strain stresses. This happens in confined region of the tokamak, as it discussed in many works, for instance, in section 12.3 in [100]. The parallel heat stresses [86] contribute significantly into the neoclassical radial electric field, which in the large aspect ratio circular tokamak can be described by the well-known Hinton formula [81]. In the 8th chapter [18], the heat-stresses were neglected by Zhdanov, as well as, by Braginskii [17] for the single-ion case. The parallel heat stresses were included into the (2.68) and (2.69) as a part of this thesis in the chapter 4 (section 4.2). It changes the plasma dynamics, and the neoclassical-like $E_r$ in the highly collisional multi-ion plasmas (Pfirsch-Schlüter regime), is formed as a result.

The collsional r.h.s. for the Coulumb collsions is written according to Eq. (8.1.3), (8.1.6) and (4.2.16) in [18], taking into account typo corrections (Appendix C [84]), which were found by the author of the thesis together with the authors of the paper [84]:

$$R^{01}_{\alpha Z} \equiv Q_{\alpha Z} = \sum_{\beta\zeta} Q_{\alpha Z\beta\zeta}, \quad Q_{\alpha Z\beta\zeta} = \frac{3}{m_\alpha + m_\beta} G^{(1)}_{\alpha Z\beta\zeta}\left(T_{\alpha Z} - T_{\beta\zeta}\right), \tag{2.72}$$

$$\begin{aligned}\mathbf{R}^{10}_{\alpha Z} \equiv \mathbf{R}_{\alpha Z} = \sum_{\beta\zeta} \mathbf{R}_{\alpha Z\beta\zeta}, \quad \mathbf{R}_{\alpha Z\beta\zeta} = G^{(1)}_{\alpha Z\beta\zeta}(\mathbf{w}_{\alpha Z} - \mathbf{w}_{\beta\zeta}) \\ + \frac{\mu_{\alpha\beta}}{T_{av}} G^{(2)}_{\alpha Z\beta\zeta}\left(\frac{\mathbf{h}_{\alpha Z}}{\rho_{\alpha Z}} - \frac{\mathbf{h}_{\beta\zeta}}{\rho_{\beta\zeta}}\right) + \left(\frac{\mu_{\alpha\beta}}{T_{av}}\right)^2 G^{(8)}_{\alpha Z\beta\zeta}\left(\frac{\mathbf{r}_{\alpha Z}}{\rho_{\alpha Z}} - \frac{\mathbf{r}_{\beta\zeta}}{\rho_{\beta\zeta}}\right),\end{aligned} \tag{2.73}$$

$$\mathbf{R}^{11}_{\alpha Z} = \frac{T_{av}}{m_\alpha}\sum_{\beta\zeta}\Big[\frac{5}{2}\frac{\mu_{\alpha\beta}}{m_\alpha}G^{(2)}_{\alpha Z\beta\zeta}(\mathbf{w}_{\alpha Z}-\mathbf{w}_{\beta\zeta}) + G^{(5)}_{\alpha Z\beta\zeta}\frac{\mathbf{h}_{\alpha Z}}{p_{\alpha Z}} + G^{(6)}_{\alpha Z\beta\zeta}\frac{\mathbf{h}_{\beta\zeta}}{p_{\beta\zeta}} + \frac{\mu_{\alpha\beta}}{T_{av}}\left(G^{(9)}_{\alpha Z\beta\zeta}\frac{\mathbf{r}_{\alpha Z}}{p_{\alpha Z}} + G^{(10)}_{\alpha Z\beta\zeta}\frac{\mathbf{r}_{\beta\zeta}}{p_{\beta\zeta}}\right)\Big], \quad (2.74)$$

$$\mathbf{R}^{12}_{\alpha Z} = \left(\frac{T_{av}}{m_\alpha}\right)^2\sum_{\beta\zeta}\Big[\frac{35}{2}\left(\frac{\mu_{\alpha\beta}}{m_\alpha}\right)^2 G^{(8)}_{\alpha Z\beta\zeta}(\mathbf{w}_{\alpha Z}-\mathbf{w}_{\beta\zeta}) + 7\frac{\mu_{\alpha\beta}}{m_\alpha}\left(G^{(9)}_{\alpha Z\beta\zeta}\frac{\mathbf{h}_{\alpha Z}}{p_{\alpha Z}} + G^{(10)}_{\alpha Z\beta\zeta}\frac{\mathbf{h}_{\beta\zeta}}{p_{\beta\zeta}}\right) + \frac{m_\alpha}{T_{av}}G^{(11)}_{\alpha Z\beta\zeta}\frac{\mathbf{r}_{\alpha Z}}{p_{\alpha Z}} + \frac{m_\beta}{T_{av}}G^{(12)}_{\alpha Z\beta\zeta}\frac{\mathbf{r}_{\beta\zeta}}{p_{\beta\zeta}}\Big], \quad (2.75)$$

$$R^{20}_{\alpha Zrs} = \sum_{\beta\zeta}\frac{T_{av}}{m_\alpha+m_\beta}\left[\frac{G^{(3)}_{\alpha Z\beta\zeta}\pi_{\alpha Zrs}}{p_{\alpha Z}} + \frac{G^{(4)}_{\alpha Z\beta\zeta}\pi_{\beta\zeta rs}}{p_{\beta\zeta}} + \frac{\mu_{\alpha\beta}}{T_{av}}\left(\frac{G^{(13)}_{\alpha Z\beta\zeta}\sigma_{\alpha Zrs}}{p_{\alpha Z}} + \frac{G^{(14)}_{\alpha Z\beta\zeta}\sigma_{\beta\zeta rs}}{p_{\beta\zeta}}\right)\right], \quad (2.76)$$

$$R^{21}_{\alpha Zrs} = \sum_{\beta\zeta}\frac{T_{av}}{m_\alpha+m_\beta}\left[\frac{7}{2}T_{av}\mu_{\alpha\beta}\left(\frac{G^{(13)}_{\alpha Z\beta\zeta}\pi_{\alpha Zrs}}{m_\alpha^2 p_{\alpha Z}} + \frac{G^{(14)}_{\alpha Z\beta\zeta}\pi_{\beta\zeta rs}}{m_\beta^2 p_{\beta\zeta}}\right) + \frac{G^{(15)}_{\alpha Z\beta\zeta}\sigma_{\alpha Zrs}}{p_{\alpha Z}} + \frac{G^{(16)}_{\alpha Z\beta\zeta}\sigma_{\beta\zeta rs}}{p_{\beta\zeta}}\right], \quad (2.77)$$

where the collisonal frequency for the Coulomb collisions and the corresponding G-objects are:

$$1/\tau^{(Zh)}_{\alpha Z\beta\zeta} = \frac{\lambda_{\alpha Z\beta\zeta}}{n_{\alpha Z}\mu_{\alpha\beta}}, \quad \lambda_{\alpha Z\beta\zeta} \stackrel{\text{def}}{=} \frac{1}{3}(2\pi)^{-3/2}Z^2 n_{\alpha Z}\zeta^2 n_{\beta\zeta}\sqrt{\mu_{\alpha\beta}}\frac{\ln\Lambda}{T_{av}^{3/2}}\left(\frac{e^2}{\varepsilon_0}\right)^2, \quad (2.78)$$

$$G^{(1)}_{\alpha Z\beta\zeta} \stackrel{\text{def}}{=} -\lambda_{\alpha Z\beta\zeta}, \quad G^{(2)}_{\alpha Z\beta\zeta} \stackrel{\text{def}}{=} \frac{3}{5}\lambda_{\alpha Z\beta\zeta}, \quad (2.79)$$

$$G^{(3)}_{\alpha Z\beta\zeta} \stackrel{\text{def}}{=} -2\left(1+\frac{3}{5}\frac{m_\beta}{m_\alpha}\right)\lambda_{\alpha Z\beta\zeta}, \quad G^{(4)}_{\alpha Z\beta\zeta} \stackrel{\text{def}}{=} \frac{4}{5}\lambda_{\alpha Z\beta\zeta}, \quad (2.80)$$

$$G^{(5)}_{\alpha Z\beta\zeta} \stackrel{\text{def}}{=} -\left(\frac{13}{10}\frac{m_\beta}{m_\alpha}+\frac{8}{5}+3\frac{m_\alpha}{m_\beta}\right)\kappa_{\alpha\beta}\lambda_{\alpha Z\beta\zeta}, \quad G^{(6)}_{\alpha Z\beta\zeta} \stackrel{\text{def}}{=} \frac{27}{10}\kappa_{\alpha\beta}\lambda_{\alpha Z\beta\zeta}, \quad (2.81)$$

$$G^{(8)}_{\alpha Z\beta\zeta} \stackrel{\text{def}}{=} -\frac{3}{14}\lambda_{\alpha Z\beta\zeta}, \quad G^{(9)}_{\alpha Z\beta\zeta} \stackrel{\text{def}}{=} \frac{3}{5}\left(\frac{23}{28}\frac{m_\beta}{m_\alpha} + \frac{8}{7} + 3\frac{m_\alpha}{m_\beta}\right)\kappa_{\alpha\beta}\lambda_{\alpha Z\beta\zeta}, \tag{2.82}$$

$$G^{(10)}_{\alpha Z\beta\zeta} \stackrel{\text{def}}{=} -\frac{45}{28}\kappa_{\alpha\beta}\lambda_{\alpha Z\beta\zeta},$$
$$G^{(11)}_{\alpha Z\beta\zeta} \stackrel{\text{def}}{=} -\left(\frac{433}{280}\frac{m_\beta^2}{m_\alpha^2} + \frac{136}{35}\frac{m_\beta}{m_\alpha} + \frac{459}{35} + \frac{32}{5}\frac{m_\alpha}{m_\beta} + 5\frac{m_\alpha^2}{m_\beta^2}\right)\kappa^2_{\alpha\beta}\lambda_{\alpha Z\beta\zeta}, \tag{2.83}$$

$$G^{(12)}_{\alpha Z\beta\zeta} \stackrel{\text{def}}{=} \frac{75}{8}\kappa^2_{\alpha\beta}\lambda_{\alpha Z\beta\zeta}, \quad G^{(13)}_{\alpha Z\beta\zeta} \stackrel{\text{def}}{=} \left(\frac{18}{35}\frac{m_\beta}{m_\alpha} + \frac{6}{5}\right)\lambda_{\alpha Z\beta\zeta}, \tag{2.84}$$

$$G^{(14)}_{\alpha Z\beta\zeta} \stackrel{\text{def}}{=} -\frac{24}{35}\frac{m_\beta}{m_\alpha}\lambda_{\alpha Z\beta\zeta}, \quad G^{(15)}_{\alpha Z\beta\zeta} \stackrel{\text{def}}{=} -\left(\frac{51}{35}\frac{m_\beta^2}{m_\alpha^2} + \frac{37}{7}\frac{m_\beta}{m_\alpha} + \frac{22}{5} + 4\frac{m_\alpha}{m_\beta}\right)\kappa_{\alpha\beta}\lambda_{\alpha Z\beta\zeta}, \tag{2.85}$$

$$G^{(16)}_{\alpha Z\beta\zeta} \stackrel{\text{def}}{=} \frac{24}{7}\frac{m_\beta}{m_\alpha}\kappa_{\alpha\beta}\lambda_{\alpha Z\beta\zeta}, \quad \kappa_{\alpha\beta} \stackrel{\text{def}}{=} \frac{\mu_{\alpha\beta}}{m_\alpha + m_\beta}, \tag{2.86}$$

For practical applications, in the magnetized plasma ($\omega\tau \gg 1$) the perpendicular components (across $\mathbf{B}$) for the $\mathbf{h}_{\alpha Z}$ and the $\pi_{\alpha Z rs}$ are obtained by expanding over $(\omega\tau)^{-1}$ (2.66), (2.67), (2.68) and (2.69), as it is suggested in section 8.3 in [18]. For example, the diamagnetic heat flux in $\mathbf{b}\times\nabla T_{\alpha Z}$ direction and classical cross-field heat flux in $\nabla_\perp T_{\alpha Z}$ direction can be explicitly obtained by Eq. (8.3.1) and (8.3.3) in [18] correspondingly. Thouse are the multi-species generalisation of the single-species ones, which were derived by Braginskii [17]. Similarly, the cross-field viscosity is found Eq. (8.3.8) in [18].

For the parallel components (along $\mathbf{B}$) of the $\mathbf{h}_{\alpha Z}$ and the $\pi_{\alpha Z rs}$ and $\mathbf{R}^{10}_{\alpha Z}$ the algebraic system of the (2.66), (2.67), (2.68) and (2.69) equations should be solved numerically, using, for example, the EMIM. The matrix size can be significantly reduced, if the equations (2.66), (2.67), (2.68) and (2.69) are averaged over the charge states as suggested in section 8.4 in [18]. The relation to the specific charge states of the species can be found analytically in this case. If one of the species $\alpha Z$ has much smaller mass than the masses of other species in the mixture, for example, electrons with respect to the ions or the light main ion species with respect to the heavy impurity species, the $R^{10}_{\alpha Z\|}$, $h_{\alpha Z\|}$ and $\pi_{\alpha Z\|\|}$ can be found analytically using expressions, which were developed by Zhdanov and Yushmanov [18, 79].

### 2.4.4 Zhdanov-Yushmanov analytical expressions

For mixtures containing species with significantly different masses, it is possible to obtain the parallel kinetic coefficients analytically.

Instead of using EMIM for the case, where $\forall\beta \neq \kappa : m_\kappa \ll m_\beta$ and species $\kappa$ has only one charge state $Z_\kappa$, the expansion over small parameter $m_\kappa/m_\beta$ can be performed

and the equations for $\kappa Z_\kappa$ become separated from equations for other species. The explicit ZY expressions [18, 79] for the $R^{10}_{\kappa Z_\kappa\|}$, $h_{\kappa Z_\kappa\|}$ and $\pi_{\kappa Z_\kappa\|\|}$ transport coefficients for $\mathbf{b}\cdot\nabla = \nabla_\|$ can be obtained:

$$R^{10}_{\kappa Z_\kappa\|} = -n_{\kappa Z_\kappa}\sum_\beta \frac{\mu_{\kappa\beta}c^{(1)}_{\kappa\beta}}{\tau^{(Zh)}_{\kappa\beta}}(w_{\kappa Z_\kappa\|} - \overline{w}_{\beta\|}) - n_{\kappa Z_\kappa}\left(c^{(5)}_\kappa - 0.5c^{(2)}_{\kappa\kappa}\frac{\overline{\tau}^{(Zh)}_\kappa}{\tau^{(Zh)}_{\kappa\kappa}}\right)\nabla_\| T_{\kappa Z_\kappa}, \tag{2.87}$$

$$R^{10}_{\beta\zeta\kappa Z_\kappa\|} = \frac{n_{\beta\zeta}\zeta^2}{\overline{Z^2_\beta}}\frac{\mu_{\beta\kappa}c^{(1)}_{\beta\kappa}}{\tau^{(Zh)}_{\beta\kappa}}(w_{\kappa Z_\kappa\|} - w_{\beta\zeta\|}) + \frac{n_{\beta\zeta}\zeta^2}{\overline{Z^2_\beta}}c^{(2)}_{\beta\kappa}\frac{\overline{\tau}^{(Zh)}_\beta}{\tau^{(Zh)}_{\beta\kappa}}\frac{\mu_{\beta\kappa}}{m_\kappa}\nabla_\| T_{\kappa Z_\kappa}, \tag{2.88}$$

$$h_{\kappa Z_\kappa\|} = \frac{p_{\kappa Z_\kappa}\tau^{(Zh)}_\kappa}{m_\kappa}\left[\sum_\beta \frac{\mu_{\kappa\beta}c^{(2)}_{\beta\kappa}}{\tau^{(Zh)}_{\kappa\beta}}(w_{\kappa Z_\kappa\|} - \overline{w}_{\beta\|}) - \left(c^{(6)}_\kappa + 0.5c^{(3)}_{\kappa\kappa}\frac{\overline{\tau}^{(Zh)}_\kappa}{\tau^{(Zh)}_{\kappa\kappa}}\right)\nabla_\| T_{\kappa Z_\kappa}\right], \tag{2.89}$$

$$\pi_{\kappa Z_\kappa\|\|} = -p_{\kappa Z_\kappa}\tau^{(Zh)}_\kappa\left(c_\kappa + 0.5c_{\kappa\kappa}\frac{\overline{\tau}^{(Zh)}_\kappa}{\tau^{(Zh)}_{\kappa\kappa}}\right)W_{\|\|}, \quad R^{10}_{\kappa Z_\kappa\|} = -\sum_{\beta\zeta} R^{10}_{\beta\zeta\kappa Z_\kappa\|}, \tag{2.90}$$

where the averaged over charge states quantities are:

$$\tau^{(Zh)}_{\alpha\beta} \stackrel{\text{def}}{=} \frac{n_\alpha\mu_{\alpha\beta}}{\lambda_{\alpha\beta}}, \quad \lambda_{\alpha\beta} \stackrel{\text{def}}{=} \frac{1}{3}(2\pi)^{-3/2}\overline{Z^2_\alpha}n_\alpha\overline{Z^2_\beta}n_\beta\sqrt{\mu_{\alpha\beta}}\frac{\ln\Lambda}{T^{3/2}_{av}}\left(\frac{e^2}{\varepsilon_0}\right)^2, \tag{2.91}$$

$$\lambda_{\alpha Z\beta\zeta} = \frac{\lambda_{\alpha\beta}}{I_{\alpha Z}I_{\beta\zeta}}, \quad \tau^{(Zh)}_{\alpha Z\beta\zeta} = \frac{n_{\alpha Z}}{n_\alpha}\frac{\tau^{(Zh)}_{\alpha\beta}}{I_{\alpha Z}I_{\beta\zeta}}, \quad \tau^{(Zh)}_\alpha \stackrel{\text{def}}{=} \left(\sum_\beta \frac{\mu_{\alpha\beta}}{m_\alpha\tau^{(Zh)}_{\alpha\beta}}\right)^{-1}, \tag{2.92}$$

$$I_{\alpha Z} \stackrel{\text{def}}{=} \frac{Z^2 n_{\alpha Z}}{\overline{Z^2_\alpha}n_\alpha}, \quad \overline{Z^2_\alpha}n_\alpha \stackrel{\text{def}}{=} \sum_Z Z^2 n_{\alpha Z}, \quad n_\alpha \stackrel{\text{def}}{=} \sum_Z n_{\alpha Z}, \quad \overline{\mathbf{w}}_\alpha \stackrel{\text{def}}{=} \sum_Z I_{\alpha Z}\mathbf{w}_{\alpha Z}, \tag{2.93}$$

The transport coefficients (which are taken from section 8.4 in [18]) for the light species $\kappa Z_\kappa$ are:

$$c^{(1)}_{\kappa\beta} = c^{(1)}_{\beta\kappa} = (1+0.24Z^*_\kappa)\frac{(1+0.93Z^*_\kappa)}{\Delta_\kappa}, \quad c^{(2)}_{\beta\kappa} = 1.56(1+1.4Z^*_\kappa)\frac{(1+0.52Z^*_\kappa)}{\Delta_\kappa}, \tag{2.94}$$

$$c^{(2)}_{\kappa\beta} = 0, \quad c^{(5)}_\kappa - 0.5c^{(2)}_{\kappa\kappa}\frac{\overline{\tau}^{(Zh)}_\kappa}{\tau^{(Zh)}_{\kappa\kappa}} \approx 2.2Z^*_\kappa\frac{(1+0.52Z^*_\kappa)}{\Delta_\kappa}, \tag{2.95}$$

$$c^{(6)}_\kappa + 0.5c^{(3)}_{\kappa\kappa}\frac{\overline{\tau}^{(Zh)}_\kappa}{\tau^{(Zh)}_{\kappa\kappa}} \approx 3.9(1+1.4Z^*_\kappa)\frac{(1+1.7Z^*_\kappa)}{\Delta_\kappa}, \tag{2.96}$$

$$c_\kappa + 0.5c_{\kappa\kappa}\frac{\overline{\tau}^{(Zh)}_\kappa}{\tau^{(Zh)}_{\kappa\kappa}} \approx 0.96\frac{(1+1.4Z^*_\kappa)^2}{(1+1.8Z^*_\kappa)(1+0.6Z^*_\kappa)}, \tag{2.97}$$

$$\Delta_\kappa = (1+2.65Z^*_\kappa)(1+0.29Z^*_\kappa), \quad Z^*_\kappa = \sum_{\beta:\ m_\beta > m_\kappa}\frac{\overline{Z^2_\beta}n_\beta}{Z^2_\kappa n_\kappa}. \tag{2.98}$$

It is stated in [18] the equations for heavy species can now be solved without the light species. For example, when the electron equations are separated from the ion ones, the equations for ions can be solved without taking into account presence of electrons. A consequent separation for the light main ions and heavy impurity should be done more carefully. For instance, according to proposed scheme, the heavy impurity heat flux will depend only on $1/\tau^{(Zh)}_{imp\ imp}$, because the interaction with the main ions with a frequency $1/\tau^{(Zh)}_{imp\ main}$ will be neglected as $\propto m_{main}/m_{imp}$. However, for the trace-impurity case it can be: $m_{main}/(m_{imp}\tau^{(Zh)}_{imp\ main}) > 1/\tau^{(Zh)}_{imp\ imp}$ even for $m_{main}/m_{imp} \ll 1$, because $1/\tau^{(Zh)}_{imp\ main} \gg 1/\tau^{(Zh)}_{imp\ imp}$. As a result, the heavy impurity heat flux is calculated incorrectly. The heavy impurity hot-tail contribution is already neglected in (2.87) and (2.88) and the heavy impurity heat flux does not contribute significantly into the total ion heat transport. Thus, in the approaches, where only total ion transport is considered and heat equations for heavy impurities are not solved (such approach is used, for example, in the SOLPS-ITER code [87]), ZY expressions can be applied for the TF and the FR calculations for $m_{main}/m_{imp} \ll 1$, as it was done in [80]. Also, it is important to mention that the mass difference ordering does not affect the contribution of the difference in the heat fluxes of different charge states of the same type of ions in (2.73). Usually, for the different charge states of the heavy impurity, the charge state correction does not contribute significantly into the TF. However, to be consistent, this correction should

be calculated according the procedure from section 8.4 in [18] taking into account the typos correction in [84].

However, the $m_{main}/m_{imp} \ll 1$ assumption is not fulfilled up to the required level even for the $D+N$ and $D+Ne$ mixtures: $m_D/m_N = 1/7$ and $m_D/m_{Ne} = 1/10$. As it will be shown in sub-subsection 4.4.3.2, the difference in the FR calculations for in the $N-Ne$ range between the ZY expression and the EMIM results is $\sim 20\%$. To resolve this issue the improved version of ZY expression were developed in section 4.4, i.e. IAM. In the IAM the $m_\alpha/m_\beta$ dependence is included, where it was possible avoiding cross-terms in the system of equations, similarly to ZY method. For example, the heavy species hot-tail contribution into the TF is taken into account, which was not included into the ZY expressions. The improved expressions have the following advantages:

- Coverage $He-Ne$ impurity region by IAM with a several percent difference with respect to the EMIM is achieved.
- Correct qualitative behaviour, when approaching the light masses region is performed, i.e. the TF changes sign, when passing $m_\alpha/m_\beta = 1$ region.
- An explicit light species declaration is not required: the expressions are written uniformely for all species.
- The one-charge state restriction for the light species is removed (IAM is applicable for the $He + imp$ plasmas).
- The trace-impurity heat flux $\propto \tau^{(Zh)}_{imp\ main}$, and not $\propto \tau^{(Zh)}_{imp\ imp}$ as in the ZY procedure, which is a result of the steps on page 181 from [18]. However, for $m_\alpha \sim m_\beta$ case, the trace-impurity heat flux is not calculated accurately, because the neglected cross-terms become important. In this case the qualitative behaviour is followed correctly. This is discussed in details in subsection 4.4.1.
- The heat-stresses analytical expressions are also written (subsection 4.4.4).
- The accurate treatment of the each charge state of each type of ion is performed, using charge states corrections (4.99), (4.109), (4.117) and (4.125).

The Zhdanov closure can be applied for the various modern transport and turbulent edge and scrape-off layer codes. It is worth to make a brief overview about this kind of models. It is performed with a focus on the 2D transport SOLPS-ITER code [87, 83] and 3D turbulent GRILLIX code [89, 90].

# 3 Transport and turbulent edge and scrape-off layer codes

The plasma transport is studied numerically using various transport and turbulent edge and SOL codes. These codes are essential tools for investigating and analyzing the complex plasma dynamics in fusion devices, enabling researchers to model and simulate the behavior of plasmas under different conditions and configurations. Through numerical simulations, important insights can be gained into the transport mechanisms, turbulence characteristics, and overall plasma behavior, contributing to the advancement of fusion research and reactor design.

## 3.1 Classical, neoclassical and turbulent cross-field transport

Cross-field transport in the magnetic fusion device is a complex phenomenon. In certain cases where the transport is determined by local parameters or can be effectively characterized using local parameters, the heat transport across $\mathbf{B}$ can be approximately described by the effective thermal diffusivity $\chi_{\perp}^{eff}$. The classical ion thermal diffusivity, which can be obtained by the Zhdanov closure, by simply calculating the $\mathbf{h}_{\alpha Z\perp}$ as discussed in subsection 2.4.3, is $\chi_{\perp}^{eff} \sim 0.01\ m^2/s$ for $B = 1\ T$, $T_i = 300\ eV$ and $n_i = 5 \cdot 10^{19}\ m^{-3}$ (typical parameters of the edge plasma in present tokamaks). The classical transport always appears in the magnetic confinement devices, even in the cylindrical approximation of the toroidal or linear machines.

However, if the diamagnetic heat fluxes, which also appears in the Zhdanov closure (subsection 2.4.3) (valid in the Pfirsch-Schlüter regime), are calculated taken into account the toroidal geometry of the tokamak, the large, with respect to the classical, ion heat flux is found. The ion diamagnetic heat flux averaged over the flux surface, due to the temperature variations on the flux surface, which are the result of the interplay between the parallel and diamagnetic heat fluxes, provides the neoclassical heat flux in the Pfirsch-Schlüter regime. The neoclassical heat transport is approximately by an order of magnitude larger than the classical one: $\chi_{\perp}^{eff} \sim 0.1\ m^2/s$. This kind of heat transport can be included, by accurate treatment of the contribution from the heat transport along $\mathbf{B}$ and the mean cross-field drifts. This is can be done in the edge and SOL transport models with drifts: SOLPS-ITER (B2.5) [88, 101], EDGE2D–EIRENE [102, 103], SOLEDGE2D–EIRENE [104], UEDGE [105] and others. Edge plasmas occur sometimes in the collisionless regimes. The collisional closure should not be applied in this case. However, the transport coefficients can be corrected, mimicking the contribution from the passing and banana particles [81, 86] into the cross-field heat transport, as it was performed for the SOLPS-ITER code [83].

The neoclassical transport appears to be too small to explain the heat transport across **B** in the tokamak. Experimental cross-field heat transport is observed $\chi_{\perp}^{eff} \sim 1\ m^2/s$. This is the consequence of the micro-scale turbulence phenomenon [69]. This mechanism is not a part of the transport codes. It is added into the transport models ad-hoc by using, so-called, anomalous fluxes, which are usually introduced by means of the effective diffusion coefficients, similar to $\chi_{\perp}^{eff} \sim 1\ m^2/s$.

Seeking for the solution for the microturbulence transport behaviour, the dedicated high-fidelity models, which are based on the gyrokinetic theory [106], were developed. Most of the high-fidelity codes are focused on the core turbulent behaviour, such as GENE [107, 108], GYRO [109], ORB5 [110], etc. Besides, the reduced core turbulence models are developed to speed-up dramatically the simulations, such as TGLF [111] and QuaLiKiz [112], which for some cases capture the essential part of the plasma turbulent phenomenon.

One of the challenges of reactor-like turbulence simulations is a wide range of the times scales, which have to be resolved, i.e. the time-step should be sufficiently small to resolve the turbulence time-scales, the time of the simulation should be sufficiently large to cover the transport time scales. The difference between the turbulent and transport scales increases as $(1/\rho^*)^2$, where $\rho^* \stackrel{\text{def}}{=} \rho_i^s/a$. For the ITER-like device $1/\rho^* \sim 1000$, which provides six orders of magnitude gap between the transport and turbulent scales, i.e. the transport time scales $\sim 1\ s$, whereas the electron turbulent time scales $\sim 1\mu\ s$. The dedicated techniques are developed to separated these time scales, namely the turbulent codes are coupled with transport codes. In this ansatz, the turbulent code resolves only turbulent time-scales, whereas the transport code resolves only transport time-scales, which provides a great computational efficiency and make the reactor-like simulations feasible. It is worth to mention some examples of this kind: GENE–Tango [113], TGLF-ASTRA [114, 115], TGLF–T-GYRO [116], QuaLiKiz–JINTRAC [117].

In recent times, the turbulent models have begun to be applied for the edge and the SOL regions, such as XGC [118], GENE-X [119, 120, 121], GENE [122, 123], GKEYLL [124], PICLS [125], etc., which increases the complexity of the problem significantly due to the various additional edge and SOL effects, which we briefly touched in section 1.6. Reduced turbulent models can help to simplify this problem to a certain extent. For instance, fluid turbulence codes are developed, such as: GRILLIX [21, 89], BOUT++ [126], GBS [127], TOKAM3X [128], using the well-known Braginskii collisional closure [17]. These models are applicable to the highly collisional edge and SOL plasmas. However, the collisonless extensions of the fluid turbulent codes are also developed approaching the lower collisonallity area, such as Landau-fluid approach [129]. In the fluid models the turbulent cross-field transport depends significantly on the plasma dynamics along **B** [69]. In fact, the fluid closure in the parallel direction plays its crucial role in the turbulent plasma dynamics.

The particle and momentum transport across **B** is also usually dominated by turbulence in the tokamak devices [69]. However, it is not always the case. For heavy impurities, neoclassical particle transport can be larger than the turbulent contribution in the edge of the tokamak, for example, in the H-mode ETB [130].

Also, the $E_r$ plays its significant role in the turbulence control [82] (and references therein) and the neoclassical impurity transport. The $E_r$ in the H-mode was experimentally observed close to the neoclassical predictions [131]. This is the result of the interplay between the parallel ion viscosity and cross-field drifts [81, 86]. Thus, it is important to include neoclassical effects into the edge and SOL transport models, to study $E_r$ formation in the tokamak edge.

## 3.2 Transport along magnetic field

Transport along **B** contributes to the global particle, momentum and energy transport in the two following ways. First, it affects cross-field neoclassical and turbulent transport, as it is mentioned in section 3.1. Second, in the SOL and the PFR the parallel direction particle, momentum and energy transport towards and from the divertor targets.

Energy crosses the separatrix and then is transferred towards the target and absorbed there. The parallel energy transport is very efficient, however it is not infinitely fast. The heat conductivity contributes significantly into the energy transfer towards the target along **B** and defines the energy parallel transport properties. The energy is also transferred by means of turbulent transport across **B** from the serparatrix further into the SOL (figure 1.6). If this cross-field transport is not sufficiently efficient, the energy is deposited in a very localized area at the target. These local heat loads are a big challenge for future reactors, because they can cause material melting and severe structural damage [75]. The scale of energy propagation in the SOL is usually defined by the scrape-off layer power fall-off length ($\lambda_q$) parameter. The physical meaning of this parameter is the characteristic scale of the power deposition at the outer target, if the distances along the target are projected along **B** back to the OMP (figure 1.6). There is a famous $\lambda_q$-scaling, which was developed by Eich, using a regression procedure, based on the data collected from existing tokamaks [132]. The predictions for ITER using Eich scaling is rather unpromising: $\lambda_q \approx 1\ mm$. The predictions by the most advanced XGC model are more optimistic: $\lambda_q \approx 6\ mm$ [133]. Nonetheless, the additional radiation impurity seeding, such as Ne, will be required for the power dissipation in the divertor volume to protect the target plates from the high heat loads [75]. Impurity transport studies in the SOL and plasma edge are crucial for the tokamak-reactor operation. It is important to prevent impurity leakege from the divertor to the main plasma volume, to avoid the fuel dilution and core impurity radiation. The $\lambda_q$ sensitivity studies were performed by the SOLPS-ITER transport simulations in order to obtain the operational window of the target heat load handling [134, 135]. Theses findings suggest that the operational window become narrower for smaller $\lambda_q$. However, the acceptable target heat loads together with the acceptable Ne plasma core concentration will be achievable in ITER.

The impurity leakage from the divertor region towards the main plasmas is greatly affected by the parallel transport. The main plasma flows are responsible for transporting particles, momentum, and energy that originate from or disappear into various volumetric sources. These sources are influenced by both the behavior of the main plasma and

neutral gas, as well as the presence of impurities. Notably, radiative impurities play a significant role in contributing to the heat sources. The main plasma flows defines the impurity transport by the efficient FR between the impurity and the main ion making the impurity parallel flow velocity close the main ion one. However, in the presence of the large $\nabla_{\parallel} T_i$, which is usually the case in the highly radiative divertor, there is a large TF between the impurity and the main ion species, the physics of which is discussed in subsection 2.3.2. In the case of the presence of the TF it is mostly balanced by the FR [98]. In fact, these are the two main terms in parallel momentum balance. The impurity leakage flows are formed by this mechanism. As it is described in [98], the crucial part of the impurity transport phenomenon is a relative position of the impurity poloidal stagnation surface, i.e. the set of points where the ion poloidal flow velocity, which is directed towards the target in the vicinity of the material surface, changes direction away from the target, and the ionization source profile, which is formed by the recombined on the targets neutrals, which are transported, consequently, towards the plasma and re-ionized there. Previously in the SOLPS-ITER code, the TF and the FR were based on the ZY expressions [80], which are discussed in subsection 2.4.4. Apart from many limitation, which are mentioned in subsection 2.4.4, the infinite impurity mass assumption is the strongest one. In fact, the medium-mass impurity, such as carbon (C), nitrogen (N), Ne, is only several times larger than mass of D and T. To be able to model properly the mixture of the ions with close masses, such as D, T, He, and in the case of the non-trace concentrations of the species, a complete Zhdanov closure should be used. The complete Zhdanov closure is implemented into the 3.0.8 version of the SOLPS-ITER code as a part of the present thesis by the means of the Grad-Zhdanov module. It is explicitly shown that the infinite mass difference assumption should not be used for the D-T simulations (section 6.2.3).

## 3.3 SOLPS-ITER 2D transport code

### 3.3.1 General information

The SOLPS-ITER code is a finite volume 2D fluid transport code for the edge and SOL plasma tokamak simulations [87]. It solves the drift-reduced Braginskii equations [88, 83], such as the continuity equations for the each of ion species, the parallel momentum equation on a poloidal grid for the each of ion species, the electron and ion heat equations, the electrical charge conservation. Additionally to the drifts, the cross-field transport is introduced via the, so called, the anomalous transport, i.e. anomalous diffusion coefficients and anomalous flow velocity, which are set ad-hoc. The neutrals are implemented as either a simple fluid model or by the kinetic 3D Monte-Carlo code EIRENE [136], which solves the Boltzmann equation for the atoms and molecules including neutral-plasma and neutral-neutral (the molecular atoms and photons can be potentially included). The plasma code (B2.5) interfaces with the EIRENE code by means of background fields and fluxes crossing the plasma-wall boundary (to be precise: the sheath entrance). The EIRENE code has a feedback loop to the B2.5 using the additional r.h.s. sources in the moments equations. We note here that the neutrals do

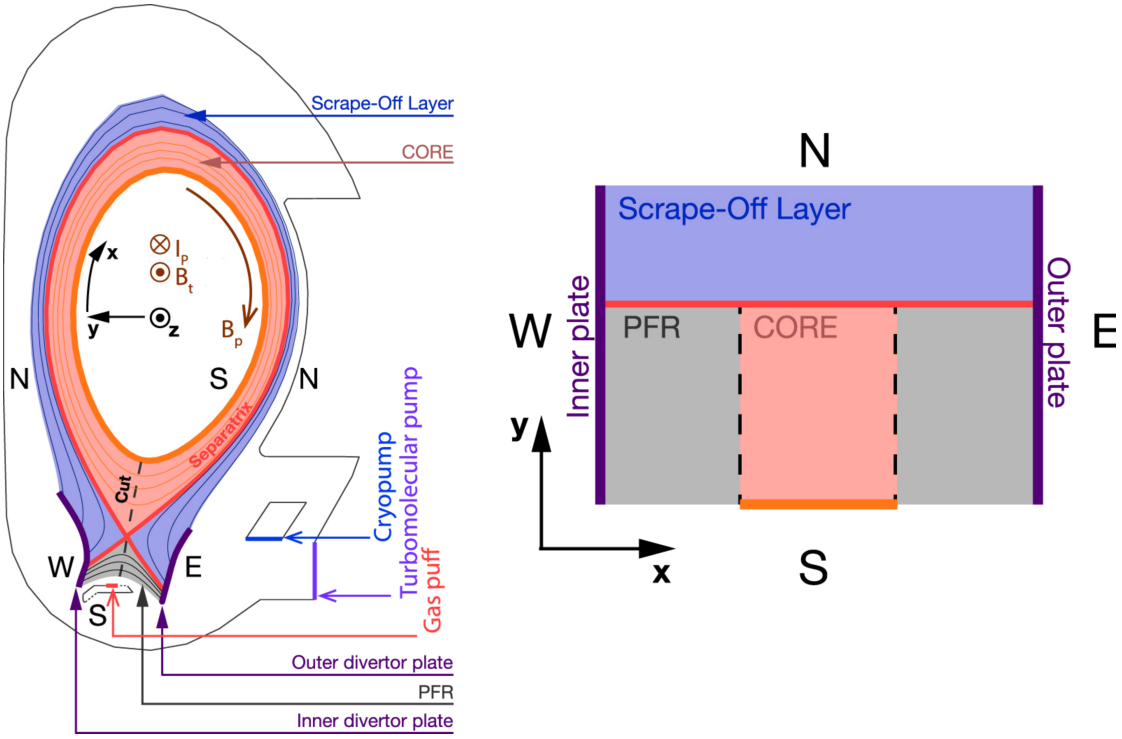


**Figure 3.1:** The SOLPS-ITER computational mesh for the ASDEX Upgrade tokamak, as example, in physical space (left) and the so-called rectangular representation of the B2.5 domain (right). Directions of curvilinear coordinates x, y and z are shown. The location of divertor targets, location of gas puff and pumps are plotted. The locations of different zones (core, SOL, PFR) and boundaries are shown on both the physical and rectangular meshes with color coding. Letters 'W', 'N', 'E', 'S' stand for 'western', 'northern', 'eastern' and 'southern' sides of the rectangular mesh correspondingly. Adapted from [20].

not contribute into the plasma distribution functions modification or the corresponding transport coefficients.

In this section we briefly describe the B2.5 plasma equations, which are implemented into the SOLPS-ITER model. In the thesis the collisional closure is discussed. Thus, the collisionless corrections [83] are omitted in this description in order to keep equations resonably short. Also boundary conditions are not discussed, because they are not important for in the scope of the thesis. The code solves the fluid equations on an orthogonal curvilinear grid (figure 3.1) where $x$ is a poloidal coordinate, $y$ is a radial coordinate and $z$ is a toroidal coordinate (3.1), as it is done in [88].

$$b_x \stackrel{\text{def}}{=} \frac{B_x}{B}, \quad h_x \stackrel{\text{def}}{=} \frac{1}{||\nabla x||}, \quad h_y \stackrel{\text{def}}{=} \frac{1}{||\nabla y||}, \quad h_z \stackrel{\text{def}}{=} \frac{1}{||\nabla z||} = 2\pi R, \quad \sqrt{g} \stackrel{\text{def}}{=} h_x h_y h_z \quad (3.1)$$

In the SOLPS-ITER code the latin letters correspond to the indexing of the ion charge states:

$$\underbrace{D^0}_{a=0},\underbrace{D^{+1}}_{a=1},\underbrace{T^0}_{a=2},\underbrace{T^{+1}}_{a=3},\underbrace{He^0}_{a=4},\underbrace{He^{+1}}_{a=5},\underbrace{He^{+2}}_{a=6}...$$

In the Zhdanov closure, the greek letters correspond to the indexing of the isonuclear sequences:

$$\underbrace{D}_{\alpha=0},\underbrace{T}_{\alpha=1},\underbrace{He}_{\alpha=2}...$$

It is essential to separate the summation over the charge states $Z$ and the summation over the isonuclear sequence $\alpha$, which is widely exploited in the Zhdanov closure [18]. For isonuclear sequence $\alpha$ and charge state $Z$, there is a one-to-one match with the Latin notation: $a(\alpha, Z)$. The relation $a(\alpha, Z)$ is a 2D array, which is used for the transition $a \leftrightarrow \alpha Z$.

The equations are written using International System of Units (SI), and temperatures are measured in J. The same choice is done for this thesis.

### 3.3.2 Continuity equations

For each ion species $z_a \neq 0$, the following continuity equation is solved:

$$\frac{\partial n_a}{\partial t} + \frac{1}{\sqrt{g}}\frac{\partial}{\partial x}\left(\frac{\sqrt{g}}{h_x}\widetilde{\Gamma}_{ax}\right) + \frac{1}{\sqrt{g}}\frac{\partial}{\partial y}\left(\frac{\sqrt{g}}{h_y}\widetilde{\Gamma}_{ay}\right) = S_a^n, \quad a = 0, 1, \ldots, ns-1 \tag{3.2}$$

$$n_e = \sum_{a=0}^{ns-1} z_a n_a, \quad n_i = \sum_{a=0}^{ns-1} n_a, \tag{3.3}$$

with the divergent part of the particle fluxes:

$$\widetilde{\Gamma}_{ax} = \left(b_x V_{\|a} + V_{ax}^{(E)} + V_{ax}^{(AN)}\right) n_a + \frac{1}{z_a e}\left(j_{ax}^{(AN)} + j_{ax}^{(in)} + \widetilde{j}_{ax}^{(vis\|)} + j_{ax}^{(vis\perp)} + \widetilde{j}_{ax}^{(visq)}\right) - D_{n,a}\frac{1}{h_x}\frac{\partial n_a}{\partial x} - \left(\frac{1}{B^2} - \frac{1}{\langle B^2\rangle}\right)\frac{B_z}{z_a e}\frac{1}{h_y}\frac{\partial n_a T_i}{\partial y}, \tag{3.4}$$

$$\widetilde{\Gamma}_{ay} = \left(V_{ay}^{(E)} + V_{ay}^{(AN)}\right) n_a + \frac{1}{z_a e}\left(j_{ay}^{(AN)} + j_{ay}^{(in)} + \widetilde{j}_{ay}^{(vis\|)} + j_{ay}^{(vis\perp)} + \widetilde{j}_{ay}^{(visq)}\right) - D_{n,a}\frac{1}{h_y}\frac{\partial n_a}{\partial y} + \left(\frac{1}{B^2} - \frac{1}{\langle B^2\rangle}\right)\frac{B_z}{z_a e}\frac{1}{h_x}\frac{\partial n_a T_i}{\partial x}, \tag{3.5}$$

where the $E \times B$ velocities are:

$$V_{ax}^{(E)} = -\frac{B_z}{B^2}\frac{1}{h_y}\frac{\partial \Phi}{\partial y}, \quad V_{ay}^{(E)} = \frac{B_z}{B^2}\frac{1}{h_x}\frac{\partial \Phi}{\partial x}. \tag{3.6}$$

To exclude the divergence-free part of the diamagnetic flux the averaged square of the **B** is used in the form of:

$$\langle B^2 \rangle = \frac{\iint\limits_{core} B^2 \sqrt{g} dx dy}{\iint\limits_{core} \sqrt{g} dx dy}. \tag{3.7}$$

The ad-hoc anomalous transport is introduced by using the prescribed $V_{ax,y}^{(AN)}$ velocity and the prescribed $D_{n,a}$ diffusion coefficient. The ion cross-field currents $j_{ax,y}^{(AN)}$, $j_{ax,y}^{(in)}$, $\widetilde{j}_{ax,y}^{(vis\|)}$, $j_{ax,y}^{(vis\perp)}$, $\widetilde{j}_{ax,y}^{(visq)}$ are defined in subsection 3.3.6.

The r.h.s. $S_a^n$ is the sources due to the ionization/recombination including external sources from the EIRENE. The elastic collisions do not contribute into the $S_a^n$. The parallel flow velocity $V_{\|a}$ is found from the parallel momentum conservation equation in section 3.3.2.

### 3.3.3 Parallel momentum conservation equations

For each ion species $z_a \neq 0$, the following parallel momentum equation is solved:

$$m_a \frac{\partial n_a V_{\|a}}{\partial t} + \frac{1}{h_z\sqrt{g}}\frac{\partial}{\partial x}\left(\frac{h_z\sqrt{g}}{h_x}\Gamma_{ax}^m\right) + \frac{1}{h_z\sqrt{g}}\frac{\partial}{\partial y}\left(\frac{h_z\sqrt{g}}{h_y}\Gamma_{ay}^m\right) + \frac{b_x}{h_x}\frac{\partial n_a T_i}{\partial x} + Z_a e n_a \frac{b_x}{h_x}\frac{\partial \Phi}{\partial x} =$$
$$= S_{a\|}^m + S_{CF_a}^m + S_{fr_a}^m + S_{Therm_a}^m + S_{AN_a}^m + S_{I_a}^m + S_{R_a}^m + S_{CX_a}^m + S_{AN_a}^m + S_{EIRENE_a}^m \tag{3.8}$$

with the divergent part of the momentum fluxes:

$$\Gamma_{ax}^m = \begin{cases} m_a V_{\|a}\Gamma_{ax}^{Cor} + \frac{4}{3}\eta_{ax}^{(CL)}\frac{\partial \ln h_z}{h_x \partial x}V_{\|a} - \eta_{ax}\frac{\partial V_{\|a}}{h_x \partial x}, & a = a_{main} \\ m_a V_{\|a}\Gamma_{ax}^{Cor} - \eta_{ax}\frac{\partial V_{\|a}}{h_x \partial x}, & \text{otherwise} \end{cases} \tag{3.9}$$

$$\Gamma_{ay}^m = m_a V_{\|a}\Gamma_{ay}^{Cor} - \eta_{ay}\frac{\partial V_{\|a}}{h_y \partial y} \tag{3.10}$$

where the corresponding particle fluxes together with the Coriolis force contribution [88] are:

$$\Gamma_{ax}^{Cor} = \left(b_x V_{\|a} + 2\frac{T_i B_z}{z_a e}\frac{\partial}{h_y \partial y}\left(\frac{1}{B^2}\right) + V_{ax}^{(E)} + V_{ax}^{(AN)}\right) n_a +$$
$$\frac{1}{z_a e}\left(j_{ax}^{(AN)} + j_{ax}^{(in)} + \widetilde{j}_{ax}^{(vis\|)} + j_{ax}^{(vis\perp)} + \widetilde{j}_{ax}^{(visq)}\right) - D_{n,a}\frac{1}{h_x}\frac{\partial n_a}{\partial x} \tag{3.11}$$

$$\Gamma_{ay}^{Cor} = \left(-2\frac{T_i B_z}{z_a e}\frac{\partial}{h_x \partial x}\left(\frac{1}{B^2}\right) + V_{ay}^{(E)} + V_{ay}^{(AN)}\right) n_a + \frac{1}{z_a e}\left(j_{ay}^{(AN)} + j_{ay}^{(in)} + \widetilde{j}_{ay}^{(vis\parallel)} + j_{ay}^{(vis\perp)} + \widetilde{j}_{ay}^{(visq)}\right) - D_{n,a}\frac{1}{h_y}\frac{\partial n_a}{\partial y} \quad (3.12)$$

additionally to the viscosity contribution into the divergence, there is a source part of the viscosity:

$$S_{a\parallel}^{m} = -\left(\nabla \cdot \overleftrightarrow{\pi}_a^{\parallel}\right)_{\parallel} = \begin{cases} -\left(\nabla \cdot \overleftrightarrow{\pi}_a^{V_\parallel}\right)_{\parallel}^{res} - \left(\nabla \cdot \overleftrightarrow{\pi}_a^{q_\parallel}\right)_{\parallel} & a = a_{main} \\ 0, & \text{otherwise} \end{cases} \quad (3.13)$$

$$\left(\nabla \cdot \overleftrightarrow{\pi}_a^{V_\parallel}\right)_{\parallel}^{res} = \begin{cases} -\frac{1}{h_z\sqrt{g}}\frac{\partial}{\partial x}\left(\frac{h_z\sqrt{g}}{h_x}\frac{4}{3}\eta_{ax}^{(CL)}\frac{\partial \ln\left(h_z B^{\frac{1}{2}}\right)}{B^{\frac{1}{2}} h_x \partial x}\right) B^{\frac{1}{2}} V_{\parallel a}, & a = a_{main} \\ 0, & \text{otherwise} \end{cases} \quad (3.14)$$

where the viscosity transport coefficients are

$$\eta_{ax} = \eta_a^{(AN)} + \frac{4}{3}\eta_{ax}^{(CL)}, \quad \eta_{ay} = \eta_a^{(AN)}, \quad (3.15)$$

where the anomalous transport coefficients represents the turbulent momentum transport and the classical transport coefficient is defined according to Braginskii:

$$\eta_{ax}^{(CL)} = 0.96 T_i n_a \tau_a^{(Br)} b_x^2, \quad (3.16)$$

$$\tau_a^{(Br)} = \frac{3}{4\sqrt{\pi}}\frac{\sqrt{m_a}T_i^{\frac{3}{2}}}{z_a^2 z_{eff} n_e \ln\Lambda}\left(\frac{4\pi\epsilon_0}{e}\right)^2. \quad (3.17)$$

$$\ln\Lambda = \begin{cases} 12 & \\ \max\{5; 23.4 - 1.15\cdot\log_{10}\left(\frac{n_e}{10^6}\right) + 3.45\cdot\log_{10}\left(\frac{T_e}{e}\right)\}, & \frac{T_e}{e} \le 50 \\ \max\{5; 25.3 - 1.15\cdot\log_{10}\left(\frac{n_e}{10^6}\right) + 2.30\cdot\log_{10}\left(\frac{T_e}{e}\right)\}, & \frac{T_e}{e} > 50 \\ \max\{5; 17.3 - 0.5\cdot\ln\left(\frac{n_e}{10^{20}}\right) + 1.5\cdot\ln\left(\frac{T_i}{e\cdot 10^3}\right)\} & \end{cases} \begin{matrix} \\ \text{Braginskii formula} \\ \\ \text{Wesson formula} \\ \text{for ion-ion collisions} \end{matrix} \quad (3.18)$$

The heat stresses are:

$$\left(\nabla \cdot \overset{\leftrightarrow}{\pi}_a^{q_\parallel}\right)_\parallel = \begin{cases} -B^{\frac{3}{2}} b_x \dfrac{\partial}{h_x \partial x}\left(\dfrac{b_x \tau_a^{(Br)}}{B^2}\dfrac{\partial\left(B^{\frac{1}{2}} q_a^{(0)}\right)}{h_x \partial x}\right), & a = a_{main} \\ 0, & \text{otherwise} \end{cases} \tag{3.19}$$

$$q_a^{(0)} = q_{a\parallel}^{(0)} + \frac{B}{B_x} q_{ax}^{(dia)} = \begin{cases} 0 & \text{outside the separatrix} \\ -\frac{\kappa_{ix}^{(CL)}}{b_x}\frac{\partial T_i}{h_x \partial x} - \frac{5}{2}\frac{B_z B}{B_x B^2}\frac{n_a T_i}{e}\frac{\partial T_i}{h_y \partial y} & \text{inside the separatrix} \end{cases}, \tag{3.20}$$

where the ion heat conductivity $\kappa_{ix}^{(CL)}$ is defined in subsection 3.3.6.

The thermal and friction forces, which are written using ZY expressions (section 2.4.4), are:

$$S_{Therm,a}^m = S_{Therm,ea}^m + S_{Therm,ia}^m \tag{3.21}$$

$$S_{fr,a}^m = S_{fr,ea}^m + S_{fr,ia}^m \tag{3.22}$$

The electron contributions are:

$$S_{Therm,ea}^m = -\alpha_{ex} c_e^{(1)} \frac{n_a z_a^2 m_e}{b_x e \zeta_e}\frac{1}{h_x}\frac{\partial T_e}{\partial x},\ z_a \neq 0 \tag{3.23}$$

$$S_{fr,ea}^m = \frac{b_x^2 e^2 z_a^2}{\sigma_\parallel^{(CL)} z_{eff}} n_e n_a \left(V_{e\parallel} - V_{a\parallel}\right),\ z_a \neq 0 \tag{3.24}$$

and the ion contributions are:

$$S_{Therm,ia}^m = \sum_{\substack{b=0 \\ b\neq a}}^{ns-1} z_a^2 z_b^2 \frac{m_p}{\zeta_p e}\frac{n_a n_b}{n_a + n_b}\alpha_{ab}\frac{1}{h_x}\frac{\partial T_i}{\partial x},\ z_a \neq 0 \tag{3.25}$$

$$S_{fr,ia}^m = \sum_{\substack{b=0 \\ b\neq a}}^{ns-1} R_{ab}^{(V_\parallel)} = \sum_{\substack{b=0 \\ b\neq a}}^{ns-1} \frac{1}{\zeta_p}\sqrt{\frac{m_p m_a m_b}{m_a + m_b}} z_a^2 z_b^2 n_a n_b K_{ab}^{(V_\parallel)}\left(V_{b\parallel} - V_{a\parallel}\right) \tag{3.26}$$

where

$$\alpha_x^{(CL)} = -b_x^2 \frac{e}{m_e} \frac{\widetilde{c}_e^{(2)}}{c_e^{(1)}} n_e \tau_e z_{eff},\ \sigma_\parallel^{(CL)} = b_x^2 \frac{e^2}{m_e} \frac{n_e \tau_e}{c_e^{(1)}} \tag{3.27}$$

$$\alpha_{ab} = \frac{\zeta_p e\,(n_a + n_b)}{m_p} \sqrt{\frac{m_a m_b}{m_a + m_b}} \left( \frac{K_{ab}^{(Therm)}}{\kappa_b} - \frac{K_{ba}^{(Therm)}}{\kappa_a} \right) b_x,\ z_a \neq 0 \tag{3.28}$$

$$\kappa_a = \sum_{r=0}^{ns-1} z_a^2 z_r^2 n_r \sqrt{\frac{m_a m_r}{m_a + m_r}} \tag{3.29}$$

$$K_{rs}^{(Therm)} = \begin{cases} c_{imp}^{(2)}, & s \neq r, & s = s_{main}, & z_r \neq 0, & z_s \neq 0 \\ 0, & r \neq r_{main}, & s \neq s_{main}, & z_r \neq 0, & z_s \neq 0 \\ 0, & r = r_{main}, & \forall s & & \end{cases} \tag{3.30}$$

$$K_{rs}^{(V_\parallel)} = \begin{cases} c_{imp}^{(1)}, & r = r_{main}, & s \neq r, & z_r \neq 0, & z_s \neq 0 \\ c_{imp}^{(1)}, & s = s_{main}, & r \neq s, & z_r \neq 0, & z_s \neq 0 \\ 1, & r \neq r_{main}, & s \neq s_{main}, & z_r \neq 0, & z_s \neq 0 \\ 0, & r = s, & \text{or} & z_r = 0, & z_s = 0 \end{cases} \tag{3.31}$$

$$\zeta_p = \frac{3}{4\sqrt{2\pi}} \frac{\sqrt{m_p} T_i^{\frac{3}{2}}}{\ln \Lambda} \left( \frac{4\pi\epsilon_0}{e^2} \right)^2,\ \zeta_e = \frac{3}{4\sqrt{2\pi}} \frac{\sqrt{m_e} T_e^{\frac{3}{2}}}{\ln \Lambda} \left( \frac{4\pi\epsilon_0}{e^2} \right)^2,\ \tau_e = \frac{\zeta_e}{z_{eff} n_e} \tag{3.32}$$

$$c_e^{(1)} = \frac{(1 + 0.24 z_{eff})\,(1 + 0.93 z_{eff})}{(1 + 2.56 z_{eff})\,(1 + 0.29 z_{eff})},\ c_e^{(2)} = 1.56 \frac{(1 + 1.4 z_{eff})\,(1 + 0.52 z_{eff})}{(1 + 2.56 z_{eff})\,(1 + 0.29 z_{eff})} \tag{3.33}$$

$$c_{imp}^{(1)} = \frac{(1 + 0.24 z_{eff\_imp})\,(1 + 0.93 z_{eff\_imp})}{(1 + 2.56 z_{eff\_imp})\,(1 + 0.29 z_{eff\_imp})},\ c_{imp}^{(2)} = 1.56 \frac{(1 + 1.4 z_{eff\_imp})\,(1 + 0.52 z_{eff\_imp})}{(1 + 2.56 z_{eff\_imp})\,(1 + 0.29 z_{eff\_imp})} \tag{3.34}$$

$$z_{eff\_imp} = \frac{\sum\limits_{\substack{a=0 \\ a \neq a_{main}}}^{ns-1} n_a z_a^2}{n_{a_{main}} z_{a_{main}}^2},\quad z_{eff} = \frac{\sum\limits_{a=0}^{ns-1} n_a z_a^2}{n_e},\quad \widetilde{c}_e^{(2)} = \frac{c_e^{(2)}}{\left( z_{eff} + \frac{\sqrt{2}}{2} \right)}. \tag{3.35}$$

The centrifugal force and anomalous source are:

$$S_{CF_a}^m = m_a b_x n_a V_{\parallel a}^2 \frac{1}{h_z h_x} \frac{\partial h_z}{\partial x},\quad S_{AN_a}^m = -j_{ay}^{(AN)} \frac{B B_x}{B_z} \tag{3.36}$$

The rest part of the r.h.s. $S_{I_a}^m$, $S_{R_a}^m$, $S_{CX_a}^m$, $S_{EIRENE_a}^m$ is the sources due to the ionization/recombination/charge-exchange including external sources from the EIRENE.

### 3.3.4 Electron heat equation

For the electron species, the following heat equation is solved:

$$\frac{3}{2}\frac{\partial n_e T_e}{\partial t}+\frac{1}{\sqrt{g}}\frac{\partial}{\partial x}\left(\frac{\sqrt{g}}{h_x}\widetilde{q}_{ex}\right)+\frac{1}{\sqrt{g}}\frac{\partial}{\partial y}\left(\frac{\sqrt{g}}{h_y}\widetilde{q}_{ey}\right)+\frac{n_e T_e}{\sqrt{g}}\frac{\partial}{\partial x}\left(\frac{\sqrt{g}}{h_x}b_x V_{e\|}\right)$$
$$=Q_e+n_e T_e B_z\frac{1}{h_x h_y}\left(\frac{\partial\Phi}{\partial y}\frac{\partial}{\partial x}\left(\frac{1}{B^2}\right)-\frac{\partial\Phi}{\partial x}\frac{\partial}{\partial y}\left(\frac{1}{B^2}\right)\right)-\frac{j_y^{(ST)}}{en_e}\frac{\partial n_e T_e}{h_y\partial y}+Q_{Fei}+Q_e^{EIRENE} \tag{3.37}$$

with the divergent part of the electron heat fluxes:

$$\widetilde{q}_{ex}=\frac{3}{2}\Gamma_{ex}T_e-c_{071}\frac{j_x^{(\|)}}{e}T_e-\kappa_{ex}\frac{1}{h_x}\frac{\partial T_e}{\partial x}+\frac{5}{2}\left(\frac{1}{B^2}-\frac{1}{\langle B^2\rangle}\right)\frac{B_z}{e}\frac{1}{h_y}\frac{\partial n_e T_e^2}{\partial y} \tag{3.38}$$

$$\widetilde{q}_{ey}=\frac{3}{2}\Gamma_{ey}T_e-\frac{5}{2}\frac{j_y^{(ST)}}{e}T_e-\kappa_{ey}\frac{1}{h_y}\frac{\partial T_e}{\partial y}-\frac{5}{2}\left(\frac{1}{B^2}-\frac{1}{\langle B^2\rangle}\right)\frac{B_z}{e}\frac{1}{h_x}\frac{\partial n_e T_e^2}{\partial x} \tag{3.39}$$

where the corresponding particle fluxes are:

$$\Gamma_{ex}=\sum_{a=0}^{ns-1}z_a\Gamma_{ax}^{(he)}-\frac{j_x^{(\|)}}{e},\quad \Gamma_{ey}=\sum_{a=0}^{ns-1}z_a\Gamma_{ay}^{(he)} \tag{3.40}$$

$$\Gamma_{ax}^{(he)}=\left(b_x V_{a\|}+V_{ax}^{(E)}+\frac{5}{3}V_a^{(AN)}\right)n_a-\frac{5}{3}D_{n,a}\frac{1}{h_x}\frac{\partial n_a}{\partial x} \tag{3.41}$$

$$\Gamma_{ay}^{(he)}=\left(V_{ay}^{(E)}+\frac{5}{3}V_a^{(AN)}\right)n_a-\frac{5}{3}D_{n,a}\frac{1}{h_y}\frac{\partial n_a}{\partial y} \tag{3.42}$$

where the currents $j_x^{(\|)}$, $j_y^{(ST)}$ are defined in subsection 3.3.6.
The electron transport coefficients are

$$\kappa_{ex}=\kappa_e^{(AN)}+b_x^2\kappa_{ex}^{(CL)},\quad \kappa_{ey}=\kappa_e^{(AN)}+\kappa_e^{(ST)} \tag{3.43}$$

$$\kappa_e^{(AN)}=\chi_e^{(AN)}n_e \tag{3.44}$$

$$\kappa_e^{(ST)} = \begin{cases}1.6\alpha^{(ST)}\sigma^{(ST)}T_e/e^2, & y\in\left[-\Delta^{(ST)},0\right], \quad \alpha^{(ST)}\approx 2\\ 0, & y\notin\left[-\Delta^{(ST)},0\right]\end{cases} \tag{3.45}$$

$$\kappa_{ex}^{(CL)}=\frac{T_e}{m_e}f_{k_e}\left(z_{eff}\right)n_e\tau_e,\quad f_{k_e}\left(z_{eff}\right)=\frac{3.9+2.3/z_{eff}}{0.31+1.2/z_{eff}+0.41/z_{eff}^2} \tag{3.46}$$

$$c_{071} = \frac{z_{eff} c_e^{(2)}}{\left(z_{eff} + \frac{\sqrt{2}}{2}\right)} \tag{3.47}$$

The electron heat sources are:

$$Q_e = -Q_\Delta - Q_R \tag{3.48}$$

$$Q_\Delta = c_{eqp} \ln \Lambda e^{\frac{3}{2}} \frac{\sum_{a=0}^{ns-1} \frac{z_a^2 m_p}{m_a} n_a n_e}{T_e^{\frac{3}{2}}} (T_e - T_i), \quad c_{eqp} = 4.8 \cdot 10^{-15}, \tag{3.49}$$

$$Q_{Fei} = V_{e\|} \sum_{\substack{a=0 \\ z_a \neq 0}}^{ns-1} \left(S^m_{fr,ea} + S^m_{Therm,ea}\right) \tag{3.50}$$

The rest part of the r.h.s.: the B2.5 ionisation, recombination, bremsstrahlung and line radiation $Q_R$ and the EIRENE heat source $Q_e^{EIRENE}$. The electron parallel flow velocity $V_{\|e}$ is found from the Ohm's law in subsection 3.3.6.

### 3.3.5 Ion heat equation

For the ion species, the following total ion heat equation (summed over all ion species) is solved:

$$\frac{3}{2}\frac{\partial n_i T_i}{\partial t} + \frac{1}{\sqrt{g}}\frac{\partial}{\partial x}\left(\frac{\sqrt{g}}{h_x}\widetilde{q}_{ix}\right) + \frac{1}{\sqrt{g}}\frac{\partial}{\partial y}\left(\frac{\sqrt{g}}{h_y}\widetilde{q}_{iy}\right) + \sum_{a=0}^{ns-1} \frac{n_a T_i}{\sqrt{g}}\frac{\partial}{\partial x}\left(\frac{\sqrt{g}}{h_x} V_{a\|} b_x\right) =$$
$$Q_\Delta + Q_{F_{ab}} + T_i B_z \frac{1}{h_x h_y}\left(\frac{\partial \Phi}{\partial y}\frac{\partial}{\partial x}\left(\frac{1}{B^2}\right) - \frac{\partial \Phi}{\partial x}\frac{\partial}{\partial y}\left(\frac{1}{B^2}\right)\right) \sum_{\substack{a=0 \\ z_a \neq 0}}^{ns-1} n_a + Q_{vis} + Q_I^{(i)} + Q_R^{(i)} + Q_i^{EIRENE}, \tag{3.51}$$

with the divergent part of the ion heat fluxes:

$$\widetilde{q}_{ix} = \frac{3}{2}\Gamma_{ix} T_i + \frac{3}{2}\left(\frac{j_x^{(AN)} + j_x^{(in)} + \widetilde{j}_x^{(vis\|)} + j_x^{(vis\perp)} + \widetilde{j}_x^{(visq)}}{e}\right) T_i -$$
$$\kappa_{ix}\frac{1}{h_x}\frac{\partial T_i}{\partial x} - \frac{5}{2}\sum_{\substack{a=0 \\ z_a \neq 0}}^{ns-1}\left(\frac{1}{B^2} - \frac{1}{\langle B^2 \rangle}\right)\frac{B_z}{z_a e}\frac{1}{h_y}\frac{\partial n_a T_i^2}{\partial y} \tag{3.52}$$

$$\widetilde{q}_{iy} = \frac{3}{2}\Gamma_{iy}T_i + \frac{3}{2}\frac{\left(j_y^{(AN)} + \widetilde{j}_y^{(vis\parallel)} + j_y^{(vis\perp)} + \widetilde{j}_y^{(visq)} + j_y^{(in)}\right)}{e}T_i - \kappa_{iy}\frac{1}{h_y}\frac{\partial T_i}{\partial y} + \frac{5}{2}\sum_{\substack{a=0\\ z_a\neq 0}}^{ns-1}\left(\frac{1}{B^2} - \frac{1}{\langle B^2\rangle}\right)\frac{1}{h_x}\frac{\partial n_a T_i^2}{\partial x} \quad (3.53)$$

where the corresponding particle fluxes are:

$$\Gamma_{ix} = \sum_{a=0}^{ns-1}\Gamma_{ax}^{(he)}, \quad \Gamma_{iy} = \sum_{a=0}^{ns-1}\Gamma_{ay}^{(he)}. \quad (3.54)$$

The ion transport coefficients are:

$$\kappa_{ix} = \kappa_{ix}^{(AN)} + \kappa_{ix}^{(CL)}, \quad \kappa_{iy} = \kappa_{iy}^{(AN)} \quad (3.55)$$

$$\kappa_{ix}^{(AN)} = \sum_{a=0}^{ns-1}\chi_a^{(AN)}n_a, \quad \kappa_{iy}^{(AN)} = \sum_{a=0}^{ns-1}\chi_a^{(AN)}n_a \quad (3.56)$$

$$\kappa_{ix}^{(CL)} = b_x^2\sum_{\substack{a=0\\ z_a\neq 0}}^{ns-1} 3.98\frac{T_i}{m_a}n_a\tau_a^{(Br)}. \quad (3.57)$$

The ion heat sources are:

$$Q_{F_{ab}} = -\sum_{\substack{a=0\\ z_a\neq 0}}^{ns-1} V_{a\parallel}\left(S_{fr,a}^m + S_{Therm,a}^m\right) \quad (3.58)$$

$$Q_{vis} = \sum_{\substack{a=0\\ z_a\neq 0}}^{ns-1}\left(\eta_{ax}\left(\frac{\partial V_{a\parallel}}{h_x\partial x}\right)^2 + \eta_a^{(AN)}\left(\frac{\partial V_{a\parallel}}{h_y\partial y}\right)^2\right) \quad (3.59)$$

The rest part of the r.h.s.: the B2.5 ionisation, recombination $Q_R$ and $Q_I^{(i)}$, $Q_R^{(i)}$ the EIRENE heat source $Q_i^{EIRENE}$.

### 3.3.6 Charge conservation equation

$$\frac{1}{\sqrt{g}}\frac{\partial}{\partial x}\left(\frac{\sqrt{g}}{h_x}j_x\right) + \frac{1}{\sqrt{g}}\frac{\partial}{\partial y}\left(\frac{\sqrt{g}}{h_y}j_y\right) = 0 \quad (3.60)$$

$$j_x = j_x^{(AN)} + \widetilde{j}_x^{(dia)} + j_x^{(in)} + \widetilde{j}_x^{(vis\parallel)} + j_x^{(vis\perp)} + \widetilde{j}_x^{(visq)} + \widetilde{j}_x^{(s)} + j_x^{(\parallel)} \quad (3.61)$$

$$j_y = j_y^{(AN)} + \widetilde{j}_y^{(dia)} + j_y^{(in)} + \widetilde{j}_y^{(vis\|)} + j_y^{(vis\perp)} + \widetilde{j}_y^{(visq)} + \widetilde{j}_y^{(s)} + j_y^{(ST)} \tag{3.62}$$

The Ohm's law is:

$$j_x^{(\|)} = \sigma_\| \left( \frac{1}{en_e h_x} \frac{\partial n_e T_e}{\partial x} - \frac{1}{h_x} \frac{\partial \Phi}{\partial x} \right) - \alpha_{ex} \frac{1}{h_x} \frac{\partial T_e}{\partial x} - \frac{eb_x}{z_{eff}} \sum_{a=0}^{ns-1} n_a V_{a\|} \left( z_a^2 - z_a z_{eff} \right) \tag{3.63}$$

$$V_{e\|} = \frac{1}{en_e} \left[ \sum_{a=0}^{ns-1} z_a e n_a V_{a\|} - \frac{j_x^{(\|)}}{b_x} \right] \tag{3.64}$$

Divergent parts of the diamagnetic currents are:

$$\widetilde{j}_x^{(dia)} = B_z \frac{\sum\limits_{\substack{a=0 \\ z_a \neq 0}}^{ns-1} n_a \left( z_a T_e + T_i \right)}{h_y} \frac{\partial}{\partial y} \left( \frac{1}{B^2} \right), \quad \widetilde{j}_y^{(dia)} = -B_z \frac{\sum\limits_{\substack{a=0 \\ z_a \neq 0}}^{ns-1} n_a \left( z_a T_e + T_i \right)}{h_x} \frac{\partial}{\partial x} \left( \frac{1}{B^2} \right) \tag{3.65}$$

Inertial currents are:

$$j_x^{(in)} = \sum_{\substack{a=0 \\ z_a \neq 0}}^{ns-1} j_{ax}^{(in)}, \quad j_y^{(in)} = \sum_{\substack{a=0 \\ z_a \neq 0}}^{ns-1} j_{ay}^{(in)} \tag{3.66}$$

$$j_{ax}^{(in)} = \begin{cases} \dfrac{B_z}{2} \dfrac{\partial}{h_y \partial y} \left( \dfrac{1}{B^2} \right) m_a n_a V_{a\|}^2, \; z_a \neq 0 \\ 0, \; z_a = 0 \end{cases}, \quad j_{ay}^{(in)} = \begin{cases} -\dfrac{B_z}{2} \dfrac{\partial}{h_x \partial x} \left( \dfrac{1}{B^2} \right) m_a n_a V_{a\|}^2, \; z_a \neq 0 \\ 0, \; z_a = 0 \end{cases} \tag{3.67}$$

Viscosity currents are:

$$\widetilde{j}_x^{(vis\|)} = \sum_{\substack{a=0 \\ z_a \neq 0}}^{ns-1} \widetilde{j}_{ax}^{(vis\|)}, \quad \widetilde{j}_y^{(vis\|)} = \sum_{\substack{a=0 \\ z_a \neq 0}}^{ns-1} \widetilde{j}_{ay}^{(vis\|)} \tag{3.68}$$

$$\widetilde{j}_{ax}^{(vis\|)} = -\delta_{a_{main},a} \frac{B_z \sqrt{B}}{3B_x} \frac{\partial}{h_y \partial y} \left( \frac{1}{B^2} \right) \eta_{ax}^{(CL)} \frac{\partial \left( \sqrt{B} V_{a\|} \right)}{h_x \partial x}, \tag{3.69}$$

$$\widetilde{j}_{ay}^{(vis\|)} = \delta_{a_{main},a} \frac{B_z \sqrt{B}}{3B_x} \frac{\partial}{h_x \partial x} \left( \frac{1}{B^2} \right) \eta_{ax}^{(CL)} \frac{\partial \left( \sqrt{B} V_{a\|} \right)}{h_x \partial x}, \tag{3.70}$$

$$j_x^{(vis\perp)} = \sum_{\substack{a=0 \\ z_a \neq 0}}^{ns-1} j_{ax}^{(vis\perp)}, \quad \widetilde{j}_y^{(vis\perp)} = \sum_{\substack{a=0 \\ z_a \neq 0}}^{ns-1} \widetilde{j}_{ay}^{(vis\perp)} \tag{3.71}$$

$$j_{ax}^{(vis\perp)} = 0, \quad \widetilde{j}_{ay}^{(vis\perp)} = \begin{cases} -\dfrac{1}{B\sqrt{g}} \dfrac{\partial}{\partial y} \left( \dfrac{\sqrt{g}}{h_y} \dfrac{\eta_a^{(AN)}}{4} \dfrac{\partial V_{a\perp}}{h_y \partial y} \right), \; z_a \neq 0 \\ 0, \; z_a = 0 \end{cases} \tag{3.72}$$

$$V_{a\perp} = -\frac{1}{Bh_y} \frac{\partial \Phi}{\partial y} - \frac{1}{z_a e B h_y n_a} \frac{\partial n_a T_i}{\partial y} \tag{3.73}$$

$$\widetilde{j}_x^{(visq)} = \sum_{\substack{a=0 \\ z_a \neq 0}}^{ns-1} \widetilde{j}_{ax}^{(visq)}, \quad \widetilde{j}_y^{(visq)} = \sum_{\substack{a=0 \\ z_a \neq 0}}^{ns-1} \widetilde{j}_{ay}^{(visq)} \tag{3.74}$$

$$\widetilde{j}_{ax}^{(visq)} = -\delta_{a_{main},a} 0.24 \tau_a^{(Br)} b_z \frac{B_x}{B^{\frac{1}{2}}} \frac{\partial}{h_y \partial y} \left( \frac{1}{B^2} \right) \frac{\partial \left( q_a^{(0)} B^{\frac{1}{2}} \right)}{h_x \partial x} \tag{3.75}$$

$$\widetilde{j}_{ay}^{(visq)} = \delta_{a_{main},a} 0.24 \tau_a^{(Br)} b_z \frac{B_x}{B^{\frac{1}{2}}} \frac{\partial}{h_x \partial x} \left( \frac{1}{B^2} \right) \frac{\partial \left( q_a^{(0)} B^{\frac{1}{2}} \right)}{h_x \partial x} \tag{3.76}$$

Anomalous currents are:

$$j_x^{(AN)} = \sum_{\substack{a=0 \\ z_a \neq 0}}^{ns-1} j_{ax}^{(AN)}, \quad j_y^{(AN)} = \sum_{\substack{a=0 \\ z_a \neq 0}}^{ns-1} j_{ay}^{(AN)} \tag{3.77}$$

$$j_{ax}^{(AN)} = -\frac{Z_a n_a}{n_e} \sigma^{(AN)} \frac{\partial \Phi}{h_x \partial x}, \quad j_{ay}^{(AN)} = -\frac{Z_a n_a}{n_e} \sigma^{(AN)} \frac{\partial \Phi}{h_y \partial y} \tag{3.78}$$

Ion-neutral currents are:

$$\widetilde{j}_x^{(s)} = \sum_{\substack{a_0=0 \\ z_{a_0}=0 \;\&\; z_{n,a_0}=1}}^{ns-1} \sum_{\substack{a=0 \\ z_a=1 \;\&\; z_{n,a}=1}}^{ns-1} \left( -\sigma_{aa_0} b_z^2 \frac{\partial \Phi}{h_x \partial x} - \sigma_{aa_0} b_z^2 \frac{1}{z_a e n_a} \frac{\partial n_a T_i}{h_x \partial x} + \sigma_{aa_0} B_z V_{a_0 y} \right) \tag{3.79}$$

$$\widetilde{j}_y^{(s)} = \sum_{\substack{a_0=0 \\ z_{a_0}=0 \;\&\; z_{n,a_0}=1}}^{ns-1} \sum_{\substack{a=0 \\ z_a=1 \;\&\; z_{n,a}=1}}^{ns-1} \left( -\sigma_{aa_0} \frac{\partial \Phi}{h_y \partial y} - \sigma_{aa_0} \frac{1}{z_a e n_a} \frac{\partial n_a T_i}{h_y \partial y} - \sigma_{aa_0} B_z V_{a_0 x} \right) \tag{3.80}$$

$$\sigma_{aa_0} = \begin{cases} \dfrac{\tilde{\mu}_{aa_0} m_p n_a \langle V_{aa_0} \sigma_{ex} \rangle n_{a_0}}{B^2}, & z_{a_0} = 0 \;\&\; z_{n,a_0} = 1, z_a \neq 0 \;\&\; z_{n_a} = 1 \\ 0, & \text{otherwise} \end{cases} \tag{3.81}$$

$$\langle V_{aa_0}\sigma_{ex}\rangle = 3.2\cdot 10^{-15}\sqrt{\frac{T_i}{0.026e}}\sqrt{\frac{1}{\tilde{\mu}_{aa_0}}} \tag{3.82}$$

$$\tilde{\mu}_{aa_0} = \frac{\frac{m_a}{m_p}\frac{m_{a_0}}{m_p}}{\frac{m_a}{m_p}+\frac{m_{a_0}}{m_p}}, \quad V_{a_0y} = \frac{\Gamma_{a_0y}}{n_{a_0}} \tag{3.83}$$

The stochastic current with a constant prefactor $c_{\sigma^{(ST)}}$ is:

$$j_y^{(ST)} = \begin{cases} -\sigma^{(ST)}\left(\frac{1}{h_y}\frac{\partial\Phi}{\partial y} - \frac{T_e}{en_e}\frac{1}{h_y}\frac{\partial n_e}{\partial y} - \frac{0.5}{e}\frac{1}{h_y}\frac{\partial T_e}{\partial y}\right), & y\in\left[-\Delta^{(ST)},0\right] \\ 0, & y\notin\left[-\Delta^{(ST)},0\right] \end{cases} \tag{3.84}$$

$$\sigma^{(ST)} = \begin{cases} c_{\sigma^{(ST)}}en_e, & y\in\left[-\Delta^{(ST)},0\right], \quad c_{\sigma^{(ST)}} > c_{\sigma_y^{(AN)}} \\ 0, & y\notin\left[-\Delta^{(ST)},0\right] \end{cases} \tag{3.85}$$

### 3.3.7 Focus of the thesis for the model improvement

Previously, the SOLPS-ITER code was only applicable to the mixture with a single hydrogen main ion species and several heavy impurity species. The parallel strain stress-viscosity (in the complete form) (3.9), (3.14) and the heat stress-viscosity (3.19) were written only for the single hydrogen species, based on the single species model [88, 83] (and references therein). The corresponding terms for impurities were neglected. This was also true for the corresponding viscosity drift currents (3.69), (3.70), (3.75), (3.76).

The TF (3.25) and the FR (3.26) were written, based on the ZY expressions (subsection 2.4.4), which are applicable only for the heavy impurity $m_{imp} \gg m_{main}$ (this condition is not well satisfied even for medium-mass impurities: C, N, Ne [84]) and for only single main species.

The parallel ion heat conductivity (3.57) was not derived consistently. It was written with the Braginskii transport coefficient and with the multi-ion extension of the Braginskii collsional frequency (3.17), which is correct for the main ion species, but incorrect for the impurity species. For example, the collisional frequency must include the reduced mass, which turns into the mass of the light species when the heavy species mass is much larger the light species mass. Instead, the heavy impurity mass contributes into the heavy impurity collsional frequency (3.17). It is especially sensitive when the heavy impurity viscosity is calculated (3.16). For the viscosity, the single ion Braginskii coefficient was chosen for all species. In spite of incorrect treatement of the impurity viscosity, the total plasma viscosity was not significantly different from the one which is calculated using Zhdanov closure [84]. The same is also correct for the total ion conductivity [84]. It is a consequence of the minor contributions from impurity species to the total plasma momentum and heat transport. Also, the main ion heat and viscosity coefficients are not significantly different from the the Braginskii ones [84].

There is an effect, which was completely absent previously in the SOLPS-ITER code: the ion heat flux, which appears due to the modification of the light species distribution

function as a result of the flow velocity difference between ions. This heat flux is well-known for electrons [17] and was included into the SOLPS-ITER code (3.38). This flux naturally appears due to the flow velocity difference in the Zhdanov closure.

We note that previously there was an explicit separation between the main species and impurity species. In fact, the conditions (3.9), (3.14), (3.69), (3.70), (3.75), (3.76), (3.25) and (3.26) imply that different sets of equations were solved for the main and impurity ion species. This can be avoided if the Zhdanov closure is used.

Now, it should be clear to the reader that the previous version of SOLPS-ITER code was very restrictive in the way of plasma mixture choice, i.e. only hydrogen plasma with heavy impurity could be simulated. In this thesis the Zhdanov closure was implemented into the SOLPS-ITER code. The complete multi-ion generalization of the SOLPS-ITER code is performed. More accurate treatment of the TF, of the FR, as well as of the heat flux and of the heat and strain viscosity tensor, are applied for the multi-ion plasma. An additional ion velocity difference dependent heat flux is implemented. Now the fusion reactor mixtures can be simulated with the SOLPS-ITER code: $D + T$ in comparable amouts with $He$ and radiative impurities. Besides, $He$ plasmas with impurities can be modeled, which are widely used in the present days experiments [137] and will be used in the ITER machine [51].

## 3.4 GRILLIX 3D turbulent code

### 3.4.1 General information

The GRILLIX code is a global 3D fluid code for the edge and SOL plasma tokamak simulations [89]. A single ion species and electron species are considered in the model. The drift-reduced Braginskii equations [138, 139], such as the continuity equations for electron species, the total parallel momentum equation, the electron and ion heat equations, the vorticity (electrical charge conservation) equation, Faraday's and Ohm's laws are solved in the GRILLIX code. In contrast to the transport codes (for example, the SOLPS-ITER code, which is disscused in section 3.3), anomalous transport coefficients and velocities are not used. The turbulent transport is simulated self-consistently with the help of the polarisation drift [69]. The neutrals are implemented as a simple fluid model [140].

In this section we briefly describe the GRILLIX plasma equations. Similarly to the SOLPS-ITER (section 3.3), the collisonless corrections are not described, because the thesis is focused on the improvement of the collional transport coefficients. The code solves the fluid equations using the flux-coordinate independent (FCI) approach [21]. The GRILLIX code was one of the first codes that successfully implemented the FCI method for turbulence simulation. In the FCI approach the parallel derivatives at every point in a poloidal plane k (figure 3.2) are computed via finite differences by tracing along $\mathbf{B}$ to the corresponding points in the k+1 and k-1 poloidal planes. The perpendicular derivatives are solved within each poloidal plane on the Cartesian grid (figure 3.2). It allows the message passing interface (MPI) parallelisation for the parallel operations, i.e.

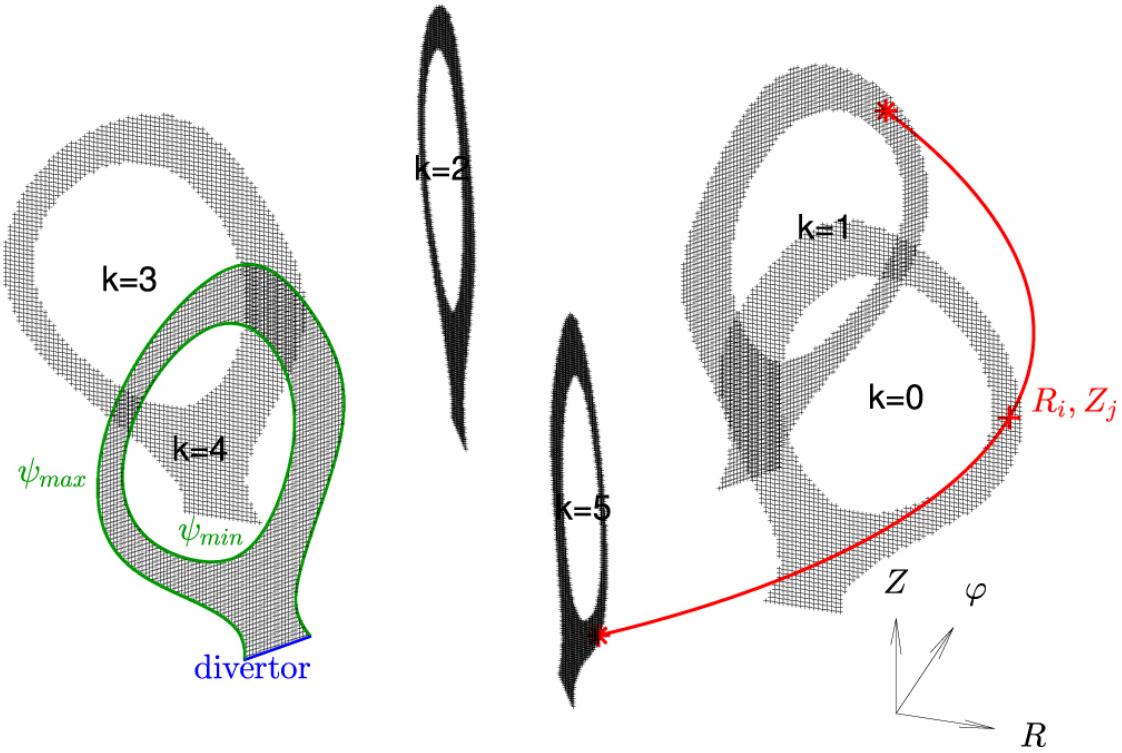


**Figure 3.2:** The GRILLIX computational mesh using FCI approach in tokamak geometry. Adapted from [21].

the perpendicular derivatives at each poloidal plane are solved on the separated MPI rank.

The equations are written using Centimetre–gram–second system of units (CGS). In the code the normalised unit less equations are implemented. We do not discuss normalisation in this thesis. In contrast to the rest part of the thesis, in the section 5.2 the CGS is used to be consistent with GRILLIX equations.

### 3.4.2 Electron continuity equation

The electron continuity equation is:

$$\frac{\partial}{\partial t} n + \nabla \cdot n \left( \mathbf{v}_E + \mathbf{v}_*^e + v_\parallel \mathbf{b} \right) = 0, \tag{3.86}$$

where the electron density $n$ and the electron parallel flow velocity $v_\parallel$ are defined in the GRILLIX code. Besides, the $E \times B$ drift $\mathbf{v}_E = c/B^2 \mathbf{B} \times \nabla\phi$ and the diamagnetic drift $\mathbf{v}_*^{e,i} = \mp c/(enB^2)\mathbf{B} \times \nabla p_{e,i}$ for the electrons $(e,-)$ and ions $(i,+)$, respectively. Here $\phi$ is the electrostatic potential. The electron and ion pressures are correspondingly $p_e = nT_e$ and $p_i = nT_i$. Aslo, $\mathbf{b} = \mathbf{B}/B$.

The (3.86) can be written as:

$$\frac{\partial}{\partial t}n + \mathbf{v}_E \cdot \nabla n + \nabla \cdot \left(n u_\parallel \mathbf{b}\right) = n\mathcal{C}(\phi) - \frac{n}{e}\mathcal{C}(T_e) - \frac{T_e}{e}\mathcal{C}(n) + \frac{1}{e}\nabla \cdot \left(j_\parallel \mathbf{b}\right). \tag{3.87}$$

where the ion parallel flow velocity $u_\parallel$ related to the $v_\parallel$ through the parallel current $j_\parallel/(en) = u_\parallel - v_\parallel$. The curvature operator is defined as:

$$\mathcal{C}(f) = -\nabla \cdot (\frac{c}{B^2}\mathbf{B} \times \nabla f) = -\left(\nabla \times \frac{c\mathbf{B}}{B^2}\right) \cdot \nabla f. \tag{3.88}$$

### 3.4.3 Vorticity equation (charge conservation equation)

The charge conservation equation $\nabla \cdot \mathbf{j} = 0$ is:

$$\nabla \cdot \left(en\mathbf{u}_{pol} - en\mathbf{v}_*^e + en\mathbf{v}_*^i + j_\parallel \mathbf{b}\right) = 0, \tag{3.89}$$

where the polarisation ion current $en\mathbf{u}_{pol}$ is a result of the 1-order inertia and viscosity drifts:

$$\mathbf{u}_{pol} = -\frac{cm_i n\left(\frac{\partial \mathbf{u}_\perp^0}{\partial t} + \left(\mathbf{v}_E + \mathbf{v}_*^i + \mathbf{u}_{pol} + u_\parallel \mathbf{b}\right) \cdot \nabla \mathbf{u}_\perp^0\right) \times \mathbf{B}}{enB^2} - \frac{c\nabla \cdot \overleftrightarrow{\pi}_i \times \mathbf{B}}{enB^2}. \tag{3.90}$$

Here $\overleftrightarrow{\pi}_i$ is a viscous-stress tensor according to Braginskii, and the $\mathbf{u}_\perp^0 = \mathbf{v}_E + \mathbf{v}_*^i$ are 0-order drifts. The vorticity equation (3.89) is written as:

$$\nabla \cdot \left[\frac{m_i c^2}{B^2} n \frac{d_i}{dt}(\nabla_\perp \phi + \frac{\nabla_\perp p_i}{en})\right] = -\mathcal{C}(p_e) - \mathcal{C}(p_i) + \nabla \cdot \left(j_\parallel \mathbf{b}\right) - \frac{1}{6}\mathcal{C}(G), \tag{3.91}$$

where the $\mathcal{C}(f)$ are defined according to (3.88) and:

$$\frac{d_i}{dt} = \frac{\partial}{\partial t} + \left(\mathbf{v}_E + u_\parallel \mathbf{b}\right) \cdot \nabla, \quad \nabla_\perp = -\mathbf{B} \times \frac{\mathbf{B} \times \nabla}{B^2}, \tag{3.92}$$

$$G = -\eta_i \left[\frac{2}{B^{3/2}} \nabla \cdot \left(u_\parallel B^{3/2} \mathbf{b}\right) - \frac{\mathcal{C}(\phi)}{2} - \frac{\mathcal{C}(p_i)}{2en}\right], \tag{3.93}$$

where the Braginskii parallel viscosity coefficient is:

$$\eta_i = 0.96 n T_i \tau_i, \qquad \tau_i = \frac{3\sqrt{M_i} T_i^{3/2}}{4\sqrt{\pi}\lambda e^4 n}, \tag{3.94}$$

where $m_i$ is an ion mass, and $\lambda$ is the Coulomb logarithm.

### 3.4.4 Parallel momentum equation

The total parallel momentum equation is:

$$m_i n \frac{d_i}{dt} u_\parallel = -\nabla_\parallel (p_e + p_i) + \frac{m_i p_i}{e} \mathcal{C}(u_\parallel) - \frac{2}{3} B^{3/2} \nabla_\parallel \frac{G}{B^{3/2}} \tag{3.95}$$

### 3.4.5 Ohm's law

The electron parallel momentum equation is:

$$-\frac{m_e}{e}\frac{d_e}{dt}\frac{j_\parallel}{en} - \frac{1}{c}\frac{\partial}{\partial t} A_\parallel = \eta_\parallel j_\parallel + \nabla_\parallel \phi - \frac{1}{en}\nabla_\parallel p_e - 0.71 \frac{1}{e}\nabla_\parallel T_e, \tag{3.96}$$

where $m_e$ is the electron mass, and the Braginskii parallel resistivity is defined as:

$$\eta_\parallel = \frac{0.51 m_e}{e^2 \tau_e n}, \quad \tau_e = \frac{3\sqrt{m_e} T_e^{3/2}}{4\sqrt{2\pi}\lambda e^4 n}, \tag{3.97}$$

For the electron inertia $-j_\parallel/(en) \approx v_\parallel$ is assumed, and :

$$\frac{d_e}{dt} = \frac{\partial}{\partial t} + \left(\mathbf{v}_E + v_\parallel \mathbf{b}\right) \cdot \nabla. \tag{3.98}$$

The induced vector potential $A_\parallel$ is found from the Faraday's law.

### 3.4.6 Faraday's law

Faraday's law is:

$$\nabla_\perp^2 A_\parallel = -\frac{4\pi}{c} j_\parallel \tag{3.99}$$

### 3.4.7 Electron temperature equation

The electron temperature equation is:

$$\begin{aligned}\frac{d_e}{dt} T_e = &-\frac{2}{3}\left[\frac{T_e}{en}\mathcal{C}(p_e) - T_e \mathcal{C}(\phi) + \frac{5}{2}\frac{T_e}{e}\mathcal{C}(T_e)\right] - \frac{2}{3} T_e \nabla \cdot \left(v_\parallel \mathbf{b}\right) + \frac{2}{3} 0.71 \frac{T_e}{en} \nabla \cdot \left(j_\parallel \mathbf{b}\right) \\ &+ \frac{2}{3}\frac{1}{n}\nabla \cdot \left(\chi_\parallel^e \nabla_\parallel T_e \mathbf{b}\right) - \frac{2 m_e}{m_i \tau_e}(T_e - T_i) + \frac{2}{3}\frac{\eta_\parallel j_\parallel^2}{n},\end{aligned} \tag{3.100}$$

where the parallel electron heat conductivity is defined as:

$$\chi_\parallel^e = 3.16 \frac{n T_e \tau_e}{m_e}. \tag{3.101}$$

### 3.4.8 Ion temperature equation

The ion temperature equation is:

$$\frac{d_i}{dt}T_i = -\frac{2}{3}\left[\frac{T_i}{en}\mathcal{C}(p_e) - T_i\mathcal{C}(\phi) - \frac{5}{2}\frac{T_i}{e}\mathcal{C}(T_i)\right] - \frac{2}{3}T_i\nabla\cdot\left(u_\parallel\mathbf{b}\right) + \frac{2}{3}\frac{T_i}{en}\nabla\cdot\left(j_\parallel\mathbf{b}\right) + \frac{2}{3}\frac{1}{n}\nabla\cdot\left(\chi^i_\parallel\nabla_\parallel T_i\mathbf{b}\right) + \frac{2m_e}{m_i\tau_e}(T_e - T_i) + \frac{2}{9n\eta_i}G^2, \tag{3.102}$$

where the parallel ion heat conductivity is defined as:

$$\chi^i_\parallel = 3.9\frac{nT_i\tau_i}{m_i}. \tag{3.103}$$

### 3.4.9 Focus of the thesis for the model improvement

In the GRILLIX code the drift-reduced form of the Braginskii equations [17] are solved for the single ion species and electron species. In the thesis, the multi-ion equations for GRILLIX code are derived. that unlike the SOLPS-ITER code (section 3.3), the equations have polarization drift (3.90). The multi-ion forms of polarisation drift and the corresponding current are discussed in detail. Also, there are the magnetic induction and the electron inertia, which are included in the Ohm's (3.96) and Faraday's laws (3.99) in the GRILLIX code, but are not included in the SOLPS-ITER code (section 3.3). Those are needed for the electromagnetic turbulence studies (the importance of the electromagnetic phenomenon in the GRILLIX code is discussed in [138] and the references therein). However, no significant changes with respect to the single ion case should be performed for the magnetic induction and the electron inertia. The Zhdanov closure (chapter 2) is used for the multi-ion fluid equations.

While the implementation of the multi-ion equations into the GRILLIX code were not performed within this thesis, the multi-species infrastructure for the GRILLIX code was prepared anticipating further development of the multi-ion GRILILLX model. Namely, additionally to the MPI parallelisation over poloidal plane ranks, the MPI parallelisation over different ions is done in the GRILLIX code, i.e. equations for each ion species in each poloidal plane is solved on a separate MPI rank. Besides, the continuous integration/continuous delivery (CI/CD) infrastructure, which is based on the MMS tests [21], is successfully tested for the simple density multi-ion equations.

# 4 New steps in the Zhdanov closure

This chapter is dedicated to the advancements made in the Zhdanov closure. We explore the relations between Zhdanov coefficients and Braginskii equations, which ensure the moment and energy conservation in collisions. Additionally, we focus on the derivation of heat stresses, which can be comparable to the strain stresses. Furthermore, we discuss an improved analytical method, which allows for more accurate and reliable calculations of kinetic coefficient. The content of this chapter was also published in [84].

## 4.1 Multi-species fluid equations

The Braginskii equations are widely employed in edge codes. Understanding the connection between Zhdanov coefficients and Braginskii equations is of paramount importance as it ensures moment and energy conservation.

First we note that Braginskii equations [17], which are used in the SOLPS-ITER code (section 3.3) and in the GRILLIX code (section 3.4) and in many other codes (section 3.1), are different from the Zhdanov equations (2.62)-(2.69). Thus, we proceed as following: 1) the equations for the first three moments of the distribution function are derived similar to Braginskii [17] without closure method; 2) the relations between variables, which are normally derived from Braginskii closure, and the Zhdanov variables, which can be obtained from the equations (2.66), (2.67), (2.68) and (2.69), are obtained; 3) the system of equations (2.66), (2.67), (2.68) and (2.69) is solved.

The kinetic equation (2.1) for species type $\alpha$ and charge state $Z$, which can be applied for both ions and electrons (for electrons $Z = -1$), for the Lorentz force as the external force $\mathbf{F}_{\alpha Z} = Ze(\mathbf{E} + [\mathbf{v} \times \mathbf{B}])$ becomes:

$$\frac{\partial f_{\alpha Z}}{\partial t} + \mathbf{v} \cdot \frac{\partial f_{\alpha Z}}{\partial \mathbf{r}} + \frac{Ze(\mathbf{E} + [\mathbf{v} \times \mathbf{B}])}{m_\alpha} \cdot \frac{\partial f_{\alpha Z}}{\partial \mathbf{v}} = C_{\alpha Z}^{elastic} + C_{\alpha Z}^{inelastic}, \tag{4.1}$$

where the collisional operator $C_{\alpha Z}$ is split into the part $C_{\alpha Z}^{elastic}$, which corresponds to the elastic collisions, and the part $C_{\alpha Z}^{inelastic}$, which corresponds to the inelastic collisions.

Following Braginkii [17], the system of equations is derived for the first three moments of the distribution function:

$$n_{\alpha Z} = \iiint f_{\alpha Z} d^3\mathbf{v}, \quad n_{\alpha Z} u_{\alpha Z k} = \iiint v_k f_{\alpha Z} d^3\mathbf{v}, \tag{4.2}$$

$$T_{\alpha Z}^{(Br)} \stackrel{\text{def}}{=} \frac{2}{3} \frac{m_\alpha}{n_{\alpha Z}} \iiint \frac{(\mathbf{v} - \mathbf{u}_{\alpha Z})^2}{2} f_{\alpha Z} d^3\mathbf{v}. \tag{4.3}$$

One can note that the density and the flow velocity definitions (4.2) correspond to (2.18) and (2.60). The resulting system of fluid equations is:

$$\partial_t n_{\alpha Z} + \nabla \cdot (\mathbf{u}_{\alpha Z} n_{\alpha Z}) = S^n_{\alpha Z} \tag{4.4}$$

$$m_\alpha \partial_t (\mathbf{u}_{\alpha Z} n_{\alpha Z}) + \nabla \cdot \overleftrightarrow{\Gamma}^m_{\alpha Z} = -\nabla (n_{\alpha Z} T^{(Br)}_{\alpha Z}) + Z e n_{\alpha Z} (\mathbf{E} + [\mathbf{u}_{\alpha Z} \times \mathbf{B}]) - \nabla \cdot \overleftrightarrow{\pi}^{(Br)}_{\alpha Z} + \mathbf{R}^{(Br)}_{\alpha Z} + \mathbf{S}^m_{\alpha Z} \tag{4.5}$$

$$\frac{3}{2} \partial_t (n_{\alpha Z} T^{(Br)}_{\alpha Z}) + \nabla \cdot (\mathbf{q}^{(Br)}_{\alpha Z} + \frac{3}{2} \mathbf{u}_{\alpha Z} n_{\alpha Z} T^{(Br)}_{\alpha Z}) + n_{\alpha Z} T^{(Br)}_{\alpha Z} \nabla \cdot \mathbf{u}_{\alpha Z} = -((\overleftrightarrow{\pi}^{(Br)}_{\alpha Z} \nabla) \mathbf{u}_{\alpha Z}) + Q^{(Br)}_{\alpha Z} + S^E_{\alpha Z} \tag{4.6}$$

In this equation system heat fluxes and stress-viscosities are defined according to Braginskii:

$$q^{(Br)}_{\alpha Z k} \stackrel{\text{def}}{=} m_\alpha \iiint \frac{(\mathbf{v} - \mathbf{u}_{\alpha Z})^2}{2} (v_k - u_{\alpha Z k}) f_{\alpha Z} d^3\mathbf{v} \tag{4.7}$$

$$\pi^{(Br)}_{\alpha Z k l} \stackrel{\text{def}}{=} m_\alpha \iiint \left[ (v_k - u_{\alpha Z k})(v_l - u_{\alpha Z l}) - \frac{\delta_{kl}}{3} (\mathbf{v} - \mathbf{u}_{\alpha Z})^2 \right] f_{\alpha Z} d^3\mathbf{v} \tag{4.8}$$

and integrals of the collisional term $C^{elastic}_{\alpha Z}$, due to Coulomb collisions, provide:

$$R^{(Br)}_{\alpha Z k} \stackrel{\text{def}}{=} m_\alpha \iiint (v_k - u_{\alpha Z k}) C^{elastic}_{\alpha Z} d^3\mathbf{v} = m_\alpha \iiint v_k C^{elastic}_{\alpha Z} d^3\mathbf{v}, \tag{4.9}$$

$$R^{(Br)}_{\alpha Z \beta \zeta k} \stackrel{\text{def}}{=} m_\alpha \iiint (v_k - u_{\alpha Z k}) C^{elastic}_{\alpha Z \beta \zeta} d^3\mathbf{v} = m_\alpha \iiint v_k C^{elastic}_{\alpha Z \beta \zeta} d^3\mathbf{v}, \tag{4.10}$$

$$Q^{(Br)}_{\alpha Z} \stackrel{\text{def}}{=} m_\alpha \iiint \frac{(\mathbf{v} - \mathbf{u}_{\alpha Z})^2}{2} C^{elastic}_{\alpha Z} d^3\mathbf{v}, \quad Q^{(Br)}_{\alpha Z \beta \zeta} \stackrel{\text{def}}{=} m_\alpha \iiint \frac{(\mathbf{v} - \mathbf{u}_{\alpha Z})^2}{2} C^{elastic}_{\alpha Z \beta \zeta} d^3\mathbf{v}, \tag{4.11}$$

$$C^{elastic}_{\alpha Z} = \sum_{\beta \zeta} C^{elastic}_{\alpha Z \beta \zeta}, \quad R^{(Br)}_{\alpha Z k} = \sum_{\beta \zeta} R^{(Br)}_{\alpha Z \beta \zeta k}, \quad Q^{(Br)}_{\alpha Z} = \sum_{\beta \zeta} Q^{(Br)}_{\alpha Z \beta \zeta}, \tag{4.12}$$

where, $k$ and $l$ are component indices. Terms $S^n_{\alpha Z}$, $\mathbf{S}^m_{\alpha Z}$, $S^E_{\alpha Z}$ describe, respectively, particle, momentum, and energy sources due to inelastic collisions $C^{inelastic}_{\alpha Z}$ between

charged species (ionization, recombination, excitation) and all interactions with neutrals, and they are considered as external parameters in this model. For instance, in SOLPS-ITER these sources are calculated by the EIRENE code [136], when the B2.5-EIRENE coupled mode is activated. In the fluid neutral mode in SOLPS-ITER and GRILLIX the Maxwell distribution function based sources are used. The momentum flux due to the flow velocity is:

$$\Gamma^{m}_{\alpha Zkl} = m_\alpha u_{\alpha Zk} u_{\alpha Zl} n_{\alpha Z} \tag{4.13}$$

As the second step of our approach the $\mathbf{q}^{(Br)}_{\alpha Z}$, $\overleftrightarrow{\pi}^{(Br)}_{\alpha Z}$, $\mathbf{R}_{\alpha Zi}$, and $Q^{(Br)}_{\alpha Z}$ should be related to the ones which can be obtained from the Zhdanov closure (section 2.4). Note, the Zhdanov temperature, heat flux and stress-viscous tensor (2.60) are defined with respect to $\mathbf{u}$:

$$T_{\alpha Z} = \frac{2}{3}\frac{m_\alpha}{n_{\alpha Z}} \iiint \frac{(\mathbf{v}-\mathbf{u})^2}{2} f_{\alpha Z} d^3\mathbf{v}, \tag{4.14}$$

$$h_{\alpha Zk} = m_\alpha \iiint \frac{(\mathbf{v}-\mathbf{u})^2}{2}(v_k - u_k) f_{\alpha Z} d^3\mathbf{v} - \frac{5}{2} w_{\alpha Zk} n_{\alpha Z} T_{\alpha Z}, \tag{4.15}$$

$$\pi_{\alpha Zkl} = m_\alpha \iiint \left[(v_k - u_k)(v_l - u_l) - \frac{\delta_{kl}}{3}(\mathbf{v}-\mathbf{u})^2\right] f_{\alpha Z} d^3\mathbf{v}, \tag{4.16}$$

whereas the Braginskii temperature, heat flux and stress-viscous tensor are defined with respect to $\mathbf{u}_{\alpha Z}$ (4.3), (4.7) and (4.8). Thus, the result of the closure, which is performed via solution of the equations, that is expressed in the heat flux, viscosity, friction term (r.h.s. of the mometntum equation (2.73)), and heat exchange term, can be applied for the Braginskii system of equations (4.4)-(4.6) using corrections due to difference in definitions:

$$T_{\alpha Z} = T^{(Br)}_{\alpha Z} + \frac{1}{3} m_\alpha \mathbf{w}^2_{\alpha Z}, \tag{4.17}$$

$$q^{(Br)}_{\alpha Zk} = h_{\alpha Zk} + n_{\alpha Z} w_{\alpha Zk} m_\alpha \mathbf{w}^2_{\alpha Z} - w_{\alpha Zs}\pi_{\alpha Zsk}, \tag{4.18}$$

$$\pi^{(Br)}_{\alpha Zkl} = \pi_{\alpha Zkl} - m_\alpha n_{\alpha Z} w_{\alpha Zk} w_{\alpha Zl} + m_\alpha n_{\alpha Z} \frac{\delta_{kl}}{3} \mathbf{w}^2_{\alpha Z}. \tag{4.19}$$

The introduced corrections (4.17)-(4.19) are usually the same order as second order collisional terms, which are neglected in the Zhdanov method. Thus, for most applications they can be omitted. A similar correction should be applied to the heat exchange term:

$$Q^{(Br)}_{\alpha Z\beta\zeta} = Q_{\alpha Z\beta\zeta} - \mathbf{w}_{\alpha Z}\cdot\mathbf{R}_{\alpha Z\beta\zeta}, \qquad \boxed{Q^{(Br)}_{\alpha Z} = Q_{\alpha Z} - \mathbf{w}_{\alpha Z}\cdot\mathbf{R}_{\alpha Z},} \tag{4.20}$$

where after the Zhdanov closure application (2.72):

$$Q_{\alpha Z} = \sum_{\beta\zeta} Q_{\alpha Z\beta\zeta}, \quad Q_{\alpha Z\beta\zeta} = -3\left(\frac{\mu_{\alpha\beta}}{m_\alpha + m_\beta}\right)\frac{n_{\alpha Z}}{\tau^{(Zh)}_{\alpha Z\beta\zeta}}(T_{\alpha Z} - T_{\beta\zeta}). \tag{4.21}$$

One can recognize a heat source due to friction between different species in the second term of (4.20). This term for electrons represents a Joule heating.

The friction term $\mathbf{R}^{(Br)}_{\alpha Z}$ defined according to (4.9) does not need correction provided that Coulomb collisions do not lead to particle sources and sinks and three possible definitions are equivalent:

$$\mathbf{R}^{(Br)}_{\alpha Z} = m_\alpha \iiint (\mathbf{v} - \mathbf{u}_{\alpha Z}) C^{elastic}_{\alpha Z} d^3\mathbf{v} = m_\alpha \iiint \mathbf{v} C^{elastic}_{\alpha Z} d^3\mathbf{v} =$$
$$m_\alpha \iiint (\mathbf{v} - \mathbf{u}) C^{elastic}_{\alpha Z} d^3\mathbf{v} = \mathbf{R}_{\alpha Z}, \qquad \boxed{\mathbf{R}^{(Br)}_{\alpha Z} = \mathbf{R}_{\alpha Z}.} \tag{4.22}$$

Therefore the friction term $\mathbf{R}_{\alpha Z}$, which is found using the Zhdanov method (2.73), may be directly substituted into the system (4.4) - (4.6).

It is worth notice that important properties of the $\mathbf{R}_{\alpha Z}$ and $Q^{(Br)}_{\alpha Z}$ are preserved after Zhdanov closure application. We start with $\mathbf{R}_{\alpha Z\beta\zeta}$ (2.73):

$$\mathbf{R}_{\alpha Z\beta\zeta} = -\frac{\mu_{\alpha\beta} n_{\alpha Z}}{\tau^{(Zh)}_{\alpha Z\beta\zeta}}(\mathbf{w}_{\alpha Z} - \mathbf{w}_{\beta\zeta})$$
$$+ \frac{3}{5}\frac{\mu_{\alpha\beta}}{T_{av}}\frac{\mu_{\alpha\beta} n_{\alpha Z}}{\tau^{(Zh)}_{\alpha Z\beta\zeta}}\left(\frac{\mathbf{h}_{\alpha Z}}{\rho_{\alpha Z}} - \frac{\mathbf{h}_{\beta\zeta}}{\rho_{\beta\zeta}}\right) - \frac{3}{14}\left(\frac{\mu_{\alpha\beta}}{T_{av}}\right)^2 \frac{\mu_{\alpha\beta} n_{\alpha Z}}{\tau^{(Zh)}_{\alpha Z\beta\zeta}}\left(\frac{\mathbf{r}_{\alpha Z}}{\rho_{\alpha Z}} - \frac{\mathbf{r}_{\beta\zeta}}{\rho_{\beta\zeta}}\right) \tag{4.23}$$

From (2.78) one can obtain following symmetry $n_{\alpha Z}/\tau^{(Zh)}_{\alpha Z\beta\zeta} = n_{\beta\zeta}/\tau^{(Zh)}_{\beta\zeta\alpha Z}$. Thus, for any $\mathbf{w}_{\alpha Z}$, $\mathbf{h}_{\alpha Z}$, $\mathbf{r}_{\alpha Z}$, $\mathbf{w}_{\beta\zeta}$, $\mathbf{h}_{\beta\zeta}$ and $\mathbf{r}_{\beta\zeta}$, the Newton's third law in pairs for any two fluids $\alpha Z$ and $\beta\zeta$ is satisfied:

$$\mathbf{R}_{\alpha Z\beta\zeta} = -\mathbf{R}_{\beta\zeta\alpha Z}. \tag{4.24}$$

Also, for any $T_{\alpha Z}$ and $T_{\beta\zeta}$, taking into account (4.21) and $n_{\alpha Z}/\tau^{(Zh)}_{\alpha Z\beta\zeta} = n_{\beta\zeta}/\tau^{(Zh)}_{\beta\zeta\alpha Z}$ (2.78), one can find:

$$Q_{\alpha Z\beta\zeta} = -Q_{\beta\zeta\alpha Z}. \tag{4.25}$$

Consequently, the total momentum conservation in collisions is also satisfied:

$$\sum_{\alpha Z}\mathbf{R}_{\alpha Z} = \sum_{\alpha Z}\sum_{\beta\zeta}\mathbf{R}_{\alpha Z\beta\zeta} = \frac{1}{2}\sum_{\alpha Z}\sum_{\beta\zeta}\mathbf{R}_{\alpha Z\beta\zeta} + \frac{1}{2}\sum_{\alpha Z}\sum_{\beta\zeta}\mathbf{R}_{\alpha Z\beta\zeta} =$$
$$\frac{1}{2}\sum_{\alpha Z}\sum_{\beta\zeta}\mathbf{R}_{\alpha Z\beta\zeta} + \frac{1}{2}\sum_{\beta\zeta}\sum_{\alpha Z}\mathbf{R}_{\alpha Z\beta\zeta} = \frac{1}{2}\sum_{\alpha Z}\sum_{\beta\zeta}\left(\mathbf{R}_{\alpha Z\beta\zeta} + \mathbf{R}_{\beta\zeta\alpha Z}\right) = 0. \tag{4.26}$$

A similar derivation can be performed for the heat exchange. Using (4.20), (4.21), (4.24) and (4.25) one can obtain:

$$Q^{(Br)}_{\alpha Z\beta\zeta} + Q^{(Br)}_{\beta\zeta\alpha Z} = Q_{\alpha Z\beta\zeta} - \mathbf{w}_{\alpha Z}\cdot\mathbf{R}_{\alpha Z\beta\zeta} + Q_{\beta\zeta\alpha Z} - \mathbf{w}_{\beta\zeta}\cdot\mathbf{R}_{\beta\zeta\alpha Z} =$$
$$-\mathbf{u}_{\alpha Z}\cdot\mathbf{R}_{\alpha Z\beta\zeta} - \mathbf{u}_{\beta\zeta}\cdot\mathbf{R}_{\beta\zeta\alpha Z} - \mathbf{u}\cdot\left(\mathbf{R}_{\alpha Z\beta\zeta} + \mathbf{R}_{\beta\zeta\alpha Z}\right) = -\left(\mathbf{u}_{\alpha Z} - \mathbf{u}_{\beta\zeta}\right)\cdot\mathbf{R}_{\alpha Z\beta\zeta} \tag{4.27}$$

So the energy conservation in collisions is:

$$\sum_{\alpha Z}Q^{(Br)}_{\alpha Z} = \sum_{\alpha Z}\sum_{\beta\zeta}Q^{(Br)}_{\alpha Z\beta\zeta} = \frac{1}{2}\sum_{\alpha Z}\sum_{\beta\zeta}\left(Q^{(Br)}_{\alpha Z\beta\zeta} + Q^{(Br)}_{\beta\zeta\alpha Z}\right) =$$
$$-\frac{1}{2}\left(\sum_{\alpha Z}\sum_{\beta\zeta}\mathbf{u}_{\alpha Z}\cdot\mathbf{R}_{\alpha Z\beta\zeta} + \sum_{\alpha Z}\sum_{\beta\zeta}\mathbf{u}_{\beta\zeta}\cdot\mathbf{R}_{\beta\zeta\alpha Z}\right) =$$
$$-\frac{1}{2}\left(\sum_{\alpha Z}\sum_{\beta\zeta}\mathbf{u}_{\alpha Z}\cdot\mathbf{R}_{\alpha Z\beta\zeta} + \sum_{\beta\zeta}\sum_{\alpha Z}\mathbf{u}_{\beta\zeta}\cdot\mathbf{R}_{\beta\zeta\alpha Z}\right) =$$
$$-\sum_{\alpha Z}\sum_{\beta\zeta}\mathbf{u}_{\alpha Z}\cdot\mathbf{R}_{\alpha Z\beta\zeta} = -\sum_{\alpha Z}\mathbf{u}_{\alpha Z}\cdot\mathbf{R}_{\alpha Z}. \tag{4.28}$$

Details about the conservative property of collisions can be found, for instance, in [17].

## 4.2 Heat stresses

As demonstrated in subsection 2.4.3, the heat stresses are found to be significant and comparable to the strain stresses. Thus, the heat stresses cannot be neglected.

Originally, in the 8th chapter of Zhdanov's monograph [18], the heat stresses are assumed small and not considered. Nevertheless, in the 4th chapter, the potential inclusion

of these heat stresses is discussed. To take into account heat stresses using Zhdanov approach one has to modify (2.68) and (2.69). As we discussed in subsection 2.4.3, the terms, which are responsible for the heat stresses, were neglected for (2.68) and (2.69). To include the heat stresses one have to take a one step back and consider the general moment equation (A1.8) from [18] for $m = 2$:

$$\frac{dn_{\alpha Z}b^{2,n}_{\alpha Zrs}}{dt} + \frac{2}{5}\frac{\partial}{\partial x_t}\left[\frac{5+2n}{2\gamma_{\alpha Z}}\left\{n_{\alpha Z}b^{1,n}_{\alpha Z}\boldsymbol{\delta}\right\}_t + \left\{n_{\alpha Z}b^{1,n+1}_{\alpha Z}\boldsymbol{\delta}\right\}_t\right] + 2p_{\alpha Z}\left\{\frac{\partial u_r}{\partial x_s}\right\}\delta_{n0} - \omega_{\alpha Z}\{n_{\alpha Z}b^{2,n}_{\alpha Zlr}e_{slm}b_m\} = R^{2,n}_{\alpha Zrs}, \quad (4.29)$$

where:

$$\left\{n_{\alpha Z}b^{1,n}_{\alpha Z}\boldsymbol{\delta}\right\}_t = n_{\alpha Z}b^{1,n}_{\alpha Zr}\delta_{ts} + n_{\alpha Z}b^{1,n}_{\alpha Zs}\delta_{tr} - \frac{2}{3}n_{\alpha Z}b^{1,n}_{\alpha Zt}\delta_{rs}. \quad (4.30)$$

Thus:

$$\frac{\partial}{\partial x_t}\left\{n_{\alpha Z}b^{1,n}_{\alpha Z}\boldsymbol{\delta}\right\}_t = 2\left(\frac{1}{2}\frac{\partial(n_{\alpha Z}b^{1,n}_{\alpha Zr})}{\partial x_s} + \frac{1}{2}\frac{\partial(n_{\alpha Z}b^{1,n}_{\alpha Zs})}{\partial x_r} - \frac{1}{3}\frac{\partial(n_{\alpha Z}b^{1,n}_{\alpha Zt})}{\partial x_t}\delta_{rs}\right) = 2\left\{\frac{\partial(n_{\alpha Z}b^{1,n}_{\alpha Zr})}{\partial x_s}\right\} \quad (4.31)$$

Neglecting $\frac{dn_{\alpha Z}b^{2,n}_{\alpha Zrs}}{dt}$ and $\left\{n_{\alpha Z}b^{1,n}_{\alpha Z}\boldsymbol{\delta}\right\}_t\frac{\partial}{\partial x_t}\frac{1}{\gamma_{\alpha Z}}$ (using estimations $w_{\alpha Z\|} \sim \lambda/L_\|\sqrt{m_\alpha/T_{av}}\Delta T_{av}/m_\alpha$ and $h_{\alpha Z\|} \sim n_{\alpha Z}\lambda/L_\|\sqrt{T_{av}/m_\alpha}\Delta T_{av}$) for $n = 0$ and $n = 1$ one correspondingly can get:

$$\frac{2}{\gamma_{\alpha Z}}\left\{\frac{\partial(n_{\alpha Z}b^{1,0}_{\alpha Zr})}{\partial x_s}\right\} + \frac{4}{5}\left\{\frac{\partial(n_{\alpha Z}b^{1,1}_{\alpha Zr})}{\partial x_s}\right\} + 2p_{\alpha Z}\left\{\frac{\partial u_r}{\partial x_s}\right\} - \omega_{\alpha Z}\{n_{\alpha Z}b^{2,0}_{\alpha Zlr}e_{slm}b_m\} = R^{2,0}_{\alpha Zrs}, \quad (4.32)$$

$$\frac{7}{2\gamma_{\alpha Z}}\frac{4}{5}\left\{\frac{\partial(n_{\alpha Z}b^{1,1}_{\alpha Zr})}{\partial x_s}\right\} + \frac{4}{5}\left\{\frac{\partial(n_{\alpha Z}b^{1,2}_{\alpha Zr})}{\partial x_s}\right\} - \omega_{\alpha Z}\{n_{\alpha Z}b^{2,1}_{\alpha Zlr}e_{slm}b_m\} = R^{2,1}_{\alpha Zrs}. \quad (4.33)$$

Taking into account (2.58), one can write:

$$\frac{2}{\gamma_{\alpha Z}}\left\{\frac{\partial(\rho_{\alpha Z}w_{\alpha Zr})}{\partial x_s}\right\} + \frac{4}{5}\left\{\frac{\partial h_{\alpha Zr}}{\partial x_s}\right\} + 2p_{\alpha Z}\left\{\frac{\partial u_r}{\partial x_s}\right\} - \omega_{\alpha Z}\{\pi_{\alpha Zlr}e_{slm}b_m\} = R^{2,0}_{\alpha Zrs}, \quad (4.34)$$

$$\frac{7}{2\gamma_{\alpha Z}}\frac{4}{5}\left\{\frac{\partial h_{\alpha Zr}}{\partial x_s}\right\}+\frac{4}{5}\left\{\frac{\partial r_{\alpha Zr}}{\partial x_s}\right\}-\omega_{\alpha Z}\{\sigma_{\alpha Zlr}e_{slm}b_m\}=R^{2,1}_{\alpha Zrs}, \tag{4.35}$$

The additional vector moment contribution is usually $\sim 4$ times smaller than the heat flux contribution. Thus, the $\frac{4}{5}\left\{\frac{\partial r_{\alpha Zr}}{\partial x_s}\right\}$ term can be neglected in the additional tensorial moment equation (4.35). Note that (4.34) and (4.35) turns into the standard Zhdanov (2.68) and (2.69), if $\left\{\frac{\partial(\rho_{\alpha Z}w_{\alpha Zr})}{\partial x_s}\right\}$ and $\left\{\frac{\partial h_{\alpha Zr}}{\partial x_s}\right\}$ terms are neglected. This terms are kept in this thesis. Using estimation $w_{\alpha Z\parallel}\sim\lambda/L_\parallel\sqrt{m_\alpha/T_{av}}\Delta T_{av}/m_\alpha$ we only neglect $w_{\alpha Zr}\frac{\partial(\rho_{\alpha Z})}{\partial x_s}$ and (4.34) becomes:

$$2p_{\alpha Z}\left\{\frac{\partial w_{\alpha Zr}}{\partial x_s}\right\}+\frac{4}{5}\left\{\frac{\partial h_{\alpha Zr}}{\partial x_s}\right\}+2p_{\alpha Z}\left\{\frac{\partial u_r}{\partial x_s}\right\}-\omega_{\alpha Z}\{\pi_{\alpha Zlr}e_{slm}b_m\}=R^{2,0}_{\alpha Zrs}, \tag{4.36}$$

Finally, the rank-2 tensorial equations are:

$$W^{h_{\alpha Z}}_{rs}+p_{\alpha Z}W^{u_{\alpha Z}}_{rs}-\omega_{\alpha Z}\{\pi_{\alpha Zlr}e_{slm}b_m\}=R^{2,0}_{\alpha Zrs}, \tag{4.37}$$

$$\frac{7}{2\gamma_{\alpha Z}}W^{h_{\alpha Z}}_{rs}-\omega_{\alpha Z}\{\sigma_{\alpha Zlr}e_{slm}b_m\}=R^{2,1}_{\alpha Zrs}, \tag{4.38}$$

where:

$$W^{u_{\alpha Z}}_{rs}=2\left[\frac{1}{2}\Big(\frac{\partial u_{\alpha Zr}}{\partial x_s}+\frac{\partial u_{\alpha Zs}}{\partial x_r}\Big)-\frac{1}{3}\delta_{rs}\nabla\cdot\mathbf{u}_{\alpha Z}\right], \tag{4.39}$$

$$W^{h_{\alpha Z}}_{rs}=\frac{4}{5}\left[\frac{1}{2}\Big(\frac{\partial h_{\alpha Zr}}{\partial x_s}+\frac{\partial h_{\alpha Zs}}{\partial x_r}\Big)-\frac{1}{3}\delta_{rs}\nabla\cdot\mathbf{h}_{\alpha Z}\right]. \tag{4.40}$$

It should be mentioned that $u_{\alpha Zr}\approx u_r$ ($w_{\alpha Zr}<u_r$) is assumed in (4.37) in the corresponding Eq (26) in [84]. We keep $u_{\alpha Zr}$ further in the transport coefficients.

The terms $W^{h_{\alpha Z}}_{rs}$ represents the Zhdanov heat stresses. The heat term appears in both (4.37) and (4.38), whereas the strain term appers only in (4.37). This leads to the different transport coefficients for the heat flux and the flow velocity dependent viscous-stress tensors. It is important to note that similar heat stresses can be obtained from the general moment equation for rank-2 tensorial moments (C8) from [99].

## 4.3 Parallel transport coefficients

The classical transport across $\mathbf{B}$ can be studied according to paragraph 8.3 in [18]. We focus on the transport along $\mathbf{B}$ (parallel transport) in this section. The parallel transport coefficients are found, as a solution of system (2.66), (2.67), (4.37) and (4.38).

### 4.3.1 Heat flux

#### 4.3.1.1 System of rank-1 equations

The rank-1 equations (2.66) and (2.67) can be solved independently of the rank-2 (4.37) and (4.38), because the rank-2 moments do not contribute into the r.h.s. of the equations for the rank-1 moments, due to the orthogonality of the tensorial Hermite polynomials (subsection 2.4.2).

In the plasmas without magnetic field $\mathbf{B} = 0$, the terms $-\rho_{\alpha Z}\omega_{\alpha Z}\mathbf{h}_{\alpha Z} \times \mathbf{b}$ and $-\rho_{\alpha Z}\omega_{\alpha Z}\mathbf{r}_{\alpha Z} \times \mathbf{b}$ are equal to zero. Also, the components along $\mathbf{B}$ (parallel components) of these terms are equal to zero. Thus, the equations (2.66) and (2.67) without the $-\rho_{\alpha Z}\omega_{\alpha Z}\mathbf{h}_{\alpha Z} \times \mathbf{b}$ and $-\rho_{\alpha Z}\omega_{\alpha Z}\mathbf{r}_{\alpha Z} \times \mathbf{b}$ terms are solved for the plasmas without magnetic field $\mathbf{B} = 0$. The results are evidently applicable also for parallel components in case $\mathbf{B} \neq 0$.

$$\frac{5}{2}\frac{p_{\alpha Z}}{m_\alpha}\nabla T_{\alpha Z} = \frac{T_{av}}{m_\alpha}\sum_{\beta\zeta}\Big[\frac{5}{2}\frac{\mu_{\alpha\beta}}{m_\alpha}G^{(2)}_{\alpha Z\beta\zeta}(\mathbf{w}_{\alpha Z} - \mathbf{w}_{\beta\zeta}) + G^{(5)}_{\alpha Z\beta\zeta}\frac{\mathbf{h}_{\alpha Z}}{p_{\alpha Z}} + G^{(6)}_{\alpha Z\beta\zeta}\frac{\mathbf{h}_{\beta\zeta}}{p_{\beta\zeta}} + \frac{\mu_{\alpha\beta}}{T_{av}}\left(G^{(9)}_{\alpha Z\beta\zeta}\frac{\mathbf{r}_{\alpha Z}}{p_{\alpha Z}} + G^{(10)}_{\alpha Z\beta\zeta}\frac{\mathbf{r}_{\beta\zeta}}{p_{\beta\zeta}}\right)\Big] \quad (4.41)$$

$$0 = \left(\frac{T_{av}}{m_\alpha}\right)^2\sum_{\beta\zeta}\Big[\frac{35}{2}\left(\frac{\mu_{\alpha\beta}}{m_\alpha}\right)^2 G^{(8)}_{\alpha Z\beta\zeta}(\mathbf{w}_{\alpha Z} - \mathbf{w}_{\beta\zeta}) + 7\frac{\mu_{\alpha\beta}}{m_\alpha}\left(G^{(9)}_{\alpha Z\beta\zeta}\frac{\mathbf{h}_{\alpha Z}}{p_{\alpha Z}} + G^{(10)}_{\alpha Z\beta\zeta}\frac{\mathbf{h}_{\beta\zeta}}{p_{\beta\zeta}}\right) + \frac{m_\alpha}{T_{av}}G^{(11)}_{\alpha Z\beta\zeta}\frac{\mathbf{r}_{\alpha Z}}{p_{\alpha Z}} + \frac{m_\beta}{T_{av}}G^{(12)}_{\alpha Z\beta\zeta}\frac{\mathbf{r}_{\beta\zeta}}{p_{\beta\zeta}}\Big] \quad (4.42)$$

#### 4.3.1.2 Averaged over charge states heat flux

An important step in the derivation is a summing over the charge stats of each species type, which is proposed by Zhdanov [18]. The corresponding moments for the each charge states in this case can be found analytically using the relation with the moments, which are averaged over charge states. This approach is the main reason of the lengthy $\alpha Z$ notation, which is chosen in the thesis. Despite, this provides the following significant simplifications. First, the matrix for the EMIM is significantly reduced, i.e. the amount of the equations is now proportional to the $\alpha^{max}$ instead of total number of different fluid species in the mixture (different charge states, are treated as a separate fluid) ($n_s$). Second, this allows to separate equations by neglecting small terms of the order of the

mass ratio between the light and the heavy species, which is exploited in subsection 4.4.1. Otherwise, this could not be done, because different charge states of the same species type has the same mass. Consequently, their equations could not be separated in the IAM. After summing over $Z$, contracting the summation over $\zeta$ and moving h-/r-dependent collisional terms to the l.h.s. and the rest to the r.h.s., one can have:

$$\sum_{\beta}\left[\overline{G}^{(5)}_{\alpha\beta}\frac{\overline{\mathbf{h}}_{\alpha}}{p_{\alpha}}+\overline{G}^{(6)}_{\alpha\beta}\frac{\overline{\mathbf{h}}_{\beta}}{p_{\beta}}+\frac{m_{\alpha}}{T_{av}}\left(\frac{\mu_{\alpha\beta}}{m_{\alpha}}\overline{G}^{(9)}_{\alpha\beta}\frac{\overline{\mathbf{r}}_{\alpha}}{p_{\alpha}}+\frac{\mu_{\alpha\beta}}{m_{\alpha}}\overline{G}^{(10)}_{\alpha\beta}\frac{\overline{\mathbf{r}}_{\beta}}{p_{\beta}}\right)\right]= \\ \frac{5}{2}n_{\alpha}\widetilde{\nabla T_{\alpha}}-\sum_{\beta}\frac{5}{2}\frac{\mu_{\alpha\beta}}{m_{\alpha}}\overline{G}^{(2)}_{\alpha\beta}(\overline{\mathbf{w}}_{\alpha}-\overline{\mathbf{w}}_{\beta}) \quad (4.43)$$

$$\sum_{\beta}\left[7\left(\frac{\mu_{\alpha\beta}}{m_{\alpha}}\overline{G}^{(9)}_{\alpha\beta}\frac{\overline{\mathbf{h}}_{\alpha}}{p_{\alpha}}+\frac{\mu_{\alpha\beta}}{m_{\alpha}}\overline{G}^{(10)}_{\alpha\beta}\frac{\overline{\mathbf{h}}_{\beta}}{p_{\beta}}\right)+\frac{m_{\alpha}}{T_{av}}\overline{G}^{(11)}_{\alpha\beta}\frac{\overline{\mathbf{r}}_{\alpha}}{p_{\alpha}}+\frac{m_{\beta}}{T_{av}}\overline{G}^{(12)}_{\alpha\beta}\frac{\overline{\mathbf{r}}_{\beta}}{p_{\beta}}\right]= \\ -\sum_{\beta}\frac{35}{2}\left(\frac{\mu_{\alpha\beta}}{m_{\alpha}}\right)^{2}\overline{G}^{(8)}_{\alpha\beta}(\overline{\mathbf{w}}_{\alpha}-\overline{\mathbf{w}}_{\beta}) \quad (4.44)$$

where

$$G^{(n)}_{\alpha Z\beta\zeta}=I_{\alpha Z}I_{\beta\zeta}\overline{G}^{(n)}_{\alpha\beta},\quad I_{\alpha Z}=\frac{Z^{2}n_{\alpha Z}}{\overline{Z^{2}_{\alpha}}n_{\alpha}},\quad \overline{G}^{(n)}_{\alpha\beta}\overset{\text{def}}{=}\sum_{Z}\sum_{\zeta}G^{(n)}_{\alpha Z\beta\zeta}, \quad (4.45)$$

$$\overline{\mathbf{w}}_{\alpha}=\sum_{Z}I_{\alpha Z}\mathbf{w}_{\alpha Z},\quad \overline{\mathbf{h}}_{\alpha}\overset{\text{def}}{=}\sum_{Z}\frac{p_{\alpha}I_{\alpha Z}\mathbf{h}_{\alpha Z}}{p_{\alpha Z}},\quad \overline{\mathbf{r}}_{\alpha}\overset{\text{def}}{=}\sum_{Z}\frac{p_{\alpha}I_{\alpha Z}\mathbf{r}_{\alpha Z}}{p_{\alpha Z}}, \quad (4.46)$$

$$n_{\alpha}\widetilde{\nabla T_{\alpha}}\overset{\text{def}}{=}\sum_{Z}n_{\alpha Z}\nabla T_{\alpha Z},\quad \overline{Z^{2}_{\alpha}}n_{\alpha}=\sum_{Z}Z^{2}n_{\alpha Z},\quad n_{\alpha}=\sum_{Z}n_{\alpha Z},\quad p_{\alpha}\overset{\text{def}}{=}\sum_{Z}p_{\alpha Z} \quad (4.47)$$

The (4.43) and (4.44) is a system of linear algebraic equations $2\alpha^{max}\times 2\alpha^{max}$, which can be written in the form:

$$\sum_{\beta=1..2\alpha^{max}}\check{a}_{\alpha\beta}X_{\beta}=\check{b}_{\alpha} \quad (4.48)$$

where:

$$X_{\beta}\overset{\text{def}}{=}\begin{cases}\frac{\overline{\mathbf{h}}_{\beta}}{p_{\beta}}, & \beta=1..\alpha^{max}\\ \frac{\overline{\mathbf{r}}_{\beta}}{p_{\beta}}, & \beta=\alpha^{max}+1..2\alpha^{max}\end{cases} \quad (4.49)$$

The coefficients and the r.h.s. of the system of linear algebraic equations (4.48) and its solution are described in appendix C.1. As a result, the heat flux, which is averaged over charge states according (4.46), is obtained in the form of:

$$\overline{\mathbf{h}}_\alpha = -\sum_\beta \kappa_{\alpha\beta}^{(h_T^A)} \widetilde{\nabla T_\beta} + p_\alpha \sum_\beta c_{\beta\alpha}^{(h_w^A)} (\overline{\mathbf{w}}_\alpha - \overline{\mathbf{w}}_\beta), \tag{4.50}$$

where coefficients $\kappa_{\alpha\beta}^{(h_T^A)}$ and $c_{\beta\alpha}^{(h_w^A)}$ depends on the coefficients of the inverse matrix according to appendix C.1.

#### 4.3.1.3 Charge states corrections for the heat flux

We follow the procedure from section 8.4 in [18] taking account typo corrections in [91]. The detailed derivation is performed in appendix C.2. As a result the heat flux for each charge state can be expressed in the form of:

$$\mathbf{h}_{\alpha Z} = \mathbf{h}_{\alpha Z}^T + \mathbf{h}_{\alpha Z}^{\mathbf{w}}, \tag{4.51}$$

$$\mathbf{h}_{\alpha Z}^T = -\frac{n_{\alpha Z}}{n_\alpha} \sum_\beta \kappa_{\alpha\beta}^{(h_T^A)} \widetilde{\nabla T_\beta} - \frac{n_{\alpha Z}}{n_\alpha} \kappa_\alpha^{(h_T^B)} \left( \frac{\overline{Z_\alpha^2}}{\overline{Z^2}} \nabla T_{\alpha Z} - \widetilde{\nabla T_\alpha} \right), \tag{4.52}$$

$$\mathbf{h}_{\alpha Z}^{\mathbf{w}} = p_{\alpha Z} \sum_\beta c_{\beta\alpha}^{(h_w)} (\mathbf{w}_{\alpha Z} - \overline{\mathbf{w}}_\beta), \tag{4.53}$$

where coefficients $\kappa_\alpha^{(h_T^B)}$ and $c_{\beta\alpha}^{(h_w)}$ can be found in appendix C.2. Note, (4.51) represents another form of Eq. (8.4.6) from [18].

### 4.3.2 Additional vector moment

#### 4.3.2.1 Averaged over charge states additional vector moment

Solving the system of linear algebraic equations (4.48) (details in appendix D.1) we get:

$$\overline{\mathbf{r}}_\alpha = -\frac{T_{av}}{m_\alpha} \sum_\beta \kappa_{\alpha\beta}^{(r_T^A)} \widetilde{\nabla T_\beta} + p_\alpha \frac{T_{av}}{m_\alpha} \sum_\beta c_{\beta\alpha}^{(r_w^A)} (\overline{\mathbf{w}}_\alpha - \overline{\mathbf{w}}_\beta), \tag{4.54}$$

where coefficients $\kappa_{\alpha\beta}^{(r_T^A)}$ and $c_{\beta\alpha}^{(r_w^A)}$ depends on the coefficients of the inverse matrix according to appendix D.1.

#### 4.3.2.2 Charge states corrections for the additional vector moment

Similar to the heat flux, the charge states corrections are derived in appendix D.2. Thus, one can obtain:

$$\mathbf{r}_{\alpha Z} = -\frac{n_{\alpha Z}}{n_\alpha}\frac{T_{av}}{m_\alpha}\sum_\beta \kappa_{\alpha\beta}^{(r_T^A)}\widetilde{\nabla T_\beta} - \frac{n_{\alpha Z}}{n_\alpha}\frac{T_{av}}{m_\alpha}\kappa_\alpha^{(r_T^B)}\left(\frac{\overline{Z_\alpha^2}}{Z^2}\nabla T_{\alpha Z} - \widetilde{\nabla T_\alpha}\right) + p_{\alpha Z}\frac{T_{av}}{m_\alpha}\sum_\beta c_{\beta\alpha}^{(r_w)}(\mathbf{w}_{\alpha Z} - \overline{\mathbf{w}}_\beta), \quad (4.55)$$

where coefficients $\kappa_\alpha^{(r_T^B)}$ and $c_{\beta\alpha}^{(r_w)}$ can be found in appendix D.2.

### 4.3.3 Thermal and Friction forces

#### 4.3.3.1 Useful relations for the friction term

The friction term (r.h.s. of the mometntum equation (2.73)) can be summed over the charge states:

$$\mathbf{R}_\alpha \overset{\text{def}}{=} \sum_Z \mathbf{R}_{\alpha Z} = \sum_\beta \left[\overline{G}_{\alpha\beta}^{(1)}(\overline{\mathbf{w}}_\alpha - \overline{\mathbf{w}}_\beta) + \frac{\mu_{\alpha\beta}}{T_{av}}\overline{G}_{\alpha\beta}^{(2)}\left(\frac{\overline{\mathbf{h}}_\alpha}{m_\alpha n_\alpha} - \frac{\overline{\mathbf{h}}_\beta}{m_\beta n_\beta}\right) + \left(\frac{\mu_{\alpha\beta}}{T_{av}}\right)^2 \overline{G}_{\alpha\beta}^{(8)}\left(\frac{\overline{\mathbf{r}}_\alpha}{m_\alpha n_\alpha} - \frac{\overline{\mathbf{r}}_\beta}{m_\beta n_\beta}\right)\right]. \quad (4.56)$$

The relation between the friction term for each charge states and the friction term, which is summed over charges states, can be obtained using (2.73) and (4.56):

$$\mathbf{R}_{\alpha Z} = I_{\alpha Z}\mathbf{R}_\alpha + I_{\alpha Z}\sum_\beta \left[\overline{G}_{\alpha\beta}^{(1)}(\mathbf{w}_{\alpha Z} - \overline{\mathbf{w}}_\alpha) + \frac{\mu_{\alpha\beta}}{m_\alpha}\overline{G}_{\alpha\beta}^{(2)}\left(\frac{\mathbf{h}_{\alpha Z}}{p_{\alpha Z}} - \frac{\overline{\mathbf{h}}_\alpha}{p_\alpha}\right) + \left(\frac{\mu_{\alpha\beta}}{m_\alpha}\right)^2 \frac{m_\alpha}{T_{av}}\overline{G}_{\alpha\beta}^{(8)}\left(\frac{\mathbf{r}_{\alpha Z}}{p_{\alpha Z}} - \frac{\overline{\mathbf{r}}_\alpha}{p_\alpha}\right)\right], \quad (4.57)$$

where the charge states corrections from appendices C.2 and D.2 can be used.

#### 4.3.3.2 Summed over charge states thermal force

One can take the terms (4.56), which are proportional to the temperature gradients, to obtain the TF. The TF, which is summed over charge states, is:

$$\mathbf{R}_{\alpha}^{T} = \sum_{\beta} \left[ \frac{\mu_{\alpha\beta}}{T_{av}} \overline{G}_{\alpha\beta}^{(2)} \left( \frac{\overline{\mathbf{h}}_{\alpha}^{T}}{m_{\alpha} n_{\alpha}} - \frac{\overline{\mathbf{h}}_{\beta}^{T}}{m_{\beta} n_{\beta}} \right) + \left( \frac{\mu_{\alpha\beta}}{T_{av}} \right)^{2} \overline{G}_{\alpha\beta}^{(8)} \left( \frac{\overline{\mathbf{r}}_{\alpha}^{T}}{m_{\alpha} n_{\alpha}} - \frac{\overline{\mathbf{r}}_{\beta}^{T}}{m_{\beta} n_{\beta}} \right) \right] \tag{4.58}$$

Using the heat flux and the additional vector moments from the sub-subsections 4.3.1.2 and 4.3.2.1 one can obtain the TF in the form of:

$$\mathbf{R}_{\alpha}^{T} = -\sum_{\beta} n_{\beta} \tilde{c}_{\alpha\beta}^{(R_T^A)} \widetilde{\nabla T_{\beta}}, \tag{4.59}$$

where the detailed procedure and the transport coefficient $\tilde{c}_{\alpha\beta}^{(R_T^A)}$ are described in the appendix E.1.

#### 4.3.3.3 Charge states corrections for the thermal force

Using relation (4.57) one can derive the TF for the each of the charge states (details in appendix E.2):

$$\mathbf{R}_{\alpha Z}^{T} = -I_{\alpha Z} \sum_{\beta} n_{\beta} \tilde{c}_{\alpha\beta}^{(R_T^A)} \widetilde{\nabla T_{\beta}} - n_{\alpha} I_{\alpha Z} c_{\alpha}^{(R_T^B)} \left( \frac{\overline{Z_{\alpha}^{2}}}{\overline{Z^{2}}} \nabla T_{\alpha Z} - \widetilde{\nabla T_{\alpha}} \right), \tag{4.60}$$

where the coefficient $c_{\alpha}^{(R_T^B)}$ can be found in appendix E.2. Note, (4.60) represents another form of the second and the third terms in Eq. (8.4.5) from [18].

#### 4.3.3.4 Summed over charge states friction force

One can take the terms (4.56), which are proportional to the flow velocities, to obtain the FR. The FR, which is summed over charge states, is:

$$\mathbf{R}_{\alpha}^{\mathbf{w}} = \sum_{\beta} \left[ \overline{G}_{\alpha\beta}^{(1)} (\overline{\mathbf{w}}_{\alpha} - \overline{\mathbf{w}}_{\beta}) + \frac{\mu_{\alpha\beta}}{T_{av}} \overline{G}_{\alpha\beta}^{(2)} \left( \frac{\overline{\mathbf{h}}_{\alpha}^{\mathbf{w}}}{m_{\alpha} n_{\alpha}} - \frac{\overline{\mathbf{h}}_{\beta}^{\mathbf{w}}}{m_{\beta} n_{\beta}} \right) + \left( \frac{\mu_{\alpha\beta}}{T_{av}} \right)^{2} \overline{G}_{\alpha\beta}^{(8)} \left( \frac{\overline{\mathbf{r}}_{\alpha}^{\mathbf{w}}}{m_{\alpha} n_{\alpha}} - \frac{\overline{\mathbf{r}}_{\beta}^{\mathbf{w}}}{m_{\beta} n_{\beta}} \right) \right] \tag{4.61}$$

Using the heat flux and the additional vector moments from the subsubsections 4.3.1.2 and 4.3.2.1 one can obtain the FR in the form of:

$$\mathbf{R}_{\alpha}^{\mathbf{w}} = -n_{\alpha} \sum_{\beta} \frac{\mu_{\alpha\beta}}{\tau_{\alpha\beta}^{(Zh)}} c_{\beta\alpha}^{(R_w^A)} (\overline{\mathbf{w}}_{\alpha} - \overline{\mathbf{w}}_{\beta}) \tag{4.62}$$

where the detailed procedure and the transport coefficient $c_{\beta\alpha}^{(R_w^A)}$ are described in the appendix F.1.

#### 4.3.3.5 Charge states corrections for the friction force

Using relation (4.57) one can derive the FR for the each of the charge states (details in appendix F.2):

$$\mathbf{R}_{\alpha Z}^{\mathbf{w}} = -n_\alpha I_{\alpha Z} \sum_\beta \frac{\mu_{\alpha\beta}}{\tau_{\alpha\beta}^{(Zh)}} c_{\beta\alpha}^{(R_w)} (\mathbf{w}_{\alpha Z} - \overline{\mathbf{w}}_\beta), \tag{4.63}$$

where the coefficient $c_{\beta\alpha}^{(R_w)}$ can be found in appendix F.2. Note, (4.63) represents another form of the first term in Eq. (8.4.5) from [18].

### 4.3.4 Viscous-stress tensor

#### 4.3.4.1 System of rank-2 equations

The rank-2 equations (4.37) and (4.38) can be solved independently of the rank-1 (2.66) and (2.67), because the rank-1 moments do not contribute into the r.h.s. of the equations for the rank-2 moments, due to the orthogonality of the tensorial Hermite polynomials (subsection 2.4.2).

In the plasmas without magnetic field $\mathbf{B} = 0$, the terms $-\omega_{\alpha Z}\{\pi_{\alpha Zlr} e_{slm} b_m\}$ and $-\omega_{\alpha Z}\{\sigma_{\alpha Zlr} e_{slm} b_m\}$ are equal to zero. Also, the components along $\mathbf{B}$ (parallel components) of these terms are equal to zero. Thus, the equations (2.66) and (2.67) without the $-\omega_{\alpha Z}\{\pi_{\alpha Zlr} e_{slm} b_m\}$ and $-\omega_{\alpha Z}\{\sigma_{\alpha Zlr} e_{slm} b_m\}$ terms are solved for the plasmas without magnetic field $\mathbf{B} = 0$. The results are evidently applicable also for parallel components in case $\mathbf{B} \neq 0$.

$$p_{\alpha Z} W_{rs}^{u_{\alpha Z}} + W_{rs}^{h_{\alpha Z}} = \sum_{\beta\zeta} \frac{T_{av}}{m_\alpha + m_\beta} \left[ \frac{G_{\alpha Z\beta\zeta}^{(3)} \pi_{\alpha Zrs}}{p_{\alpha Z}} + \frac{G_{\alpha Z\beta\zeta}^{(4)} \pi_{\beta\zeta rs}}{p_{\beta\zeta}} + \frac{\mu_{\alpha\beta}}{T_{av}} \left( \frac{G_{\alpha Z\beta\zeta}^{(13)} \sigma_{\alpha Zrs}}{p_{\alpha Z}} + \frac{G_{\alpha Z\beta\zeta}^{(14)} \sigma_{\beta\zeta rs}}{p_{\beta\zeta}} \right) \right], \tag{4.64}$$

$$\frac{7}{2} \frac{T_{av}}{m_\alpha} W_{rs}^{h_{\alpha Z}} = \sum_{\beta\zeta} \frac{T_{av}}{m_\alpha + m_\beta} \left[ \frac{7}{2} T_{av} \mu_{\alpha\beta} \left( \frac{G_{\alpha Z\beta\zeta}^{(13)} \pi_{\alpha Zrs}}{m_\alpha^2 p_{\alpha Z}} + \frac{G_{\alpha Z\beta\zeta}^{(14)} \pi_{\beta\zeta rs}}{m_\beta^2 p_{\beta\zeta}} \right) + \frac{G_{\alpha Z\beta\zeta}^{(15)} \sigma_{\alpha Zrs}}{p_{\alpha Z}} + \frac{G_{\alpha Z\beta\zeta}^{(16)} \sigma_{\beta\zeta rs}}{p_{\beta\zeta}} \right], \tag{4.65}$$

#### 4.3.4.2 Summed over charge states viscous-stress tensor

The equations (4.64) and (4.65) are summed over $Z$. Contracting the summation over $\zeta$, one can get:

$$\sum_{\beta}\frac{T_{av}}{m_{\alpha}+m_{\beta}}\left[\frac{\overline{G}^{(3)}_{\alpha\beta}\overline{\pi}_{\alpha rs}}{p_{\alpha}}+\frac{\overline{G}^{(4)}_{\alpha\beta}\overline{\pi}_{\beta rs}}{p_{\beta}}+\frac{\mu_{\alpha\beta}}{T_{av}}\left(\frac{\overline{G}^{(13)}_{\alpha\beta}\overline{\sigma}_{\alpha rs}}{p_{\alpha}}+\frac{\overline{G}^{(14)}_{\alpha\beta}\overline{\sigma}_{\beta rs}}{p_{\beta}}\right)\right]= W^{\overline{h}_{\alpha}}_{rs}+p_{\alpha}\widetilde{W^{u_{\alpha}}_{rs}}, \quad (4.66)$$

$$\sum_{\beta}\frac{T_{av}}{m_{\alpha}+m_{\beta}}\left[\frac{7}{2}T_{av}\mu_{\alpha\beta}\left(\frac{\overline{G}^{(13)}_{\alpha\beta}\overline{\pi}_{\alpha rs}}{m^2_{\alpha}p_{\alpha}}+\frac{\overline{G}^{(14)}_{\alpha\beta}\overline{\pi}_{\beta rs}}{m^2_{\beta}p_{\beta}}\right)+\frac{\overline{G}^{(15)}_{\alpha\beta}\overline{\sigma}_{\alpha rs}}{p_{\alpha}}+\frac{\overline{G}^{(16)}_{\alpha\beta}\overline{\sigma}_{\beta rs}}{p_{\beta}}\right]= \frac{7}{2}\frac{T_{av}}{m_{\alpha}}W^{\overline{h}_{\alpha}}_{rs}, \quad (4.67)$$

where:

$$n_{\alpha}\widetilde{W^{u_{\alpha}}_{rs}}\stackrel{\text{def}}{=}\sum_{Z}n_{\alpha Z}W^{u_{\alpha Z}}_{rs}, \quad W^{\overline{h}_{\alpha}}_{rs}\stackrel{\text{def}}{=}\frac{4}{5}\left[\frac{1}{2}\Big(\frac{\partial\overline{h}^{*}_{\alpha r}}{\partial x_s}+\frac{\partial\overline{h}^{*}_{\alpha s}}{\partial x_r}\Big)-\frac{1}{3}\delta_{rs}\nabla\cdot\overline{\mathbf{h}}^{*}_{\alpha}\right], \quad (4.68)$$

$$\overline{\mathbf{h}}^{*}_{\alpha}\stackrel{\text{def}}{=}\sum_{Z}\mathbf{h}_{\alpha Z}, \quad \overline{\pi}_{\alpha rs}=\sum_{z}\frac{p_{\alpha}I_{\alpha Z}\pi_{\alpha Zrs}}{p_{\alpha Z}}, \quad \overline{\sigma}_{\alpha rs}=\sum_{z}\frac{p_{\alpha}I_{\alpha Z}\sigma_{\alpha Zrs}}{p_{\alpha Z}}. \quad (4.69)$$

Note, the form (4.68) is more accurate than the form (A.10) from [84], where $\overline{\mathbf{h}}_{\alpha}=\sum_{Z}Z^2\mathbf{h}_{\alpha Z}/\overline{Z^2_{\alpha}}$ was used. For the practical applications difference between $\overline{\mathbf{h}}_{\alpha}$ and $\overline{\mathbf{h}}^{*}_{\alpha}$ in the heat stress tensor can be omitted. One can assume $W^{u_{\alpha Z}}_{rs}\approx W_{rs}$, which is equivalent to $\mathbf{u}_{\alpha Z}\approx\mathbf{u}$ and to neglecting the $\left\{\frac{\partial w_{\alpha Zr}}{\partial x_s}\right\}$ in (4.36). Thus, the Eq. (26) and (27) from [84] is the partial case of the system (4.66) and (4.67).

The (4.66) and (4.67) is a system of linear algebraic equations $2\alpha^{max}\times 2\alpha^{max}$, which can be written in the form:

$$\sum_{\beta=1..2\alpha^{max}}\check{c}_{\alpha\beta}Y_{\beta}=\check{d}_{\alpha} \quad (4.70)$$

where:

$$Y_{\beta}=\begin{cases}\frac{\overline{\pi}_{\beta rs}}{p_{\beta}}, & \beta=1..\alpha^{max}\\ \frac{\overline{\sigma}_{\beta rs}}{p_{\beta}}, & \beta=\alpha^{max}+1..2\alpha^{max}\end{cases} \quad (4.71)$$

The coefficients and the r.h.s. of the system of linear algebraic equations (4.70) and its solution are described in appendix G.1. As a result, the viscous-stress tensor, which is averaged over charge states according (4.69), is obtained in the form of:

$$\overline{\pi}_{\alpha rs} = -\sum_{\beta} \check{c}_{\alpha\beta}^{(\pi_u^A)} \tau_{\alpha\beta}^{(Zh)} p_\beta \widetilde{W_{rs}^{u_\beta}} - \sum_{\beta} \check{c}_{\alpha\beta}^{(\pi_h^A)} \tau_{\alpha\beta}^{(Zh)} W_{rs}^{\overline{h}_\beta}, \tag{4.72}$$

where the transport coefficients $\check{c}_{\alpha\beta}^{(\pi_u^A)}$ and $\check{c}_{\alpha\beta}^{(\pi_h^A)}$ are described in the appendix G.1. Note, the first term in (4.72) represents strain stresses, whereas the second term in (4.72) represents heat stresses.

#### 4.3.4.3 Charge states corrections for the viscous-stress tensor

Similar to the rank-1 moments, the charge states corrections can be found for rank-2 moments. Finally, the viscous-stress tensor for each of the charge states is:

$$\pi_{\alpha Zrs} = \pi_{\alpha Zrs}^u + \pi_{\alpha Zrs}^h, \tag{4.73}$$

$$\pi_{\alpha Zrs}^u = -p_{\alpha Z} \sum_{\beta} \check{c}_{\alpha\beta}^{(\pi_u^A)} \tau_{\alpha\beta}^{(Zh)} \frac{n_\beta}{n_\alpha} \widetilde{W_{rs}^{u_\beta}} - 2p_{\alpha Z} c_\alpha^{(\pi_u^B)} \tau_{\alpha\alpha}^{(Zh)} \left( \frac{\overline{Z_\alpha^2}}{Z^2} W_{rs}^{u_{\alpha Z}} - \widetilde{W_{rs}^{u_\alpha}} \right), \tag{4.74}$$

$$\pi_{\alpha Zrs}^h = -p_{\alpha Z} \sum_{\beta} \check{c}_{\alpha\beta}^{(\pi_h^A)} \tau_{\alpha\beta}^{(Zh)} \frac{1}{p_\alpha} W_{rs}^{\overline{h}_\beta} - 2p_{\alpha Z} c_\alpha^{(\pi_h^B)} \tau_{\alpha\alpha}^{(Zh)} \left( \frac{\overline{Z_\alpha^2}}{Z^2} \frac{1}{p_{\alpha Z}} W_{rs}^{h_{\alpha Z}} - \frac{1}{p_\alpha} W_{rs}^{\overline{h}_\alpha} \right), \tag{4.75}$$

where coefficients $c_\alpha^{(\pi_u^B)}$ and $c_\alpha^{(\pi_h^B)}$ can be found in appendix G.2.

Thus, using the EMIM, the systems (4.48) and (4.70) can be solved. Consequently, the transport coefficients are obtained. As a result, the system of the fluid Braginskii equations (4.4)-(4.6) is closed and can be solved using numerical methods.

However, this method can be improved further, by analysing the coefficients of matrices of the systems (4.48) and (4.70). The cross elements are found small, when $m_\alpha \ll m_\beta$. Neglecting, the small cross elements, the (4.48) and (4.70) can be solved analytically, when the mixture consists of light and heavy species. As a result, the solution can be expressed in terms of explicit mathematical functions. The analytical derivation of the transport coefficients is performed in section 4.4.

## 4.4 Improved analytical expressions

The original Zhdanov-Yushmanov analytical expressions are applicable for mixtures of species with significantly different masses. However, by taking into account the mass dependence, the results become more accurate, and the range of available plasma mixtures that can be effectively modeled with these expressions becomes much wider.

### 4.4.1 Matrix coefficients analysis

Let us consider the mixture with one light and several heavy species. We relate index 1 to the light species, whereas indices $2..\alpha^{max}$ correspond to heavy species ($m_1 \ll m_j : j = 2..\alpha^{max}$). This is only for the convenience of further discussion. In fact, in contrast to the ZY expressions (subsection 2.4.4), the IAM does not require explicit declaration, which species are assumed as the light species. The light species can have any index in the mixture.

One can analyze the coefficients for the matrices $\check{A}$ (C.5)-(C.8) and $\check{C}$ (G.5)-(G.8). We preform this analysis in the 13N-moment approximation (without $\mathbf{r}_{\alpha Z}$ and $\sigma_{\alpha Zrs}$). Similar estimations can be done in the 21N-moment approximation. We consider coefficients $\check{a}_{\alpha\beta} = \check{G}^{(6)}_{\alpha\beta} : \ \alpha \neq \beta$ and $\check{a}_{\beta\beta} = \check{G}^{(6)}_{\beta\beta} + \sum_\gamma \check{G}^{(5)}_{\beta\gamma} : \ \alpha = \beta$.

For the heavy trace-impurity case, where $\overline{Z_1^2} n_1 \gg \overline{Z_j^2} n_j$, $\overline{Z_1^2} n_1 / \overline{Z_j^2} n_j > \sqrt{m_j/m_1} : j = 2..\alpha^{max}$, the light main species coefficients (using (B.1)), are related as:

$$\check{a}_{11} \approx \check{G}^{(6)}_{11} + \check{G}^{(5)}_{11}, \quad \check{a}_{1j} = \check{G}^{(6)}_{1j}, \quad \frac{\check{a}_{11}}{\check{a}_{1j}} \propto \frac{m_j}{m_1} \frac{\overline{Z_1^2} n_1}{\overline{Z_j^2} n_j}, \quad \frac{\overline{\mathbf{h}}_1}{p_1} \propto -\frac{n_1}{(\overline{Z_1^2} n_1)^2 \sqrt{m_1}} \frac{\zeta_p}{\sqrt{m_p}} \widetilde{\nabla T_1}. \tag{4.76}$$

The $\check{a}_{1j}$ can be neglected and the light species heat flux can be obtained as (4.76). This represents the independence of the light species distribution function from the collisions with the heavy trace-impurity species. The heavy trace-impurity species coefficients are:

$$\check{a}_{jj} \approx \check{G}^{(5)}_{j1}, \quad \check{a}_{j1} = \check{G}^{(6)}_{j1}, \quad \check{a}_{ji} = \check{G}^{(6)}_{ji}, \quad \frac{\check{a}_{jj}}{\check{a}_{j1}} \propto \frac{m_j}{m_1}, \quad \frac{\check{a}_{jj}}{\check{a}_{ji}} \propto \sqrt{\frac{m_1}{\mu_{ji}}} \frac{\overline{Z_1^2} n_1}{\overline{Z_i^2} n_i}, \quad i \neq j. \tag{4.77}$$

The heavy trace-impurity distribution function depends on the collisions with the light main species and independent of collisions with trace-impurity species. Note, this case is in conflict with the procedure, which was proposed by Zhdanov on page 181 in [18]. It is clear that the heavy trace-impurity equations cannot be solved without main light species contribution: the ZY heavy impurity heat flux $\propto \tau^{(Zh)}_{imp\ imp}$. In fact, this Zhdanov procedure cannot be applied, when $\sqrt{m_j/m_1} < \overline{Z_1^2} n_1 / \overline{Z_j^2} n_j$. However, the Zhdanov procedure on page 181 in [18] is well applicable for the ion equations separation from the electrons ones (since $\overline{Z_e^2} n_e \leq \sum_\alpha \overline{Z_\alpha^2} n_\alpha : \alpha \in ions$).

The diagonal matrix element $\check{a}_{jj}$ is $\propto m_j/m_1$ times larger than the non-diagonal matrix element $\check{a}_{j1}$. Thus:

$$\frac{\overline{\mathbf{h}}_j}{p_j} \propto \frac{m_1}{m_j}\frac{\overline{\mathbf{h}}_1}{p_1} - \frac{n_j}{\overline{Z_1^2}n_1\overline{Z_j^2}n_j\sqrt{m_1}}\frac{\zeta_p}{\sqrt{m_p}}\widetilde{\nabla T_j} + \frac{m_1}{m_j}(\overline{\mathbf{w}}_j - \overline{\mathbf{w}}_1), \tag{4.78}$$

or, using (4.76), one can get:

$$\frac{\overline{\mathbf{h}}_j}{p_j} \propto -\frac{m_1}{m_j}\frac{n_1}{(\overline{Z_1^2}n_1)^2\sqrt{m_1}}\frac{\zeta_p}{\sqrt{m_p}}\widetilde{\nabla T_1} - \frac{n_j}{\overline{Z_1^2}n_1\overline{Z_j^2}n_j\sqrt{m_1}}\frac{\zeta_p}{\sqrt{m_p}}\widetilde{\nabla T_j} + \frac{m_1}{m_j}(\overline{\mathbf{w}}_j - \overline{\mathbf{w}}_1). \tag{4.79}$$

The ratio between the first and the second terms is $\propto \frac{m_1}{m_j}\frac{\overline{Z_j^2}}{\overline{Z_1^2}}$. For some cases, the $\frac{m_1}{m_j}\frac{\overline{Z_j^2}}{\overline{Z_1^2}} \sim 1$. If we neglect the first term, the heavy impurity hot-tail is captured only qualitatively (for $\widetilde{\nabla T_1} \sim \widetilde{\nabla T_j}$). The exact transport coefficient for the heavy impurity heat flux is not calculated correctly in this case.

In non-trace-impurity case, where $\overline{Z_1^2}n_1 \ll \overline{Z_j^2}n_j : \ j = 2..\alpha^{max}$, (the impurities can have close masses) the light main species coefficients (using (B.1)), are related as:

$$\check{a}_{11} \approx \sum_k \check{G}^{(5)}_{1k}, \quad \check{a}_{1j} = \check{G}^{(6)}_{1j}, \quad \frac{\check{a}_{11}}{\check{a}_{1j}} \propto \frac{m_j}{m_1}\frac{\sum_k \overline{Z_k^2}n_k}{\overline{Z_j^2}n_j}, \tag{4.80}$$

The $\check{a}_{1j}$ can be neglected also for this case. Note, the collisions between main and impurity species contribute significantly into the main species distribution function. The heavy trace-impurity species coefficients are:

$$\check{a}_{jj} = \check{G}^{(6)}_{jj} + \sum_k \check{G}^{(5)}_{jk}, \quad \check{a}_{j1} = \check{G}^{(6)}_{j1}, \quad \check{a}_{ji} = \check{G}^{(6)}_{ji}, \quad \frac{\check{a}_{jj}}{\check{a}_{j1}} \propto \frac{m_j}{m_1}\frac{\sum_k \sqrt{\mu_{jk}}\overline{Z_k^2}n_k}{\sqrt{m_1}\overline{Z_1^2}n_1} \tag{4.81}$$

$$\frac{\check{a}_{jj}}{\check{a}_{ji}} \propto \frac{\sum_k \sqrt{\mu_{jk}}\overline{Z_k^2}n_k}{\sqrt{\mu_{ji}}\overline{Z_i^2}n_i}, \quad i \neq j. \tag{4.82}$$

In this case (4.81) justifies the heavy species equations separation from the light heavy species equations, which is discussed by Zhdanov on page 181 in [18], because the $\check{a}_{j1}$ is small with respect to the $\check{a}_{jj}$. In the general case, where the mass ratios $m_j/m_i$ can be arbitrary, the (4.82) does not allow to neglect $\check{a}_{ji}$ non-diagonal elements. Thus, if there are more then one heavy species, and $\check{a}_{ji}$ is neglected, the accurate calculation of the heavy species heat fluxes is not guaranteed.

The intermediate $\overline{Z_1^2}n_1 \sim \overline{Z_j^2}n_j : \ j = 2..\alpha^{max}$ case can be analyzed in the similar way, as it is done for the two asymptotic cases above. Similar analysis can be performed of the rank-2 equation matrix $\check{C}$ (G.5)-(G.8).

The friction term in the 13N-moment approximation can be written as:

$$\mathbf{R}_\alpha = \mathbf{R}_\alpha^{\mathbf{w}1} + \mathbf{R}_\alpha^{\mathbf{h}2}, \quad \mathbf{R}_\alpha^{\mathbf{w}1} = \sum_\beta \overline{G}_{\alpha\beta}^{(1)}(\overline{\mathbf{w}}_\alpha - \overline{\mathbf{w}}_\beta), \tag{4.83}$$

$$\mathbf{R}_\alpha^{\mathbf{h}2} = \sum_\gamma \frac{\mu_{\alpha\gamma}}{m_\alpha}\overline{G}_{\alpha\gamma}^{(2)}\left(\frac{\overline{\mathbf{h}}_\alpha}{p_\alpha} - \frac{m_\alpha}{m_\gamma}\frac{\overline{\mathbf{h}}_\gamma}{p_\gamma}\right), \tag{4.84}$$

where the largest contribution into the heat flux part (4.84) comes from the term where the species $\alpha$ and $\gamma$ have significantly different (light-heavy species term). For the heavy species with close masses terms (heavy-heavy species terms) heat fluxes cancel each others in (4.84), which make these terms small with respect to the light-heavy species terms. In the trace-impurity case the heavy-heavy species terms can be assumed equal to zero. We note that the heavy species heat flux contribution in the light-heavy species term is reduced by the mass ratio factor. Thus, the light species heat flux plays its major role in the (4.84), which can be calculated without non-diagonal elements $\check{a}_{1j}$. This is the essential idea behind the ZY analytical expression derivation (subsection 2.4.4). The light species heat fluxes (and additional vector moments) can be calculated independently of the heavy species equations, if the $(m_1/m_j)^n : \ n > 1$ order terms are neglected, because the non-diagonal elements $\check{a}_{1j}$ disappear according to (4.76) and (4.80). Besides, the heavy heat flux contribution disappears in the light-heavy species term in (4.84). Also, in the mixture of the electrons, light main ions and heavy impurity, which is commonly considered for the plasma simulations [98], the impurity heat flux does not contribute significantly into the ion energy transport. Thus, the electron and ion heat parallel conductivities and the parallel flow velocity difference heat fluxes, the ion parallel viscosities, the parallel electron, main ion and impurities TF and FR can be obtained using ZY analytical expressions, if $m_{main}/m_{imp} \ll 1$. However, this condition is usually not well satisfied in fusion plasmas.

Following Zhdanov and Yushmanov, in the IAM the non-diagonal elements are neglected to solve equations (4.43)-(4.44) and (4.66)-(4.67) for each species independently from the other species equations solutions. In particular, this implies that the contributions to the heat-flux equations for each species from the hot-tails of the other species are not taken into account, and only the zero-order Maxwell distribution functions contribution of other species is included. Approaching the low mass impurities range, the $(m_1/m_j)^n : \ n > 1$ order terms are included into the diagonal elements of the $\check{A}$ and $\check{C}$, which suppose to provide more accurate solution than ZY expressions in such case. In test cases, which are performed in subsection 6.1.2, the IAM provides much closer solutions to the EMIM results than the ZY expressions. The heat fluxes are calculated for all the species and all the terms are kept in (4.84). As a result, the heavy species

heat fluxes are taken into account for the TF and FR calculations. As we discussed previously the heavy species heat flux can deviate from the exact one, if the non-diagonal elements are omitted. However, the qualitatively correct heavy species heat flux contribution make the friction term calculations more accurate (subsection 4.4.3). We note that, these procedure is preformed uniformly for all species. As a result, the explicit light species declaration, which is done in the ZY method, is not required in the IAM.

It is important to emphasise, that the charge state averaging procedure, which is performed in subsections 4.3.1.2 and 4.3.4.2, is essential for the IAM. The cross terms in the systems (4.41)-(4.42) and (4.64)-(4.65) can not be assumed small in case of $m_1 \ll m_j : \quad j = 2..\alpha^{max}$, because the cross terms of the different charge states of the one type of species have the same mass. In the IAM the moments and friction terms for the each charge states are found using analytical corrections identically as it was done in the EMIM in sub-subsections 4.3.1.3, 4.3.2.2, 4.3.3.3, 4.3.3.5 and 4.3.4.3. Note that in contrast to the ZY expressions, the light species can have several charge states in the IAM. For instance, the IAM can be applied for He plasmas with impurities.

For the 21N-moment approximationa similar matrix coefficient analysis can be carried out. In this case, the $\check{A}$ (C.5)-(C.8) and $\check{C}$ (G.5)-(G.8) should be split into the blocks:

$$\check{A} = \begin{bmatrix} \check{A}_{11} & \check{A}_{12} \\ \check{A}_{21} & \check{A}_{22} \end{bmatrix}; \quad \check{C} = \begin{bmatrix} \check{C}_{11} & \check{C}_{12} \\ \check{C}_{21} & \check{C}_{22} \end{bmatrix}; \tag{4.85}$$

where each block can be written:

$$\check{A}_{qp} = \begin{bmatrix} \check{a}^{qp}_{11} & \check{a}^{qp}_{12} & \cdots & \check{a}^{qp}_{1\alpha^{max}} \\ \check{a}^{qp}_{21} & \check{a}^{qp}_{22} & \cdots & \check{a}^{qp}_{2\alpha^{max}} \\ \vdots & \vdots & \ddots & \vdots \\ \check{a}^{qp}_{\alpha^{max}1} & \check{a}^{qp}_{\alpha^{max}2} & \cdots & \check{a}^{qp}_{\alpha^{max}\alpha^{max}} \end{bmatrix}; \quad \check{C}_{qp} = \begin{bmatrix} \check{c}^{qp}_{11} & \check{c}^{qp}_{12} & \cdots & \check{c}^{qp}_{1\alpha^{max}} \\ \check{c}^{qp}_{21} & \check{c}^{qp}_{22} & \cdots & \check{c}^{qp}_{2\alpha^{max}} \\ \vdots & \vdots & \ddots & \vdots \\ \check{c}^{qp}_{\alpha^{max}1} & \check{c}^{qp}_{\alpha^{max}2} & \cdots & \check{c}^{qp}_{\alpha^{max}\alpha^{max}} \end{bmatrix}; \tag{4.86}$$

In the IAM the 21N-moment approximation used. The non-diagonal elements of each block $\check{a}^{qp}_{ij} : i \neq j$ and $\check{c}^{qp}_{ij} : i \neq j$ are neglected. Also, the complete friction term form (4.56) is used. The IAM transport coefficients are derived in the following subsections.

### 4.4.2 Heat flux

According to our program, we neglect the cross terms, which depend on the $\overline{\mathbf{h}}_\beta$ and $\overline{\mathbf{r}}_\beta$ for $\beta \neq \alpha$, in the rank-1 equations (4.43) and (4.44):

$$\begin{aligned} &\overline{G}^{(5)}_{\alpha\alpha}\frac{\overline{\mathbf{h}}_\alpha}{p_\alpha} + \overline{G}^{(6)}_{\alpha\alpha}\frac{\overline{\mathbf{h}}_\alpha}{p_\alpha} + \sum_{\beta\neq\alpha}\overline{G}^{(5)}_{\alpha\beta}\frac{\overline{\mathbf{h}}_\alpha}{p_\alpha} + \\ &\frac{m_\alpha}{2T_{av}}\left(\overline{G}^{(9)}_{\alpha\alpha}\frac{\overline{\mathbf{r}}_\alpha}{p_\alpha} + \overline{G}^{(10)}_{\alpha\alpha}\frac{\overline{\mathbf{r}}_\alpha}{p_\alpha}\right) + \sum_{\beta\neq\alpha}\frac{\mu_{\alpha\beta}}{T_{av}}\overline{G}^{(9)}_{\alpha\beta}\frac{\overline{\mathbf{r}}_\alpha}{p_\alpha} = \frac{5}{2}n_\alpha\widetilde{\nabla T_\alpha} - \sum_\beta\left[\frac{5}{2}\frac{\mu_{\alpha\beta}}{m_\alpha}\overline{G}^{(2)}_{\alpha\beta}(\overline{\mathbf{w}}_\alpha - \overline{\mathbf{w}}_\beta)\right], \end{aligned} \tag{4.87}$$

$$\frac{7}{2}\left(\overline{G}^{(9)}_{\alpha\alpha}\frac{\overline{\mathbf{h}}_\alpha}{p_\alpha}+\overline{G}^{(10)}_{\alpha\alpha}\frac{\overline{\mathbf{h}}_\alpha}{p_\alpha}\right)+\sum_{\beta\neq\alpha}7\frac{\mu_{\alpha\beta}}{m_\alpha}\overline{G}^{(9)}_{\alpha\beta}\frac{\overline{\mathbf{h}}_\alpha}{p_\alpha}+$$
$$\frac{m_\alpha}{T_{av}}\overline{G}^{(11)}_{\alpha\alpha}\frac{\overline{\mathbf{r}}_\alpha}{p_\alpha}+\frac{m_\alpha}{T_{av}}\overline{G}^{(12)}_{\alpha\alpha}\frac{\overline{\mathbf{r}}_\alpha}{p_\alpha}+\sum_{\beta\neq\alpha}\frac{m_\alpha}{T_{av}}\overline{G}^{(11)}_{\alpha\beta}\frac{\overline{\mathbf{r}}_\alpha}{p_\alpha}=-\sum_\beta\Big[\frac{35}{2}\left(\frac{\mu_{\alpha\beta}}{m_\alpha}\right)^2\overline{G}^{(8)}_{\alpha\beta}(\overline{\mathbf{w}}_\alpha-\overline{\mathbf{w}}_\beta)\Big]. \tag{4.88}$$

Combining G-objects into the coefficients and using Z-variables (appendix B), one can get:

$$-\tilde{\alpha}_{11\alpha}\lambda_{\alpha\alpha}\frac{\overline{\mathbf{h}}_\alpha}{p_\alpha}+\frac{m_\alpha}{T_{av}}\tilde{\alpha}_{12\alpha}\lambda_{\alpha\alpha}\frac{\overline{\mathbf{r}}_\alpha}{p_\alpha}=\frac{5}{2}n_\alpha\widetilde{\nabla T_\alpha}-\frac{3}{2}\sum_\beta\Big[\frac{\mu_{\alpha\beta}}{m_\alpha}\lambda_{\alpha\beta}(\overline{\mathbf{w}}_\alpha-\overline{\mathbf{w}}_\beta)\Big] \tag{4.89}$$

$$\tilde{\alpha}_{21\alpha}\lambda_{\alpha\alpha}\frac{\overline{\mathbf{h}}_\alpha}{p_\alpha}-\frac{m_\alpha}{T_{av}}\tilde{\alpha}_{22\alpha}\lambda_{\alpha\alpha}\frac{\overline{\mathbf{r}}_\alpha}{p_\alpha}=\frac{15}{4}\sum_\beta\Big[\left(\frac{\mu_{\alpha\beta}}{m_\alpha}\right)^2\lambda_{\alpha\beta}(\overline{\mathbf{w}}_\alpha-\overline{\mathbf{w}}_\beta)\Big] \tag{4.90}$$

where $\lambda_{\alpha\beta}$ is defined according to (2.91) and the $\tilde{\alpha}_{**\alpha}$ coefficients are:

$$\tilde{\alpha}_{11\alpha}\overset{\text{def}}{=}\frac{4}{5}+\frac{13\sqrt{2}}{10}Z^s_{5\alpha},\quad \tilde{\alpha}_{21\alpha}\overset{\text{def}}{=}7\tilde{\alpha}_{12\alpha}\overset{\text{def}}{=}\frac{6}{5}+\frac{69\sqrt{2}}{20}Z^s_{9\alpha},\quad \tilde{\alpha}_{22\alpha}\overset{\text{def}}{=}\frac{9}{7}+\frac{433\sqrt{2}}{280}Z^s_{11\alpha}. \tag{4.91}$$

The heat flux solution of the (4.89) and (4.90) is:

$$\overline{\mathbf{h}}_\alpha=\frac{5}{2}\frac{p_\alpha n_\alpha}{\lambda_{\alpha\alpha}}\frac{\tilde{\alpha}_{22\alpha}}{\tilde{\alpha}_{12\alpha}\tilde{\alpha}_{21\alpha}-\tilde{\alpha}_{11\alpha}\tilde{\alpha}_{22\alpha}}\widetilde{\nabla T_\alpha}+$$
$$\frac{p_\alpha}{\lambda_{\alpha\alpha}}\sum_\beta\left[\frac{\frac{15}{4}\left(\frac{\mu_{\alpha\beta}}{m_\alpha}\right)^2\tilde{\alpha}_{12\alpha}-\frac{3}{2}\frac{\mu_{\alpha\beta}}{m_\alpha}\tilde{\alpha}_{22\alpha}}{\tilde{\alpha}_{12\alpha}\tilde{\alpha}_{21\alpha}-\tilde{\alpha}_{11\alpha}\tilde{\alpha}_{22\alpha}}\lambda_{\alpha\beta}(\overline{\mathbf{w}}_\alpha-\overline{\mathbf{w}}_\beta)\right]. \tag{4.92}$$

Using (4.91) one can write:

$$\overline{\mathbf{h}}_\alpha=-\frac{125}{32}\frac{p_\alpha n_\alpha}{\lambda_{\alpha\alpha}}\frac{1}{\tilde{\Delta}_\alpha}\left(1+\frac{433\sqrt{2}}{360}Z^*_{22\alpha}\right)\nabla T_\alpha+$$
$$\frac{25}{16}\frac{p_\alpha}{\lambda_{\alpha\alpha}}\frac{1}{\tilde{\Delta}_\alpha}\sum_\beta\left[\frac{\mu_{\alpha\beta}}{m_\alpha}\Big(\frac{3}{2}-\frac{1}{2}\frac{\mu_{\alpha\beta}}{m_\alpha}+\frac{433\sqrt{2}}{240}Z^s_{11\alpha}-\frac{23\sqrt{2}}{16}\frac{\mu_{\alpha\beta}}{m_\alpha}Z^s_{9\alpha}\Big)\lambda_{\alpha\beta}(\overline{\mathbf{w}}_\alpha-\overline{\mathbf{w}}_\beta)\right] \tag{4.93}$$

Combining the transport coefficients, one can obtain the final form of the heat flux:

$$\overline{\mathbf{h}}_\alpha=-\frac{p_\alpha n_\alpha}{\lambda_{\alpha\alpha}}c^{(h^A_T)}_\alpha\widetilde{\nabla T_\alpha}+p_\alpha\sum_\beta c^{(h^A_w)}_{\beta\alpha}(\overline{\mathbf{w}}_\alpha-\overline{\mathbf{w}}_\beta), \tag{4.94}$$

where coefficients are:

$$c_{\alpha}^{(h_T^A)} \stackrel{\text{def}}{=} \frac{125}{32}\frac{1}{\tilde{\Delta}_\alpha}\left(1+\frac{433\sqrt{2}}{360}Z_{11\alpha}^s\right), \tag{4.95}$$

$$c_{\beta\alpha}^{(h_w^A)} = \frac{1}{\tilde{\Delta}_\alpha}\frac{25\sqrt{2}}{16}\frac{\mu_{\alpha\beta}}{m_\alpha}\sqrt{\frac{\mu_{\alpha\beta}}{m_\alpha}}\left[\frac{3}{2}+\frac{433\sqrt{2}}{240}Z_{11\alpha}^s-\frac{1}{2}\frac{\mu_{\alpha\beta}}{m_\alpha}\left(1+\frac{23\sqrt{2}}{8}Z_{9\alpha}^s\right)\right]\frac{\overline{Z_\beta^2}n_\beta}{\overline{Z_\alpha^2}n_\alpha}, \tag{4.96}$$

$$\tilde{\Delta}_\alpha \stackrel{\text{def}}{=} \frac{5629}{1152}Z_{5\alpha}^s Z_{11\alpha}^s-\frac{529}{128}{Z_{9\alpha}^s}^2+\frac{65\sqrt{2}}{32}Z_{5\alpha}^s+\frac{433\sqrt{2}}{288}Z_{11\alpha}^s-\frac{23\sqrt{2}}{16}Z_{9\alpha}^s+1. \tag{4.97}$$

The heat flux (4.94) can be written in the form of (4.50), if the transport coefficients are written as:

$$\kappa_{\alpha\beta}^{(h_T^A)} = \delta_{\alpha\beta}\frac{p_\alpha n_\alpha}{\lambda_{\alpha\alpha}}c_\alpha^{(h_T^A)} \tag{4.98}$$

Evidently, the analytical charge-state corrections can be applied identically, as it is performed in sub-subsection 4.3.1.3 and appendix C.2, to obtain an explicit representation of the heat flux for the each charge state:

$$\mathbf{h}_{\alpha Z} = \mathbf{h}_{\alpha Z}^T + \mathbf{h}_{\alpha Z}^{\mathbf{w}} \tag{4.99}$$

$$\mathbf{h}_{\alpha Z}^T = -\frac{p_{\alpha Z}n_\alpha}{\lambda_{\alpha\alpha}}c_\alpha^{(h_T^A)}\widetilde{\nabla T_\alpha}-\frac{p_{\alpha Z}n_\alpha}{\lambda_{\alpha\alpha}}c_\alpha^{(h_T^B)}\left(\frac{\overline{Z_\alpha^2}}{Z^2}\nabla T_{\alpha Z}-\widetilde{\nabla T_\alpha}\right) \tag{4.100}$$

$$\mathbf{h}_{\alpha Z}^{\mathbf{w}} = p_{\alpha Z}\sum_\beta c_{\beta\alpha}^{(h_w)}(\mathbf{w}_{\alpha Z}-\overline{\mathbf{w}}_\beta) \tag{4.101}$$

The IAM expression should asymptotically match the ZY ones. Let us consider the $m_\alpha/m_\beta \to 0$ limit. The $Z_{c\alpha}^* \approx Z_{5\alpha}^s \approx Z_{9\alpha}^s \approx Z_{11\alpha}^s \approx Z_\alpha^*$ and:

$$\tilde{\Delta}_\alpha \approx \frac{217}{288}{Z_\alpha^*}^2+\frac{151\sqrt{2}}{72}Z_\alpha^*+1 \approx \Delta_\alpha, \tag{4.102}$$

where $\Delta_\alpha$ is defined according to (2.98). The heat conductivity coefficient turns into:

$$\frac{m_\alpha}{\tau_\alpha^{(Zh)}}\frac{n_\alpha}{\lambda_{\alpha\alpha}}c_\alpha^{(h_T^A)} = (1+\sqrt{2}Z^*_{c\alpha})c_\alpha^{(h_T^A)} \approx \frac{125}{32}\frac{1}{\Delta_\alpha}(1+\sqrt{2}Z^*_\alpha)\left(1+\frac{433\sqrt{2}}{360}Z^*_\alpha\right) \approx c_\alpha^{(6)} + 0.5c_{\alpha\alpha}^{(3)}\frac{\overline{\tau}_\alpha^{(Zh)}}{\tau_{\alpha\alpha}^{(Zh)}}, \quad (4.103)$$

where $c_\alpha^{(6)} + 0.5c_{\alpha\alpha}^{(3)}\frac{\overline{\tau}_\alpha^{(Zh)}}{\tau_{\alpha\alpha}^{(Zh)}}$ is defined according to (2.96). The **w**-dependent heat flux transport coefficient is:

$$\frac{m_\alpha}{\tau_\alpha^{(Zh)}}\frac{\tau_{\alpha\beta}^{(Zh)}}{\mu_{\alpha\beta}}c_{\beta\alpha}^{(h_w^A)} = \sqrt{\frac{m_\alpha}{2\mu_{\alpha\beta}}}\frac{\overline{Z_\alpha^2}n_\alpha}{\overline{Z_\beta^2}n_\beta}(1+\sqrt{2}Z^*_{c\alpha})c_{\beta\alpha}^{(h_w^A)} \approx \frac{25}{16}\frac{1}{\Delta_\alpha}(1+\sqrt{2}Z^*_\alpha)\left(1+\frac{11\sqrt{2}}{30}Z^*_\alpha\right) \approx c_{\beta\alpha}^{(2)}, \quad (4.104)$$

where $c_{\beta\alpha}^{(2)}$ is defined according to (2.94).

To check how accurate the IAM and the ZY expressions reproduce the EMIM results, the mixture of D + C + another impurity is considered. The type of this another impurity is varied from H to Ne along the horizontal axis in figure 4.1a. In these test cases, the amount of C and another impurity is chosen according to the rules $\overline{Z_C^2}n_C/n_D = 0.5$, $\overline{Z_{imp}^2}n_{imp}/n_D = 1.0$. For the $imp = H, T$, this rule leads to the equal concentrations of each hydrogen isotope: $n_{H/T} = n_D$, whereas for the $imp = Ne$, this rule leads to the $n_{Ne} < n_D$. Those are typical cases: mixture of different isotopes with comparable concentrations and the D plasmas with the non-trace radiative Ne impurity correspondingly.

The D heat conductivity one can write in the Braginskii-like form:

$$h_{D\|}^T = -c_D^{(h_T eff)}\frac{n_D T\tau_D^{(Zh)}}{m_D}\nabla_\| T_D, \quad (4.105)$$

where the transport coefficient $c_D^{(h_T eff)}$ is shown in figure 4.1a. In the region from Ne to He the non-diagonal terms, which take into account impurities heat fluxes, do not play a significant role. Thus, the difference between the IAM and the EMIM is small (smaller than the method accuracy). There is $\sim 10\%$ difference between two methods for the H-T range. Let us briefly analyze the matrix coefficients. There are four comparable terms in (4.43) (if r-moment contribution is not considered to simplify the analysis): two terms due to D-D interactions hot-tails with the non-modified $f_{\alpha Z}^0$, one term due to interactions of the D hot-tail with the $f_{\alpha Z}^0$ for another hydrogen isotope and one term due to interactions of the another hydrogen isotope hot-tail with the $f_{\alpha Z}^0$ for D. The

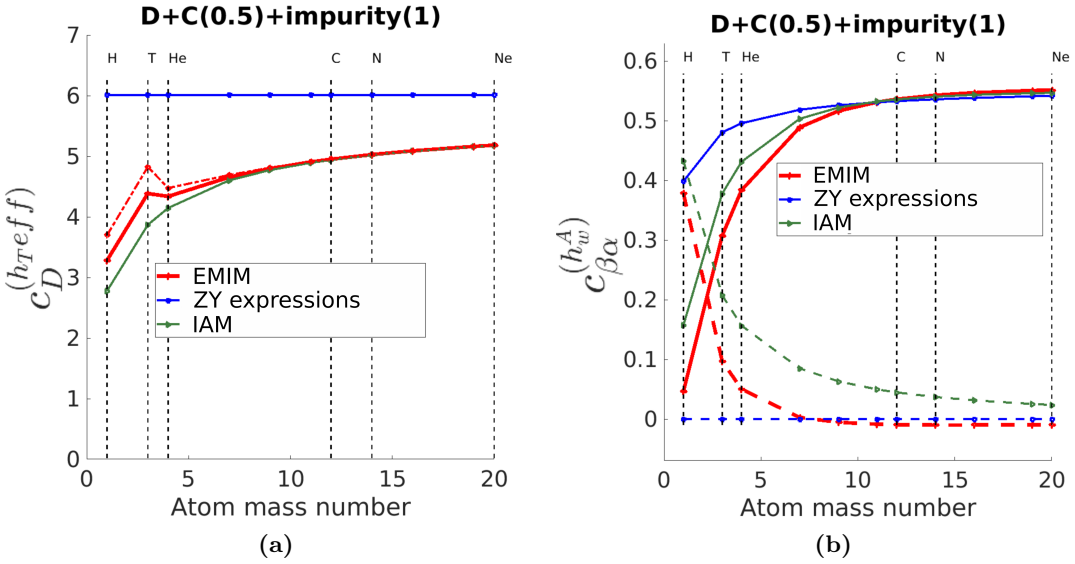


**Figure 4.1:** (a) The heat conductivity transport coefficient for deuterium, using the EMIM, the ZY expression and the IAM, for the D + C + another impurity case with equal distribution between charge states. The additional impurity is varied along the horizontal axis. The dash-dotted line shows the case where: $\widetilde{\nabla_\parallel T_\beta} = 2\times\nabla_\parallel T_D : \beta \neq D$. The number in parentheses at the top of the figure gives normalised impurity density ($= \overline{Z_\beta^2} n_\beta / n_D : \beta \neq D$) and is kept constant. (b) The velocity dependent part of the heat flux transport coefficient for the deuterium due to D/impurity velocity difference $c^{(h_w^A)}_{imp\ D}$ (solid) and for another impurity due to impurity/D velocity difference $c^{(h_w^A)}_{D\ imp}$ (dashed), using the EMIM, the ZY expression and the IAM, for D + C + another impurity.

latter is neglected according to the IAM procedure (4.87). Therefore, around dozens percent of accuracy are lost (figure 4.1a).

One can also consider the case where the temperature of impurities is different from the main ion temperature. It is especially important for the temperature gradients [18]. To test the contribution from the different temperature, we tried: $\widetilde{\nabla_\parallel T_\beta} = 2\times\nabla_\parallel T_D : \beta \neq D$, the dash-dotted line in figure 4.1a. Evidently, there is a small contribution from the impurity temperatures for the He-Ne range and additionally dozens percent of the IAM-EMIM difference for the H-T range. However the D-T temperature difference is usually small, due to the close masses and thermalization times (for example see Figure 11 in [141]).

The ZY expressions coefficients, which depend only on $Z^*_\alpha$ and are constant for $\overline{Z_C^2} n_C / n_D = 0.5$, $\overline{Z_{imp}^2} n_{imp} / n_D = 1.0$, deviate significantly from the EMIM results (figure 4.1a). The absence of mass dependence in (2.96) coefficient is a too strong assumption in the middle-mass impurity range. The $m_D / m_\beta \approx 0 : \beta \neq D$ assumption should be avoided in Z-variables in (4.103) for the heat conductivity calculations.

The D **w**-dependent heat transport coefficient $c^{(h_w^A)}_{imp\ D}$ is calculate more accurate, i. e. closer to the EMIM, by the IAM than by the ZY expressions, while approaching light impurity region (figure 4.1b). The IAM $c^{(h_w^A)}_{H\ D}$ is approaching zero as expected, whereas the ZY $c^{(h_w^A)}_{H\ D}$ is still large ($\approx 0.4$). Note that according to (2.94) $c^{(h_w^A)}_{D\ imp} = 0$. The EMIM $c^{(h_w^A)}_{D\ imp}$ approaching zero and become small already for impurity heavier than He. The IAM coefficient is larger than the EMIM coefficient in the He-Ne region. Thus, the more accurate solution can be achieved for the mixtures with the middle mass impurities by setting $c^{(h_w^A)}_{\beta\alpha} = 0$ for $m_\alpha/m_\beta < 1$.

### 4.4.3 Thermal and friction forces

#### 4.4.3.1 Thermal force

For the TF and the FR expression, the additional vector moment $\overline{\mathbf{r}}_\alpha$ should be derived from (4.89)-(4.90). The derivation of the $\overline{\mathbf{r}}_\alpha$, as well as, the TF and the FR derivations are performed in appendix H. We note that (4.56) is used without changes. In contrast to the ZY expressions, the hot-tails of all species are taken into account. The main difference between the IAM and the EMIM is that the hot-tails are calculated according to the approximate expressions (4.94) and (H.3).

The TF is:

$$\mathbf{R}^T_\alpha = -\sum_\beta n_\beta \tilde{c}^{(R_T^A)}_{\alpha\beta} \widetilde{\nabla T_\beta}, \tag{4.106}$$

where:

$$\tilde{c}^{(R_T^A)}_{\alpha\beta} = \delta_{\alpha\beta} \sum_\gamma c^{(R_T^A)}_{\alpha\gamma} \frac{\overline{Z^2_\gamma} n_\gamma}{\overline{Z^2_\alpha} n_\alpha} - c^{(R_T^A)}_{\beta\alpha} \frac{\overline{Z^2_\alpha} n_\alpha}{\overline{Z^2_\beta} n_\beta}, \tag{4.107}$$

$$c^{(R_T^A)}_{\alpha\beta} = \frac{1}{\tilde{\Delta}_\alpha} \frac{25\sqrt{2}}{16} \left(\frac{\mu_{\alpha\beta}}{m_\alpha}\right)^{3/2} \left[\frac{3}{2}\left(1 + \frac{433\sqrt{2}}{360} Z^s_{11\alpha}\right) - \frac{1}{2}\frac{\mu_{\alpha\beta}}{m_\alpha}\left(1 + \frac{23\sqrt{2}}{8} Z^s_{9\alpha}\right)\right], \tag{4.108}$$

where Z-varibles can be found in appendix B and the $\tilde{\Delta}_\alpha$ is defined according to (4.97). The TF for each charge state can be found analytically, similarly to the approach, which is described in sub-subsection 4.3.3.3 and appendix E.2:

$$\mathbf{R}^T_{\alpha Z} = -I_{\alpha Z} \sum_\beta n_\beta \tilde{c}^{(R_T^A)}_{\alpha\beta} \widetilde{\nabla T_\beta} - n_\alpha I_{\alpha Z} c^{(R_T^B)}_\alpha \left(\frac{\overline{Z^2_\alpha}}{Z^2} \nabla T_{\alpha Z} - \widetilde{\nabla T_\alpha}\right), \tag{4.109}$$

where the coefficient $c_\alpha^{(R_T^B)}$ can be found in appendix E.2. Thus, the (4.109) is the analytical expression of the TF for the species $\alpha Z$.

The IAM TF transport coefficient should be close to the corresponding ZY one for $m_\alpha/m_\beta \to 0$. In this asymptotic case, $Z^s_{2\alpha} \approx Z^s_{8\alpha} \approx Z^s_{9\alpha} \approx Z^s_{11\alpha} \approx Z^*_\alpha$. Besides, $\tilde{c}^{(R_T^A)}_{\alpha\beta} = c^{(R_T^A)}_{\beta\alpha} \frac{\overline{Z^2_\alpha} n_\alpha}{\overline{Z^2_\beta} n_\beta} \approx 0 : \ \beta \neq \alpha$ and:

$$\tilde{c}^{(R_T^A)}_{\alpha\alpha} = \sum_\beta c^{(R_T^A)}_{\alpha\beta} \frac{\overline{Z^2_\beta} n_\beta}{\overline{Z^2_\alpha} n_\alpha} - c^{(R_T^A)}_{\alpha\alpha} = \sum_{\beta\neq\alpha} c^{(R_T^A)}_{\alpha\beta} \frac{\overline{Z^2_\beta} n_\beta}{\overline{Z^2_\alpha} n_\alpha} =$$
$$\frac{1}{\tilde{\Delta}_\alpha} \frac{25\sqrt{2}}{16} \left[ \frac{3}{2} Z^s_{2\alpha} \left( 1 + \frac{433\sqrt{2}}{360} Z^s_{11\alpha} \right) - \frac{1}{2} Z^s_{8\alpha} \left( 1 + \frac{23\sqrt{2}}{8} Z^s_{9\alpha} \right) \right] \approx$$
$$\frac{25\sqrt{2}}{16} \frac{1}{\Delta_\alpha} Z^*_\alpha \left( 1 + \frac{11\sqrt{2}}{30} Z^*_\alpha \right) \approx c^{(5)}_\kappa - 0.5 c^{(2)}_{\kappa\kappa} \frac{\overline{\tau}^{(Zh)}_\kappa}{\tau^{(Zh)}_{\kappa\kappa}}, \quad (4.110)$$

where $c^{(5)}_\kappa - 0.5 c^{(2)}_{\kappa\kappa} \frac{\overline{\tau}^{(Zh)}_\kappa}{\tau^{(Zh)}_{\kappa\kappa}}$ is defined according to (2.95).

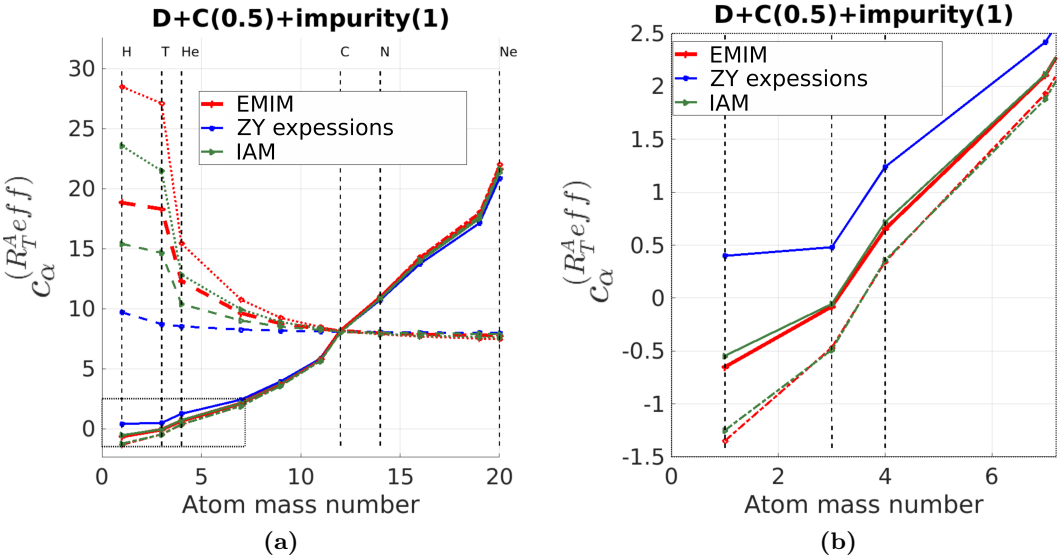


**Figure 4.2:** (a) The TF transport coefficient for another impurity (solid) and for carbon (dashed) using EMIM, the ZY expressions and the IAM for D+C+another impurity. Dash-dotted (another impurity) and dotted (carbon) lines are plotted for the case where $\widetilde{\nabla_\parallel T_\beta} = 2 \times \nabla_\parallel T_D : \beta \neq D$. (See the caption to figure 4.1a for additional information). (b) Zoom of the dotted box in (a).

The EMIM, the ZY expressions and the IAM can be compared also of the TF. The TF for C and another impurity, which summed over all charge states, can be studied. Similar to the heat flux, the $\widetilde{\nabla_\parallel T_\beta} = 2 \times \nabla_\parallel T_D : \beta \neq D$ case is also tested, to obtain the

contribution from the impurity temperature gradient to the TF. One can rewrite (4.109) in the form of:

$$R^T_{\alpha\|} = n_\alpha c_\alpha^{(R^A_T eff)} \nabla_\| T_D, \tag{4.111}$$

then the transport coefficient for $c_\alpha^{(R^A_T eff)}$ for C and another impurity, which is varied along the horizontal axis, is plotted in figures 4.2a, 4.2b.

For D plasmas with impurity heavier than C, the original ZY expressions results in a several percent deviation from the EMIM result. Moreover, in the region of heavy impurities, the impurity $\widetilde{\nabla_\| T_\beta} : \beta \neq D$ does not play a significant role (Figure 4.2a). The D hot-tail provides the largest contribution into the impurity TF. Thus, $\nabla_\| T_D$ is a major effect in such cases.

However, in the light impurity region the ZY results differs significantly from the EMIM ones, whereas the IAM results are closer to the EMIM ones. The analytical ZY expression results provides up to 15% deviation and up to 90% deviation for the D+C+Li and D+C+He mixtures, correspondingly (figure 4.2b) (for $\widetilde{\nabla_\| T_\beta} = \nabla_\| T_D : \beta \neq D$). If the temperature of the impurity is different, the deviation can be even larger. In contrast to the ZY approach, the IAM TF coefficients for the D+C+Li mixture are only 1% and 6% deviations with respect to the EMIM ones for Li (figure 4.2b) and for C (figure 4.2a), correspondingly. Even for the D+C+He mixture, the IAM TF is up to 10% and up to 16% different from the EMIM TF for the He (figure 4.2b) and the C (figure 4.2a) impurities, correspondingly. Thus, the IAM is suitable for the He impurity transport simulations, whereas the ZY expressions provides invalid results.

It is worth to mention that the change of the impurity $\widetilde{\nabla_\| T_\beta}$ is captured reasonably well by the IAM, because the impurity hot-tail, which is greatly affected by the $\widetilde{\nabla_\| T_\beta} : \beta \neq D$, is taken into account in the improved TF formulation. The IAM can be used for the multi-temperature models, for the cases where $T_{\alpha Z}$ are not sufficiently different for different species to change the the transport coefficients (the exact criteria is not dissused herein), and the $T_{av}$ can be used for those calculations, but the $\nabla_\| T_{\alpha Z}$ are different to change the hot-tails. If the temperatures are very different in the mixture, the complete multi-temperature models, like the one, which is discussed in [92, 99], should be used.

For the hydrogen (H) impurity, its hot-tail has a larger contribution into the TF than the D hot-tail, because of $m_D/m_H = 2$ ratio, which is expressed in (E.2). Thus, the IAM provides the qualitatively correct TF for the impurity, which is lighter than the main ion species. However, there are dozen percent differences with respect to the EMIM answers (figure 4.2a). For more accurate calculations in case of comparable masses, the EMIM is required. Evidently, the ZY expressions provide the incorrect sign for the $R^T_{H\|}$, because the contribution from the impurity hot-tail is neglected there.

#### 4.4.3.2 Friction force

The FR is derived identically as in appendix F.1:

$$\mathbf{R}_{\alpha}^{\mathbf{w}} = -n_{\alpha} \sum_{\beta} \frac{\mu_{\alpha\beta}}{\tau_{\alpha\beta}^{(Zh)}} c_{\beta\alpha}^{(R_w^A)} (\overline{\mathbf{w}}_{\alpha} - \overline{\mathbf{w}}_{\beta}) \tag{4.112}$$

where:

$$c_{\beta\alpha}^{(R_w^A)} = 1 + c_{\beta\alpha}^{(R_w^A 1)} + c_{\beta\alpha}^{(R_w^A 2)} + c_{\beta\alpha}^{(R_w^A 3)}. \tag{4.113}$$

$$c_{\beta\alpha}^{(R_w^A 1)} = -\sum_{\gamma\neq\alpha} \frac{\mu_{\alpha\gamma}}{m_{\alpha}} \sqrt{\frac{\mu_{\alpha\gamma}}{\mu_{\alpha\beta}}} \frac{\overline{Z_{\gamma}^2} n_{\gamma}}{\overline{Z_{\beta}^2} n_{\beta}} \Big[ \frac{3}{5} c_{\beta\alpha}^{(h_w^A)} - \frac{3}{14} \frac{\mu_{\alpha\gamma}}{m_{\alpha}} c_{\beta\alpha}^{(r_w^A)} \Big] \tag{4.114}$$

$$c_{\beta\alpha}^{(R_w^A 2)} = \sum_{\gamma\neq\alpha} \frac{\mu_{\alpha\gamma}}{m_{\gamma}} \sqrt{\frac{\mu_{\alpha\gamma}}{\mu_{\alpha\beta}}} \frac{\overline{Z_{\gamma}^2} n_{\gamma}}{\overline{Z_{\beta}^2} n_{\beta}} \Big[ \frac{3}{5} c_{\beta\gamma}^{(h_w^A)} - \frac{3}{14} \frac{\mu_{\alpha\gamma}}{m_{\gamma}} c_{\beta\gamma}^{(r_w^A)} \Big] \tag{4.115}$$

$$c_{\beta\alpha}^{(R_w^A 3)} = -\frac{\mu_{\alpha\beta}}{m_{\beta}} \sum_{\gamma} \Big[ \frac{3}{5} c_{\gamma\beta}^{(h_w^A)} - \frac{3}{14} \frac{\mu_{\alpha\beta}}{m_{\beta}} c_{\gamma\beta}^{(r_w^A)} \Big] \tag{4.116}$$

$c_{\beta\alpha}^{(h_w^A)}$ and $c_{\beta\alpha}^{(r_w^A)}$ in (4.114), (4.115) and (4.116) are expressed analytically according to (4.96) and (H.5).

The FR for each charge state can be found, similarly to the approach, which is described in sub-subsection 4.3.3.5 and appendix F.2:

$$\mathbf{R}_{\alpha Z}^{\mathbf{w}} = -n_{\alpha} I_{\alpha Z} \sum_{\beta} \frac{\mu_{\alpha\beta}}{\tau_{\alpha\beta}^{(Zh)}} c_{\beta\alpha}^{(R_w)} (\mathbf{w}_{\alpha Z} - \overline{\mathbf{w}}_{\beta}), \tag{4.117}$$

where

$$c_{\beta\alpha}^{(R_w)} = \delta_{\alpha\beta} \sum_{\gamma} \sqrt{\frac{\mu_{\alpha\gamma}}{\mu_{\alpha\beta}}} \frac{\overline{Z_{\gamma}^2} n_{\gamma}}{\overline{Z_{\beta}^2} n_{\beta}} [c_{\gamma\alpha}^{(R_w^B)} - c_{\gamma\alpha}^{(R_w^A)}] + c_{\beta\alpha}^{(R_w^A)}, \tag{4.118}$$

where the coefficient $c_{\beta\alpha}^{(R_w^B)}$ can be expressed analytically accoridng to (F.23) in appendix F.2. Thus, the (4.117) is the analytical expression for the FR for species $\alpha Z$.

The IAM FR transport coefficient should be close to the corresponding ZY one for $m_{\alpha}/m_{\beta} \to 0$. In this asymptotic case, $Z_{2\alpha}^s \approx Z_{5\alpha}^s \approx Z_{8\alpha}^s \approx Z_{9\alpha}^s \approx Z_{11\alpha}^s \approx Z_{\alpha}^*$. Besides, for $\beta \neq \alpha$ the $c_{\beta\alpha}^{(R_w^A 2)} \approx 0$ and $c_{\beta\alpha}^{(R_w^A 3)} \approx 0$ and:

$$c_{\beta\alpha}^{(R_w^A)} \approx 1 + c_{\beta\alpha}^{(R_w^A 1)} = 1 - \sum_{\gamma\neq\alpha} \frac{\mu_{\alpha\gamma}}{m_\alpha} \sqrt{\frac{\mu_{\alpha\gamma}}{\mu_{\alpha\beta}} \frac{\overline{Z_\gamma^2} n_\gamma}{\overline{Z_\beta^2} n_\beta}} \left[ \frac{3}{5} c_{\beta\alpha}^{(h_w^A)} - \frac{3}{14} \frac{\mu_{\alpha\gamma}}{m_\alpha} c_{\beta\alpha}^{(r_w^A)} \right] =$$

$$1 - \frac{1}{\tilde{\Delta}_\alpha} \frac{\mu_{\alpha\beta}}{m_\alpha} \left[ \frac{15\sqrt{2}}{16} \left( \frac{3}{2} + \frac{433\sqrt{2}}{240} Z_{11\alpha}^s - \frac{1}{2} \frac{\mu_{\alpha\beta}}{m_\alpha} \left( 1 + \frac{23\sqrt{2}}{8} Z_{9\alpha}^s \right) \right) \sum_{\gamma\neq\alpha} \frac{\mu_{\alpha\gamma}}{m_\alpha} \sqrt{\frac{\mu_{\alpha\gamma}}{m_\alpha} \frac{\overline{Z_\gamma^2} n_\gamma}{\overline{Z_\alpha^2} n_\alpha}} \right.$$

$$\left. + \frac{5\sqrt{2}}{16} \left( \frac{5}{2} \frac{\mu_{\alpha\beta}}{m_\alpha} - \frac{3}{2} + \frac{65\sqrt{2}}{16} \frac{\mu_{\alpha\beta}}{m_\alpha} Z_{5\alpha}^s - \frac{69\sqrt{2}}{16} Z_{9\alpha}^s \right) \sum_{\gamma\neq\alpha} \left( \frac{\mu_{\alpha\gamma}}{m_\alpha} \right)^2 \sqrt{\frac{\mu_{\alpha\gamma}}{m_\alpha} \frac{\overline{Z_\gamma^2} n_\gamma}{\overline{Z_\alpha^2} n_\alpha}} \right] \approx$$

$$\frac{1}{\Delta_\alpha} \left( \frac{2}{9} Z_\alpha^{*2} + \frac{61\sqrt{2}}{72} Z_\alpha^* + 1 \right) \approx c_{\beta\alpha}^{(1)} \quad (4.119)$$

where $c_{\beta\alpha}^{(1)}$ is defined according to (2.94).

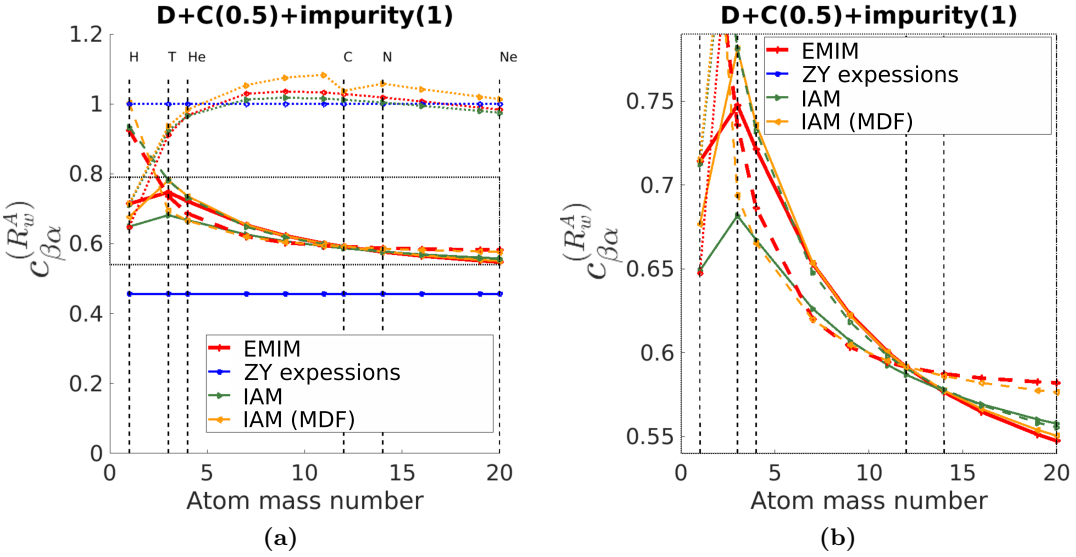


**Figure 4.3:** (a) The FR transport coefficient for another impurity/D (solid), for C/D (dashed) and for another impurity/C (dotted) using the EMIM, the ZY experssions, the IAM and the IAM (MDF) for the D + C + another impurity case. (See the caption to figure 4.1a for additional information). (b) Zoom of the dotted box in (a).

The EMIM, the ZY expressions, the IAM are tested for the FR in the D + C + another impurity cases. In figures 4.3a and 4.3b the $c_{\beta\alpha}^{(R_w^A)}$, which is used in (4.112), is plotted. The ZY expressions underestimate significantly the FR with respect to the EMIM: 37% for He/D, 23 % for C/D, 17% for Ne/D.

The ZY FR is reduced with respect to the FR in quasihydrodynamic approximation, because the collisions in case of the flow velocity difference between D and impurities form the tail of the D distribution function, which is expressed in terms of $\mathbf{h}_D^{\mathbf{w}}$ (and $\mathbf{r}_D^{\mathbf{w}}$),

as a result of the solution of the 3-order and 5-order vector moment equations (4.41)-(4.42). The D tail leads to the $c_{\beta D}^{(R_w^A)} < 1 : \ \beta \neq D$ (blue solid line in figure 4.3a). There are three main factors, which makes the EMIM $c_{\beta D}^{(R_w^A)} : \ \beta \neq D$ larger then the ZY one (figure 4.3a). 1) According to (F.3), the $\mathbf{h}_D^{\mathbf{w}}$ and $\mathbf{r}_D^{\mathbf{w}}$ contributions into the FR is factored by $\mu_{D\beta}/m_D$ and $(\mu_{D\beta}/m_D)^2 : \ \beta \neq D$, correspondingly, whereas in the ZY approach the $\mu_{D\beta}/m_D \approx 1$ is assumed. 2) The D tail is smaller, if the D species is not infinitely lighter than impurity species (for $\mathbf{h}_D^{\mathbf{w}}$ it can be seen in figure 4.1b). 3) the contribution from the impurity tail into the FR is not taken account in the ZY expressions. The impurity hot tail compensate the FR reduction effect from the D tail (F.3), making the FR larger.

In the IAM, the $\mu_{D\beta}/m_D : \ \beta \neq D$ factors and the impurity $\overline{\mathbf{h}}_\beta^{\mathbf{w}}$ and $\overline{\mathbf{r}}_\beta^{\mathbf{w}}$ are taken into account. Besides, the The D tail is calculated more accurately by the IAM than by the ZY expressions (figure 4.1b). As a result, the IAM and the EMIM FR are close to each other (figure 4.3b). As it is discussed in subsection 4.4.2, the heat fluxes (and additional vector moments) can be obtained more accurately, if $c_{\beta\alpha}^{(h_w^A)}$ and $c_{\beta\alpha}^{(r_w^A)} : m_\beta < m_\alpha$ can be set to zero, instead of deriving them by IAM. This leads to the more accurate $c_{\beta\alpha}^{(R_w^A)}$ calculation. The FR becomes even closer to the EMIM result: improved analytical method, where the $c_{\beta\alpha}^{(h_w^A)}$ and $c_{\beta\alpha}^{(r_w^A)} : m_\beta < m_\alpha$ are set to zero (IAM (MDF)) in figures 4.3a and 4.3b.

Also, the impurity-impurity FR are plotted as dotted lines in figure 4.3a. Since, the FR coefficients for the impurity-impurity interaction was not presented by the ZY, the quasihydrodynamic FR could be used instead. The IAM provides closer to the EMIM coefficient, when the mass difference between impurities becomes large (H-T range for another impurity in figure 4.3a), than the quasihydrodynamic coefficient $c_{\beta\alpha}^{(R_w^A)} = 1$.

### 4.4.4 Viscous-stress tensor

Similar, to the rank-1 equations (subsection 4.4.2), the cross terms, which depend on the $\overline{\pi}_{\beta rs}$ and $\overline{\sigma}_{\beta rs}$ for $\beta \neq \alpha$, are neglected in the rank-2 equations (4.66) and (4.67) (details one can find in appendix I). As a result, the viscous-stress tensor, which is averaged over the charge states , is expressed as:

$$\overline{\pi}_{\alpha rs} = -\frac{m_\alpha n_\alpha}{\lambda_{\alpha\alpha}} c_\alpha^{(\pi_u^A)} p_\alpha \widetilde{W_{rs}^{u_\alpha}} - \frac{m_\alpha n_\alpha}{\lambda_{\alpha\alpha}} c_\alpha^{(\pi_h^A)} W_{rs}^{\overline{h}_\alpha}, \tag{4.120}$$

where coefficients are:

$$c_\alpha^{(\pi_u^A)} = \frac{1025}{1068} \frac{1}{\Delta_\alpha^\pi} \left(1 + \frac{204\sqrt{2}}{205} Z_{22\alpha}^\pi\right), \tag{4.121}$$

$$c_\alpha^{(\pi_h^A)} = \frac{1655}{1068}\frac{1}{\Delta_\alpha^\pi}\left(1 + \frac{204\sqrt{2}}{331}Z_{22\alpha}^\pi + \frac{252\sqrt{2}}{331}Z_{12\alpha}^\pi\right), \tag{4.122}$$

$$\Delta_\alpha^\pi = \frac{204}{89}Z_{11\alpha}^\pi Z_{22\alpha}^\pi - \frac{108}{89}{Z_{12\alpha}^\pi}^2 + \frac{205\sqrt{2}}{178}Z_{11\alpha}^\pi + \frac{102\sqrt{2}}{89}Z_{22\alpha}^\pi - \frac{54\sqrt{2}}{89}Z_{12\alpha}^\pi + 1, \tag{4.123}$$

The viscous-stress tensor (4.120) can be written in the form of (4.72), if the transport coefficients are written as:

$$\check{c}_{\alpha\beta}^{(\pi_u^A)} = 2c_\alpha^{(\pi_u^A)}\delta_{\alpha\beta}, \quad \check{c}_{\alpha\beta}^{(\pi_h^A)} = 2c_\alpha^{(\pi_h^A)}\delta_{\alpha\beta}. \tag{4.124}$$

Evidently, the analytical charge-state corrections can be applied identically, as it is performed in sub-subsection 4.3.4.3 and appendix G.2, to obtain an explicit representation of the stress-viscuos tensor for the each charge state:

$$\pi_{\alpha Zrs} = \pi^u_{\alpha Zrs} + \pi^h_{\alpha Zrs} \tag{4.125}$$

$$\pi^u_{\alpha Zrs} = -p_{\alpha Z}\sum_\beta \check{c}_{\alpha\beta}^{(\pi_u^A)}\tau_{\alpha\beta}^{(Zh)}\frac{n_\beta}{n_\alpha}\widetilde{W_{rs}^{u_\beta}} - 2p_{\alpha Z}c_\alpha^{(\pi_u^B)}\tau_{\alpha\alpha}^{(Zh)}\left(\frac{\overline{Z_\alpha^2}}{Z^2}W_{rs}^{u_{\alpha Z}} - \widetilde{W_{rs}^{u_\alpha}}\right) \tag{4.126}$$

$$\pi^h_{\alpha Zrs} = -p_{\alpha Z}\sum_\beta \check{c}_{\alpha\beta}^{(\pi_h^A)}\tau_{\alpha\beta}^{(Zh)}\frac{1}{p_\alpha}W_{rs}^{\bar{h}_\beta} - 2p_{\alpha Z}c_\alpha^{(\pi_h^B)}\tau_{\alpha\alpha}^{(Zh)}\left(\frac{\overline{Z_\alpha^2}}{Z^2}\frac{1}{p_{\alpha Z}}W_{rs}^{h_{\alpha Z}} - \frac{1}{p_\alpha}W_{rs}^{\bar{h}_\alpha}\right) \tag{4.127}$$

The IAM strain viscosity coefficient $c_\alpha^{(\pi_u^A)}$ should asymptotically match the ZY one. Let us consider the $m_\alpha/m_\beta \to 0$ limit. The $Z_{c\alpha}^* = Z_{11\alpha}^\pi = Z_{12\alpha}^\pi = Z_{22\alpha}^\pi = Z_\alpha^*$ and:

$$\Delta_\alpha^\pi \approx \frac{96}{89}{Z_\alpha^*}^2 + \frac{301\sqrt{2}}{178}Z_\alpha^* + 1. \tag{4.128}$$

The strain viscosity coefficient turns into:

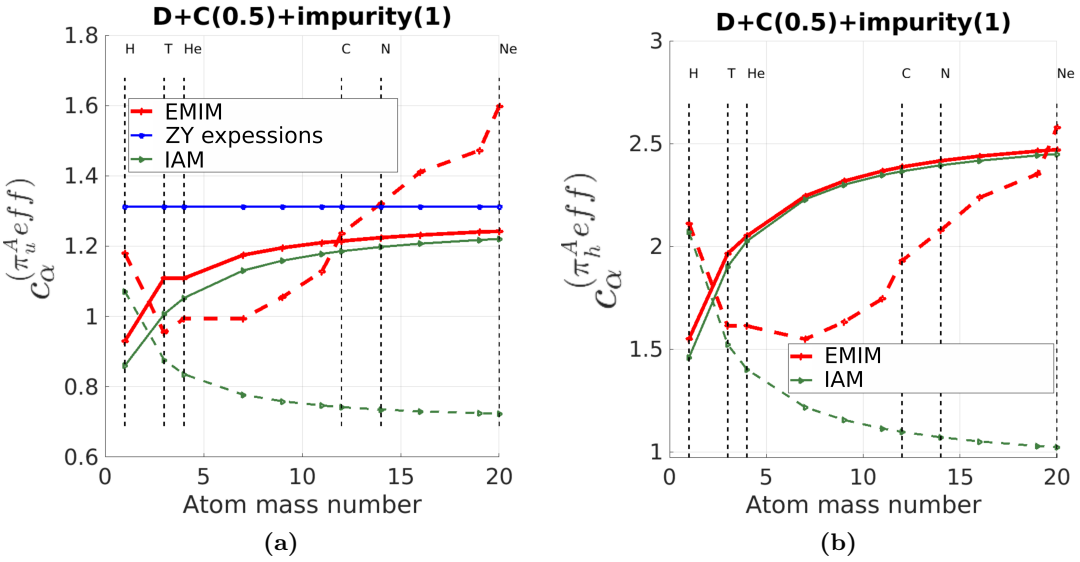


**Figure 4.4:** (a) The effective strain viscosity coefficient for D (solid) and for another impurity (dashed) using the EMIM, the ZY experssions and the IAM for the D + C + another impurity case. (b) The effective heat stress coefficient D (solid) and for another impurity (dashed) using the EMIM and the IAM for the D + C + another impurity case. (See the caption to figure 4.1a for additional information).

$$\frac{m_\alpha}{\tau_\alpha^{(Zh)}}\frac{n_\alpha}{\lambda_{\alpha\alpha}}c_\alpha^{(\pi_u^A)} = (1+\sqrt{2}Z_{c\alpha}^*)c_\alpha^{(\pi_u^A)} \approx \frac{1025}{1068}\frac{(1+\sqrt{2}Z_\alpha^*)(1+\frac{204\sqrt{2}}{205}Z_\alpha^*)}{\frac{96}{89}Z_\alpha^{*2}+\frac{301\sqrt{2}}{178}Z_\alpha^*+1} \approx \left(c_\kappa + 0.5c_{\kappa\kappa}\frac{\overline{\tau}_\kappa^{(Zh)}}{\tau_{\kappa\kappa}^{(Zh)}}\right), \quad (4.129)$$

where $\left(c_\kappa + 0.5c_{\kappa\kappa}\frac{\overline{\tau}_\kappa^{(Zh)}}{\tau_{\kappa\kappa}^{(Zh)}}\right)$ is defined according to (2.97).

The viscous-stress tensor is tested for the D + C + another impurity case. The EMIM, the ZY expressions and the IAM are compared. For this test we assume $\forall\alpha,\beta$ : $\widetilde{W_{rs}^{u_\alpha}} = \widetilde{W_{rs}^{u_\beta}}$ and $W_{rs}^{\bar{h}_\beta}/n_\beta = W_{rs}^{\bar{h}_\alpha}/n_\alpha$. Then, the (4.72) can be re-written as following:

$$\overline{\pi}_{\alpha rs} = -p_\alpha\tau_\alpha^{(Zh)}c_\alpha^{(\pi_u^A eff)}\widetilde{W_{rs}^{u_\alpha}} - \tau_\alpha^{(Zh)}c_\alpha^{(\pi_h^A eff)}W_{rs}^{\bar{h}_\alpha}, \quad (4.130)$$

where the coefficients $c_\alpha^{(\pi_u^A eff)}$, $c_\alpha^{(\pi_h^A eff)}$ are plotted in figures 4.4a and 4.4b, correspondingly. For D, in case of presence of the light or middle mass impurities, the ZY expressions provide significantly larger $c_\alpha^{(\pi_u^A eff)}$ than the EMIM, whereas the IAM shows reasonable match with the EMIM (figure 4.4a). Thus, the mass ratio between main ions and impurities cannot be assumed infinitely large for the considered range of impurity

masses. The D heat stress coefficients $c_\alpha^{(\pi_h^A eff)}$, which are calculated using the IAM and the EMIM, are found close for both methods (figure 4.4b). The heat stress were not considered in ZY analytical method, as well as, in the original set of rank-2 equations (2.68)-(2.69). For the case $m_D/m_{imp} \approx 1$ and $n_{imp}/n_D \approx 1$, the IAM provides smaller (close, within 10%) than the EMIM viscous-stress coefficients $c_\alpha^{(\pi_u^A eff)}$, $c_\alpha^{(\pi_h^A eff)}$. However, for the heavy impurity the viscous-stress tensor is captured only qualitatively, as expected. Nonetheless, the heavy impurity viscous-stress tensor, in the considered impurity concentrations, does not contribute significantly into the $\pi_{rs}$, which is usually of interest.

## 4.5 Conclusions according to the improvements of the Zhdanov closure

This chapter focuses on the advancements made in the Zhdanov closure. In section 4.1, we derived the corresponding relations between Braginskii and Zhdanov moments, such as $T_{\alpha Z}$ (4.17), $\mathbf{h}_{\alpha Z}$ (4.18), $\pi_{\alpha Z rs}$ (4.19) and r.h.s.'s of the momentum (4.22) and the heat (4.20) equations. These relations are crucial for implementing the Zhdanov closure in Braginskii equation-based codes such as SOLPS-ITER (section 3.3) and GRILLIX (section 3.4). While the corrections to the moments (4.17), (4.18) and (4.19) are typically small under collisional conditions, the r.h.s. relations (4.20) and (4.22) play a vital role in ensuring energy and momentum balances during collisions.

To account for heat stresses in the Zhdanov closure, we utilized the general rank-2 moment equation (section 4.2). While Zhdanov neglected heat stresses for 21N-moment approximation (chapter 8 in [18]) in comparison with the strain stresses, this assumption is valid only when considering temperature and flow velocity changes of the order of: $\Delta T \sim T$ and $\Delta V_\parallel \sim \sqrt{T/m}$. As discussed in subsection (2.4.3), heat stresses are of equal importance as strain stresses on closed flux surfaces, particularly in the collisional Pfirsch-Schlüter regime [81]. Therefore, this thesis focuses on obtaining the multi-species heat stresses.

In section 4.3, we derive the complete closure for averaged quantities over charge states (heat flux, TF, FR, stress-viscous tensor) and the analytical corrections for the each charge state, considering mistake corrections in the Zhdanov monograph (appendix A). These quantities are expressed in terms of transport coefficients using the Zhdanov ansatz, resulting in systems of algebraic equations for the rank-1 (4.43)-(4.44) and rank-2 (4.66)-(4.67) moments. Consequently, the transport coefficients are expressed through elements of inverse matrices, where the original matrices represent the system of algebraic equations.

Finally, in section 4.4, we present improved versions of the ZY expressions. Unlike the ZY expressions, which are only applicable for impurities with much larger masses than the main ion, the IAM provides accurate expressions for a wide range of impurities including He-Ne in D plasmas. Also, the IAM also qualitatively describes mixtures of species with similar masses, which is not always the case of the ZY expressions (e.g. the

ZY TF). Moreover, the IAM can be applied to light main species with multiple charge states (e.g. He plasmas with impurities), while ZY expressions are limited to a single charge state for main ion species. The IAM successfully describes the heat flux for heavy impurities, where ZY analytical ansatz fails (e.g. in the trace-impurity case), resulting in a heat conductivity proportional to $\propto \tau^{(Zh)}_{imp\ imp}$. The IAM provides a qualitatively correct heat conductivity for heavy trace impurities: $\propto \tau^{(Zh)}_{imp\ main}$.

It is important to note that we utilized the IAM to test and analyze the implementation of the EMIM. The results obtained from the EMIM and the IAM closely match asymptotically. When discrepancies occur between the IAM and the EMIM results, we investigate the contributions from non-diagonal matrix elements. Thus, apart from its own value, the IAM proves to be valuable for testing the full implementation of the Zhdanov closure.

# 5 Multi-ion closure for the fluid codes

By employing the Zhdanov closure and the advancements presented in chapter 4, it becomes feasible to achieve a complete multi-ion generalization of the fluid edge codes. This significant development offers the capability to model a wide range of plasma mixtures, including those with ions of close masses and non-trace concentrations, such as D+T+He+impurities. The improvements made to the SOLPS-ITER and GRILLIX models utilizing the Zhdanov closure are thoroughly discussed in this chapter.

## 5.1 SOLPS-ITER

### 5.1.1 General remarks

The Zhdanov closure has been fully implemented into the SOLPS-ITER code by means of the Zhdanov-Grad (ZG) module (Grad-Zhdanov module in [85, 91]). Both the EMIM and the IAM are available for ion transport coefficients. Using the ZG module, the complete multi-ion generalisation of the SOLPS-ITER code has been performed, i.e. all explicit separations between main ions and impurities (all if main ion conditions) have been removed. Fluid equations have been written uniformly for all ion species. Thus, the difference in the behaviour between ion species are defined explicitly according to those densities, masses and charges.

The electron transport coefficients are obtained according to Eq. (8.2.8) in [18] or (2.94)-(2.98). This were performed previously in the SOLPS-ITER code (partly in [80]). We only recall in appendix J.1 the relation between the SOLPS-ITER electron transport coefficients and the Eq. (8.2.8) in [18].

The ion transport coefficients, which are calculated using the ZG module, are discussed further. The ion-electron equations separation procedure, which was proposed by Zhdanov on page 181 in [18], can be applied to solve ion equation without electron contribution. Thus, the subscript $\alpha$ represents different ion species types.

### 5.1.2 Ion parallel heat flux

We have implemented the velocity-dependent part of the heat flux in the subsection, which was previously not accounted for in the SOLPS-ITER code. We also performed a comparison between the 3.0.7 version and the updated ion heat conductivity formulations. Although the difference between the old and improved calculations for realistic plasma mixtures is within approximately 5%, the significance lies in the fact that the ion heat transport is now calculated self-consistently with the other closure terms.

Previously the parallel ion heat conductivity was written based on the simple multi-ion extension of the Braginskii heat conductivity (3.57) with the fixed factor 3.9. The $\tau_a^{(Br)}$ (3.17) is only correct for the light main ion species, whereas the $\tau_a^{(Br)}$ is incorrect for the heavy impurity ion species. Fortunately, impurities usually do not contribute significantly into the global heat transport. In the ZG module, the $T_i$=$T_{\alpha Z}$: $\forall\alpha,\ Z$ is assumed for the heat flux. The improved SOLPS-ITER ion heat conductivity is derived by summing the (4.52) over $\alpha Z$:

$$\kappa_{\alpha Z x}^{(CL)} = b_x^2 \left[ \frac{n_{\alpha Z}}{n_\alpha} \sum_\beta \kappa_{\alpha\beta}^{(h_T^A)} + \frac{n_{\alpha Z}}{n_\alpha} \kappa_\alpha^{(h_T^B)} \left( \frac{\overline{Z_\alpha^2}}{Z^2} - 1 \right) \right], \tag{5.1}$$

$$\kappa_{\alpha x}^{(CL)} = \sum_Z \kappa_{\alpha Z}^{(CL)} = b_x^2 \left[ \sum_\beta \kappa_{\alpha\beta}^{(h_T^A)} + \kappa_\alpha^{(h_T^B)} \left( \sum_Z \frac{\overline{Z_\alpha^2}}{Z^2} \frac{n_{\alpha Z}}{n_\alpha} - 1 \right) \right], \tag{5.2}$$

$$\kappa_{ix}^{(CL)} = \sum_\alpha \kappa_{\alpha x}^{(CL)} = b_x^2 \sum_\alpha \left[ \sum_\beta \kappa_{\alpha\beta}^{(h_T^A)} + \kappa_\alpha^{(h_T^B)} \left( \sum_Z \frac{\overline{Z_\alpha^2}}{Z^2} \frac{n_{\alpha Z}}{n_\alpha} - 1 \right) \right]. \tag{5.3}$$

This conductivity (5.3) replaces the (3.57), when the ZG module is activated. One can compare the EMIM heat conductivity ($\kappa_{ix}^{(CL)} = c_{Calc}^{eff}$ in figure 5.1) and the old form (3.57) ($\kappa_{ix}^{(CL)} = c_{SOLPS}^{eff}$ in figure 5.1).

It is important to emphasise that the heat flux, which is the result of the distribution function tail formation, due to the flow velocity difference between different ions, is not derived in the single ion Braginskii closure [17]. Therefore, this contribution to the heat transport was not previously considered in the SOLPS-ITER code. This part of the heat flux can give an appreciable contribution when in the case of non-trace impurity case. Thus, the flow velocity dependent part of the heat flux:

$$\frac{\sqrt{g}}{h_x} h_{ix}^V = \frac{\sqrt{g}}{h_x} b_x T_i \sum_{\alpha Z} n_{\alpha Z} \sum_\beta c_{\beta\alpha}^{(h_w)} (w_{\alpha Z\parallel} - \overline{w}_{\beta\parallel}), \tag{5.4}$$

is added into the ion poloidal heat flux (3.52). The improved versions of the ion and electron heat balance sources are expressed in appendix J.2.

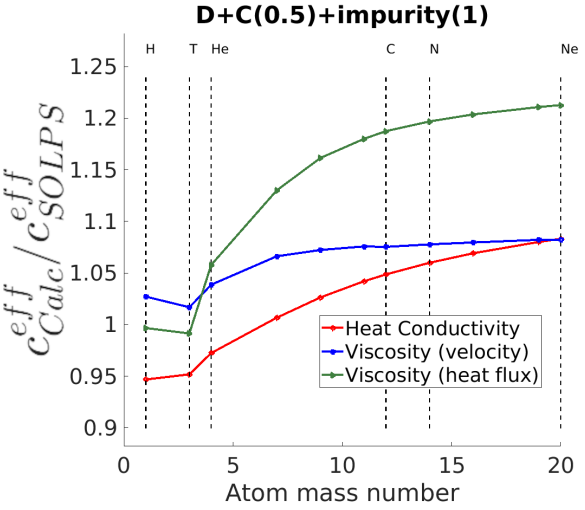


**Figure 5.1:** The ratio between the total ion heat conductivities, the total ion viscosity coefficients (velocity and heat flux dependent viscous-stress tensors), which are calculate using EMIM $c^{eff}_{Calc}$, and which are calcuated using 3.0.7 SOLPS-ITER formulation $c^{eff}_{SOLPS}$, for the D + C + another impurity case. (See the caption to figure 4.1a for additional information).

### 5.1.3 Ion thermal and friction forces

We have successfully implemented new formulations of the TF and FR. To evaluate the effectiveness of these new formulations, a detailed comparison with the previous 3.0.7 formulations (Zhdanov-Yushmanov expressions) is conducted in subsection 4.4.3. This comparison is crucial in validating the improvements and assessing the impact of the updated formulations on the overall performance of the model.

Using (4.60), the original 3.0.7 SOLPS-ITER TF (3.25) is replaced by:

$$S^m_{Therm,ia} = [a \to \alpha Z, \text{ then } a(\alpha, Z)] = R^T_{\alpha Z\|} = \\ - I_{\alpha Z} \sum_\beta n_\beta \tilde{c}^{(R^A_T)}_{\alpha\beta} b_x \frac{\widetilde{\partial T_\beta}}{h_x \partial x} - n_\alpha c^{(R^B_T)}_\alpha \left( \frac{n_{\alpha Z}}{n_\alpha} b_x \frac{\partial T_{\alpha Z}}{h_x \partial x} - I_{\alpha Z} b_x \frac{\widetilde{\partial T_\alpha}}{h_x \partial x} \right). \quad (5.5)$$

Temperature gradients are kept different, using (4.17) relation:

$$\frac{\widetilde{\partial T_\alpha}}{h_x \partial x} = \sum_Z \frac{n_{\alpha Z}}{n_\alpha} \frac{\partial T_{\alpha Z}}{h_x \partial x}, \quad T_{\alpha Z} = T_i + \frac{1}{3} m_\alpha \mathbf{w}^2_{\alpha Z}. \quad (5.6)$$

The $\mathbf{w}^2_{\alpha Z}$ contribution is usually small (quadratic term according to Zhdanov ordering), sometimes it is convenient to assume $T_{\alpha Z} \approx T_i$. In this case one can write:

$$S^m_{Therm,ia} = [a \to \alpha Z, \text{ then } a(\alpha, Z)] =$$
$$R^T_{\alpha Z\|} = -I_{\alpha Z}\left[\sum_\beta n_\beta \tilde{c}^{(R^A_T)}_{\alpha\beta} + n_\alpha c^{(R^B_T)}_\alpha \left(\frac{\overline{Z^2_\alpha}}{\overline{Z^2}} - 1\right)\right] b_x \frac{\partial T_i}{h_x \partial x}. \quad (5.7)$$

Using (4.63), the original 3.0.7 SOLPS-ITER FR (3.26) is replaced by:

$$S^m_{fr,ia} = [a \to \alpha Z] = R^{\mathbf{w}}_{\alpha Z\|} = -n_\alpha I_{\alpha Z} \sum_\beta \frac{\mu_{\alpha\beta}}{\tau^{(Zh)}_{\alpha\beta}} c^{(R_w)}_{\beta\alpha}(w_{\alpha Z\|} - \overline{w}_{\beta\|}). \quad (5.8)$$

The 3.0.7 SOLPS-ITER TF and FR were based on the ZY expressions. Thus, in figures 4.2a and 4.3a, the corresponding comparisons between the 3.0.7 SOLPS-ITER and the ZG module TF and FR formulations are performed.

### 5.1.4 Ion viscous-stress tensor divergence

Additionally, we conducted a comprehensive comparison between the 3.0.7 version and the newly updated viscous-stress formulations. The results reveal that the difference in the total plasma viscosity between the old and improved calculations, for realistic plasma mixtures, is within approximately 20% (as depicted in figure 5.1). However, it is important to highlight that the implementation of the ZG formulation is crucial for achieving a consistent multi-ion generalization of the code for subsequent D-T plasmas application.

One can take the divergence of the viscous-stress tensor (4.73) in the SOLPS-ITER geometry (3.1) similarly, as it was done in [88, 83]:

$$(\nabla \cdot \overleftrightarrow{\pi}^u_{\alpha Z})_\| = -\frac{4}{3} b_x B^{3/2} \frac{\partial}{h_x \partial x}\left[\frac{b_x}{B^2}\frac{n_{\alpha Z}}{n_\alpha}\left[\sum_\beta \check{c}^{(\pi^A_u)}_{\alpha\beta}\tau^{(Zh)}_{\alpha\beta}\sum_\zeta p_{\beta\zeta}\frac{\partial}{h_x\partial x}\left(\frac{\sqrt{B}}{b_x}u_{\beta\zeta x}\right) + \right.\right.$$
$$\left.\left. 2c^{(\pi^B_u)}_\alpha \tau^{(Zh)}_{\alpha\alpha}\left(\frac{\overline{Z^2_\alpha}}{Z^2}p_\alpha \frac{\partial}{h_x\partial x}\left(\frac{\sqrt{B}}{b_x}u_{\alpha Z x}\right) - \sum_\zeta p_{\alpha\zeta}\frac{\partial}{h_x\partial x}\left(\frac{\sqrt{B}}{b_x}u_{\alpha\zeta x}\right)\right)\right]\right] \quad (5.9)$$

$$(\nabla \cdot \overleftrightarrow{\pi}^h_{\alpha Z})_\| = -\frac{8}{15} b_x B^{3/2} \frac{\partial}{h_x \partial x}\left[\frac{b_x}{B^2}\frac{n_{\alpha Z}}{n_\alpha}\left[\sum_\beta \left(\check{c}^{(\pi^A_h)}_{\alpha\beta}\tau^{(Zh)}_{\alpha\beta}\frac{\partial}{h_x\partial x}\left(\frac{\sqrt{B}}{b_x}\overline{h}^*_{\beta x}\right)\right) + \right.\right.$$
$$\left.\left. 2c^{(\pi^B_h)}_\alpha \tau^{(Zh)}_{\alpha\alpha}\left(\frac{\overline{Z^2_\alpha} n_\alpha}{Z^2 n_{\alpha Z}}\frac{\partial}{h_x\partial x}\left(\frac{\sqrt{B}}{b_x}h_{\alpha Z x}\right) - \frac{\partial}{h_x\partial x}\left(\frac{\sqrt{B}}{b_x}\overline{h}^*_{\alpha x}\right)\right)\right]\right] \quad (5.10)$$

Note that (5.9) and (5.10) turns into the Eq. (44) in [84], if $u_{\alpha Zr} \approx u_r$ is assumed. Further in the thesis, the general case is considered, where the $u_{\alpha Zr}$ are kept in (5.9).

In contrast to [83], the contributions from the $\mathbf{E}\times\mathbf{B}$ and diamagnetic velocities into the poloidal velocity $V_{ax}$ in the parts of the viscous-stress tensor divergence (3.9) and (3.14) are neglected. For the (5.9) implementation into SOLPS-ITER code, only the parallel component of velocity is kept, following the original code structure. The $\mathbf{E}\times\mathbf{B}$ and diamagnetic velocities contributions can be added as additional terms later.

One can extract the terms with $u_{\alpha Z\|}$ dependence in (5.9) to solve implicitly the parallel momentum transport for species $\alpha Z$ (details can be found appendix J.3). Splitting into the divergence and source parts (appendix J.3) and using SOLPS-ITER notation ($u_{\alpha Z\|} \to V_{\|a}$), the (5.9) and (5.10) can be written in terms of momentum fluxes (similar to (3.9)):

$$\Gamma^m_{ax} = \begin{cases} m_a V_{\|a}\Gamma^{Cor}_{ax} + \frac{4}{3}\eta^{(CL)}_{ax}\frac{\partial \ln h_z}{h_x\partial x}V_{\|a} - \eta_{ax}\frac{\partial V_{\|a}}{h_x\partial x}, & z_a \neq 0 \\ m_a V_{\|a}\Gamma^{Cor}_{ax} - \eta_{ax}\frac{\partial V_{\|a}}{h_x\partial x}, & z_a = 0 \end{cases}, \tag{5.11}$$

where the coefficient $\eta^{(CL)}_{\alpha Zx}$ is defined as following:

$$\eta^{(CL)}_{ax} = [a \to \alpha Z] = \eta^{(CL)}_{\alpha Zx} = \left[\frac{\eta^{(u_iA)}_{\alpha\alpha x}}{p_\alpha} + \frac{\eta^{(u_iB)}_{\alpha x}}{p_\alpha}\left(\frac{1}{I_{\alpha Z}} - 1\right)\right]\frac{n_{\alpha Z}}{n_\alpha}p_{\alpha Z}, \tag{5.12}$$

where $\frac{\eta^{(u_iA)}_{\alpha\beta x}}{p_\alpha}$ and $\frac{\eta^{(u_iB)}_{\alpha x}}{p_\alpha}$ are defined as following:

$$\frac{\eta^{(u_iA)}_{\alpha\beta x}}{p_\alpha} = b_x^2\frac{\eta^{(u_iA)}_{\alpha\beta}}{p_\alpha}; \quad \frac{\eta^{(u_iA)}_{\alpha\beta}}{p_\alpha} = \check{c}^{(\pi^A_u)}_{\alpha\beta}\tau^{(Zh)}_{\alpha\beta}; \quad \frac{\eta^{(u_iB)}_{\alpha x}}{p_\alpha} = b_x^2\frac{\eta^{(u_iB)}_{\alpha}}{p_\alpha}; \quad \frac{\eta^{(u_iB)}_{\alpha}}{p_\alpha} = 2c^{(\pi^B_u)}_{\alpha}\tau^{(Zh)}_{\alpha\alpha}, \tag{5.13}$$

and sources (similar to (3.13)):

$$S^m_{a\|} = -\left(\nabla\cdot\overleftrightarrow{\pi}^{\|}_a\right)_\| = \begin{cases} -\left(\nabla\cdot\overleftrightarrow{\pi}^{V_\|}_a\right)^{res}_\| - \left(\nabla\cdot\overleftrightarrow{\pi}^{V_\|}_a\right)^{ai}_\| - \left(\nabla\cdot\overleftrightarrow{\pi}^{h_i}_a\right)_\|, & z_a \neq 0 \\ 0, & z_a = 0 \end{cases} \tag{5.14}$$

$$\left(\nabla\cdot\overleftrightarrow{\pi}^{V_\|}_a\right)^{res}_\| = -\frac{1}{h_z\sqrt{g}}\frac{\partial}{\partial x}\left(\frac{h_z\sqrt{g}}{h_x}\frac{4}{3}\eta^{(CL)}_{ax}\frac{\partial \ln\left(h_z B^{\frac{1}{2}}\right)}{B^{\frac{1}{2}}h_x\partial x}\right)B^{\frac{1}{2}}V_{\|a} \tag{5.15}$$

$$\left(\nabla\cdot\overleftrightarrow{\pi}_a^{V_\parallel}\right)_\parallel^{ai} = [a\to\alpha Z] = \\ -\frac{4}{3}b_x B^{3/2}\frac{\partial}{h_x\partial x}\left[\frac{1}{B^2 b_x}\frac{n_{\alpha Z}}{n_\alpha}\left[\sum_{\beta\neq\alpha}\frac{\eta_{\alpha\beta x}^{(u_i A)}}{p_\alpha}\sum_\zeta p_{\beta\zeta}\frac{\partial}{h_x\partial x}\left(\sqrt{B}u_{\beta\zeta\parallel}\right)+\right.\right. \\ \left.\left.\left(\frac{\eta_{\alpha\alpha x}^{(u_i A)}}{p_\alpha}-\frac{\eta_{\alpha x}^{(u_i B)}}{p_\alpha}\right)\sum_{\zeta\neq Z}p_{\alpha\zeta}\frac{\partial}{h_x\partial x}\left(\sqrt{B}u_{\alpha\zeta\parallel}\right)\right]\right]. \quad (5.16)$$

The heat flux dependent part of the viscous-stress tensor divergence (5.10) can be written as following:

$$\left(\nabla\cdot\overleftrightarrow{\pi}_a^{h_i}\right)_\parallel = [a\to\alpha Z] = \\ = -\frac{8}{15}B^{3/2}b_x\frac{\partial}{h_x\partial x}\left[\frac{1}{B^2 b_x}\frac{n_{\alpha Z}}{n_\alpha}\left[\sum_\beta\frac{\eta_{\alpha\beta x}^{(h_i A)}}{p_\alpha}\frac{\partial}{h_x\partial x}\left(\sqrt{B}\frac{\overline{h}_{\beta x}^{*(0)}}{b_x}\right)+\right.\right. \\ \left.\left.\frac{\eta_{\alpha x}^{(h_i B)}}{p_\alpha}\left(\frac{1}{I_{\alpha Z}}\frac{\partial}{h_x\partial x}\left(\sqrt{B}\frac{h_{\alpha Z x}^{(0)}}{b_x}\right)-\frac{\partial}{h_x\partial x}\left(\sqrt{B}\frac{\overline{h}_{\alpha x}^{*(0)}}{b_x}\right)\right)\right]\right], \quad (5.17)$$

where the coefficients $\frac{\eta_{\alpha\beta x}^{(h_i A)}}{p_\alpha}$ and $\frac{\eta_{\alpha x}^{(h_i B)}}{p_\alpha}$ are:

$$\frac{\eta_{\alpha\beta x}^{(h_i A)}}{p_\alpha} = b_x^2\frac{\eta_{\alpha\beta}^{(h_i A)}}{p_\alpha};\quad \frac{\eta_{\alpha\beta}^{(h_i A)}}{p_\alpha} = \check{c}_{\alpha\beta}^{(\pi_h^A)}\tau_{\alpha\beta}^{(Zh)};\quad \frac{\eta_{\alpha x}^{(h_i B)}}{p_\alpha} = b_x^2\frac{\eta_\alpha^{(h_i B)}}{p_\alpha};\quad \frac{\eta_\alpha^{(h_i B)}}{p_\alpha} = 2c_\alpha^{(\pi_h^B)}\tau_{\alpha\alpha}^{(Zh)}, \quad (5.18)$$

where in the poloidal heat fluxes, the parallel heat conductivity and the diamagnetic contributions are taken into account:

$$\frac{\overline{h}_{\alpha x}^{*(0)}}{b_x} = \overline{h}_{\alpha\parallel}^{*} + \frac{\overline{h}_{\alpha x}^{*(dia)}}{b_x} = \begin{cases} 0 & \text{outside the separatrix} \\ -\frac{\kappa_{\alpha x}^{(CL)}}{b_x}\frac{\partial T_i}{h_x\partial x} - \frac{5}{2}\frac{B_z B}{B_x B^2}\sum_Z\frac{n_{\alpha Z}T_i}{Ze}\frac{\partial T_i}{h_y\partial y} & \text{inside the separatrix} \end{cases}, \quad (5.19)$$

$$\frac{h_{\alpha Z x}^{(0)}}{b_x} = h_{\alpha Z\parallel} + \frac{h_{\alpha Z x}^{(dia)}}{b_x} = \begin{cases} 0 & \text{outside the separatrix} \\ -\frac{\kappa_{\alpha Z x}^{CL}}{b_x}\frac{\partial T_i}{h_x\partial x} - \frac{5}{2}\frac{B_z B}{B_x B^2}\frac{n_{\alpha Z}T_i}{Ze}\frac{\partial T_i}{h_y\partial y} & \text{inside the separatrix} \end{cases}, \quad (5.20)$$

where conductivities are defined according to (5.2) and (5.1), correspondingly.

It is worth to mentioned that the viscous momentum fluxes (3.9) and the viscous sources (3.14), (3.19) are written only for the single main ion species $a = a_{main}$. This prevents the complete multi-ion generalisation of the code. Using ZG module, the viscous momentum fluxes (5.11) and the viscous sources (5.14) are written uniformly for all ion species. Besides, the viscous-drift currents, which were also previously implemented only for the main ion species (3.69), (3.70), (3.75) and (3.76), are written for all species in appendix J.4. Thus, the complete multi-ion generalisation of the SOLPS-ITER code is performed. The viscous heat source is left the same according to (3.59). However, the updated transport coefficient (5.12) is applied there.

## 5.2 GRILLIX

### 5.2.1 General remarks

The multi-ion equations are written for the GRILLIX 3D fluid turbulent code. The main difference with respect to the transport code, which is discussed in the section 5.1, is the polarisation drift due to inertia and viscosity. The implementation of the multi-ion polarization drift into the ion continuity equation is not a trivial task. The single-ion GRILLIX code uses the electron continuity equation to avoid this problem. The continuity equation for the each of ion species is combined with the vorticity equation using Zhdanov ordering to avoid implementation of the polarization flux divergence for each species, which leads to the large matrix inversion similar to Eq. (76) in [142].

In this section, the equations are written in the CGS, following the notation in the GRILLIX code.

### 5.2.2 Multi-species drift reduction

The first step involves performing a drift reduction procedure in the multi-species case. This procedure is essential to simplify the modeling of plasma dynamics and improve computational efficiency when dealing with multiple ion species.

The equation for the flow velocity for species $\alpha Z$ can be derived by combining (4.4) and (4.5):

$$m_\alpha n_{\alpha Z} \frac{\mathrm{d}_{\alpha Z}\mathbf{u}_{\alpha Z}}{\mathrm{d}t} = -\nabla(n_{\alpha Z}T_{\alpha Z}) + Zen_{\alpha Z}(\mathbf{E} + \frac{1}{c}[\mathbf{u}_{\alpha Z}\mathbf{B}]) - \nabla\cdot\overleftrightarrow{\pi}_{\alpha Z} + \mathbf{R}_{\alpha Z} + \mathbf{S}^m_{\alpha Z} - \mathbf{u}_{\alpha Z}S^n_{\alpha Z} \quad (5.21)$$

where $\frac{\mathrm{d}_{\alpha Z}}{\mathrm{d}t} = (\partial_t + \mathbf{u}_{\alpha Z}\cdot\nabla)$. The (5.21) is multiplied vectorially by $\mathbf{B}$, also the Lorentz force is balanced by other terms. As a result, the perpendicular velocity can be written as following:

$$\mathbf{u}^\perp_{\alpha Z} = \mathbf{u}^{dia}_{\alpha Z} + \mathbf{v}_E + \mathbf{u}^{inert}_{\alpha Z} + \mathbf{u}^{vis}_{\alpha Z} + \mathbf{u}^{\mathbf{R}}_{\alpha Z} + \mathbf{u}^{ion-neut}_{\alpha Z}, \quad (5.22)$$

where the zeroth-order diamagnetic and $\mathbf{E}\times\mathbf{B}$ are:

$$\mathbf{u}^{dia}_{\alpha Z} = -\frac{c\nabla(n_{\alpha Z}T_{\alpha Z})\times\mathbf{B}}{Zen_{\alpha Z}B^2}, \quad \mathbf{v}_E = \frac{c\mathbf{E}\times\mathbf{B}}{B^2}, \tag{5.23}$$

and the first-order polarisation drifts [143], such as: inertia, viscous, friction and ion-neutral drifts are:

$$\mathbf{u}^{inert}_{\alpha Z} = -\frac{cm_\alpha n_{\alpha Z}\frac{\mathrm{d}_{\alpha Z}\mathbf{u}^{\perp 0}_{\alpha Z}}{\mathrm{d}t}\times\mathbf{B}}{Zen_{\alpha Z}B^2}, \quad \mathbf{u}^{vis}_{\alpha Z} = -\frac{c\nabla\cdot\overleftrightarrow{\pi}_{\alpha Z}\times\mathbf{B}}{Zen_{\alpha Z}B^2}, \tag{5.24}$$

$$\mathbf{u}^{\mathbf{R}}_{\alpha Z} = \frac{c\mathbf{R}_{\alpha Z}\times\mathbf{B}}{Zen_{\alpha Z}B^2}, \quad \mathbf{u}^{ion-neut}_{\alpha Z} = \frac{c(\mathbf{S}^m_{\alpha Z} - \mathbf{u}_{\alpha Z}S^n_{\alpha Z})\times\mathbf{B}}{Zen_{\alpha Z}B^2}. \tag{5.25}$$

The zeroth-order drifts $\mathbf{u}^{\perp 0}_{\alpha Z} = \mathbf{u}^{dia}_{\alpha Z} + \mathbf{v}_E$ contribute into the inertia drifts. Following GRILLIX equations, we neglect $\mathbf{u}^{\mathbf{R}}_{\alpha Z}$ and $\mathbf{u}^{ion-neut}_{\alpha Z}$. Those can be added later. The drift implementation can be significantly simplified, if the first-order Zhdanov diffusion velocity $\mathbf{w}_{\alpha Z} = \mathbf{u}_{\alpha Z} - \mathbf{u}$ is neglected in the first-order inertia drifts:

$$\mathbf{u}^{inert}_{\alpha Z} = -\frac{cm_\alpha n_{\alpha Z}\frac{\mathrm{d}\mathbf{u}^{\perp 0}}{\mathrm{d}t}\times\mathbf{B}}{Zen_{\alpha Z}B^2}, \quad \frac{\mathrm{d}\mathbf{u}^{\perp 0}}{\mathrm{d}t} = (\partial_t + \mathbf{u}\cdot\nabla)\left[\mathbf{u}^{dia} + \mathbf{v}_E\right] \tag{5.26}$$

$$\mathbf{u}^{dia} = -\sum_{\alpha Z}\tilde{\rho}_{\alpha Z}\frac{c\nabla(n_{\alpha Z}T_{\alpha Z})\times\mathbf{B}}{Zen_{\alpha Z}B^2}, \quad \rho = \sum_{\alpha Z}\rho_{\alpha Z}, \quad \tilde{\rho}_{\alpha Z} = \frac{\rho_{\alpha Z}}{\rho}. \tag{5.27}$$

It is worth to mention that the electrostatic potential ($\varphi$) and mass dependencies of the polarisation drift are taken into account. In the $\mathbf{u}^{inert}_{\alpha Z}$, the species specific advection and diamagnetic drifts are replaced by the mass-averaged ones, which can be done under Zhdanov ordering, when the:

$$\delta^\perp = \frac{|\mathbf{w}^{\perp 0}_{\alpha Z}|}{|\mathbf{u}^{\perp 0}|} = \frac{|\mathbf{u}^{dia} - \mathbf{u}^{dia}_{\alpha Z}|}{|\mathbf{u}^{dia} + \mathbf{v}_E|}, \quad \delta^\parallel = \frac{w^\parallel_{\alpha Z}}{u^\parallel} \tag{5.28}$$

are small. Thus, the inertia drift currents are:

$$\mathbf{j}^{inert}_{\alpha Z} = Zen_{\alpha Z}\mathbf{u}^{inert}_{\alpha Z} = -c\rho_{\alpha Z}\frac{\frac{\mathrm{d}\mathbf{u}^{\perp 0}}{\mathrm{d}t}\times\mathbf{B}}{B^2} \tag{5.29}$$

$$\mathbf{j}^{inert} = \sum_{\alpha Z}\mathbf{j}^{inert}_{\alpha Z} = -c\rho\frac{\frac{\mathrm{d}\mathbf{u}^{\perp 0}}{\mathrm{d}t}\times\mathbf{B}}{B^2} \tag{5.30}$$

We note that the inertia drift current, which corresponds to the species $\alpha Z$, relates to the total inertia drift current simply as following:

$$\boxed{\mathbf{j}^{inert}_{\alpha Z} = \tilde{\rho}_{\alpha Z}\mathbf{j}^{inert}} \tag{5.31}$$

The viscosity drift currents are:

$$\mathbf{j}^{vis}_{\alpha Z} = Zen_{\alpha Z}\mathbf{u}^{vis}_{\alpha Z} = -\frac{c\nabla\cdot\overleftrightarrow{\pi}_{\alpha Z}\times\mathbf{B}}{B^2} \tag{5.32}$$

$$\mathbf{j}^{vis} = \sum_{\alpha Z}\mathbf{j}^{vis}_{\alpha Z} = -\frac{c\nabla\cdot\overleftrightarrow{\pi}\times\mathbf{B}}{B^2}, \quad \overleftrightarrow{\pi} = \sum_{\beta\zeta}\overleftrightarrow{\pi}_{\beta\zeta}. \tag{5.33}$$

Let us consider the current and the flow velocity in the forms of:

$$\tilde{\mathbf{j}}^{vis}_{\alpha Z} = \tilde{\rho}_{\alpha Z}\mathbf{j}^{vis}, \quad \tilde{\mathbf{j}}^{vis}_{\alpha Z} = Zen_{\alpha Z}\tilde{\mathbf{u}}^{vis}_{\alpha Z}, \quad \tilde{\mathbf{u}}^{vis}_{\alpha Z} = -\frac{c\tilde{\rho}_{\alpha Z}\nabla\cdot\overleftrightarrow{\pi}\times\mathbf{B}}{Zen_{\alpha Z}B^2}, \tag{5.34}$$

The $\tilde{\mathbf{u}}^{vis}_{\alpha Z}$ does not match exactly the $\mathbf{u}^{vis}_{\alpha Z}$ and therefore does not represent the solution of the momentum equation in the perpendicular direction for species $\alpha Z$. However, using $\tilde{\mathbf{u}}^{vis}_{\alpha Z}$, the total current is calculated correctly. The particle balance is still satisfied. Besides, for the most practical purposes $\tilde{\mathbf{u}}^{vis}_{\alpha Z} \approx \mathbf{u}^{vis}_{\alpha Z}$ can be assumed.

### 5.2.3 Multi-ion continuity equations

In this subsection, we perform the crucial step of implementing the polarization flux divergence using the results obtained in subsection 5.2.2. This step is essential to accurately account for the polarization drift effects of each ion species in the plasma, and it builds upon the previous calculations of the multi-species drift reduction.

Instead of solving of the electron continuity (3.87), we solve the continuity equation for each of ion species $\alpha Z$ using (4.4):

$$\begin{aligned}\frac{\partial}{\partial t}n_{\alpha Z} + \mathbf{v}_E\cdot\nabla n_{\alpha Z} + \nabla\cdot\left(n_{\alpha Z}u_{\parallel\alpha Z}\mathbf{b}\right) = n_{\alpha Z}\mathcal{C}(\phi) + \frac{n_{\alpha Z}}{Ze}\mathcal{C}(T_i) + \frac{T_i}{Ze}\mathcal{C}(n_{\alpha Z}) \\ - \frac{1}{Ze}\nabla\cdot\mathbf{j}^{inert}_{\alpha Z} - \frac{1}{Ze}\nabla\cdot\tilde{\mathbf{j}}^{vis}_{\alpha Z} + S^n_{\alpha Z}\end{aligned} \tag{5.35}$$

The direct implementation of $\mathbf{j}^{inert}_{\alpha Z}$ and $\tilde{\mathbf{j}}^{vis}_{\alpha Z}$ should be avoided, due to the complexity. In the single ion GRILLIX equations the electron continuity (3.87) equation is solved, where the electron inertia and viscosity is neglected. The following step is vital in our approach. By combining this equation with the vorticity equation (3.91), we can obtain

an equivalent solution to the continuity equation for a single ion (3.87). In the case of multiple ion species, we can utilize the vorticity equation to simplify the continuity equations for all ion species. This simplification is an important aspect of our ansatz. Thus, using relations between the total and species-resolved polarization currents (5.31) and (5.34), one can re-write continuity equation (5.35) in the form of:

$$\frac{\partial}{\partial t}n_{\alpha Z} + \mathbf{v}_E \cdot \nabla n_{\alpha Z} + \nabla \cdot \left(n_{\alpha Z} u_{\parallel \alpha Z}\mathbf{b}\right) = n_{\alpha Z}\mathcal{C}(\phi) + \frac{n_{\alpha Z}}{Ze}\mathcal{C}(T_i) + \frac{T_i}{Ze}\mathcal{C}(n_{\alpha Z}) - \frac{1}{Ze}\left(\mathbf{j}^{inert} + \tilde{\mathbf{j}}^{vis}\right)\cdot\nabla\tilde{\rho}_{\alpha Z} - \frac{1}{Ze}\tilde{\rho}_{\alpha Z}\nabla\cdot\left(\mathbf{j}^{inert} + \tilde{\mathbf{j}}^{vis}\right) + S^n_{\alpha Z}, \quad (5.36)$$

where the divergence $\nabla \cdot \left(\mathbf{j}^{inert} + \tilde{\mathbf{j}}^{vis}\right)$ can be found using the vorticity equation:

$$-\nabla \cdot \left(\mathbf{j}^{inert} + \tilde{\mathbf{j}}^{vis}\right) = -T_e\mathcal{C}(n_e) - n_e\mathcal{C}(T_e) - T_i\mathcal{C}(n_i) - n_i\mathcal{C}(T_i) + \nabla\cdot\left(j_\parallel\mathbf{b}\right) \quad (5.37)$$

As a result, the ion continuity equation is:

$$\frac{\partial}{\partial t}n_{\alpha Z} + \mathbf{v}_E \cdot \nabla n_{\alpha Z} + \nabla \cdot \left(n_{\alpha Z} u_{\parallel \alpha Z}\mathbf{b}\right) = n_{\alpha Z}\mathcal{C}(\phi) + \frac{n_{\alpha Z}}{Ze}\mathcal{C}(T_i) + \frac{T_i}{Ze}\mathcal{C}(n_{\alpha Z}) - \frac{1}{Ze}\left(\mathbf{j}^{inert} + \tilde{\mathbf{j}}^{vis}\right)\cdot\nabla\tilde{\rho}_{\alpha Z} - \frac{1}{Ze}\tilde{\rho}_{\alpha Z}\left(T_e\mathcal{C}(n_e) + n_e\mathcal{C}(T_e) + T_i\mathcal{C}(n_i) + n_i\mathcal{C}(T_i)\right) + \frac{1}{Ze}\tilde{\rho}_{\alpha Z}\nabla\cdot\left(j_\parallel\mathbf{b}\right) + S^n_{\alpha Z} \quad (5.38)$$

It is important to mention that for a single ion case ($Z = 1$) the (5.38) turns into the GRILLIX Braginskii electron continuity equation (3.87).

### 5.2.4 Vorticity equation in the multi-ion case

The multi-ion generalization of the single-ion vorticity equation (3.91) can be expressed as following:

$$\nabla\cdot\left(\frac{c^2\rho}{B^2}\frac{d_i}{dt}\left[\sum_{\alpha Z}\tilde{\rho}_{\alpha Z}\frac{\nabla_\perp(n_{\alpha Z}T_{\alpha Z})}{Zen_{\alpha Z}} + \nabla_\perp\phi\right]\right) = -\mathcal{C}(p_e) - \mathcal{C}(p_i) + \nabla\cdot\left(j_\parallel\mathbf{b}\right) - \frac{1}{6}\mathcal{C}(G), \quad (5.39)$$

where $\sum_{\alpha Z}\tilde{\rho}_{\alpha Z}\frac{\nabla_\perp(n_{\alpha Z}T_{\alpha Z})}{Zen_{\alpha Z}}$ is a part of the $\mathbf{u}^{dia}$ (5.27). The r.h.s. of the (5.39) represents the $\nabla\cdot\mathbf{j}^{inert}$ (5.30), where the diamagnetic cancellation with the viscous-stress tensor, similar to the single-ion GRILLIX model [138], is performed. The rest part of the $\nabla\cdot\mathbf{j}^{vis}$ (5.33) appears in the (5.39) in the form of $-\frac{1}{6}\mathcal{C}(G)$, where the $G$ is a multi-ion generalization of the single-ion GRILLIX one (3.93) using the parallel-parallel

components $\pi_{|||}$ of Zhdanov viscouss-stress tensor (4.73) and the coordinate-independent form of the viscouss-stress tensor divergence Eq. (B7) in [84]. Evidently, for a single ion case ($Z = 1$) the (5.39) turns into the GRILLIX Braginskii vorticity equation (3.91).

### 5.2.5 Ohm's law

The electron momentum equation is written according to Zhdanov (paragraph 8.2 in [18]). As a result, the multi-ion generalization of the Ohm's law (3.96) is done as following:

$$-\frac{m_e}{e}\frac{d_e}{dt}\frac{j_\parallel}{en} - \frac{1}{c}\frac{\partial}{\partial t}A_\parallel = \nabla_\parallel\phi - \frac{1}{en_e}\nabla_\parallel p_e + \eta_\parallel\left(j_\parallel + j_\parallel^{diff}\right) - \frac{\beta_\parallel}{e}\nabla_\parallel T_e, \tag{5.40}$$

where the electrical conductivity is:

$$\eta_\parallel = \frac{m_e}{e^2 n_e \tau_e}\alpha_\parallel, \qquad \tau_e = \frac{n_e m_e}{\lambda_{ei}}, \quad \lambda_{ei} = \frac{1}{3}(2\pi)^{-3/2} n_e^2 Z_{eff}\sqrt{m_e}\frac{\lambda}{T_e^{3/2}}(4\pi)^2 e^4, \tag{5.41}$$

$$\tau_e = \frac{3\sqrt{m_e}T_e^{3/2}}{4\sqrt{2\pi}n_e Z_{eff}\lambda e^4}, \quad Z_{eff} = \frac{1}{n_e}\sum_{\alpha Z} Z^2 n_{\alpha Z}, \tag{5.42}$$

and the Zhdanov kinetic coefficients are:

$$\alpha_\parallel = 1 - \frac{0.22 + 0.73/Z_{eff}}{0.31 + 1.20/Z_{eff} + 0.41/Z_{eff}^2}, \quad \beta_\parallel = \frac{0.47 + 0.94/Z_{eff}}{0.31 + 1.20/Z_{eff} + 0.41/Z_{eff}^2}. \tag{5.43}$$

It is worth to mention that $\alpha_\parallel \approx 0.51$ and $\beta_\parallel \approx 0.73$ for $Z_{eff} = 1$. Also, there is correction current:

$$j_\parallel^{diff} = -\sum_{\alpha Z} Z e n_{\alpha Z} u_{\parallel \alpha Z} + \sum_{\alpha Z}\frac{Z^2 e n_{\alpha Z}}{Z_{eff}} u_{\parallel \alpha Z}. \tag{5.44}$$

which is a result of the Zhdanov closure. Note, the $j_\parallel^{diff} \neq 0$ for multi-ion mixture. Besides, the $j_\parallel^{diff}$ is required to satisfy the momentum conservation in e-i collisions.

### 5.2.6 Electron temperature equation

First, it is necessary to consider the divergence of the electron parallel heat flux Eq. (8.2.7) in [18] and the electron heat source (4.20), (4.21):

$$
\begin{aligned}
-\nabla\cdot\left(h_{\|e}\mathbf{b}\right)+Q_e-w_{e\|}R_{e\|} &= \nabla\cdot\left(\chi^e_{\|}\nabla_{\|}T_e\mathbf{b}\right)-\frac{3}{\tau_e}\sum_{\beta\zeta}\left(\frac{\zeta^2 n_{\beta\zeta}}{Z_{eff}}\frac{m_e}{m_\beta}\right)(T_e-T_i)\\
&+\nabla\cdot\left(\beta_{\|}\frac{T_e}{e}\left(j_{\|}+j^{diff}_{\|}\right)\mathbf{b}\right)-w_{e\|}\frac{m_e}{e\tau_e}\alpha_{\|}\left(j_{\|}+j^{diff}_{\|}\right)+w_{e\|}n_e\beta_{\|}\mathbf{b}\cdot\nabla T_e\approx\\
&\nabla\cdot\left(\chi^e_{\|}\nabla_{\|}T_e\mathbf{b}\right)-\frac{3}{\tau_e}\sum_{\alpha Z}\left(\frac{Z^2 n_{\alpha Z}}{Z_{eff}}\frac{m_e}{m_\alpha}\right)(T_e-T_i)+\beta_{\|}\frac{T_e}{e}\nabla\cdot\left(j_{\|}\mathbf{b}\right)+\eta_{\|}j^2_{\|}, \quad (5.45)
\end{aligned}
$$

where for the "≈" sign the $j^{diff}_{\|}$ is neglected and the $w_{\|e}\approx -j_{\|}/(en_e)$ assumption is applied. Later, these assumptions can be relaxed by means of additional terms in the electron temperature equation.

Finally, the multi-ion generalization of the electron temperature equation (3.100) can be written as following:

$$
\begin{aligned}
\frac{d_e}{dt}T_e =& -\frac{2}{3}\left[\frac{T_e}{en_e}\mathcal{C}(p_e)-T_e\mathcal{C}(\phi)+\frac{5}{2}\frac{T_e}{e}\mathcal{C}(T_e)\right]-\frac{2}{3}T_e\nabla\cdot\left(v_{\|}\mathbf{b}\right)+\frac{2}{3}\beta_{\|}\frac{T_e}{en_e}\nabla\cdot\left(j_{\|}\mathbf{b}\right)\\
&+\frac{2}{3}\frac{1}{n_e}\nabla\cdot\left(\chi^e_{\|}\nabla_{\|}T_e\mathbf{b}\right)-\frac{2}{\tau_e}\sum_{\alpha Z}\left(\frac{Z^2 n_{\alpha Z}}{Z_{eff}n_e}\frac{m_e}{m_\alpha}\right)(T_e-T_i)+\frac{2}{3}\frac{\eta_{\|}j^2_{\|}}{n_e}, \quad (5.46)
\end{aligned}
$$

where the parallel electron heat conductivity is defined as:

$$
\boxed{\chi^e_{\|}=\gamma_{\|}\frac{n_eT_e\tau_e}{m_e},} \qquad \gamma_{\|}=\frac{3.9+2.3/Z_{eff}}{0.31+1.20/Z_{eff}+0.41/Z^2_{eff}}, \quad (5.47)
$$

It is worth to mention that $\gamma_{\|}\approx 3.29$ for $Z_{eff}=1$. Note that for a single ion case ($Z=1$) the (5.40) and (5.46) turn into the GRILLIX Braginskii Ohm's law (3.96) and electron temperature equations (3.100), correspondingly.

Using the Zhdanov closure for ions (section 4.3), the generalized for arbitrary mixtures ion parallel momentum (3.95) and ion temperature equations (3.102) can be derived in the similar way, as it is performed for the electron ones (5.40) and (5.46). Thus, the equations for $u_{\alpha Z\|}$ and $T_i$ can be found.

### 5.2.7 MPI multi-species infrastructure and MMS tests

In this subsection, we delve into the essence of the code design for the multiple ion treatment and the integration test infrastructure. This approach is crucial for preventing bugs and ensuring the reliability of our implementation. By carefully designing and conducting integration tests, we can identify and address potential issues at an early stage, thereby improving the overall robustness and performance of the code.

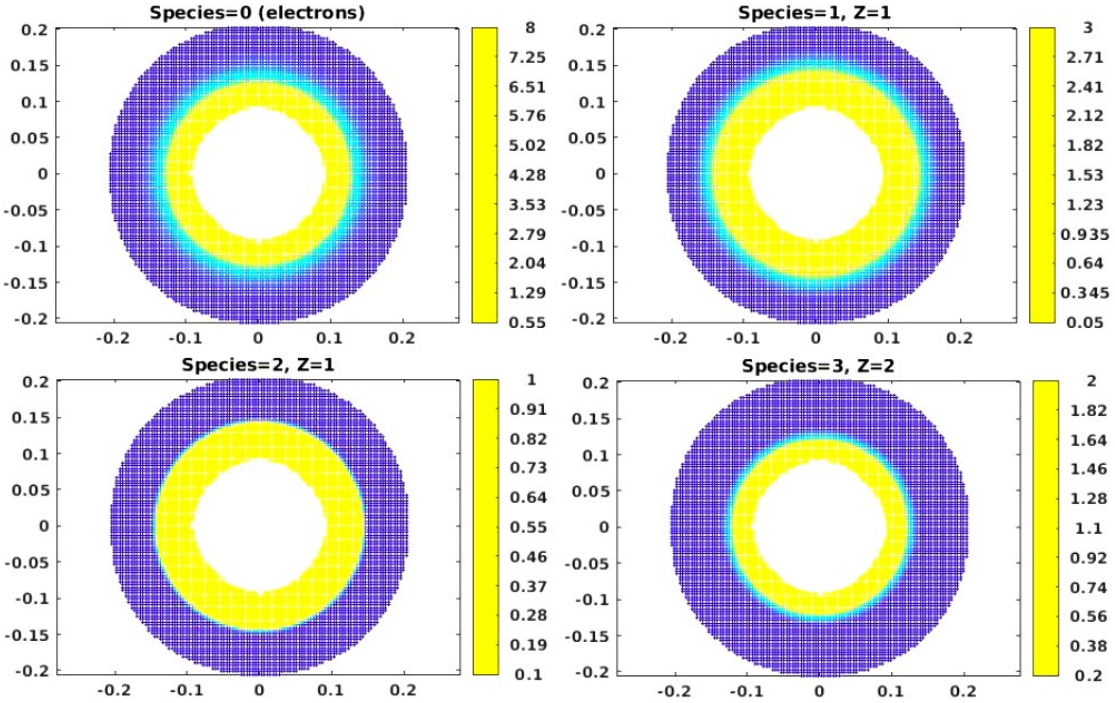


**Figure 5.2:** An example of initial profiles of electrons (rank 0), $D^+$ (rank 1), $T^+$ (rank 2), $He^{+2}$ (rank 3) in the circular geometry in the multi-ion GRILLIX mode.

Previously in the GRILLIX code, the MPI parallelization over different poloidal planes (figure 3.2), i.e. the perpendicular dynamics of each of fluid equations are solved at the different MPI rank for each poloidal plane. The multi-ion model for GRILLIX is additionally parallelized over different ion-species. In particular, the continuity equation (5.38) for each species $\alpha Z$ is solved in parallel at the different ion rank. Then, the $n_e$ at the electron rank is calculated using MPI communication according to the $n_e = \sum_{\alpha Z} Z n_{\alpha Z}$. In figure 5.2, the initial density profiles for the mixture of $D^+$, $T^+$, $He^{+2}$ in the circular geometry are plotted. The $n_e$ (figure 5.2) is a result of $MPI\_reduce$ command application over the ion ranks.

Before implementing the multi-ion equations into the GRILLIX code, the CI/CD infrastructure is prepared using the method of manufactured solutions (MMS) [144]. The integration tests in the slab and circular geometries are automatically performed for any new changes introduced by git commit in the GRILLIX gitlab repository. The convergence results for the 8, 16, 32 and 64 numbers of poloidal planes (parallel resolution) with the proportionally increased the perpendicular grid resolution and the time-step for the simple density equation:

$$\frac{\partial}{\partial t} n_{\alpha Z} = S^n_{\alpha Z} \tag{5.48}$$

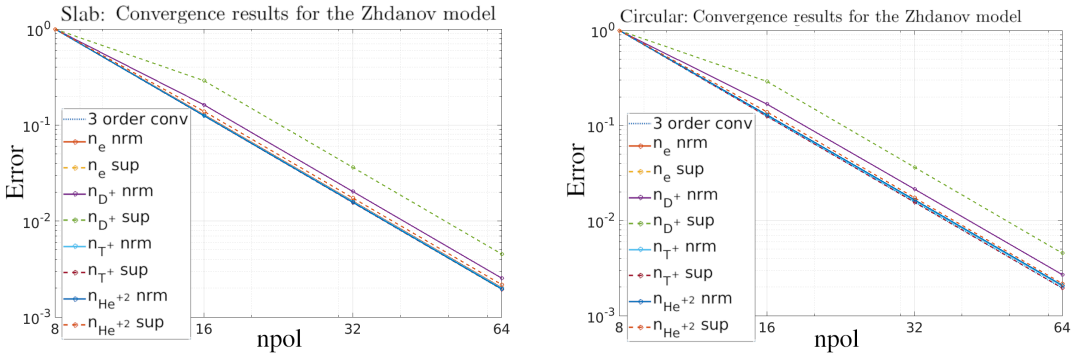


**Figure 5.3:** Numerical error of MMS verification procedure. The sup- and L2-norms (nrm) for $D^+$, $T^+$, $He^{+2}$ densities (normalized to the npol=8 values) for the slab (a) and circular (b) geometries. The 3 order convergence, which should be reached asymptotically, is plotted. Starting from 8 the number of planes is doubled together with the perpendicular grid resolution and the time-step.

are pictured in figures 5.3a and 5.3b for the slab and circular geometries, correspondingly.

Thus, the multi-species infrastructure is prepared of the further implementation of the model, which is based on the Zhdanov closure.

## 5.3 Conclusions according to the improvements of the SOLPS-ITER and GRILLIX models

The Zhdanov closure is fully integrated into the SOLPS-ITER code as a part of the ZG module. The implementation includes the derivation of transport coefficients for various quantities such as heat flux, the TF and the FR, the strain and the heat parallel stresses utilizing the IAM and the EMIM. Moreover, the ion velocity difference heat flux, which was absent in previous versions of the SOLPS-ITER model, has been incorporated. The differences between the old ZY and new IAM/EMIM formulations of the TF and FR in the SOLPS-ITER code are discussed in subsection 4.4.3. Furthermore, the discrepancy between the previous and updated formulations of heat conductivity and viscosity in the SOLPS-ITER code are illustrated in figure 5.1.

This comprehensive integration of the Zhdanov closure enables the complete multi-ion generalization of the SOLPS-ITER model. The equations have been unified to apply uniformly to all ion species without the need for conditional statements differentiating between main and impurity species. It is important to note that this generalization would not have been achievable without the derivation in section 4.2 of multi-species heat stress, which in the single-ion form are an essential component of the original SOLPS-ITER model [83] and cannot be omitted.

As a demonstration of the model's readiness, simulations using a 50-50 D-T mixture are presented in section 6.2, highlighting the capability of the model to accurately capture the behavior of such a mixture. This accomplishment further solidifies the applicability and effectiveness of the ZG module within the SOLPS-ITER framework.

In the GRILLIX code, the drift-reduced multi-ion equations have been formulated. The introduction of polarization drifts for each ion species in the equations is achieved by utilizing the Zhdanov ordering. This approach simplifies the treatment of polarization flux divergence, eliminating the need for species-resolved implementation [142]. This divergence is expressed using the vorticity equation.

It is important to highlight that the single-ion Braginskii equations can be viewed as a special case within the framework of the new multi-ion equations. Specifically, when considering a single-ion mixture with an ion charge state of $Z = 1$, the new multi-ion equations reduce to the familiar standard GRILLIX equations. This observation underscores the connection between the multi-ion formulation and the previously established single-ion approach, providing a clear relationship between the two.

To ensure the accuracy and reliability of the model implementation, the CI/CD procedure is employed, utilizing MMS integration tests. This rigorous approach guarantees the robustness of the implemented model. Additionally, the MPI infrastructure is prepared to accommodate the multi-ion equations. However, it is important to note that the full integration of these equations into the GRILLIX code is still pending and is a task reserved for future model development.

# 6 SOLPS-ITER simulations with the Zhdanov-Grad module

The new capabilities of the SOLPS-ITER code for the mixtures of ions with close masses are demonstrated in this chapter.

## 6.1 ITER modeling with D+He+Ne mixture

In this section, we focus on the D+He+Ne SOLPS-ITER modeling in the ITER tokamak. While the main plasma parameters do not exhibit significant changes after the implementation of the improved approach, the helium transport undergoes considerable alterations due to the new TF and FR formulations. Specifically, the separatrix-averaged relative concentration of He experiences a substantial decrease of approximately 30% compared to the previous formulations. This plays a crucial role in the studies of helium exhaust and is of particular importance in tokamak scenarios like ITER. The content of this section was also published in [85].

### 6.1.1 Main plasma parameters

The ITER baseline scenario simulation with the energy flux through the separatrix $P_{SOL} \approx 100\ MW$ and D+He+Ne mixture is carried out with the 3.0.7 SOLPS-ITER version with the ZG module implemented. The D fueling and Ne seeding are chosen to obtain plasma parameters in between 1b and 2b from [74]. Namely, the divertor neutral pressure $p_n = 7.5\ Pa$ and the separatrix-averaged Ne concentration $c_{Ne} = 1.0\%$. The simulation has been performed with full drifts and currents activated and with EIRENE kinetic neutrals.

The reference simulation with the ZY expressions is catalogued in the ITER integrated modeling analysis suite (IMAS) database as 123270. The simulations with the ZG module activated using IAM and EMIM are catalogued in the IMAS database as 123271 and 123272, correspondingly. The TF, the FR and the heat conductivity is calculated according to the ZG, while the velocity dependent part of the heat flux are disabled, and the viscous-stress tensor is calculated according to the previous 3.0.7 model.

It is noteworthy that the Zhdanov closure has already been partially implemented in the 3.0.7 SOLPS-ITER model. One significant improvement is the consideration of the effective plasma charge ($Z_{eff}$) dependence in the electron parallel heat conductivity, which is responsible for a major portion of heat transport along $\mathbf{B}$ in the SOL. Unlike the simple Braginskii formulation [17], the Zhdanov formulation (J.3) accounts for this dependence. Additionally, the ZG ion heat conductivity deviates from the 3.0.7 model

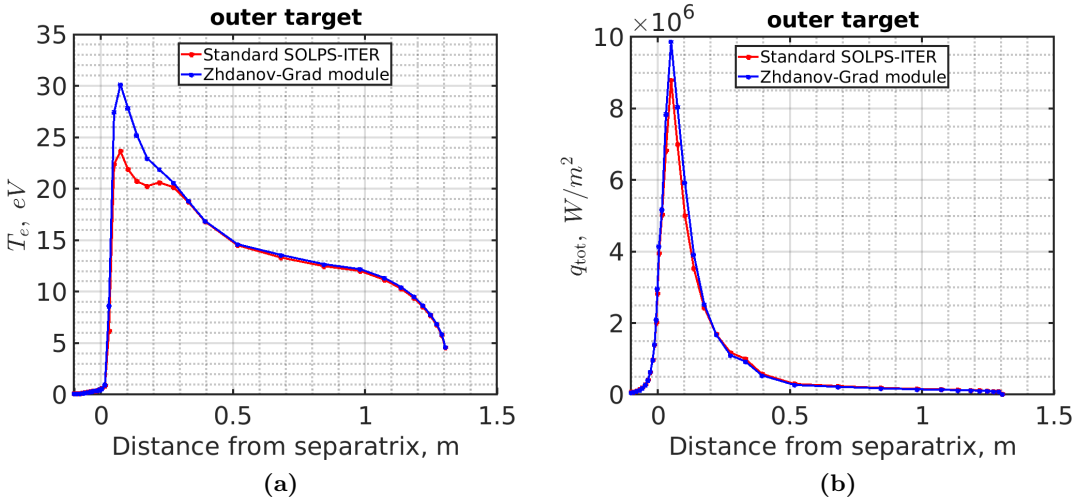


**Figure 6.1:** ITER outer target profiles for the Standard SOLPS-ITER 3.0.7 model and the Zhdanov-Grad module activated. (a) Electron temperature. (b) Total surface power loads, which includes the energy flux of ions and electrons, ion recombination loads, energy flux from recycled neutrals (which return a portion of the incoming energy back to the plasma volume), radiation loads, and other interactions involving neutrals and the plasma-facing surface.

by approximately 5% when considering a realistic plasma mixture (as shown in figure 5.1). As a result, the main plasma parallel transport undergo minimal changes following the activation of the ZG module. Figures 6.1a and 6.1b present the outer target profiles for both the 3.0.7 SOLPS-ITER and the improved ZG model. The minor changes in the $T_e$ profile (as depicted in figure 6.1a) are primarily attributed to the redistribution of Ne impurity in the plasma volume due to the improved TF and FR formulation. Notably, the ZG TF and FR make a significant contribution to He transport, which plays a major role in addressing the He exhaust problem [145].

### 6.1.2 Helium transport in deuterium plasmas

As we discussed in section 4.4, the IAM and EMIM should act similarly for the He and Ne impurities. This is confirmed in these test simulations. No visible difference in impurity transport is observed between the IAM and EMIM applied. Namely, the He separatrix-averaged concentration $c_{He}$, which is affected more than $c_{Ne}$, diverge insignificantly, i.e. $c_{He}^{IAM} = 0.62\%$ for the IAM and $c_{He}^{EMIM} = 0.57\%$ for the EMIM. Thus, the IAM is studied further.

This is in contrast to the difference found between the "Standard SOLPS-ITER" case with the ZY expressions applied and the "Zhdanov-Grad module" case with the IAM applied. The separatrix-averaged He concentration is observed $c_{He}^{Standard} = 0.89\%$ the "Standard SOLPS-ITER" case vs $c_{He} = 0.62\%$ for the IAM case. Thus, the infinite mass

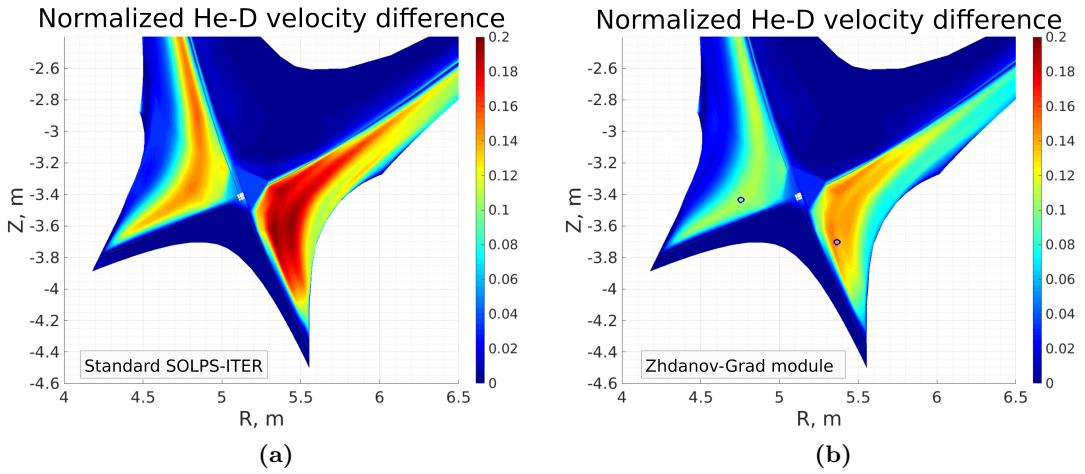


**Figure 6.2:** The flow velocity difference between the $He^{+2}$ ion species and $D^+$ ion species, normalized to the $D^+$ velocity $|u_{\|He^{+2}} - u_{\|D^+}|/\sqrt{T_i/m_D}$ using (a) the Standard SOLPS-ITER model, which is based on the ZY expressions, and (b) the ZG module in the IAM mode. Blue circles define spatial points where ion distribution functions are studied in figures 6.3a and 6.3b.

ratio between main and impurity ions assumption is too strong for the D-He interaction and should not be applied for the TF and FR kinetic coefficients calculations.

The IAM TF coefficient for D-He is smaller than the ZY TF one (figure 4.2b), according to the mechanism of the He "hot-tail" contribution, which is qualitatively discussed in section 2.3.2. The IAM FR coefficient for D-He is larger than the ZY FR one (figure 4.3a). In this modeling, in the He parallel momentum equation the FR counterbalances the TF according to the mechanism, which is discussed in details in [98]. As a result, the He-D flow velocity difference is smaller for ZG module activated (figure 6.2b) with respect to the "Standard SOLPS-ITER" model (figure 6.2a). The He poloidal stagnation surface is shifted further from the target plates leading to the smaller for the "Zhdanov-Grad module" case He leakage from the divertor region than for the "Standard SOLPS-ITER" case (for more details we refer to [85]). Thus, the $c_{He}^{Standard} = 0.89\%$ is larger than the $c_{He}^{IAM} = 0.62\%$. This test shows the importance of accurate treatment of the TF and FR for the low mass impurity taking into account the $m_D/m_{He} > 0$ mass ratio. Smaller, but visible, the finite mass-ratio effect is observed in these simulations also for Ne impurity [85].

### 6.1.3 Ion distribution functions

The effect of the distribution function "hot-tail" on the TF is qualitatively discussed in subsection 2.3.2. In this subsection, the shape of the ion distribution effect is studied on the real example, i.e. the ITER SOL simulations. The two spatial positions in the divertor region are chosen for the analysis: one is at the high field side (HFS) and another is at the low field side (LFS) (blue circles in figure 6.2b). The ion distribution function,

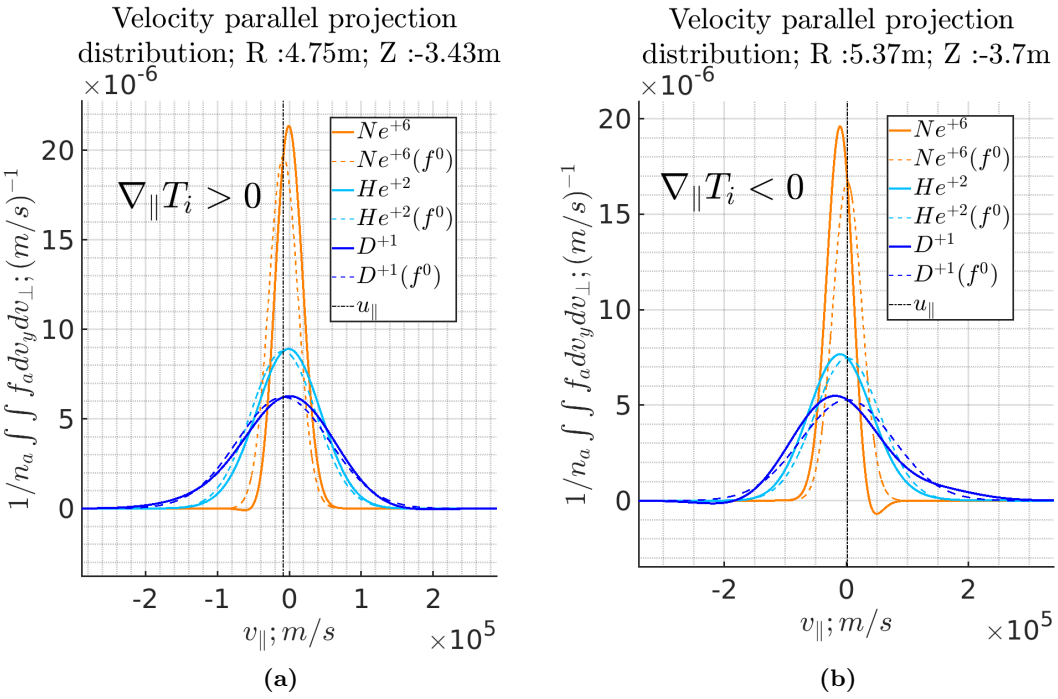


**Figure 6.3:** Distribution functions of the $D^+$, $He^{+2}$ and $Ne^{+6}$ ion species (the most populated charge states of the particular species type in the chosen divertor locations) at the (a) HFS and (b) LFS in the divertor region (at the spatial points marked by blue circles in figure 6.2b). $f^0$ is the non-modified Maxwell function.

which is used to obtain kinetic coefficients, can be reconstructed based on its moments, which are calculated in the code. The 21N-moment approximation of the distribution function (2.59) can be re-written using parallel components of vector moments $w_{\parallel\alpha Z}$, $h_{\parallel\alpha Z}$ and $r_{\parallel\alpha Z}$:

$$f_{\alpha Z}(\mathbf{c}) = n_{\alpha Z}\left(\frac{m_\alpha}{2\pi T_i}\right)^{3/2}\exp\left(-\frac{m_\alpha c^2}{2T_i}\right)\cdot \left[1+\gamma_{\alpha Z}w_{\parallel\alpha Z}c_\parallel+\frac{1}{5}\gamma_{\alpha Z}^2\left(\frac{h^T_{\parallel\alpha Z}}{p_{\alpha Z}}+\frac{h^w_{\parallel\alpha Z}}{p_{\alpha Z}}\right)c_\parallel\left(c^2-\frac{5}{\gamma_{\alpha Z}}\right)+ \frac{1}{70}\gamma_{\alpha Z}^3\left(\frac{r^T_{\parallel\alpha Z}\gamma_{\alpha Z}}{p_{\alpha Z}}+\frac{r^w_{\parallel\alpha Z}\gamma_{\alpha Z}}{p_{\alpha Z}}\right)c_\parallel\left(c^4-\frac{14}{\gamma_{\alpha Z}}c^2+\frac{35}{\gamma_{\alpha Z}^2}\right)\right] \quad (6.1)$$

where the moments $h^T_{\parallel\alpha Z}$ and $r^T_{\parallel\alpha Z}$ represent the modification of the distribution function due to the $\nabla_\parallel T_i$, and the moments $h^w_{\parallel\alpha Z}$ and $r^w_{\parallel\alpha Z}$ represent the modification of the distribution function due ion flow velocity difference. Thus, the moments $h^T_{\parallel\alpha Z}$ and

$r^T_{\|\alpha Z}$ contribute into the TF, and the moments $h^w_{\|\alpha Z}$ and $r^w_{\|\alpha Z}$ contribute into the FR. In figures 6.3a and 6.3b predicted ion distribution functions at the HFS and at the LFS, correspondingly (blue circles in figure 6.2b). The distribution functions are contracted over the perpendicular velocities.

In the IAM, the finite ion mass ratio is considered in collisions for the momentum r.h.s. integration, which affects the TF and FR coefficients. Also, the IAM TF for He is reduced with respect to the ZY TF, because the He "hot-tail" is taken into account in IAM (the mechanism is qualitatively discussed in section 2.3.2). The He velocities contribute significantly into the relative velocity in collisions $\mathbf{g}$ due to the close $m_D$ and $m_{He}$. Thus, the shape of the He distribution function contribution into the TF cannot be neglected. The impurity "hot-tail" contributes less for the heavier impurity, such as Ne, and becomes negligible while approaching $m_D/m_{imp} \to 0$. As it is shown in figure 4.2a, the ZY and IAM TF coefficients are close in this limit. It is important to mention that when the ion masses become close, the TF approaches zero, as it is shown in figure 4.2b, because the contributions from the "hot-tails" of both species counterbalance each other according to (2.29) and (4.58). This effect is considered in details, when the D-T TF is analysed in details in subsections 6.2.3 and 6.2.4.

The FR coefficient is modified because of the light species (D in this case) distribution function shaping due to the collisions with the non-trace heavy species, which have different than light species flow velocity. This phenomenon is well-known and taken into account, for instance, for the Spitzer resistivity or for the ZY FR. However, for the species with the close masses the modification of the D distribution function become smaller than for the $m_D/m_{imp} \to 0$ limit (figure 4.1b). As a result, the IAM FR transport coefficient become larger than the ZY one, as it is described in figure 4.3a. Thus, the impurity TF becomes smaller, and the impurity FR transport coefficient after the ZG module activation. As a result, the flow velocity difference between impurity and main species become smaller (subsection 6.1.2).

The contribution of TF and FR to the He transport, as discussed in subsection 6.1.2, can be further investigated by considering the shaping of the distribution function. The figures 6.3a and 6.3b show the TF-FR counterbalance from the kinetic point of view. The TF appears due to the D "hot-tail" $h^T_{\|D}/r^T_{\|D}$ (blue solid vs blue dashed in figures 6.3a and 6.3b). The impurity distribution function shift $w_{\|imp}$ towards the $\nabla_\| T_i$ with respect to the Maxwell distribution function with the mass-average flow velocity $u_\|$ (cyan/orange solid vs cyan/orange dashed in figures 6.3a and 6.3b) forms the required FR. Note, in these simulations, due to the small amount of impurities, the D flow velocity $u_{\|D}$ is close to the $u_\|$. Thus, the TF occur mostly by means of $w_{\|imp}$ in this case. Also, figure 6.3b represents the case, which demonstrates that the parallel stagnation point is different for the impurity and the main species due to the TF effect: the D flow velocity is close to zero (slightly positive), whereas the impurity flow velocity is negative (towards upstream) due to the $w_{\|imp}$.

In figure 6.3b, a negative part of the Ne distribution can be observed. Due to the polynomial approximation, negative parts of distribution functions appear in Zhdanov [18] and Braginskii closures [17], however inside the area of theory applicability they are

small and do not contribute to the result. In these ITER simulations at the LFS, the $\nabla_{\parallel} T_i$ is sufficiently large to make the Ne diffusive velocity $w_{\parallel Ne}$ ≈60% of the Ne thermal velocity $\sqrt{T_i/m_{Ne}}$. In such a case the simulation is on the boundary of the applicability of the linear Zhdanov theory. Moreover, modeling with the ions heavier than Ne can be problematic, since their thermal velocity is even smaller. The non-linear terms in the collisional operator become large and should be taken into account in such cases.

## 6.2 JET-like modeling with D+T+Ne mixture

In this section, we delve into the SOLPS-ITER modeling for a fusion plasma mixture. The D+T+Ne mixiture is simulated in a JET-like tokamak configuration. A notable improvement is achieved with the introduction of the ZG module of the code, as it now allows simulations of mixtures with comparable concentrations of D and T, which was not possible in previous versions. Consequently, we demonstrate the new capability of the 3.0.8 SOLPS-ITER code.

The study focuses on the impact of the TF on the separation of hydrogen isotopes. Specifically, the study reveals a notable observation of a 30% predominance of T over D at the HFS near the X-point level. This finding is of considerable importance in understanding the behavior of isotopes in the fusion plasma and has implications for optimizing the performance of tokamak devices. The content of this section was also published in [91].

### 6.2.1 Modeling setup

The D+T+Ne plasma mixture is modeled in a JET-like configuration (figure 6.4a) as a test case. The ZG module is enabled in the EMIM mode. The wall geometry and the magnetic equilibrium are taken from the JET D+Ne SOLPS-ITER simulations, which were published in [146]. Our test simulations do not intend to match a real JET experiment, but is rather performed in order to present the new SOLPS-ITER modelling capability for D+T mixtures, particularly considering the recent DT campaign carried out on JET.

**Table 6.1:** Main simulation parameters for the D+T+Ne mixture in the JET-like configuration

| $P_{SOL}$, $MW$ | $\Gamma^{core}_{D(T)}$, $ions/s$ | $\Gamma^{puff}_{D(T)}$, $atoms/s$ | D(T) albedo | $p^{neut}_{D}$, $Pa$ | $p^{neut}_{T}$, $Pa$ | $c^{sep}_{Ne}$ |
|---|---|---|---|---|---|---|
| 18 | $7.5 \cdot 10^{20}$ | $1.7 \cdot 10^{22}$ | 0.991 | 4.7 | 5.3 | 0.02 |

The simulation is performed with drifts and currents enabled. The neutrals are treated kinetically by means of the EIRENE code [147]. In the table 6.1, the main plasma parameters are collected, which are defined by the inputs. The power crossing the separatrix is $P_{SOL} \approx 18\ MW$ and equally distributed between the electron and ion channels. The anomalous transport coefficients are chosen similar to [146] (figure 6.4b). Mimicking the source from NBI, the isotopes fluxes through the core boundary (yellow

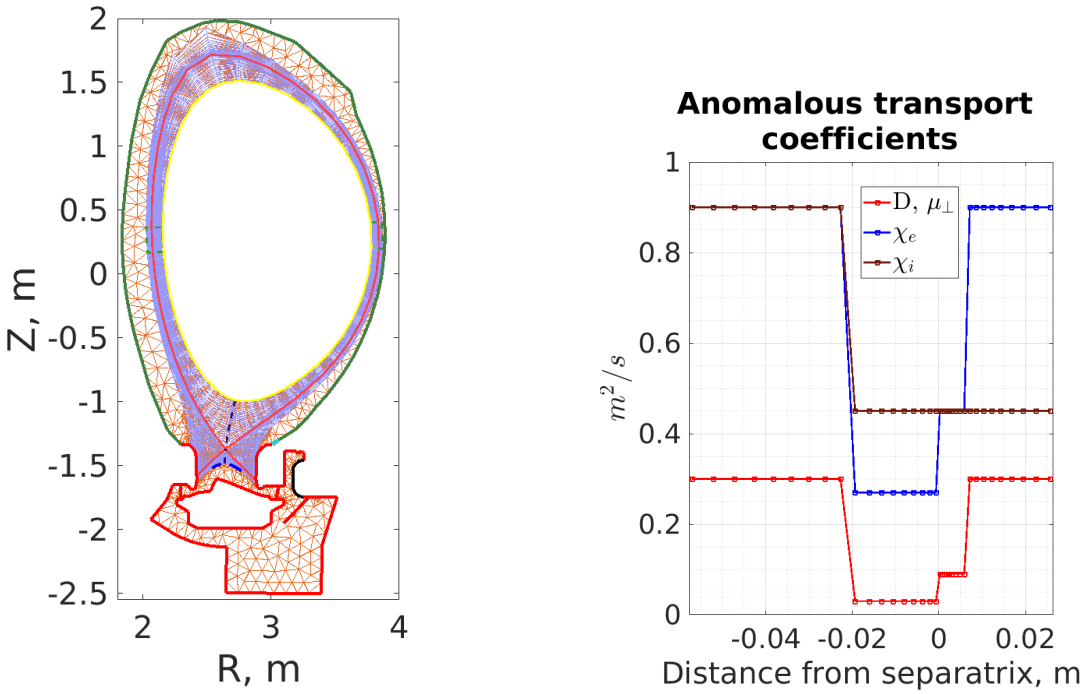


(a) (b)

**Figure 6.4:** (a) JET-like modeling geometry including plasma fluid (purple) and kinetic neutral (orange) numerical grids. Beryllium wall - green. Tungsten wall - red. Core boundary - yellow. Puffing surface - cyan. Pumping surfaces - black. Blue surfaces indicate neutral pressure measurements surfaces. Green dashed lines indicate OMP and IMP. (b) Anomalous transport coefficients at the OMP.

solid line in figure 6.4a) are chosen correspondingly $\Gamma_D^{core} = \Gamma_T^{core} = 7.5 \cdot 10^{20}$ $ions/s$. On JET two hydrogen isotopes are puffed in different poloidal locations [148]. To exclude the contribution of the puffing location effect on the hydrogen isotope transport behavior the D and T puffing locations are chosen the same. From the technical point of view, in this test simulation, it was convenient to place the D-T puffing location above the outer divertor plate (cyan zone in figure 6.4a). The puffing fluxes are imposed as $\Gamma_D^{puff} = \Gamma_T^{puff} = 1.7 \cdot 10^{22}$ $atoms/s$. The albedo coefficient on the cryo-pump surfaces (black in figure 6.4a) is set equal for all species (table 6.1). The recycling coefficient on all other surfaces is chosen to be equal to 1.0, i.e all either D or T species, not reflected as atoms from the W or Be surfaces according to the TRIM-database reflection probability, are emitted as part of either $D_2$ or $T_2$ molecules, respectively [147, 149]. In this simulation, $DT$ molecules are not considered. Thus, the throughput and the pumping speed are established according to the input parameters (table 6.1). As a result, the neutral pressure $p_D^{neut} = 4.7$ $Pa$ and $p_T^{neut} = 5.3$ $Pa$ in the PFR (calculated along the blue surfaces in figure 6.4a) is observed in the simulation. Also, the established OMP profiles are plotted in figures 6.5a and 6.5b.

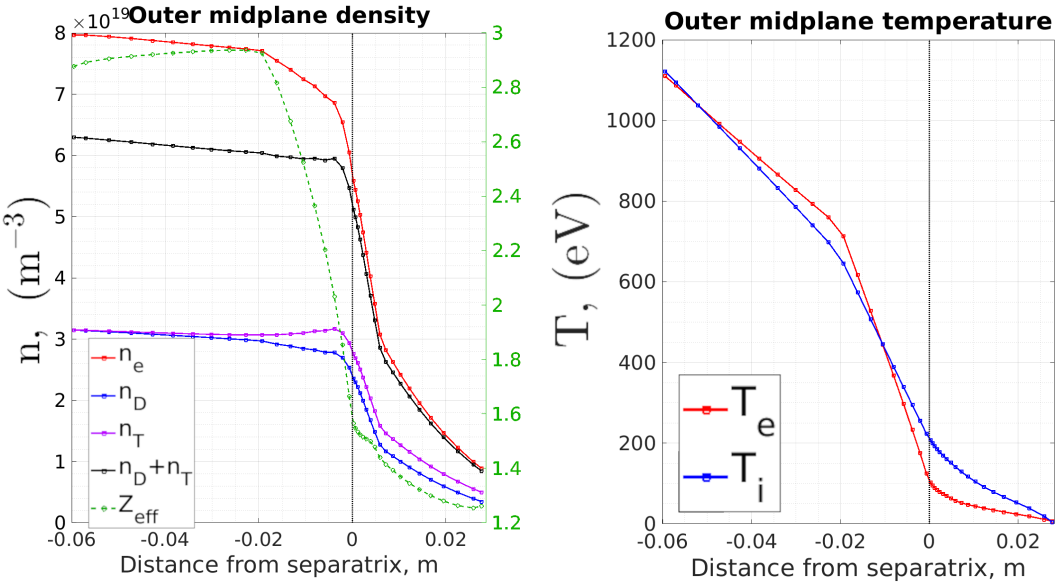


(a) (b)

**Figure 6.5:** Plasma profiles at the OMP. (a) Left axis: electron density ($n_e$) (red), D ion density ($n_D$) (blue), T ion density ($n_T$) (magenta), total hydrogen isotope ion density (black); right axis: $Z_{eff}$ (dashed yellow). (b) Electron temperature ($T_e$) (red), ion temperature ($T_i$) (blue).

To maintain the applicability of collisional theory in the study, there is a deliberate effort to achieve a high collisionality regime in both the SOL and divertor. This is accomplished by introducing a relatively high concentration of Ne impurity in the modeling. The average Ne concentration at the separatrix $c_{Ne}^{sep} \approx 2\%$, as well as $Z_{eff}$ in the confinement region can reach up to 3 (as shown in figure 6.5a). As a result, the strong radiation in the divertor is achieved, creating conditions of low temperature and high density (illustrated in figures 6.6a and 6.6b). These conditions contribute to the high collisionality observed in the SOL.

It should be noted that pronounced detachment occurs on both the inner and outer divertor targets when using the specified simulation parameters. Along the target plates, $T_e$ of approximately 1eV is observed (figure 6.6b). The peak heat load on the outer target reaches 2.2 $MW/m^2$, while on the inner target it is 1.5 $MW/m^2$. This simulation qualitatively corresponds to the Ne 6.0e19 atoms/s seeding run described in [146] and the run with a peak outer target heat load of 2 $MW/m^2$ mentioned in [150].

### 6.2.2 Collisional theory applicability

The Knudsen number according to the $\nabla_\parallel T_i$ scale in the form of $Kn = \lambda_D^{eff} \cdot |\nabla_\parallel T_i / (T_i^{loc\ max} - T_i^{loc\ min})|$ can be applied for the main ion collisionality analysis. Here the $\lambda_D^{eff}$ is the D effective mean-free path, and $T_i^{loc\ max}, T_i^{loc\ min}$ are the local extrema along $\mathbf{B}$. Thus,

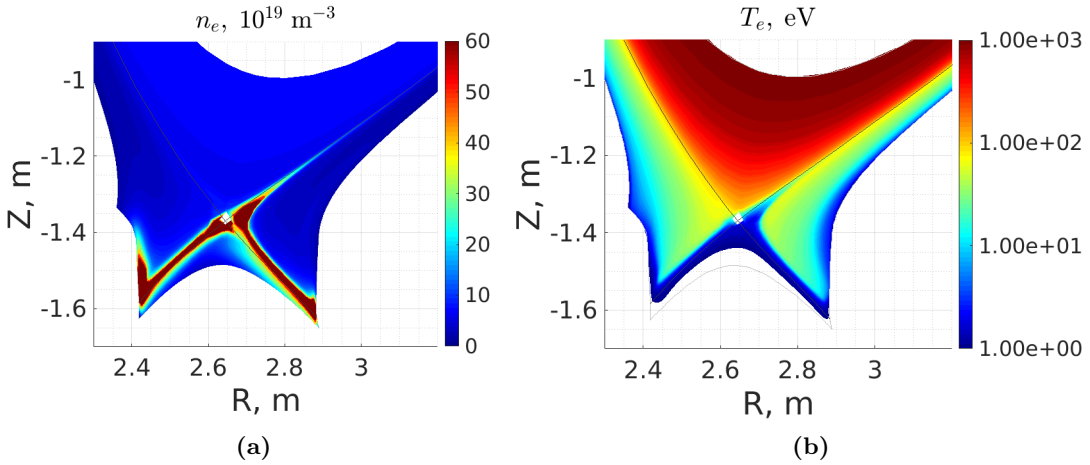


**Figure 6.6:** (a) $n_e$ 2D profile in the divertor. (b) $T_e$ 2D profile in the divertor.

the $L_\parallel = (|\nabla_\parallel T_i/(T_i^{loc\ max} - T_i^{loc\ min})|)^{-1}$ is a characteristic distance in the parallel direction between two local extrema. On the closed flux surfaces, this distance is between the top and the bottom of the tokamak. In the SOLPS-ITER modeling with drifts, the poloidal $T_i$ variation on the closed flux surfaces is driven by the diamagnetic drift and has neoclassical nature [83]. In the SOL, $L_\parallel$ is a characteristic distance in the parallel direction between the upstream point and the target.

Using the relation $\nu_i^* \approx L_\parallel/(\pi\lambda_D^{eff})\varepsilon^{-3/2}$, where $\nu_i^*$ is defined according to Eq. (6.87) in [81], the $Kn \approx \varepsilon^{-3/2}/(\pi\nu_i^*)$. Therefore, $Kn > 1/\pi$ corresponds to $\nu_i^* < \varepsilon^{-3/2}$. We confirm that in the JET H-mode, the pedestal is in the platue-banana regime (shown in figure 6.7a). Thus, the neoclassical corrections, similar to the ones used in [83], are applied on closed flux surfaces. However, in the SOL, $Kn \leq 0.1$. Subsequently, one can expect a thermal D ion collides 10-100 times on the distance between the upstream and the target along $\mathbf{B}$ (figure 6.7a).

Another criterion that can be utilized in the SOL is the Zhdanov parallel heat flux, denoted as $h_{\parallel D^+}$, which is normalized to the convective heat flux carried by ions with the thermal velocity of $\sqrt{T_i/m_D} \cdot p_{D^+}$ (as shown in figure 6.7b). This coefficient is the third term in the polynomial correction to the Maxwell distribution function (6.1). For an accurate polynomial approximation, all coefficients in (6.1) should be smaller than unity. Among the other coefficients in the distribution function approximation for D (and also for T) (6.1), the heat-flux-dependent coefficient is found to be the closest to unity in the essential regions of the domain. In the confinement region, this criterion is satisfied. However, the Knudsen number (figure 6.7a) indicates that the mean-free path is greater than the top-bottom connection length, implying the need to consider non-local kinetic effects. Local collisional closure is applicable in the collisional SOL, but in regions with steep gradients, the solution approaches the boundary of collisional theory applicability. One should be cautious when using simplistic analysis, as non-local suprathermal particles can exhibit non-collisional behavior under these conditions and

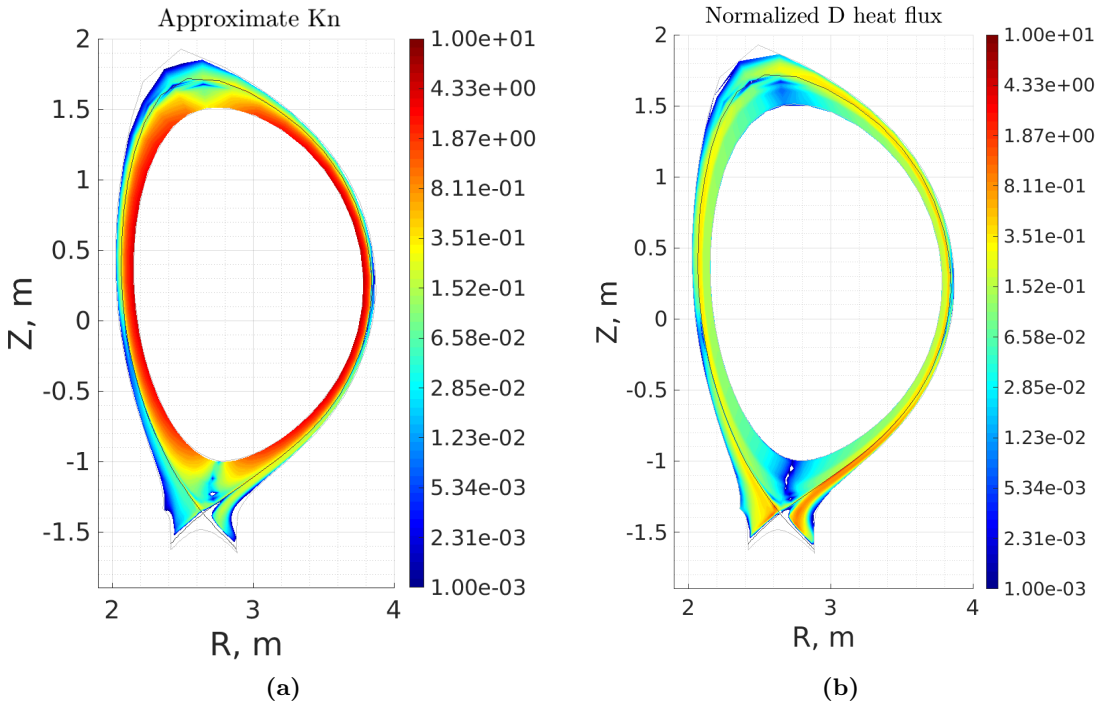


**Figure 6.7:** (a) The Knudsen number according to the $\nabla_{\parallel} T_i$ scale (b) The normalized D parallel heat flux (before flux limiting application) $|h_{\parallel D^+}/(\sqrt{T_i/m_D} \cdot p_{D^+})|$. The colour bar is on a logarithmic scale and the white region is below the scale.

significantly contribute to the heat flux [151]. For studying the contribution of kinetic effects to transport along **B**, the KIPP kinetic code was coupled with a 1D version of the SOLPS code [152] and can be applied in the future for one flux-tube for cross-comparison with our local model. In this section, the Ne transport is not studied in details, otherwise the Zhdanov closure applicability should also be checked of Ne, as it is done in subsection 6.1.3.

### 6.2.3 Difference in the hydrogen isotope transport in the SOL

In this D+T+Ne test simulations, no obvious differences observed in the main plasma and impurity transport behaviour with respect to the D+Ne SOLPS-ITER simulations from [146]. However, a direct one to one comparison between the pure-D and D/T plasmas is left for future studies, which can reveal the isotope effect on main and impurity ions transport parameters.

In the thesis, we focus on the D-T TF phenomenon, which is a direct consequence of the Zhdanov closure applied. The D-T TF leads to the isotope separation in the presence of $\nabla_{\parallel} T_i$. As illustrated in figure 6.8a, the T accumulation at the HFS divertor entrance with respect to D is observed. Before studying this phenomenon in detail, a simple test

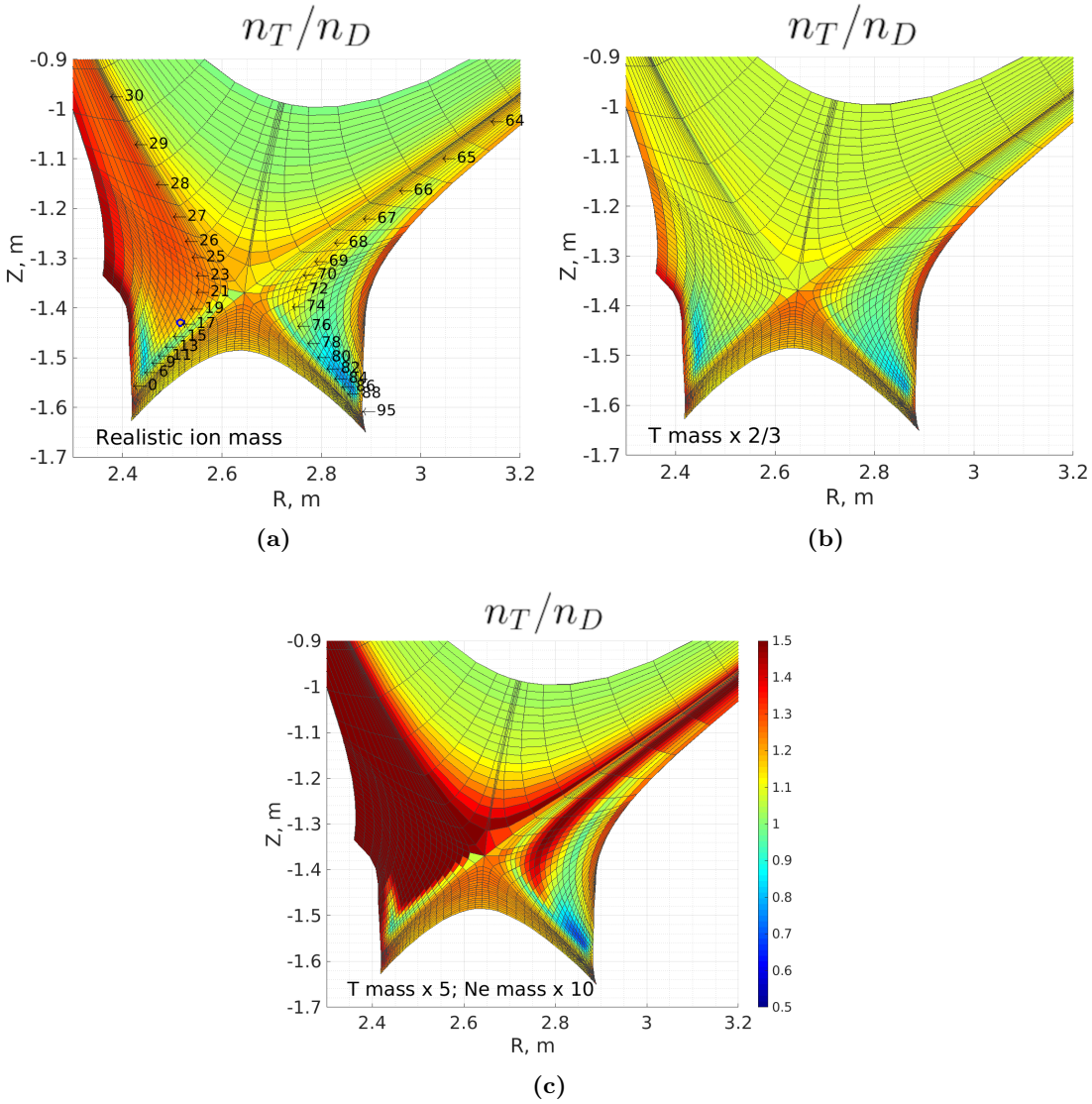


**Figure 6.8:** The T and D ion density ratio $n_T/n_D$ as a result artificial adjustment of the isotope mass ratio $m_T/m_D$ for the TF and FR kinetic coefficients calculation. (a) a realistic ion mass is used: $m_T/m_D = 1.5$; (b) T mass is factored by 2/3: $m_T/m_D = 1$; (c) T mass is factored by 5: $m_T/m_D = 7.5$, Ne mass is factored by 10 (to keep Ne heavier than both hydrogen isotopes). Black numbers represent poloidal cell numbers in the reference flux tube (number 7 from the separatrix), where the TF effect is analysed (figures 6.10a and 6.10a). In the poloidal cell number 17, the ion distribution functions analysis is performed in figure 6.11.

is performed to demonstrate that this T vs D HFS accumulation is a result of the TF effect.

Based on (4.58) and the qualitative understanding of the TF (subsection 2.3.2), one can note that the "hot-tails" of the different species counterbalance each other in the momentum r.h.s. reducing TF to zero, if the mass of the species become close to each other. Thus, the mass of T is artificially reduced by factor of 2/3 for the TF and FR kinetic coefficients calculation. The D-T TF, i.e. the one which is obtained by subtracting the TF due to D-Ne and T-Ne interactions from the total TF, become close to zero. As shown in figure 6.8b the $n_T/n_D \to 1$ at the HFS divertor entrance. The inner-outer $n_T/n_D$ divertor asymmetry is also reduced (figure 6.8b). This is a clear evidence of the TF contribution into the isotope separation phenomenon in the SOL.

One can approach the opposite limit: the mass ratio is artificially increased by multiplying $m_T \times 5$ ($m_T/m_D = 7.5$) for the TF and FR calculation. Effectively, the kinetic coefficients become closer to the ZY expression ones according to (4.110) and (4.119). Subsequently, the D-T TF increases dramatically, which leads to even larger T over D predominance at the HFS (figure 6.8c) than for the reference "realistic ion mass" case (figure 6.8a). This level of T accumulation at the HFS is due to our $m_T/m_D \to \infty$ exercise and purely non-physical. This test shows that the original SOLPS-ITER model with the ZY TF should not be applied for D-T simulations. Moreover, the further increasing of $m_T/m_D$ leads to the numerical convergence problems due to the large non-physical TF. Thus, apart from small changes, which is needed for impurity assumption relaxation, the ZG module implementation is necessary to introduce T in comparable to D amounts in the modeling.

There is also $n_T/n_D > 1$ in the PFR and in the vicinity of targets in all three cases, including "T mass $\times$ 2/3" case with the suppressed D-T TF (figure 6.8b). This is a result of the difference in the neutral dynamics of the hydrogen isotopes. This phenomenon is out of the thesis scope. For details we refer the reader to [91].

### 6.2.4 Thermal force and poloidal flows

As illustrated in previous studies, such as [150], when the ion $\nabla B$ drift is directed towards the lower X-point, the main ion poloidal flows from the LFS to the HFS are generated (indicated by the blue arrow in figure 6.9a). These flows originate from the LFS X-point level (blue circle in figure 6.9a) as a result of drift and recycling flows [150].

In this thesis, we analyze the influence of both these poloidal flows and the TF of D-T on the T build-up at the inner divertor entrance, which is observed in figure 6.8a. It is convenient to plot the SOL region in figure 6.8a on the numerical rectangular SOLPS-ITER mesh: figure 6.9b, where the flux tubes are positioned parallel to the horizontal axis.

The close ion poloidal flows enter $F_T^{ion\ inner}/F_D^{ion\ inner} = 1.15$ (with a slight predominance of T in the flow) into the HFS divertor region (indicated by the blue arrow in figures 6.9a and 6.9b). Further in the inner divertor region the ion poloidal flows, which are marked by the magenta arrows in figures 6.9a and 6.9b are additionally fed by the

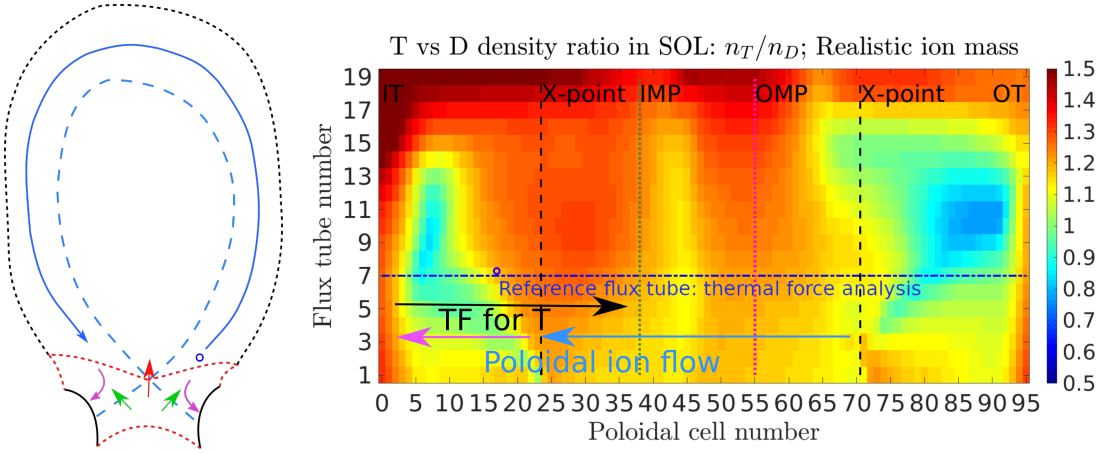


**Figure 6.9:** (a) Schematic of the main fluxes in the SOL. Blue arrow - poloidal ion flow in SOL from the LFS towards the HFS. Blue circle - approximate stagnation point of poloidal flows. Magenta arrows - poloidal ion fluxes in the divertor region. Green arrows - neutral fueling from the PFR to the SOL below X-point. Red arrow - neutral fueling of the confined region. (b) Ratio T to D ion density in the SOL for the "realistic ion mass" case (the same as in figure 6.8a) plotted on the numerical rectangular SOLPS-ITER mesh: vertical scale - numerical magnetic flux tube number, beginning from the separatrix and ending at the computational boundary in the far-SOL; horizontal scale - poloidal cell number from the inner target (IT) to the outer target (OT). Dark blue dash-dotted horizontal line - the reference flux tube, where the TF effect is analysed (figures 6.10a and 6.10a); black dashed vertical line - divertor entrance; green dotted vertical line - IMP poloidal location; magenta dotted vertical line - OMP location.

D and T neutral flows from the PFR. Those define the T vs D ratio in the flow towards the inner target.

For further analysis one can consider the reference flux tube (number 7 from the separatrix), which is marked in figure 6.9b. Qualitatively similar behaviour is also observed in several neighbouring flux tubes from both sides. As illustrated in figure 6.10b, the parallel flow ratio $n_T u_T^{\parallel}/n_D u_D^{\parallel} \approx 1$ in this flux tube, which are formed by the close neutral D and T flows from the PFR. In the inner divertor the T-D TF, which is obtained by subtracting the TF due to D-Ne and T-Ne interactions from the total TF, is counterbalanced by the T-D FR, i.e. the part of the T FR, which is proportional to the $u_T^{\parallel} - u_D^{\parallel}$, as it is shown in figure 6.10a. Similar behavior is also observed in the outer divertor (figure 6.10a). Note, in the vicinity of the target (poloidal cell numbers from 0 to 6) the TF is much smaller than FR (figure 6.10a). Besides, the $n_T u_T^{\parallel}/n_D u_D^{\parallel} > 1$ due to the neutral dynamics, which is discussed in details in [91], and the $u_T^{\parallel}/u_D^{\parallel} \approx 1$ due to the strong FR.

Further from the target (poloidal cell numbers from 6 to 23), the $T_i$, which is marked as red dashed line in figure 6.10b, increases dramatically, which forms the TF. The

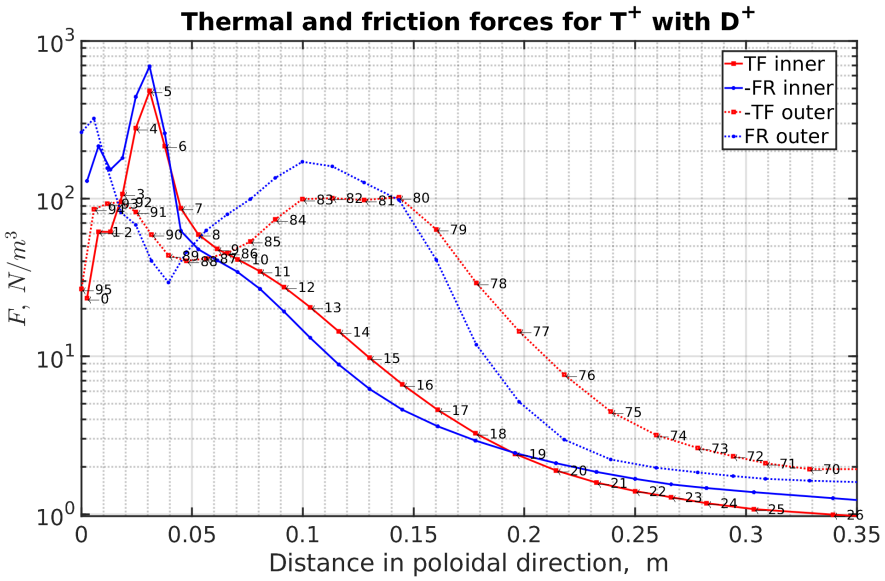


(a)

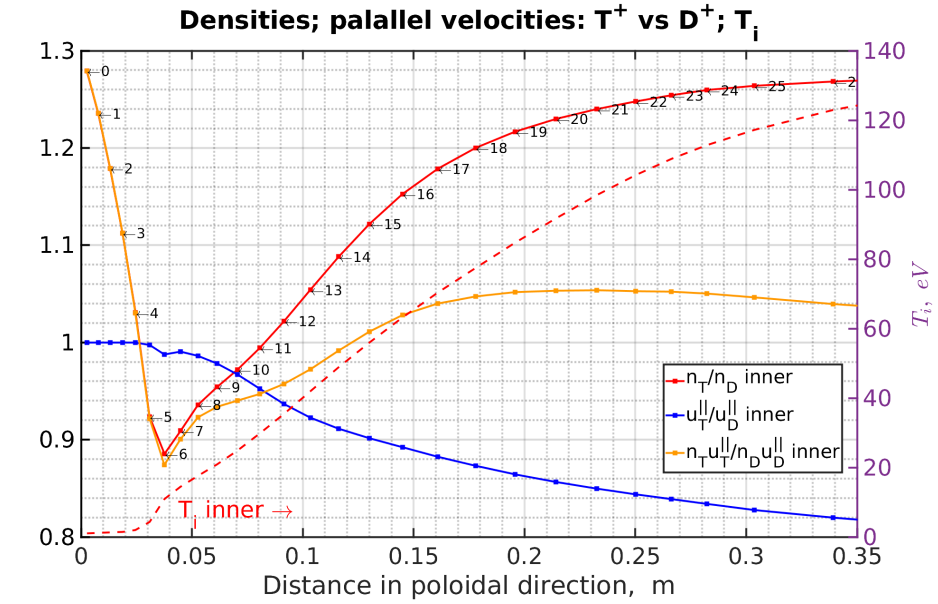


(b)

**Figure 6.10:** (a) The TF (red) and FR (blue), which act on the T species due to the D-T interactions (due to the D-T flow velocity difference for FR), in the inner (solid) and outer (dashed) divertor in the reference flux tube shown in figure 6.9b (poloidal distance from the corresponding target is marked along the horizontal axis). Numbers correspond to the poloidal numerical cells (horizontal axis in figure 6.9b). (b) Solid lines: ratio of T vs D ion densities (red), ion parallel velocities (blue) and ion parallel fluxes (yellow) in the inner divertor in the reference flux tube (left vertical scale). Dashed line: $T_i$ (right vertical scale).

counterbalancing FR forms the $u_T^{\parallel} - u_D^{\parallel}$ and $u_T^{\parallel}/u_D^{\parallel} < 1$ (figure 6.10b). Due to the particle conservation $n_T u_T^{\parallel}/n_D u_D^{\parallel} \approx 1$, the T predominance over D $n_T/n_D > 1$ (shown as a red solid line in figure 6.10b) is formed at the inner divertor entrance. Thus, the large $n_T/n_D$ peak at the HFS X-point level (figure 6.9b) is a result of the D-T TF and poloidal flows. There is also a smaller $n_T/n_D$ peak at the OMP due to the combination of two effects: overall larger T than D concentration in the poloidal flow, which appears from the LFS X-point level and towards the HFS X-point level, and the $\nabla B$ drift driven $T_i$ poloidal variation mediating the $n_T/n_D$ poloidal varation. This effect is smaller and not considered in the present work.

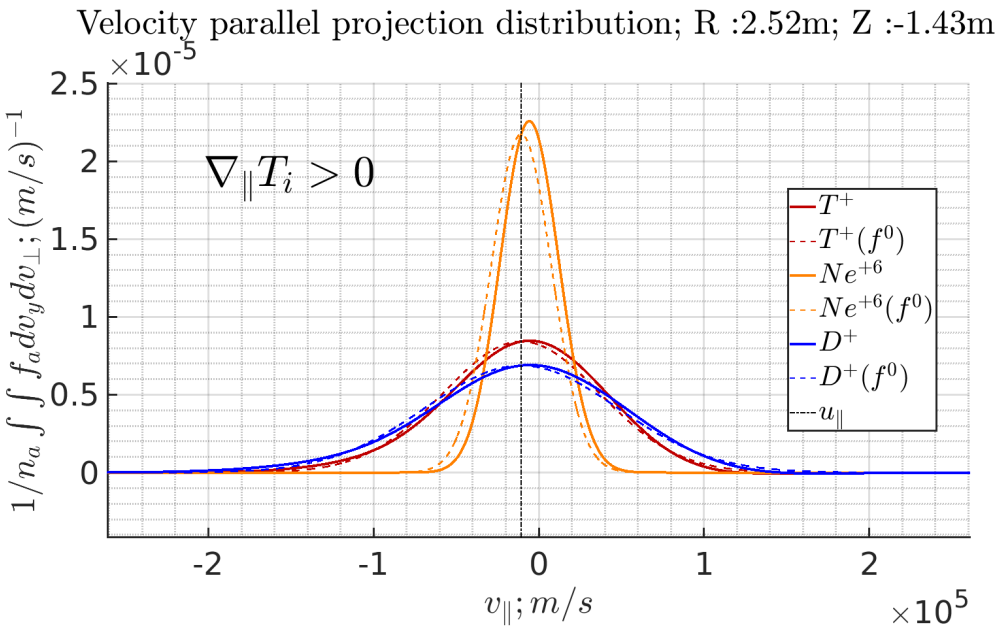


**Figure 6.11:** Distribution functions of the $D^+$, $T^+$ and $Ne^{+6}$ ion species at the HFS in the reference flux tube number 7 from the separatrix and poloidal cell number 17 (see figures 6.8a and 6.9b). $f^0$ is the non-modified Maxwell function.

It should be noted that according to the collisionality criteria, which are expressed in figures 6.7a and 6.7b, the collisional Zhdanov closure is well applicable in the HFS divertor. Also, in figure 6.11, one can observe small Zhdanov corrections to the Maxwell distribution functions, which confirms the linear theory applicability. This allows to apply the new ZG module to study D-T TF contribution into isotope transport in JET SOL.

## 6.3 Conclusions according to the SOLPS-ITER modeling results with Zhdanov-Grad module

In this chapter, we conducted test simulations using the SOLPS-ITER code with the ZG module to showcase the enhanced capabilities of the model. Specifically, we explored D+He+Ne mixture, allowing us to investigate the transport dependence of He on the TF and FR in ITER baseline scenario. We emphasized the significance of considering the $m_D/m_{He} > 0$ contribution in the kinetic coefficients, which leads to the 30% decrease in the separatrix-averaged He relative concentration. Also, we discussed the analysis of distribution functions for D, He and Ne ion species in the ITER divertor, providing insights into the nature of impurity TF, a previously unexplored aspect. Furthermore, we discussed the feasibility of employing the Zhdanov closure for modeling He and Ne impurities.

Additionally, the simulations explored the Zhdanov theory's boundary in terms of linear theory applicability, considering the SOL parameters of ITER. The thesis cautioned about the inclusion of non-linear terms in the collisional operator when dealing with impurities heavier than Ne.

The major accomplishment of this thesis was the successful simulation of a plasma mixture relevant to a reactor scenario, specifically the D-T mixture with impurities, using the SOLPS-ITER code. Prior to the implementation of the ZG module, the SOLPS-ITER was limited to modeling only one hydrogen species with impurities. In this chapter, we performed test simulations for the D+T+Ne mixture in a JET-like configuration, accounting for drifts and kinetic neutrals. Our study examined the applicability of collisional closure in the JET H-mode SOL and analyzed the impact of the D-T TF on isotope separation in the SOL. Notably, the study observed 30% T predominance over D at the HFS at the X-point level, influenced by the effect of the D-T TF and poloidal ion flows in the SOL. Furthermore, it demonstrated that the previous SOLPS-ITER model should not be used for simulations involving different hydrogen isotopes due to significant overestimation of the D-T TF, which leads to numerical issues and non-physical results.

# 7 Conclusion & Outlook

## 7.1 Summary

The simulations of the edge and SOL regions in magnetic fusion devices are very challenging but also hold immense importance in the field. The parameters of the edge and SOL plasma regions have a substantial impact on the overall performance of the plasma. The behavior of plasma can be characterized using either 6D kinetic or 5D gyrokinetic equations incorporating a collisional operator. However, solving these equations numerically requires significant computational resources. In certain regions, particularly in the plasma edge and SOL, highly collisional conditions usually occur, which enable simplifications. The highly collisional regime refers to the conditions that the macroscopic parameters experience gradual variations over length scales that are parallel (or perpendicular) to the mean free path (or gyroradius), as well as over time scales between collisions (or gyromotion periods). This enables the utilization of a moment approach and collisional closure to solve the kinetic equation. In particular, by contracting the distribution function over the velocity space, it becomes possible to solve the system of 3D fluid equations.

For the single ion plasma, the well-known Braginskii closure [17] is used for many transport [88, 102, 104] and turbulent fluid codes [21, 126, 127, 128]. However, for the multi-ion plasmas, when either close ion masses or non-trace concentration of several ions species is considered (for example reactor relevant D+T+He+impurities mixture), the more advanced multi-species closure, such as the Zhdanov closure [18], should be applied. Recently, this closure has been partly implemented into the SOLEDGE3X code [141]: the Zhdanov closure has been applied for the vector moments, but not for tensorial moments. The multi-temperature extension of the Zhdanov closure is under development [92, 99] and supposed to be implemented into the SOLEDGE3X code.

In this thesis, the improvement of the multi-ion models based on the Zhdanov closure is performed for the SOLPS-ITER and GRILLIX codes. First, in chapter 4, new advances in the Zhdanov collisional theory is carried out. The SOLPS-ITER and GRILLIX codes are based on the Bragiskii set of equations, which differ from the Zhdanov ones. Thus, in section 4.1, the specific relations between Zhdanov and corresponding Braginskii moments and r.h.s.'s are obtained (4.17), (4.18), (4.19), (4.22) and (4.20). The corrections for the moments $T_{\alpha Z}$ (4.17), $\mathbf{h}_{\alpha Z}$ (4.18), $\pi_{\alpha Z rs}$ (4.19) are found small according to the Zhdanov ordering, whereas the collisional r.h.s. corrections for the $\mathbf{R}_{\alpha Z}$ (4.22) and $Q_{\alpha Z}$ (4.20) are necessary to conserve momentum and energy in collisions, correspondingly. In particular, the correction (4.20) represents the well-known Joule heating and can not be omitted.

The heat stresses for the fully ionized collisional multi-species plasma are derived in section 4.2 using a general rank-2 moment equation from [18] and [99]. They were not previously obtained by Zhdanov for the 21N-moment approximation (8th chapter in [18]). These heat stress can be comparable with the strain stresses, which were originaly derived in [18], for example the Pfirsch-Schlüter regime (section 12.3 in [100] and [86, 81]). The single-ion heat stress has been implemented into the SOLPS-ITER code [88, 83]. The multi-ion generalization of the SOLPS-ITER heat stress is performed. Additionally, the flow velocities of each species are taken into account for the viscous-stress tensor, whereas $u_{\alpha Zr} \approx u_r$ was assumed there by Zhdanov [18].

The transport coefficients for the rank-1 and rank-2 moments are derived in section 4.3 using guidance from [18]. Besides, the TF and FR are obtained in subsections 4.3.3. Performing this, several mistakes were found in the original monograph [18]. The corresponding mistake corrections are described in appendix A. Also, the charge states corrections are derived for rank-2 moments from scratch (sub-subsection 4.3.4.3), because they are not present in [18]. The viscous-stress tensor is written taking into account heat stresses and the species resolved flow velocities, according to the results from section 4.2. In this section the EMIM for the transport coefficient is discussed.

The improved versions of the ZY expressions are obtained in section 4.4. In contrast to the ZY expressions, which are limited to cases where the impurity mass greatly exceeds the main ion mass, the IAM offers accurate formulas for impurities in D plasmas within the He-Ne range. Moreover, the IAM exhibits correct qualitative behavior when dealing with mixtures of species that have similar masses, which is not always the case with the ZY expressions (e.g., the ZY TF). Additionally, the IAM can be applied to light main species with multiple charge states (e.g., He plasmas with impurities), while the ZY expressions are only applicable to a single charge state. The ZY analytical approach fails to describe the heat flux for heavy impurities (such as in trace-impurity scenarios), where the heat conductivity is proportional to $\tau^{(Zh)}_{imp\ imp}$. However, the IAM successfully provides a qualitatively accurate heat conductivity for heavy trace impurities, which is proportional to $\tau^{(Zh)}_{imp\ main}$.

The improvements of the SOLPS-ITER and GRILLIX models, which are performed in the thesis, are described in chapter 5. The SOLPS-ITER code incorporates the Zhdanov closure as part of the ZG module, enabling the calculation of transport coefficients for various parameters such as the heat flux, the TF, the FR, the strain and the heat parallel stresses (section 5.1). The IAM and EMIM are used to derive these coefficients. Additionally, the SOLPS-ITER model now includes the ion velocity difference heat flux, which was not present in previous versions. This implementation results in a complete multi-ion generalization of the SOLPS-ITER model, allowing for uniform equations across all ion species without specifying main or impurity species. It should be noted that this generalization would not have been possible without the derivation of multi-species heat stress (see in section 4.2 and subsection 4.3.4), which is a crucial component of the original SOLPS-ITER model.

As for the GRILLIX code, the equations for multiple ion species have been formulated. The polarization drifts for each ion species are introduced using the total po-

larization current, following the Zhdanov ordering. This approach avoids the explicit implementation of polarization flux divergence in the continuity equation by expressing it through the vorticity equation. The model implementation undergoes the CI/CD procedure through the MMS integration tests. The MPI infrastructure is prepared to handle the multi-ion equations. However, the actual implementation of these equations into the GRILLIX code has not yet been carried out and has been left for future model developments.

Finally, the test SOLPS-ITER simulations are carried out in chapter 6. These simulations are meant to demonstrate the capability of the improved multi-ion model of the SOLPS-ITER code. The ITER D+He+Ne and JET-like D+T+Ne modeling is performed. Specifically, the influence of the TF and FR on He transport in the ITER baseline scenario is investigated. The importance of considering the contribution of $m_D/m_{He} > 0$ to the kinetic coefficients is also discussed. The implementation of the new TF and FR formulation results in a significant 30% decrease in the separatrix-averaged He relative concentration for a constant He core source and engineering pumping speed compared to the old formulation. Furthermore, the chapter presents an analysis of the distribution functions for D, He and Ne ions in the ITER divertor, shedding light on the nature of impurity TF. The feasibility of employing the Zhdanov closure for modeling He and Ne impurities is examined. Namely, the simulations explore the limits of the Zhdanov theory in terms of its applicability to linear theory, taking into account the SOL parameters of ITER. The thesis cautions against including nonlinear terms in the collisional operator when dealing with impurities heavier than Ne.

The main accomplishment of the thesis is the successful simulation of a plasma mixture relevant to a reactor scenario, specifically the D-T mixture with impurities, using the SOLPS-ITER code. Prior to the implementation of the ZG module, the SOLPS-ITER model only allowed for modeling one hydrogen species with impurity. In this chapter, test simulations are conducted for the D+T+Ne mixture in a JET-like configuration, considering drifts and kinetic neutrals. The study examines the applicability of collisional closure in the JET H-mode SOL and analyzes the impact of the D-T TF on isotope separation in the SOL. Notably, the study observes 30% predominance of T over D at the HFS at the X-point level, influenced by the effect of the D-T TF and poloidal ion flows in the SOL. Furthermore, it is demonstrated that the previous SOLPS-ITER model should not be used for simulations involving different hydrogen isotopes due to significant overestimation of the D-T TF, which leads to numerical issues and non-physical results.

## 7.2 Outlook

Significant advancements are made in the further development of the Zhdanov closure. Currently, there is ongoing work on the multi-temperature generalization of the Zhdanov collisional theory, as discussed in references [92, 99]. This advancement is crucial as it captures new transport behaviors resulting from temperature differences among ion species, which cannot be accounted for by the original 21N-moment Zhdanov closure

[18] that assumes a common temperature for the mixture for the kinetic coefficient calculations.

The ZG module is currently being prepared for integration into the new wide-grid version of the SOLPS-ITER code [153]. This updated version allows for the extension of the computational domain up to the material wall. In the current 3.0.8 SOLPS-ITER version, the last simulated flux surface in the SOL and the PFR is limited by intersections with device material elements, imposing constraints on the variety of tokamak configurations that can be modeled. Furthermore, phenomena occurring in the far-SOL region, such as first wall sputtering, recycling, and far-SOL transport, cannot be adequately studied with the 3.0.8 SOLPS-ITER code. By detaching the ZG module from the SOLPS-ITER code and publishing it as a separate Fortran library, it can be applied to other fluid codes.

The infrastructure of the GRILLIX code is prepared to accommodate the implementation of multi-ion fluid equations. In the future, a fully multi-ion fluid turbulence model can be applied, enabling investigation of impurity turbulent transport behavior in the plasma edge and SOL in the magnetic fusion devices. Additionally, the turbulence phenomenon in D-T mixtures can be studied and compared with pure-D mixtures using the multi-ion GRILLIX model.

Following the test simulations conducted in the thesis, simulations can be carried out for actual JET experiments involving a D-T mixture, which is successfully conducted during the DTE2 JET campaign. Predictive simulations for ITER, involving D+T+He+Ne mixtures, should also be performed using the SOLPS-ITER code. Studying hydrogen isotope transport in ITER is particularly important due to the different injection methods for D and T species in the machine, which are currently designed for ITER, with T fueling performed through pellet injection in the core and D fueling employing both pellet injection in the core and gas puff into the divertor.

He plasmas serve as excellent test beds for validating our fluid models, such as SOLPS-ITER and GRILLIX, due to their higher collisionality compared to D plasmas. For example, highly collisional conditions are also present in the H-mode pedestal of the ASDEX Upgrade tokamak (as shown in figure 1.8b). Accurately representing the main plasma and impurity transport, particularly in the Pfirsch-Schlüter regime, is essential in our fluid models. When investigating pure-He or He+impurities plasmas, the multi-ion closure should be applied. Exploring these mixtures could be an interesting avenue for future studies using our multi-ion fluid models based on the Zhdanov closure.

# Bibliography


[1] PAGES 2k Consortium. Consistent multidecadal variability in global temperature reconstructions and simulations over the common era. *Nature geoscience*, 12(8):643–649, 2019.

[2] C. P. Morice, J. J. Kennedy, N. A. Rayner, J. P. Winn, E. Hogan, R. E. Killick, R. J. H. Dunn, T. J. Osborn, P. D. Jones, and I. R. Simpson. An updated assessment of near-surface temperature change from 1850: The hadcrut5 data set. *Journal of Geophysical Research: Atmospheres*, 126(3):e2019JD032361, 2021. e2019JD032361 2019JD032361. URL: `https://agupubs.onlinelibrary.wiley.com/doi/abs/10.1029/2019JD032361`, `doi:https://doi.org/10.1029/2019JD032361`.

[3] Temperature date sets (hadcrut, crutem, hadcrut5, crutem5), Mar 2023. URL: `https://crudata.uea.ac.uk/cru/data//temperature/#datdow`.

[4] Global surface temperature, Mar 2023. URL: `https://climate.nasa.gov/vital-signs/global-temperature/`.

[5] National Oceanic and Atmospheric Administration. GLOBALVIEW+$CO_2$ database: direct mesuments (1979-2022), ice-core data based on: Rubino at al., JGR 118 (2013), MacFarling Meure et al., GRL 33 (2006), Neftel et al., Nature 315 (1985), Petitet at al., Nature 399 (1999), Siegnthaler et al., Science 310 (2005), Lüthi et al., Nature 453 (2008). URL: `https://gml.noaa.gov/ccgg/trends/history.html`.

[6] Carbon dioxide concentration, Mar 2023. URL: `https://climate.nasa.gov/vital-signs/carbon-dioxide/`.

[7] S. E. Wurzel and S. C. Hsu. Progress toward fusion energy breakeven and gain as measured against the lawson criterion. *Physics of Plasmas*, 29(6):062103, 2022. URL: `https://doi.org/10.1063/5.0083990`, `doi:10.1063/5.0083990`.

[8] G. Haxel, J. Hedrick, and G. Orris. *Rare Earth Element Resources: A Basis for High Technology*. 09 2002.

[9] D. Maisonnier, I. Cook, P. Sardain, R. Andreani, L. D. Pace, R. Forrest, L. Giancarli, S. Hermsmeyer, P. Norajitra, N. Taylor, and D. Ward. *A CONCEPTUAL STUDY OF COMMERCIAL FUSION POWER PLANTS*. EUROPEAN FUSION DEVELOPMENT AGREEMENT, 2005.

[10] P. Magaud, G. Marbach, and I. J. Cook. Nuclear fusion reactors. 2004.

[11] U. Stroth. *Plasmaphysik*. Springer, 2011.

[12] Y. Song, X. Zou, X. Gong, A. Becoulet, R. Buttery, P. Bonoli, T. Hoang, R. Maingi, J. Qian, X. Zhong, A. Liu, E. Li, R. Ding, J. Huang, Q. Zang, H. Liu, L. Wang, L. Zhang, G. Li, Y. Sun, A. Garofalo, T. Osborne, T. Leonard, S. G. Baek, G. Wallace, L. Xu, B. Zhang, S. Wang, Y. Chu, T. Zhang, Y. Duan, H. Lian, X. Zhang, Y. Jin, L. Zeng, B. Lyu, B. Xiao, Y. Huang, Y. Wang, B. Shen, N. Xiang, Y. Wu, J. Wu, X. Wang, B. Ding, M. Li, X. Zhang, C. Qin, W. Xi, J. Zhang, L. Huang, D. Yao, Y. Hu, G. Zuo, Q. Yuan, Z. Zhou, M. Wang, H. Xu, Y. Xie, Z. Wang, J. Chen, G. Xu, J. Hu, K. Lu, F. Liu, X. Wu, B. Wan, J. Li, and null null. Realization of thousand-second improved confinement plasma with Super I-mode in Tokamak EAST. *Science Advances*, 9(1):eabq5273, 2023. URL: `https://www.science.org/doi/abs/10.1126/sciadv.abq5273`, `doi:10.1126/sciadv.abq5273`.

[13] ITER organization. EAST DEMONSTRATES 1000-SECOND STEADY-STATE PLASMA, APRIL 04, 2022. URL: `https://www.iter.org/newsline/-/3740`.

[14] EUROfusion. European researchers achieve fusion energy record, FEBRUARY 8, 2022. URL: `https://euro-fusion.org/eurofusion-news/european-researchers-achieve-fusion-energy-record/`.

[15] ITER organization. JET MAKES HISTORY, AGAIN, FEBRUARY 14, 2022. URL: `https://www.iter.org/newsline/-/3722`.

[16] F. Reimold. Experimental studies and modeling of divertor plasma detachment in h-mode discharges in the asdex upgrade tokamak. page 138, 2015.

[17] S. Braginskii. Transport processes in a plasma. *Reviews of Plasma Physics, edited by MA Leontovich Consultants Bureau, Consultants Bureau, New York*, 1, 1965.

[18] V. Zhdanov. *Transport Processes in Multicomponent Plasma*. Taylor & Francis, London, New York, English edition, 10 2002.

[19] Tony873004. Borisov approaches the ecliptic plane between the orbits of Jupiter (pink) and Mars (orange). URL: `https://en.wikipedia.org/wiki/2I/Borisov#/media/File:Interstellar_visitors.jpg`.

[20] I. Y. Senichenkov, E. G. Kaveeva, V. A. Rozhansky, S. P. Voskoboynikov, I. Y. Veselova, N. V. Shtyrkhunov, D. P. Coster, X. Bonnin, and the ASDEX Upgrade Team. Approaching the radiating X-point in SOLPS-ITER modeling of ASDEX Upgrade H-mode discharges. *Plasma Physics and Controlled Fusion*, 63(5):055011, apr 2021. URL: `https://dx.doi.org/10.1088/1361-6587/abe886`, `doi:10.1088/1361-6587/abe886`.

[21] A. Stegmeir, D. Coster, A. Ross, O. Maj, K. Lackner, and E. Poli. GRILLIX: a 3D turbulence code based on the flux-coordinate independent approach. *Plasma*

*Physics and Controlled Fusion*, 60(3):035005, jan 2018. URL: https://dx.doi.org/10.1088/1361-6587/aaa373, doi:10.1088/1361-6587/aaa373.

[22] BP Statistical Review of World Energy 2022 — 71st edition. *BP*, 2022. URL: https://www.bp.com/content/dam/bp/business-sites/en/global/corporate/pdfs/energy-economics/statistical-review/bp-stats-review-2021-full-report.pdf.

[23] World Energy Outlook 2022. *International Energy Agency*, 2022. URL: https://iea.blob.core.windows.net/assets/4ed140c1-c3f3-4fd9-acae-789a4e14a23c/WorldEnergyOutlook2021.pdf.

[24] S. van den Brink, R. Kleijn, B. Sprecher, and A. Tukker. Identifying supply risks by mapping the cobalt supply chain. *Resources, Conservation and Recycling*, 156:104743, 2020. URL: https://www.sciencedirect.com/science/article/pii/S0921344920300653, doi:https://doi.org/10.1016/j.resconrec.2020.104743.

[25] G. Federici, C. Bachmann, L. Barucca, C. Baylard, W. Biel, L. Boccaccini, C. Bustreo, S. Ciattaglia, F. Cismondi, V. Corato, C. Day, E. Diegele, T. Franke, E. Gaio, C. Gliss, T. Haertl, A. Ibarra, J. Holden, G. Keech, R. Kembleton, A. Loving, F. Maviglia, J. Morris, B. Meszaros, I. Moscato, G. Pintsuk, M. Siccinio, N. Taylor, M. Tran, C. Vorpahl, H. Walden, and J. You. Overview of the DEMO staged design approach in Europe. *Nuclear Fusion*, 59(6):066013, apr 2019. URL: https://dx.doi.org/10.1088/1741-4326/ab1178, doi:10.1088/1741-4326/ab1178.

[26] G. Federici, L. Boccaccini, F. Cismondi, M. Gasparotto, Y. Poitevin, and I. Ricapito. An overview of the EU breeding blanket design strategy as an integral part of the DEMO design effort. *Fusion Engineering and Design*, 141:30–42, 2019. URL: https://www.sciencedirect.com/science/article/pii/S0920379619301590, doi:https://doi.org/10.1016/j.fusengdes.2019.01.141.

[27] G. Caruso, S. Ciattaglia, B. Colling, L. D. Pace, D. Dongiovanni, M. D'Onorio, M. Garcia, X. Jin, J. Johnston, D. Leichtle, T. Pinna, M. Porfiri, W. Raskob, N. Taylor, N. Terranova, and R. Vale. DEMO – The main achievements of the Pre – Concept phase of the safety and environmental work package and the development of the GSSR. *Fusion Engineering and Design*, 176:113025, 2022. URL: https://www.sciencedirect.com/science/article/pii/S0920379622000254, doi:https://doi.org/10.1016/j.fusengdes.2022.113025.

[28] Z. Vizvary, W. Arter, C. Bachmann, T. Barrett, B. Chuilon, P. Cooper, E. Flynn, M. Firdaouss, T. Franke, J. Gerardin, R. Gowland, M. Kovari, F. Maviglia, M. Richiusa, E. V. R. Adame, C. Vorpahl, A. Wilde, and Y. Xue. European DEMO first wall shaping and limiters design and analysis status. *Fusion Engineering and Design*, 158:111676, 2020. URL: https://www.sciencedirect.com/

science/article/pii/S0920379620302246, doi:https://doi.org/10.1016/j.fusengdes.2020.111676.

[29] Lithium. *U.S. Geological Survey.*, 2023. URL: https://pubs.usgs.gov/periodicals/mcs2023/mcs2023-lithium.pdf.

[30] Beryllium. *U.S. Geological Survey.*, 2023. URL: https://pubs.usgs.gov/periodicals/mcs2023/mcs2023-beryllium.pdf.

[31] Lea. *U.S. Geological Survey.*, 2023. URL: https://pubs.usgs.gov/periodicals/mcs2023/mcs2023-lead.pdf.

[32] Tungsten. *U.S. Geological Survey.*, 2023. URL: https://pubs.usgs.gov/periodicals/mcs2021/mcs2021-tungsten.pdf.

[33] A. Bradshaw, T. Hamacher, and U. Fischer. Is nuclear fusion a sustainable energy form? *Fusion Engineering and Design*, 86(9):2770–2773, 2011. Proceedings of the 26th Symposium of Fusion Technology (SOFT-26). URL: https://www.sciencedirect.com/science/article/pii/S0920379610005119, doi:https://doi.org/10.1016/j.fusengdes.2010.11.040.

[34] International Nuclear Safety Advisory Group. *The Chernobyl Accident: Updating of INSAG-1: INSAG-7: a Report*. Number 7. International Atomic Energy Agency, 1992.

[35] *The Fukushima Daiichi Accident*. Non-serial Publications. INTERNATIONAL ATOMIC ENERGY AGENCY, Vienna, 2015. URL: https://www.iaea.org/publications/10962/the-fukushima-daiichi-accident.

[36] *Three Mile Island : a nuclear crisis in historical perspective*. Berkeley : University of California Press ; [Washington, D.C.: Nuclear Regulatory Commission], 2004.

[37] E. Sartori. Nuclear data for radioactive waste management. *Annals of Nuclear Energy*, 62:579–589, 2013. URL: https://www.sciencedirect.com/science/article/pii/S0306454913000790, doi:https://doi.org/10.1016/j.anucene.2013.02.003.

[38] D. Perrault. Safety issues to be taken into account in designing future nuclear fusion facilities. *Fusion Engineering and Design*, 109-111:1733–1738, 2016. Proceedings of the 12th International Symposium on Fusion Nuclear Technology-12 (ISFNT-12). URL: https://www.sciencedirect.com/science/article/pii/S0920379615302994, doi:https://doi.org/10.1016/j.fusengdes.2015.10.012.

[39] A. Litnovsky, J. Schmitz, F. Klein, K. De Lannoye, S. Weckauf, A. Kreter, M. Rasinski, J. W. Coenen, C. Linsmeier, J. Gonzalez-Julian, M. Bram, I. Povstugar, T. Morgan, D. Nguyen-Manh, M. Gilbert, D. Sobieraj, and J. S. Wróbel.

Smart Tungsten-based Alloys for a First Wall of DEMO. *Fusion Engineering and Design*, 159:111742, 2020. URL: https://www.sciencedirect.com/science/article/pii/S0920379620302908, doi:https://doi.org/10.1016/j.fusengdes.2020.111742.

[40] N. Taylor, S. Ciattaglia, H. Boyer, D. Coombs, X. Z. Jin, K. Liger, J. C. Mora, G. Mazzini, T. Pinna, and E. Urbonavičius. Resolving safety issues for a demonstration fusion power plant. *Fusion Engineering and Design*, 124:1177–1180, 2017. Proceedings of the 29th Symposium on Fusion Technology (SOFT-29) Prague, Czech Republic, September 5-9, 2016. URL: https://www.sciencedirect.com/science/article/pii/S0920379617301011, doi:https://doi.org/10.1016/j.fusengdes.2017.02.018.

[41] Department of Energy. DOE National Laboratory Makes History by Achieving Fusion Ignition, DECEMBER 13, 2022. URL: https://www.energy.gov/articles/doe-national-laboratory-makes-history-achieving-fusion-ignition.

[42] C. Orth, S. Payne, and W. Krupke. A diode pumped solid state laser driver for inertial fusion energy. *Nuclear Fusion*, 36(1):75, jan 1996. URL: https://dx.doi.org/10.1088/0029-5515/36/1/I06, doi:10.1088/0029-5515/36/1/I06.

[43] J. H. Schultz, T. Antaya, J. Feng, C.-y. Gung, N. Martovetsky, J. V. Minervini, P. Michael, A. Radovinsky, and P. Titus. The ITER Central Solenoid. In *21st IEEE/NPS Symposium on Fusion Engineering SOFE 05*, pages 1–4, 2005. doi:10.1109/FUSION.2005.252874.

[44] A. Polevoi, A. Ivanov, S. Medvedev, G. Huijsmans, S. Kim, A. Loarte, E. Fable, and A. Kuyanov. Reassessment of steady-state operation in ITER with NBI and EC heating and current drive. *Nuclear Fusion*, 60(9):096024, aug 2020. URL: https://dx.doi.org/10.1088/1741-4326/aba335, doi:10.1088/1741-4326/aba335.

[45] E. Joffrin. Advanced tokamak scenario developments for the next step. *Plasma Physics and Controlled Fusion*, 49(12B):B629, nov 2007. URL: https://dx.doi.org/10.1088/0741-3335/49/12B/S59, doi:10.1088/0741-3335/49/12B/S59.

[46] Equipe Tore Supra (prepared by F. Saint-Laurent). Steady state operation and control experiments on Tore Supra. *Nuclear Fusion*, 40(6):1047, jun 2000. URL: https://dx.doi.org/10.1088/0029-5515/40/6/303, doi:10.1088/0029-5515/40/6/303.

[47] J. Garcia. Deuterium-tritium experiments in JET with the ITER-like wall. In *TTF 2022 - US-EU Joint Transport Taskforce Workshop*, Santa Rosa (CA), United States, April 2022. URL: https://hal-cea.archives-ouvertes.fr/cea-03659111.

[48] M. Kikuchi and M. Azumi. Frontiers in fusion research II. *Introduction to modern tokamak physics. Heidelberg etc.: Springer*, 2015.

[49] M. Shimada, D. Campbell, V. Mukhovatov, M. Fujiwara, N. Kirneva, K. Lackner, M. Nagami, V. Pustovitov, N. Uckan, J. Wesley, N. Asakura, A. Costley, A. Donné, E. Doyle, A. Fasoli, C. Gormezano, Y. Gribov, O. Gruber, T. Hender, W. Houlberg, S. Ide, Y. Kamada, A. Leonard, B. Lipschultz, A. Loarte, K. Miyamoto, V. Mukhovatov, T. Osborne, A. Polevoi, and A. Sips. Chapter 1: Overview and summary. *Nuclear Fusion*, 47(6):S1, jun 2007. URL: https://dx.doi.org/10.1088/0029-5515/47/6/S01, doi:10.1088/0029-5515/47/6/S01.

[50] P. Rodriguez-Fernandez, A. Creely, M. Greenwald, D. Brunner, S. Ballinger, C. Chrobak, D. Garnier, R. Granetz, Z. Hartwig, N. Howard, J. Hughes, J. Irby, V. Izzo, A. Kuang, Y. Lin, E. Marmar, R. Mumgaard, C. Rea, M. Reinke, V. Riccardo, J. Rice, S. Scott, B. Sorbom, J. Stillerman, R. Sweeney, R. Tinguely, D. Whyte, J. Wright, and D. Yuryev. Overview of the SPARC physics basis towards the exploration of burning-plasma regimes in high-field, compact tokamaks. *Nuclear Fusion*, 62(4):042003, mar 2022. URL: https://dx.doi.org/10.1088/1741-4326/ac1654, doi:10.1088/1741-4326/ac1654.

[51] ITER organization. *ITER Research Plan within the Staged Approach (Level III – Provisional Version)*. ITER organization, 2018. URL: https://www.iter.org/technical-reports?id=9.

[52] A. J. Creely, M. J. Greenwald, S. B. Ballinger, D. Brunner, J. Canik, J. Doody, T. Fülöp, D. T. Garnier, R. Granetz, T. K. Gray, and et al. Overview of the SPARC tokamak. *Journal of Plasma Physics*, 86(5):865860502, 2020. doi:10.1017/S0022377820001257.

[53] D. Chandler — MIT News Office. MIT-designed project achieves major advance toward fusion energy, September 8, 2021. URL: https://news.mit.edu/2021/MIT-CFS-major-advance-toward-fusion-energy-0908.

[54] ITER Physics Basis Editors, I. P. E. G. Chairs, Co-Chairs, I. J. C. Team, and P. I. Unit. Chapter 1: Overview and summary. *Nuclear Fusion*, 39(12):2137, dec 1999. URL: https://dx.doi.org/10.1088/0029-5515/39/12/301, doi:10.1088/0029-5515/39/12/301.

[55] ITER Physics Expert Group on Confinement, Transport, I. P. E. G. on Confinement Modelling, Database, and I. P. B. Editors. Chapter 2: Plasma confinement and transport. *Nuclear Fusion*, 39(12):2175, dec 1999. URL: https://dx.doi.org/10.1088/0029-5515/39/12/302, doi:10.1088/0029-5515/39/12/302.

[56] H. R. Koslowski. Operational limits and limiting instabilities in tokamak machines. *Fusion Science and Technology*, 49:147–154, 02 2006. doi:10.13182/FST06-A1114.

[57] M. Bernert, T. Eich, A. Kallenbach, D. Carralero, A. Huber, P. T. Lang, S. Potzel, F. Reimold, J. Schweinzer, E. Viezzer, H. Zohm, and the ASDEX Upgrade team. The H-mode density limit in the full tungsten ASDEX Upgrade tokamak. *Plasma Physics and Controlled Fusion*, 57(1):014038, nov 2014. URL: https://dx.doi.org/10.1088/0741-3335/57/1/014038, doi:10.1088/0741-3335/57/1/014038.

[58] M. Greenwald, J. Terry, S. Wolfe, S. Ejima, M. Bell, S. Kaye, and G. Neilson. A new look at density limits in tokamaks. *Nuclear Fusion*, 28(12):2199, 1988.

[59] N. Uckan. ITER physics design guidelines: 1989. *INTERNATIONAL ATOMIC ENERGY AGENCY*, 1990.

[60] M. Keilhacker, A. Gibson, C. Gormezano, P. Lomas, P. Thomas, M. Watkins, P. Andrew, B. Balet, D. Borba, C. Challis, I. Coffey, G. Cottrell, H. D. Esch, N. Deliyanakis, A. Fasoli, C. Gowers, H. Guo, G. Huysmans, T. Jones, W. Kerner, R. König, M. Loughlin, A. Maas, F. Marcus, M. Nave, F. Rimini, G. Sadler, S. Sharapov, G. Sips, P. Smeulders, F. Söldner, A. Taroni, B. Tubbing, M. von Hellermann, D. Ward, and J. Team. High fusion performance from deuterium-tritium plasmas in JET. *Nuclear Fusion*, 39(2):209, feb 1999. URL: https://dx.doi.org/10.1088/0029-5515/39/2/306, doi:10.1088/0029-5515/39/2/306.

[61] V. Mukhovatov, Y. Shimomura, A. Polevoi, M. Shimada, M. Sugihara, G. Bateman, J. Cordey, O. Kardaun, G. Pereverzev, I. Voitsekhovich, J. Weiland, O. Zolotukhin, A. Chudnovskiy, A. Kritz, A. Kukushkin, T. Onjun, A. Pankin, and F. Perkins. Comparison of ITER performance predicted by semi-empirical and theory-based transport models. *Nuclear Fusion*, 43(9):942, aug 2003. URL: https://dx.doi.org/10.1088/0029-5515/43/9/318, doi:10.1088/0029-5515/43/9/318.

[62] J. Hughes, P. Snyder, M. Reinke, B. LaBombard, S. Mordijck, S. Scott, E. Tolman, S. Baek, T. Golfinopoulos, R. Granetz, M. Greenwald, A. Hubbard, E. Marmar, J. Rice, A. White, D. Whyte, T. Wilks, and S. Wolfe. Access to pedestal pressure relevant to burning plasmas on the high magnetic field tokamak Alcator C-Mod. *Nuclear Fusion*, 58(11):112003, sep 2018. URL: https://dx.doi.org/10.1088/1741-4326/aabc8a, doi:10.1088/1741-4326/aabc8a.

[63] T. Hender, J. Wesley, J. Bialek, A. Bondeson, A. Boozer, R. Buttery, A. Garofalo, T. Goodman, R. Granetz, Y. Gribov, O. Gruber, M. Gryaznevich, G. Giruzzi, S. Günter, N. Hayashi, P. Helander, C. Hegna, D. Howell, D. Humphreys, G. Huysmans, A. Hyatt, A. Isayama, S. Jardin, Y. Kawano, A. Kellman, C. Kessel, H. Koslowski, R. L. Haye, E. Lazzaro, Y. Liu, V. Lukash, J. Manickam, S. Medvedev, V. Mertens, S. Mirnov, Y. Nakamura, G. Navratil, M. Okabayashi, T. Ozeki, R. Paccagnella, G. Pautasso, F. Porcelli, V. Pustovitov, V. Riccardo, M. Sato, O. Sauter, M. Schaffer, M. Shimada, P. Sonato, E. Strait, M. Sugihara, M. Takechi, A. Turnbull, E. Westerhof, D. Whyte, R. Yoshino, H. Zohm, D. the ITPA MHD, and M. C. T. Group. Chapter 3: MHD stability, operational limits

and disruptions. *Nuclear Fusion*, 47(6):S128, jun 2007. URL: https://dx.doi.org/10.1088/0029-5515/47/6/S03, doi:10.1088/0029-5515/47/6/S03.

[64] J. Vega, A. Murari, s. Dormido-Canto, G. Rattá, M. Gelfusa, J. Mailloux, N. Abid, K. Abraham, P. de Abreu, O. Adabonyan, P. Adrich, V. Afanasev, M. Afzal, T. Ahlgren, L. Aho-Mantila, N. Aiba, M. Airila, M. Akhtar, R. Albanese, and I. Zychor. Disruption prediction with artificial intelligence techniques in tokamak plasmas. *Nature Physics*, 18:1–10, 06 2022. doi:10.1038/s41567-022-01602-2.

[65] M. Hoelzl, D. Hu, E. Nardon, G. T. A. Huijsmans, J. Team, and A. U. Team. First predictive simulations for deuterium shattered pellet injection in ASDEX Upgrade. *Physics of Plasmas*, 27(2):022510, 02 2020. URL: https://doi.org/10.1063/1.5133099, doi:10.1063/1.5133099.

[66] D. Paoletti, P. Fanelli, R. De Luca, C. Stefanini, F. Vivio, V. G. Belardi, S. Trupiano, G. Calabrò, J.-H. You, and R. Neu. Thermomechanical Analysis of a PFC Integrating W Lattice Armour in Response to Different Plasma Scenarios Predicted in the EU-DEMO Tokamak. *Journal of Nuclear Engineering*, 3(4):421–434, 2022. URL: https://www.mdpi.com/2673-4362/3/4/28, doi:10.3390/jne3040028.

[67] T. Klinger et al. Overview of first Wendelstein 7-X high-performance operation. *Nuclear Fusion*, 59(11):112004, jun 2019. URL: https://dx.doi.org/10.1088/1741-4326/ab03a7, doi:10.1088/1741-4326/ab03a7.

[68] J. Wesson and D. J. Campbell. *Tokamaks*, volume 149. Oxford university press, 2011.

[69] P. Manz. *The Microscopic Picture of Plasma Edge Turbulence*. Technische Universität München, 2018.

[70] P. C. Stangeby et al. *The plasma boundary of magnetic fusion devices*, volume 224. Institute of Physics Pub. Philadelphia, Pennsylvania, 2000.

[71] ASDEX Team. The H-Mode of ASDEX. *Nuclear Fusion*, 29(11):1959, nov 1989. URL: https://dx.doi.org/10.1088/0029-5515/29/11/010, doi:10.1088/0029-5515/29/11/010.

[72] ITER Physics Expert Group on Disruptions, Plasma Control, and MHD and ITER Physics Basis Editors. Chapter 3: MHD stability, operational limits and disruptions. *Nuclear Fusion*, 39(12):2251, dec 1999. URL: https://dx.doi.org/10.1088/0029-5515/39/12/303, doi:10.1088/0029-5515/39/12/303.

[73] E. Viezzer, M. Austin, M. Bernert, K. Burrell, P. Cano-Megias, X. Chen, D. Cruz-Zabala, S. Coda, M. Faitsch, O. Février, L. Gil, C. Giroud, T. Happel, G. Harrer, A. Hubbard, J. Hughes, A. Kallenbach, B. Labit, A. Merle, H. Meyer, C. Paz-Soldan, P. Oyola, O. Sauter, M. Siccinio, D. Silvagni, and E. Solano. Prospects of core–edge integrated no-ELM and small-ELM scenarios for future fusion devices. *Nuclear Materials and Energy*,

34:101308, 2023. URL: https://www.sciencedirect.com/science/article/pii/S2352179122001892, doi:https://doi.org/10.1016/j.nme.2022.101308.

[74] E. Kaveeva, V. Rozhansky, I. Senichenkov, E. Sytova, I. Veselova, S. Voskoboynikov, X. Bonnin, R. Pitts, A. Kukushkin, S. Wiesen, and D. Coster. SOLPS-ITER modelling of ITER edge plasma with drifts and currents. *Nuclear Fusion*, 60(4):046019, mar 2020. URL: https://doi.org/10.1088%2F1741-4326%2Fab73c1, doi:10.1088/1741-4326/ab73c1.

[75] R. Pitts, X. Bonnin, F. Escourbiac, H. Frerichs, J. Gunn, T. Hirai, A. Kukushkin, E. Kaveeva, M. Miller, D. Moulton, V. Rozhansky, I. Senichenkov, E. Sytova, O. Schmitz, P. Stangeby, G. De Temmerman, I. Veselova, and S. Wiesen. Physics basis for the first ITER tungsten divertor. *Nuclear Materials and Energy*, 20:100696, 2019. URL: https://www.sciencedirect.com/science/article/pii/S2352179119300237, doi:https://doi.org/10.1016/j.nme.2019.100696.

[76] N. Offeddu, W. Han, C. Theiler, T. Golfinopoulos, J. Terry, E. Marmar, C. Wüthrich, C. Tsui, H. de Oliveira, B. Duval, D. Galassi, D. Oliveira, D. Mancini, and the TCV Team. Cross-field and parallel dynamics of SOL filaments in TCV. *Nuclear Fusion*, 62(9):096014, aug 2022. URL: https://dx.doi.org/10.1088/1741-4326/ac7ed7, doi:10.1088/1741-4326/ac7ed7.

[77] H. Grad. On the kinetic theory of rarefied gases. *Communications on Pure and Applied Mathematics*, 2(4):331–407, 1949. URL: https://onlinelibrary.wiley.com/doi/abs/10.1002/cpa.3160020403, doi:https://doi.org/10.1002/cpa.3160020403.

[78] H. Grad. Asymptotic theory of the Boltzmann equation. *The Physics of Fluids*, 6(2):147–181, 1963.

[79] V. Zhdanov and P. Yushmanov. Diffusion and heat transfer in a multicomponent completely ionized plasma. *Journal of Applied Mechanics and Technical Physics - J APPL MECH TECH PHYS*, 21:453–461, 07 1980. doi:10.1007/BF00916477.

[80] E. Sytova, E. Kaveeva, V. Rozhansky, I. Senichenkov, S. Voskoboynikov, D. Coster, X. Bonnin, and R. A. Pitts. Impact of a new general form of friction and thermal forces on SOLPS-ITER modelling results. *Contributions to Plasma Physics*, 58(6-8):622–628, 2018. URL: https://onlinelibrary.wiley.com/doi/abs/10.1002/ctpp.201700135, doi:https://doi.org/10.1002/ctpp.201700135.

[81] F. L. Hinton and R. D. Hazeltine. Theory of plasma transport in toroidal confinement systems. *Rev. Mod. Phys.*, 48:239–308, Apr 1976. URL: https://link.aps.org/doi/10.1103/RevModPhys.48.239, doi:10.1103/RevModPhys.48.239.

[82] C. Angioni, N. Bonanomi, E. Fable, P. Schneider, G. Tardini, T. Luda, G. Staebler, and the ASDEX Upgrade Team. The dependence of tokamak l-mode confinement

on magnetic field and plasma size, from a magnetic field scan experiment at asdex upgrade to full-radius integrated modelling and fusion reactor predictions. *Nuclear Fusion*, 63(5):056005, mar 2023. URL: https://dx.doi.org/10.1088/1741-4326/acc193, doi:10.1088/1741-4326/acc193.

[83] V. Rozhansky, E. Kaveeva, P. Molchanov, I. Veselova, S. Voskoboynikov, D. Coster, G. Counsell, A. Kirk, and S. Lisgo. New B2SOLPS5.2 transport code for H-mode regimes in tokamaks. *Nuclear Fusion*, 49(2):025007, jan 2009. URL: https://doi.org/10.1088%2F0029-5515%2F49%2F2%2F025007, doi:10.1088/0029-5515/49/2/025007.

[84] S. O. Makarov, D. P. Coster, V. A. Rozhansky, A. A. Stepanenko, V. M. Zhdanov, E. G. Kaveeva, I. Y. Senichenkov, and X. Bonnin. Equations and improved coefficients for parallel transport in multicomponent collisional plasmas: Method and application for tokamak modeling. *Physics of Plasmas*, 28(6):062308, 2021. URL: https://doi.org/10.1063/5.0047618, doi:10.1063/5.0047618.

[85] S. O. Makarov, D. P. Coster, V. A. Rozhansky, S. P. Voskoboynikov, E. G. Kaveeva, I. Y. Senichenkov, A. A. Stepanenko, V. M. Zhdanov, and X. Bonnin. Impact of the improved parallel kinetic coefficients on the helium and neon transport in SOLPS-ITER for ITER. *Contributions to Plasma Physics*, 62(5-6):e202100165, 2022. URL: https://onlinelibrary.wiley.com/doi/abs/10.1002/ctpp.202100165, doi:https://doi.org/10.1002/ctpp.202100165.

[86] S. Hirshman and D. Sigmar. Neoclassical transport of impurities in tokamak plasmas. *Nuclear Fusion*, 21(9):1079–1201, sep 1981. URL: https://doi.org/10.1088%2F0029-5515%2F21%2F9%2F003, doi:10.1088/0029-5515/21/9/003.

[87] R. Schneider, X. Bonnin, K. Borrass, D. Coster, H. Kastelewicz, D. Reiter, V. Rozhansky, and B. Braams. Plasma edge physics with B2-EIRENE. *Contributions to Plasma Physics*, 46(1-2):3–191, 2006.

[88] V. Rozhansky, S. Voskoboynikov, E. Kaveeva, D. Coster, and R. Schneider. Simulation of tokamak edge plasma including self-consistent electric fields. *Nuclear Fusion*, 41(4):387–401, apr 2001. URL: https://doi.org/10.1088%2F0029-5515%2F41%2F4%2F305, doi:10.1088/0029-5515/41/4/305.

[89] A. Stegmeir, A. Ross, T. Body, M. Francisquez, W. Zholobenko, D. Coster, O. Maj, P. Manz, F. Jenko, B. N. Rogers, and K. S. Kang. Global turbulence simulations of the tokamak edge region with GRILLIX. *Physics of Plasmas*, 26(5):052517, 2019. URL: https://doi.org/10.1063/1.5089864, doi:10.1063/1.5089864.

[90] W. Zholobenko, A. Stegmeir, T. Body, A. Ross, P. Manz, O. Maj, D. Coster, F. Jenko, M. Francisquez, B. Zhu, and B. Rogers. Thermal dynamics in the flux-coordinate independent turbulence code GRILLIX. *Contributions to Plasma Physics*, 60(5-6):e201900131, 2020. URL: https://

onlinelibrary.wiley.com/doi/abs/10.1002/ctpp.201900131, doi:https://doi.org/10.1002/ctpp.201900131.

[91] S. Makarov, D. Coster, E. Kaveeva, V. Rozhansky, I. Senichenkov, I. Veselova, S. Voskoboynikov, A. Stepanenko, X. Bonnin, and R. Pitts. Implementation of SOLPS-ITER code with new Grad–Zhdanov module for D–T mixture. *Nuclear Fusion*, 63(2):026014, jan 2023. URL: https://dx.doi.org/10.1088/1741-4326/acab76, doi:10.1088/1741-4326/acab76.

[92] M. Raghunathan, Y. Marandet, H. Bufferand, G. Ciraolo, P. Ghendrih, P. Tamain, and E. Serre. Generalized collisional fluid theory for multi-component, multi-temperature plasma using the linearized boltzmann collision operator for scrape-off layer/edge applications. *Plasma Physics and Controlled Fusion*, 63(6):064005, may 2021. URL: https://dx.doi.org/10.1088/1361-6587/abf670, doi:10.1088/1361-6587/abf670.

[93] L. Schiff. *Quantum Mechanics*. International series in pure and applied physics. McGraw-Hill, 1955. URL: https://books.google.de/books?id=7ApRAAAAMAAJ.

[94] S. Chapman and T. Cowling. *The Mathematical Theory of Non-uniform Gases: An Account of the Kinetic Theory of Viscosity, Thermal Conduction and Diffusion in Gases*. Cambridge Mathematical Library. Cambridge University Press, 1990.

[95] M. Beurskens, S. Bozhenkov, O. Ford, P. Xanthopoulos, A. Zocco, Y. Turkin, A. Alonso, C. Beidler, I. Calvo, D. Carralero, T. Estrada, G. Fuchert, O. Grulke, M. Hirsch, K. Ida, M. Jakubowski, C. Killer, M. Krychowiak, S. Kwak, S. Lazerson, A. Langenberg, R. Lunsford, N. Pablant, E. Pasch, A. Pavone, F. Reimold, T. Romba, A. von Stechow, H. Smith, T. Windisch, M. Yoshinuma, D. Zhang, R. Wolf, and the W7-X Team. Ion temperature clamping in Wendelstein 7-X electron cyclotron heated plasmas. *Nuclear Fusion*, 61(11):116072, oct 2021. URL: https://dx.doi.org/10.1088/1741-4326/ac1653, doi:10.1088/1741-4326/ac1653.

[96] G. Staebler and F. Hinton. Currents in the scrape-off layer of diverted tokamaks. *Nuclear Fusion*, 29(10):1820, oct 1989. URL: https://dx.doi.org/10.1088/0029-5515/29/10/017, doi:10.1088/0029-5515/29/10/017.

[97] A. Kallenbach, A. Carlson, G. Pautasso, A. Peeters, U. Seidel, and H.-P. Zehrfeld. Electric currents in the scrape-off layer in ASDEX Upgrade. *Journal of Nuclear Materials*, 290-293:639–643, 2001. 14th Int. Conf. on Plasma-Surface Interactions in Controlled Fusion D evices. URL: https://www.sciencedirect.com/science/article/pii/S0022311500004451, doi:https://doi.org/10.1016/S0022-3115(00)00445-1.

[98] I. Y. Senichenkov, E. G. Kaveeva, E. A. Sytova, V. A. Rozhansky, S. P. Voskoboynikov, I. Y. Veselova, D. P. Coster, X. Bonnin, and F. R. and. On mechanisms of impurity leakage and retention in the tokamak divertor. *Plasma*

*Physics and Controlled Fusion*, 61(4):045013, mar 2019. URL: https://doi.org/10.1088%2F1361-6587%2Fab04d0, doi:10.1088/1361-6587/ab04d0.

[99] M. Raghunathan, Y. Marandet, H. Bufferand, G. Ciraolo, P. Ghendrih, P. Tamain, and E. Serre. Multi-temperature generalized Zhdanov closure for scrape-off layer/edge applications. *Plasma Physics and Controlled Fusion*, 64(4):045005, feb 2022. URL: https://dx.doi.org/10.1088/1361-6587/ac414d, doi:10.1088/1361-6587/ac414d.

[100] P. Helander and D. J. Sigmar. *Collisional transport in magnetized plasmas*, volume 4. Cambridge University Press, 2005.

[101] M. Baelmans, D. Reiter, R. Weynants, and R. Schneider. Computational assessment of effects of electric fields and currents in tokamak edge plasmas. *Journal of Nuclear Materials*, 220-222:982–986, 1995. Plasma-Surface Interactions in Controlled Fusion Devices. URL: https://www.sciencedirect.com/science/article/pii/0022311594004587, doi:https://doi.org/10.1016/0022-3115(94)00458-7.

[102] A. Chankin. Classical drifts in the tokamak SOL and divertor: models and experiment. *Journal of Nuclear Materials*, 241-243:199–213, 1997. URL: https://www.sciencedirect.com/science/article/pii/S0022311597800402, doi:https://doi.org/10.1016/S0022-3115(97)80040-2.

[103] G. J. Radford, A. V. Chankin, G. Corrigan, R. Simonini, J. Spence, and A. Taroni. The Particle and Heat Drift Fluxes and their Implementation into the EDGE2D Transport Code. *Contributions to Plasma Physics*, 36(2-3):187–191, 1996. URL: https://onlinelibrary.wiley.com/doi/abs/10.1002/ctpp.2150360217, doi:https://doi.org/10.1002/ctpp.2150360217.

[104] H. Bufferand, C. Baudoin, J. Bucalossi, G. Ciraolo, J. Denis, N. Fedorczak, D. Galassi, P. Ghendrih, R. Leybros, Y. Marandet, N. Mellet, J. Morales, N. Nace, E. Serre, P. Tamain, and M. Valentinuzzi. Implementation of drift velocities and currents in SOLEDGE2D–EIRENE. *Nuclear Materials and Energy*, 12:852–857, 2017. Proceedings of the 22nd International Conference on Plasma Surface Interactions 2016, 22nd PSI. URL: https://www.sciencedirect.com/science/article/pii/S2352179116301946, doi:https://doi.org/10.1016/j.nme.2016.11.031.

[105] T. D. Rognlien, D. D. Ryutov, N. Mattor, and G. D. Porter. Two-dimensional electric fields and drifts near the magnetic separatrix in divertor tokamaks. *Physics of Plasmas*, 6(5):1851–1857, 1999. URL: https://doi.org/10.1063/1.873488, doi:10.1063/1.873488.

[106] A. J. Brizard and T. S. Hahm. Foundations of nonlinear gyrokinetic theory. *Rev. Mod. Phys.*, 79:421–468, Apr 2007. URL: https://link.aps.org/doi/10.1103/RevModPhys.79.421, doi:10.1103/RevModPhys.79.421.

[107] F. Jenko, W. Dorland, M. Kotschenreuther, and B. N. Rogers. Electron temperature gradient driven turbulence. *Physics of Plasmas*, 7(5):1904–1910, 2000. URL: https://doi.org/10.1063/1.874014, doi:10.1063/1.874014.

[108] T. Görler, X. Lapillonne, S. Brunner, T. Dannert, F. Jenko, F. Merz, and D. Told. The global version of the gyrokinetic turbulence code GENE. *Journal of Computational Physics*, 230(18):7053–7071, 2011. URL: https://www.sciencedirect.com/science/article/pii/S0021999111003457, doi:https://doi.org/10.1016/j.jcp.2011.05.034.

[109] J. Candy and R. E. Waltz. Anomalous Transport Scaling in the DIII-D Tokamak Matched by Supercomputer Simulation. *Phys. Rev. Lett.*, 91:045001, Jul 2003. URL: https://link.aps.org/doi/10.1103/PhysRevLett.91.045001, doi:10.1103/PhysRevLett.91.045001.

[110] S. Jolliet, A. Bottino, P. Angelino, R. Hatzky, T. Tran, B. Mcmillan, O. Sauter, K. Appert, Y. Idomura, and L. Villard. A global collisionless pic code in magnetic coordinates. *Computer Physics Communications*, 177(5):409–425, 2007. URL: https://www.sciencedirect.com/science/article/pii/S0010465507002251, doi:https://doi.org/10.1016/j.cpc.2007.04.006.

[111] G. M. Staebler, J. E. Kinsey, and R. E. Waltz. A theory-based transport model with comprehensive physics. *Physics of Plasmas*, 14(5):055909, 2007. URL: https://doi.org/10.1063/1.2436852, doi:10.1063/1.2436852.

[112] C. Bourdelle, X. Garbet, F. Imbeaux, A. Casati, N. Dubuit, R. Guirlet, and T. Parisot. A new gyrokinetic quasilinear transport model applied to particle transport in tokamak plasmas. *Physics of Plasmas*, 14(11):112501, 2007. URL: https://doi.org/10.1063/1.2800869, doi:10.1063/1.2800869.

[113] A. D. Siena, A. B. Navarro, T. Luda, G. Merlo, M. Bergmann, L. Leppin, T. Görler, J. Parker, L. LoDestro, T. Dannert, K. Germaschewski, B. Allen, J. Hittinger, B. Dorland, G. Hammett, F. Jenko, the ASDEX Upgrade Team, and the EUROfusion MST1 Team. Global gyrokinetic simulations of ASDEX Upgrade up to the transport timescale with GENE–Tango. *Nuclear Fusion*, 62(10):106025, sep 2022. URL: https://dx.doi.org/10.1088/1741-4326/ac8941, doi:10.1088/1741-4326/ac8941.

[114] E. Fable, C. Angioni, A. A. Ivanov, K. Lackner, O. Maj, S. Y. Medvedev, G. Pautasso, G. V. Pereverzev, W. Treutterer, and the ASDEX Upgrade Team. Dynamical coupling between magnetic equilibrium and transport in tokamak scenario modelling, with application to current ramps. *Plasma Physics and Controlled Fusion*, 55(7):074007, jun 2013. URL: https://dx.doi.org/10.1088/0741-3335/55/7/074007, doi:10.1088/0741-3335/55/7/074007.

[115] G. V. Pereverzev and P. N. Yushmanov. ASTRA. Automated System for Transport Analysis in a Tokamak. *IPP report, Garching: Max-Planck-Institut für Plasmaphysik.*, 5/98, 2002. URL: https://hdl.handle.net/11858/00-001M-0000-0027-4510-D, doi:10.1063/5.0082413.

[116] J. Candy, C. Holland, R. E. Waltz, M. R. Fahey, and E. Belli. Tokamak profile prediction using direct gyrokinetic and neoclassical simulation. *Physics of Plasmas*, 16(6):060704, 2009. URL: https://doi.org/10.1063/1.3167820, doi:10.1063/1.3167820.

[117] M. ROMANELLI, G. CORRIGAN, V. PARAIL, S. WIESEN, R. AMBROSINO, P. D. S. A. BELO, L. GARZOTTI, D. HARTING, F. KÖCHL, T. KOSKELA, L. LAURO-TARONI, C. MARCHETTO, M. MATTEI, E. MILITELLO-ASP, M. F. F. NAVE, S. PAMELA, A. SALMI, P. STRAND, G. SZEPESI, and E.-J. Contributors. Jintrac: A system of codes for integrated simulation of tokamak scenarios. *Plasma and Fusion Research*, 9:3403023–3403023, 2014. doi:10.1585/pfr.9.3403023.

[118] C. S. Chang, S. Ku, P. Diamond, M. Adams, R. Barreto, Y. Chen, J. Cummings, E. D'Azevedo, G. Dif-Pradalier, S. Ethier, L. Greengard, T. S. Hahm, F. Hinton, D. Keyes, S. Klasky, Z. Lin, J. Lofstead, G. Park, S. Parker, N. Podhorszki, K. Schwan, A. Shoshani, D. Silver, M. Wolf, P. Worley, H. Weitzner, E. Yoon, and D. Zorin. Whole-volume integrated gyrokinetic simulation of plasma turbulence in realistic diverted-tokamak geometry. *Journal of Physics: Conference Series*, 180(1):012057, jul 2009. URL: https://dx.doi.org/10.1088/1742-6596/180/1/012057, doi:10.1088/1742-6596/180/1/012057.

[119] D. Michels, A. Stegmeir, P. Ulbl, D. Jarema, and F. Jenko. GENE-X: A full-f gyrokinetic turbulence code based on the flux-coordinate independent approach. *Computer Physics Communications*, 264:107986, 2021. URL: https://www.sciencedirect.com/science/article/pii/S0010465521000989, doi:https://doi.org/10.1016/j.cpc.2021.107986.

[120] D. Michels, P. Ulbl, W. Zholobenko, T. Body, A. Stegmeir, T. Eich, M. Griener, G. D. Conway, and F. Jenko. Full-f electromagnetic gyrokinetic turbulence simulations of the edge and scrape-off layer of asdex upgrade with gene-x. *Physics of Plasmas*, 29(3):032307, 2022. URL: https://doi.org/10.1063/5.0082413, doi:10.1063/5.0082413.

[121] P. Ulbl, D. Michels, and F. Jenko. Implementation and verification of a conservative, multi-species, gyro-averaged, full-f, Lenard-Bernstein/Dougherty collision operator in the gyrokinetic code GENE-X. *Contributions to Plasma Physics*, 62(5-6):e202100180, 2022. URL: https://onlinelibrary.wiley.com/doi/abs/10.1002/ctpp.202100180, doi:https://doi.org/10.1002/ctpp.202100180.

[122] Q. Pan, D. Told, E. L. Shi, G. W. Hammett, and F. Jenko. Full-f version of GENE for turbulence in open-field-line systems. *Physics of Plasmas*, 25(6):062303, 2018. URL: https://doi.org/10.1063/1.5008895, doi:10.1063/1.5008895.

[123] L. A. Leppin, T. Görler, M. Cavedon, M. G. Dunne, E. Wolfrum, F. Jenko, and the ASDEX Upgrade Team. Complex structure of turbulence across the ASDEX Upgrade pedestal, 2023.

[124] E. L. Shi, G. W. Hammett, T. Stoltzfus-Dueck, and A. Hakim. Gyrokinetic continuum simulation of turbulence in a straight open-field-line plasma. *Journal of Plasma Physics*, 83(3):905830304, 2017. doi:10.1017/S002237781700037X.

[125] M. Boesl, A. Bergmann, A. Bottino, D. Coster, E. Lanti, N. Ohana, and F. Jenko. Gyrokinetic full-f particle-in-cell simulations on open field lines with PICLS. *Physics of Plasmas*, 26(12):122302, 2019. URL: https://doi.org/10.1063/1.5121262, doi:10.1063/1.5121262.

[126] B. D. Dudson and J. Leddy. Hermes: global plasma edge fluid turbulence simulations. *Plasma Physics and Controlled Fusion*, 59(5):054010, apr 2017. URL: https://dx.doi.org/10.1088/1361-6587/aa63d2, doi:10.1088/1361-6587/aa63d2.

[127] F. Halpern, P. Ricci, S. Jolliet, J. Loizu, J. Morales, A. Mosetto, F. Musil, F. Riva, T. Tran, and C. Wersal. The GBS code for tokamak scrape-off layer simulations. *Journal of Computational Physics*, 315:388–408, 2016. URL: https://www.sciencedirect.com/science/article/pii/S0021999116001923, doi:https://doi.org/10.1016/j.jcp.2016.03.040.

[128] P. Tamain, H. Bufferand, G. Ciraolo, C. Colin, D. Galassi, P. Ghendrih, F. Schwander, and E. Serre. The TOKAM3X code for edge turbulence fluid simulations of tokamak plasmas in versatile magnetic geometries. *Journal of Computational Physics*, 321:606–623, 2016. URL: https://www.sciencedirect.com/science/article/pii/S0021999116301838, doi:https://doi.org/10.1016/j.jcp.2016.05.038.

[129] B. Zhu, H. Seto, X. qiao Xu, and M. Yagi. Drift reduced landau fluid model for magnetized plasma turbulence simulations in bout++ framework. *Computer Physics Communications*, 267:108079, 2021. URL: https://www.sciencedirect.com/science/article/pii/S0010465521001910, doi:https://doi.org/10.1016/j.cpc.2021.108079.

[130] T. Pütterich, R. Dux, M. Janzer, and R. McDermott. ELM flushing and impurity transport in the H-mode edge barrier in ASDEX Upgrade. *Journal of Nuclear Materials*, 415(1, Supplement):S334–S339, 2011. Proceedings of the 19th International Conference on Plasma-Surface Interactions in Controlled Fusion. URL: https://www.sciencedirect.com/science/article/pii/S0022311510005623, doi:https://doi.org/10.1016/j.jnucmat.2010.09.052.

[131] E. Viezzer, T. Pütterich, C. Angioni, A. Bergmann, R. Dux, E. Fable, R. McDermott, U. Stroth, E. Wolfrum, and the ASDEX Upgrade Team. Evidence for the neoclassical nature of the radial electric field in the edge transport barrier of ASDEX Upgrade. *Nuclear Fusion*, 54(1):012003, dec 2013. URL: https://dx.doi.org/10.1088/0029-5515/54/1/012003, doi:10.1088/0029-5515/54/1/012003.

[132] T. Eich, A. Leonard, R. Pitts, W. Fundamenski, R. Goldston, T. Gray, A. Herrmann, A. Kirk, A. Kallenbach, O. Kardaun, A. Kukushkin, B. LaBombard, R. Maingi, M. Makowski, A. Scarabosio, B. Sieglin, J. Terry, A. Thornton, A. U. Team, and J. E. Contributors. Scaling of the tokamak near the scrape-off layer H-mode power width and implications for ITER. *Nuclear Fusion*, 53(9):093031, aug 2013. URL: https://dx.doi.org/10.1088/0029-5515/53/9/093031, doi:10.1088/0029-5515/53/9/093031.

[133] C. Chang, S. Ku, A. Loarte, V. Parail, F. Köchl, M. Romanelli, R. Maingi, J.-W. Ahn, T. Gray, J. Hughes, B. LaBombard, T. Leonard, M. Makowski, and J. Terry. Gyrokinetic projection of the divertor heat-flux width from present tokamaks to ITER. *Nuclear Fusion*, 57(11):116023, aug 2017. URL: https://dx.doi.org/10.1088/1741-4326/aa7efb, doi:10.1088/1741-4326/aa7efb.

[134] I. Veselova, E. Kaveeva, V. Rozhansky, I. Senichenkov, A. Poletaeva, R. A. Pitts, and X. Bonnin. SOLPS-ITER drift modelling of ITER burning plasmas with narrow near-SOL heat flux channels. *Nuclear Materials and Energy*, 26:100870, 2021. URL: https://www.sciencedirect.com/science/article/pii/S2352179120301368, doi:https://doi.org/10.1016/j.nme.2020.100870.

[135] A. Kukushkin, H. Pacher, G. Pacher, V. Kotov, R. Pitts, and D. Reiter. Consequences of a reduction of the upstream power SOL width in ITER. *Journal of Nuclear Materials*, 438:S203–S207, 2013. Proceedings of the 20th International Conference on Plasma-Surface Interactions in Controlled Fusion Devices. URL: https://www.sciencedirect.com/science/article/pii/S0022311513000354, doi:https://doi.org/10.1016/j.jnucmat.2013.01.027.

[136] D. Reiter, M. Baelmans, and P. Börner. The EIRENE and B2-EIRENE Codes. *Fusion Science and Technology*, 47(2):172–186, 2005. URL: https://doi.org/10.13182/FST47-172, doi:10.13182/FST47-172.

[137] E. Solano, G. Birkenmeier, E. Delabie, C. Silva, J. Hillesheim, A. Boboc, I. Carvalho, P. Carvalho, M. Chernyshova, T. Craciunescu, E. de la Luna, J. Fontdecaba, R. Henriques, P. Jacquet, I. Jepu, A. Kappatou, D. King, M. Lennholm, E. Lerche, E. Litherland-Smith, A. Loarte, M. Maslov, F. P. Diaz, V. Parail, E. Pawelec, F. Rimini, A. Shaw, P. Siren, G. Szepesi, Z. Stancar, E. Tholerus, S. Vartanian, B. Viola, H. Weisen, and J. Contributors. L–H transition threshold studies in helium plasmas at JET. *Nuclear Fusion*, 61(12):124001, oct 2021. URL: https://dx.doi.org/10.1088/1741-4326/ac2b76, doi:10.1088/1741-4326/ac2b76.

[138] W. Zholobenko. Global Braginskii turbulence simulations across the edge and scrape-off layer of diverted tokamaks, 2021.

[139] W. Zholobenko, T. Body, P. Manz, A. Stegmeir, B. Zhu, M. Griener, G. D. Conway, D. Coster, F. Jenko, and the ASDEX Upgrade Team. Electric field and turbulence in global Braginskii simulations across the ASDEX Upgrade edge and scrape-off layer. *Plasma Physics and Controlled Fusion*, 63(3):034001, feb 2021. URL: https://dx.doi.org/10.1088/1361-6587/abd97e, doi:10.1088/1361-6587/abd97e.

[140] W. Zholobenko, A. Stegmeir, M. Griener, G. Conway, T. Body, D. Coster, F. Jenko, and the ASDEX Upgrade Team. The role of neutral gas in validated global edge turbulence simulations. *Nuclear Fusion*, 61(11):116015, oct 2021. URL: https://dx.doi.org/10.1088/1741-4326/ac1e61, doi:10.1088/1741-4326/ac1e61.

[141] H. Bufferand, J. Balbin, S. Baschetti, J. Bucalossi, G. Ciraolo, P. Ghendrih, R. Mao, N. Rivals, P. Tamain, H. Yang, G. Giorgiani, F. Schwander, M. S. d'Abusco, E. Serre, J. Denis, Y. Marandet, M. Raghunathan, P. Innocente, D. Galassi, and J. Contributors. Implementation of multi-component Zhdanov closure in SOLEDGE3X. *Plasma Physics and Controlled Fusion*, 64(5):055001, mar 2022. URL: https://dx.doi.org/10.1088/1361-6587/ac4fac, doi:10.1088/1361-6587/ac4fac.

[142] A. Poulsen, J. J. Rasmussen, M. Wiesenberger, and V. Naulin. Collisional multispecies drift fluid model. *Physics of Plasmas*, 27(3):032305, 03 2020. URL: https://doi.org/10.1063/1.5140522, doi:10.1063/1.5140522.

[143] B. Scott. *Low Frequency Fluid Drift Turbulence in Magnetised Plasmas*. habilitation, Universität Düsseldorf, Düsseldorf, 2000.

[144] K. SALARI and P. KNUPP. Code Verification by the Method of Manufactured Solutions. 6 2000. URL: https://www.osti.gov/biblio/759450, doi:10.2172/759450.

[145] A. Kukushkin, H. Pacher, V. Kotov, D. Reiter, D. Coster, and G. Pacher. Effect of conditions for gas recirculation on divertor operation in ITER. *Nuclear Fusion*, 47(7):698, jun 2007. URL: https://dx.doi.org/10.1088/0029-5515/47/7/021, doi:10.1088/0029-5515/47/7/021.

[146] E. Kaveeva, V. Rozhansky, I. Veselova, I. Senichenkov, C. Giroud, R. A. Pitts, S. Wiesen, and S. Voskoboynikov. SOLPS-ITER drift modelling of JET Ne and N-seeded H-modes. *Nuclear Materials and Energy*, 28:101030, 2021. URL: https://www.sciencedirect.com/science/article/pii/S2352179121001046, doi:https://doi.org/10.1016/j.nme.2021.101030.

[147] D. Reiter, M. Baelmans, and P. Börner. The EIRENE and B2-EIRENE codes. *Fusion Science and Technology*, 47(2):172–186, 2005. URL: https://doi.org/10.13182/FST47-172, doi:10.13182/FST47-172.

[148] V. Neverov, A. Kukushkin, U. Kruezi, M. Stamp, and H. W. and. Determination of isotope ratio in the divertor of JET-ILW by high-resolution H alpha spectroscopy: H–D experiment and implications for D–T experiment. *Nuclear Fusion*, 59(4):046011, feb 2019. URL: https://doi.org/10.1088/1741-4326/ab0000, doi:10.1088/1741-4326/ab0000.

[149] D. Reiter. *The EIRENE Code User Manual*. Institut für Energie- und Klimaforschung – Plasmaphysik Forschungszentrum Jülich GmbH; P.O.B. 1913; D-52425 Jülich, Germany. URL: https://jugit.fz-juelich.de/eirene/eirene-manual.

[150] V. Rozhansky, E. Kaveeva, I. Senichenkov, I. Veselova, S. Voskoboynikov, R. A. Pitts, D. Coster, C. Giroud, and S. Wiesen. Multi-machine SOLPS-ITER comparison of impurity seeded H-mode radiative divertor regimes with metal walls. *Nuclear Fusion*, 61(12):126073, dec 2021. URL: https://doi.org/10.1088/1741-4326/ac3699, doi:10.1088/1741-4326/ac3699.

[151] A. V. Chankin, G. Corrigan, A. E. Jaervinen, and J. Contributors. Assessment of the strength of kinetic effects of parallel electron transport in the SOL and divertor of JET high radiative H-mode plasmas using EDGE2D-EIRENE and KIPP codes. *Plasma Physics and Controlled Fusion*, 60(11):115011, oct 2018. URL: https://dx.doi.org/10.1088/1361-6587/aae0a0, doi:10.1088/1361-6587/aae0a0.

[152] M. Zhao, A. Chankin, and D. Coster. An iterative algorithm of coupling the Kinetic Code for Plasma Periphery (KIPP) with SOLPS. *Computer Physics Communications*, 235:133–152, 2019. URL: https://www.sciencedirect.com/science/article/pii/S0010465518303266, doi:https://doi.org/10.1016/j.cpc.2018.09.012.

[153] W. Dekeyser, P. Boerner, S. Voskoboynikov, V. Rozhanksy, I. Senichenkov, L. Kaveeva, I. Veselova, E. Vekshina, X. Bonnin, R. Pitts, and M. Baelmans. Plasma edge simulations including realistic wall geometry with SOLPS-ITER. *Nuclear Materials and Energy*, 27:100999, 2021. URL: https://www.sciencedirect.com/science/article/pii/S2352179121000788, doi:https://doi.org/10.1016/j.nme.2021.100999.

[154] V. Zhdanov and A. Stepanenko. Kinetic theory of transport processes in partially ionized reactive plasma, I: General transport equations. *Physica A: Statistical Mechanics and its Applications*, 446:35–53, 2016. URL: https://www.sciencedirect.com/science/article/pii/S0378437115009917, doi:https://doi.org/10.1016/j.physa.2015.11.012.

[155] L. Woods. Mathematical Theory of Transport Processes in Gases. *By J.H. FERZIGER and H.G. KAPER. North-Holland, 1972. 579 pp. H£ 1.120., Journal of Fluid Mechanics*, 61(4):823–825, 1973.

# A Mistake corrections in the Zhdanov monograph

The corrections to mistakes, which are discovered in the 8th chapter of the Zhdanov monograph [18], are performed. The content of this abstract was also published in [91].

It is worth to emphasise that in this Appendix A, the temperature is given in Kelvin following the system of units, which used in [18].

- In the expressions (8.1.4), the numerator in the second term has to be changed. The correct numerator is 136, not 139:

$$G^{(11)}_{\alpha Z\beta\zeta} = -\left(\frac{433}{280}\frac{m_\beta^2}{m_\alpha^2} + \frac{136}{35}\frac{m_\beta}{m_\alpha} + \frac{459}{35} + \frac{32}{5}\frac{m_\alpha}{m_\beta} + 5\frac{m_\alpha^2}{m_\beta^2}\right)\kappa_{\alpha\beta}^2\lambda_{\alpha Z\beta\zeta} \tag{A.1}$$

- The coefficient $c_\alpha^{(5)}$ in Eq. (8.4.4) is:

$$c_\alpha^{(5)} = \frac{5}{2}\tau_\alpha^{-1}\tau_{\alpha\alpha}\frac{S_\alpha^{(11)}}{S_\alpha^{(5)}S_\alpha^{(11)} - 7(S_\alpha^{(9)})^2} = \frac{5}{2}\tau_\alpha^{-1}\tau_{\alpha\alpha}\frac{S_\alpha^{(11)}}{D_\alpha} \tag{A.2}$$

- The coefficient $c_\alpha^{(6)}$ in Eq. (8.4.4) is:

$$c_\alpha^{(6)} = \frac{S_\alpha^{(8)}S_\alpha^{(9)} - S_\alpha^{(2)}S_\alpha^{(11)}}{S_\alpha^{(5)}S_\alpha^{(11)} - 7(S_\alpha^{(9)})^2} = \frac{S_\alpha^{(8)}S_\alpha^{(9)} - S_\alpha^{(2)}S_\alpha^{(11)}}{D_\alpha} \tag{A.3}$$

- Boltzmann constant is added into (8.4.4):

$$\frac{\mathbf{h}_{\alpha z}}{p_{\alpha z}} - \frac{\overline{\mathbf{h}}_\alpha}{p_\alpha} = n_\alpha\tau_\alpha\tau_{\alpha\alpha}^{-1}c_\alpha^{(5)}\left(\frac{\overline{Z_\alpha^2}}{Z^2}k\nabla T_{\alpha z} - k\nabla T_\alpha\right) + c_\alpha^{(6)}(\mathbf{w}_{\alpha z} - \overline{\mathbf{w}}_\alpha) \tag{A.4}$$

$$\text{where } \tau_\alpha^{-1} = \sum_\beta \frac{\mu_{\alpha\beta}}{m_\alpha}\tau_{\alpha\beta}^{-1} \quad \text{(the power of } \tau_\alpha \text{ is corrected)} \tag{A.5}$$

- Following the analysis given in [154] and using expressions for the partial bracket integrals provided in [155], the r.h.s. of (8.1.6') should be changed to:

$$-\omega_{\alpha Z}\{\sigma_{\alpha Zlr}e_{slm}k_m\} = \sum_{\beta,\zeta}\frac{kT}{m_\alpha + m_\beta}\left[\frac{7}{2}kT\mu_{\alpha\beta}\left(\frac{G^{(13)}_{\alpha z\beta\zeta}\pi_{\alpha zrs}}{m_\alpha^2 p_{\alpha z}} + \frac{G^{(14)}_{\alpha z\beta\zeta}\pi_{\beta\zeta rs}}{m_\beta^2 p_{\beta\zeta}}\right) + \frac{G^{(15)}_{\alpha z\beta\zeta}\sigma_{\alpha zrs}}{p_{\alpha z}} + \frac{G^{(16)}_{\alpha z\beta\zeta}\sigma_{\beta\zeta rs}}{p_{\beta\zeta}}\right] \tag{A.6}$$

- In Eq. (8.1.7):

$$G^{(14)}_{\alpha Z\beta\zeta} = -\frac{24}{35}\frac{m_\beta}{m_\alpha}\lambda_{\alpha Z\beta\zeta} \tag{A.7}$$

$$G^{(16)}_{\alpha Z\beta\zeta} = \frac{24}{7}\kappa_{\alpha\beta}\frac{m_\beta}{m_\alpha}\lambda_{\alpha Z\beta\zeta} \tag{A.8}$$

# B G-objects, Z-varibles and S-coefficients

The lengthy G-objects and Z-varibles, which are used in the thesis, are presented in this appendix. The $\check{G}^{(n)}_{\alpha\beta}$ objects are:

$$\check{G}^{(n)}_{\alpha\beta} \stackrel{\text{def}}{=} \frac{\overline{Z^2_\alpha} n_\alpha}{Z_{eff} n_e} \frac{\overline{Z^2_\beta} n_\beta}{Z_{eff} n_e} N^{(n)}_{\alpha\beta} \tag{B.1}$$

The $\check{G}^{(n)}_{\alpha\beta}$ relates to the Zhdanov $\overline{G}^{(n)}_{\alpha\beta}$ as flowing:

$$\check{G}^{(n)}_{\alpha\beta} = \overline{G}^{(n)}_{\alpha\beta} \frac{\zeta_p}{(Z_{eff} n_e)^2 m_p} \quad n = 2, 5, 6, 8, 11, 12 \tag{B.2}$$

$$\check{G}^{(n)}_{\alpha\beta} = \overline{G}^{(n)}_{\alpha\beta} \frac{\zeta_p}{(Z_{eff} n_e)^2 m_p} \frac{\mu_{\alpha\beta}}{m_\alpha}, \quad n = 9, 10, \tag{B.3}$$

$$\check{G}^{(n)}_{\alpha\beta} = \overline{G}^{(n)}_{\alpha\beta} \frac{\zeta_p}{(Z_{eff} n_e)^2 m_p} \frac{m_p}{m_\alpha + m_\beta}, \quad n = 3, 4, 15, 16, \tag{B.4}$$

$$\check{G}^{(n)}_{\alpha\beta} = \overline{G}^{(n)}_{\alpha\beta} \frac{\zeta_p}{(Z_{eff} n_e)^2 m_p} \frac{m_p}{m_\alpha} \kappa_{\alpha\beta}, \quad n = 13, \tag{B.5}$$

$$\check{G}^{(n)}_{\alpha\beta} = \overline{G}^{(n)}_{\alpha\beta} \frac{\zeta_p}{(Z_{eff} n_e)^2 m_p} \frac{m_p}{m_\beta} \kappa_{\alpha\beta}, \quad n = 14, \tag{B.6}$$

Where $N^{(n)}_{\alpha\beta}$ is a different part of each $\check{G}^{(n)}_{\alpha\beta}$:

$$N^{(2)}_{\alpha\beta} \stackrel{\text{def}}{=} \frac{3}{5} \sqrt{\frac{\mu_{\alpha\beta}}{m_p}}, \qquad N^{(3)}_{\alpha\beta} \stackrel{\text{def}}{=} -2 \left(1 + \frac{3}{5} \frac{m_\beta}{m_\alpha}\right) \frac{m_p}{m_\alpha + m_\beta} \sqrt{\frac{\mu_{\alpha\beta}}{m_p}}, \tag{B.7}$$

$$N^{(4)}_{\alpha\beta} \stackrel{\text{def}}{=} \frac{4}{5} \frac{m_p}{m_\alpha + m_\beta} \sqrt{\frac{\mu_{\alpha\beta}}{m_p}} \qquad N^{(5)}_{\alpha\beta} \stackrel{\text{def}}{=} -\left(\frac{13}{10} \frac{m_\beta}{m_\alpha} + \frac{8}{5} + 3 \frac{m_\alpha}{m_\beta}\right) \kappa_{\alpha\beta} \sqrt{\frac{\mu_{\alpha\beta}}{m_p}}, \tag{B.8}$$

$$N^{(6)}_{\alpha\beta} \stackrel{\text{def}}{=} \frac{27}{10} \kappa_{\alpha\beta} \sqrt{\frac{\mu_{\alpha\beta}}{m_p}}, \qquad N^{(8)}_{\alpha\beta} \stackrel{\text{def}}{=} -\frac{3}{14} \sqrt{\frac{\mu_{\alpha\beta}}{m_p}}, \tag{B.9}$$

$$N^{(9)}_{\alpha\beta} \stackrel{\text{def}}{=} \frac{3}{5} \left(\frac{23}{28} \frac{m_\beta}{m_\alpha} + \frac{8}{7} + 3 \frac{m_\alpha}{m_\beta}\right) \kappa_{\alpha\beta} \frac{\mu_{\alpha\beta}}{m_\alpha} \sqrt{\frac{\mu_{\alpha\beta}}{m_p}}, \qquad N^{(10)}_{\alpha\beta} \stackrel{\text{def}}{=} -\frac{45}{28} \kappa_{\alpha\beta} \frac{\mu_{\alpha\beta}}{m_\alpha} \sqrt{\frac{\mu_{\alpha\beta}}{m_p}}, \tag{B.10}$$

$$N_{\alpha\beta}^{(11)} \stackrel{\text{def}}{=} -\left(\frac{433}{280}\frac{m_\beta^2}{m_\alpha^2}+\frac{136}{35}\frac{m_\beta}{m_\alpha}+\frac{459}{35}+\frac{32}{5}\frac{m_\alpha}{m_\beta}+5\frac{m_\alpha^2}{m_\beta^2}\right)\kappa_{\alpha\beta}^2\sqrt{\frac{\mu_{\alpha\beta}}{m_p}}, \tag{B.11}$$

$$N_{\alpha\beta}^{(12)} \stackrel{\text{def}}{=} \frac{75}{8}\kappa_{\alpha\beta}^2\sqrt{\frac{\mu_{\alpha\beta}}{m_p}}, \qquad N_{\alpha\beta}^{(13)} \stackrel{\text{def}}{=} \left(\frac{18}{35}\frac{m_\beta}{m_\alpha}+\frac{6}{5}\right)\frac{m_p}{m_\alpha}\kappa_{\alpha\beta}\sqrt{\frac{\mu_{\alpha\beta}}{m_p}}, \tag{B.12}$$

$$N_{\alpha\beta}^{(14)} \stackrel{\text{def}}{=} -\frac{24}{35}\frac{m_p}{m_\alpha}\kappa_{\alpha\beta}\sqrt{\frac{\mu_{\alpha\beta}}{m_p}}, \tag{B.13}$$

$$N_{\alpha\beta}^{(15)} \stackrel{\text{def}}{=} -\left(\frac{51}{35}\frac{m_\beta^2}{m_\alpha^2}+\frac{37}{7}\frac{m_\beta}{m_\alpha}+\frac{22}{5}+4\frac{m_\alpha}{m_\beta}\right)\frac{m_p}{m_\alpha+m_\beta}\kappa_{\alpha\beta}\sqrt{\frac{\mu_{\alpha\beta}}{m_p}}, \tag{B.14}$$

$$N_{\alpha\beta}^{(16)} \stackrel{\text{def}}{=} \frac{24}{7}\frac{m_\beta}{m_\alpha}\frac{m_p}{m_\alpha+m_\beta}\kappa_{\alpha\beta}\sqrt{\frac{\mu_{\alpha\beta}}{m_p}}, \tag{B.15}$$

The $Z$-variables are defined by:

$$Z_\alpha^* \stackrel{\text{def}}{=} \sum_{\beta:\ m_\beta>m_\alpha}\frac{\overline{Z_\beta^2}n_\beta}{\overline{Z_\alpha^2}n_\alpha}, \qquad Z_{c\alpha}^* \stackrel{\text{def}}{=} \sum_{\beta\neq\alpha}\sqrt{\frac{\mu_{\alpha\beta}}{m_\alpha}}\frac{\overline{Z_\beta^2}n_\beta}{\overline{Z_\alpha^2}n_\alpha} \tag{B.16}$$

$$Z_{2\alpha}^s \stackrel{\text{def}}{=} \sum_{\beta\neq\alpha}\left(\frac{\mu_{\alpha\beta}}{m_\alpha}\right)^{3/2}\frac{\overline{Z_\beta^2}n_\beta}{\overline{Z_\alpha^2}n_\alpha}, \quad Z_{8\alpha}^s \stackrel{\text{def}}{=} \sum_{\beta\neq\alpha}\left(\frac{\mu_{\alpha\beta}}{m_\alpha}\right)^{5/2}\frac{\overline{Z_\beta^2}n_\beta}{\overline{Z_\alpha^2}n_\alpha} \tag{B.17}$$

$$Z_{5\alpha}^s \stackrel{\text{def}}{=} \sum_{\beta\neq\alpha}\left(1+\frac{16}{13}\frac{m_\alpha}{m_\beta}+\frac{30}{13}\left(\frac{m_\alpha}{m_\beta}\right)^2\right)\left(\frac{\mu_{\alpha\beta}}{m_\alpha}\right)^{5/2}\frac{\overline{Z_\beta^2 n_\beta}}{\overline{Z_\alpha^2}n_\alpha} \tag{B.18}$$

$$Z_{9\alpha}^s \stackrel{\text{def}}{=} \sum_{\beta\neq\alpha}\left(1+\frac{32}{23}\frac{m_\alpha}{m_\beta}+\frac{84}{23}\left(\frac{m_\alpha}{m_\beta}\right)^2\right)\left(\frac{\mu_{\alpha\beta}}{m_\alpha}\right)^{7/2}\frac{\overline{Z_\beta^2}n_\beta}{\overline{Z_\alpha^2}n_\alpha} \tag{B.19}$$

$$Z_{11\alpha}^s \stackrel{\text{def}}{=} \sum_{\beta\neq\alpha}\left(1+\frac{1088}{433}\frac{m_\alpha}{m_\beta}+\frac{3672}{433}\left(\frac{m_\alpha}{m_\beta}\right)^2+\frac{1792}{433}\left(\frac{m_\alpha}{m_\beta}\right)^3+\frac{1400}{433}\left(\frac{m_\alpha}{m_\beta}\right)^4\right)\left(\frac{\mu_{\alpha\beta}}{m_\alpha}\right)^{9/2}\frac{\overline{Z_\beta^2}n_\beta}{\overline{Z_\alpha^2}n_\alpha} \tag{B.20}$$

$$Z^{\pi}_{11\alpha} \stackrel{\text{def}}{=} \sum_{\beta\neq\alpha}\left(1+\frac{5}{3}\frac{m_\alpha}{m_\beta}\right)\left(\frac{\mu_{\alpha\beta}}{m_\alpha}\right)^{3/2}\frac{\overline{Z^2_\beta}}{n_\beta}\overline{Z^2_\alpha}n_\alpha \tag{B.21}$$

$$Z^{\pi}_{12\alpha} \stackrel{\text{def}}{=} \sum_{\beta\neq\alpha}\left(1+\frac{7}{3}\frac{m_\alpha}{m_\beta}\right)\left(\frac{\mu_{\alpha\beta}}{m_\alpha}\right)^{5/2}\frac{\overline{Z^2_\beta}}{n_\beta}\overline{Z^2_\alpha}n_\alpha \tag{B.22}$$

$$Z^{\pi}_{22\alpha} \stackrel{\text{def}}{=} \sum_{\beta\neq\alpha}\left(1+\frac{185}{51}\frac{m_\alpha}{m_\beta}+\frac{154}{51}\left(\frac{m_\alpha}{m_\beta}\right)^2+\frac{140}{51}\left(\frac{m_\alpha}{m_\beta}\right)^3\right)\left(\frac{\mu_{\alpha\beta}}{m_\alpha}\right)^{7/2}\frac{\overline{Z^2_\beta}}{n_\beta}\overline{Z^2_\alpha}n_\alpha \tag{B.23}$$

S-coefficients for the heat flux:

$$S^{(2)}_\alpha \stackrel{\text{def}}{=} \sum_\beta \frac{5}{2}\frac{\mu_{\alpha\beta}}{m_\alpha}\overline{G}^{(2)}_{\alpha\beta} = \lambda_{\alpha\alpha}\Big[\frac{3}{4}+\frac{3\sqrt{2}}{2}Z^s_{2\alpha}\Big] \tag{B.24}$$

$$S^{(5)}_\alpha \stackrel{\text{def}}{=} \sum_\beta \overline{G}^{(5)}_{\alpha\beta} = -\lambda_{\alpha\alpha}\Big[\frac{59}{40}+\frac{13\sqrt{2}}{10}Z^s_{5\alpha}\Big] \tag{B.25}$$

$$S^{(8)}_\alpha \stackrel{\text{def}}{=} \sum_\beta \frac{35}{2}\left(\frac{\mu_{\alpha\beta}}{m_\alpha}\right)^2\overline{G}^{(8)}_{\alpha\beta} = -\lambda_{\alpha\alpha}\Big[\frac{15}{16}+\frac{15\sqrt{2}}{4}Z^s_{8\alpha}\Big] \tag{B.26}$$

$$S^{(9)}_\alpha \stackrel{\text{def}}{=} \sum_\beta \frac{\mu_{\alpha\beta}}{m_\alpha}\overline{G}^{(9)}_{\alpha\beta} = \lambda_{\alpha\alpha}\Big[\frac{417}{1120}+\frac{69\sqrt{2}}{140}Z^s_{9\alpha}\Big] \tag{B.27}$$

$$S^{(11)}_\alpha \stackrel{\text{def}}{=} \sum_\beta \overline{G}^{(11)}_{\alpha\beta} = -\lambda_{\alpha\alpha}\Big[\frac{1677}{896}+\frac{433\sqrt{2}}{280}Z^s_{11\alpha}\Big] \tag{B.28}$$

$$D_\alpha \stackrel{\text{def}}{=} S^{(5)}_\alpha S^{(11)}_\alpha - 7(S^{(9)}_\alpha)^2 \tag{B.29}$$

$$D^{part}_\alpha \stackrel{\text{def}}{=} \frac{89600}{160413}\frac{D_\alpha}{\lambda^2_{\alpha\alpha}} = 1+\frac{204376\sqrt{2}}{160413}Z^s_{11\alpha}+\frac{72670\sqrt{2}}{53471}Z^s_{5\alpha}-\frac{76728\sqrt{2}}{53471}Z^s_{9\alpha}+ \frac{360256}{160413}Z^s_{5\alpha}Z^s_{11\alpha}-\frac{101568}{53471}(Z^s_{9\alpha})^2 \tag{B.30}$$

S-coefficients for viscous stress tensor:

$$S_\alpha^{(3)} \stackrel{\text{def}}{=} \sum_\beta \frac{m_\alpha}{m_\alpha + m_\beta} \overline{G}_{\alpha\beta}^{(3)} = -\lambda_{\alpha\alpha}\Big[\frac{8}{5} + \frac{6\sqrt{2}}{5} Z_{11\alpha}^\pi\Big] \tag{B.31}$$

$$S_\alpha^{(13)} \stackrel{\text{def}}{=} \sum_\beta \frac{\mu_{\alpha\beta}}{m_\alpha + m_\beta} \overline{G}_{\alpha\beta}^{(13)} = \lambda_{\alpha\alpha}\Big[\frac{3}{7} + \frac{18\sqrt{2}}{35} Z_{12\alpha}^\pi\Big] \tag{B.32}$$

$$S_\alpha^{(15)} \stackrel{\text{def}}{=} \sum_\beta \frac{m_\alpha}{m_\alpha + m_\beta} \overline{G}_{\alpha\beta}^{(15)} = -\lambda_{\alpha\alpha}\Big[\frac{53}{28} + \frac{51\sqrt{2}}{35} Z_{22\alpha}^\pi\Big] \tag{B.33}$$

$$D_\alpha^\pi \stackrel{\text{def}}{=} S_\alpha^{(3)} S_\alpha^{(15)} - \frac{7}{2}\left(S_\alpha^{(13)}\right)^2 \tag{B.34}$$

$$D_\alpha^{\pi part} \stackrel{\text{def}}{=} \frac{70}{167}\frac{D_\alpha^\pi}{\lambda_{\alpha\alpha}^2} = 1 + \frac{159\sqrt{2}}{167} Z_{11\alpha}^\pi + \frac{816\sqrt{2}}{835} Z_{22\alpha}^\pi - \frac{108\sqrt{2}}{167} Z_{12\alpha}^\pi + \frac{1224}{835} Z_{11\alpha}^\pi Z_{22\alpha}^\pi - \frac{648}{835}(Z_{12\alpha}^\pi)^2 \tag{B.35}$$

where from (2.91) and (C.11):

$$\lambda_{\alpha\beta} = \overline{Z_\alpha^2} n_\alpha \overline{Z_\beta^2} n_\beta \sqrt{\mu_{\alpha\beta}} \sqrt{m_p} \zeta_p^{-1} \tag{B.36}$$

# C Heat flux derivation

## C.1 Averaged over charge states

The system of linear algebraic equations for rank-1 moments (4.43) and (4.44) using (B.2) and (B.3) turns into:

$$\sum_{\beta}\left[\check{G}^{(5)}_{\alpha\beta}\frac{\overline{\mathbf{h}}_{\alpha}}{p_{\alpha}}+\check{G}^{(6)}_{\alpha\beta}\frac{\overline{\mathbf{h}}_{\beta}}{p_{\beta}}+\frac{m_{\alpha}}{T_{av}}\check{G}^{(9)}_{\alpha\beta}\frac{\overline{\mathbf{r}}_{\alpha}}{p_{\alpha}}+\frac{m_{\alpha}}{T_{av}}\check{G}^{(10)}_{\alpha\beta}\frac{\overline{\mathbf{r}}_{\beta}}{p_{\beta}}\right]= \\ \frac{5}{2}n_{\alpha}\frac{\zeta_{p}}{(Z_{eff}n_{e})^{2}m_{p}}\widetilde{\nabla T_{\alpha}}-\sum_{\beta}\frac{5}{2}\frac{\mu_{\alpha\beta}}{m_{\alpha}}\check{G}^{(2)}_{\alpha\beta}(\overline{\mathbf{w}}_{\alpha}-\overline{\mathbf{w}}_{\beta}) \quad \text{(C.1)}$$

$$\sum_{\beta}\left[7\check{G}^{(9)}_{\alpha\beta}\frac{\overline{\mathbf{h}}_{\alpha}}{p_{\alpha}}+7\check{G}^{(10)}_{\alpha\beta}\frac{\overline{\mathbf{h}}_{\beta}}{p_{\beta}}+\frac{m_{\alpha}}{T_{av}}\check{G}^{(11)}_{\alpha\beta}\frac{\overline{\mathbf{r}}_{\alpha}}{p_{\alpha}}+\frac{m_{\beta}}{T_{av}}\check{G}^{(12)}_{\alpha\beta}\frac{\overline{\mathbf{r}}_{\beta}}{p_{\beta}}\right]= \\ -\sum_{\beta}\frac{35}{2}\left(\frac{\mu_{\alpha\beta}}{m_{\alpha}}\right)^{2}\check{G}^{(8)}_{\alpha\beta}(\overline{\mathbf{w}}_{\alpha}-\overline{\mathbf{w}}_{\beta}) \quad \text{(C.2)}$$

The (C.1) and (C.2) is a system of equation $2\alpha^{max}\times 2\alpha^{max}$, which can be written in the form of:

$$\sum_{\beta=1..2\alpha^{max}}\check{a}_{\alpha\beta}X_{\beta}=\check{b}_{\alpha} \quad \text{(C.3)}$$

where:

$$X_{\beta}=\begin{cases}\frac{\overline{\mathbf{h}}_{\beta}}{p_{\beta}},\beta=1..\alpha^{max}\\ \frac{\overline{\mathbf{r}}_{\beta}}{p_{\beta}},\beta=\alpha^{max}+1..2\alpha^{max}\end{cases} \quad \text{(C.4)}$$

and the l.h.s. coefficients are:
$\alpha=1..\alpha^{max}$
$\beta=1..\alpha^{max}$

$$\check{a}_{\alpha\beta}=\check{G}^{(6)}_{\alpha\beta},\quad \check{a}_{\alpha+\alpha^{max}\beta}=7\check{G}^{(10)}_{\alpha\beta} \quad \text{(C.5)}$$

$$\check{a}_{\alpha\beta+\alpha^{max}} = \frac{m_\alpha}{T_{av}}\check{G}^{(10)}_{\alpha\beta}, \quad \check{a}_{\alpha+\alpha^{max}\beta+\alpha^{max}} = \frac{m_\beta}{T_{av}}\check{G}^{(12)}_{\alpha\beta} \tag{C.6}$$

Addition for diagonal elements:
$\beta = 1..\alpha^{max}$

$$\check{a}_{\beta\beta} = \check{a}_{\beta\beta} + \sum_\gamma \check{G}^{(5)}_{\beta\gamma}, \quad \check{a}_{\beta+\alpha^{max}\beta} = \check{a}_{\beta+\alpha^{max}\beta} + 7\sum_\gamma \check{G}^{(9)}_{\beta\gamma} \tag{C.7}$$

$$\check{a}_{\beta\beta+\alpha^{max}} = \check{a}_{\beta\beta+\alpha^{max}} + \frac{m_\beta}{T_{av}}\sum_\gamma \check{G}^{(9)}_{\beta\gamma}, \quad \check{a}_{\beta+\alpha^{max}\beta+\alpha^{max}} = \check{a}_{\beta+\alpha^{max}\beta+\alpha^{max}} + \frac{m_\beta}{T_{av}}\sum_\gamma \check{G}^{(11)}_{\beta\gamma} \tag{C.8}$$

and the r.h.s. terms are:
$\alpha = 1..\alpha^{max}$

$$\check{b}_\alpha = \frac{5}{2}n_\alpha \frac{\zeta_p}{(Z_{eff}n_e)^2 m_p}\widetilde{\nabla T_\alpha} - \sum_\beta \frac{5}{2}\frac{\mu_{\alpha\beta}}{m_\alpha}\check{G}^{(2)}_{\alpha\beta}(\overline{\mathbf{w}}_\alpha - \overline{\mathbf{w}}_\beta) \tag{C.9}$$

$$\check{b}_{\alpha+\alpha^{max}} = -\sum_\beta \frac{35}{2}\left(\frac{\mu_{\alpha\beta}}{m_\alpha}\right)^2 \check{G}^{(8)}_{\alpha\beta}(\overline{\mathbf{w}}_\alpha - \overline{\mathbf{w}}_\beta) \tag{C.10}$$

The normalized G-objects are defined in appendix B, and the collisional frequency part is represented by $\zeta_p$, which is defined as:

$$\zeta_p \stackrel{\text{def}}{=} \frac{3}{4\sqrt{2\pi}}\frac{\sqrt{m_p}T_i^{\frac{3}{2}}}{\ln\Lambda}\left(\frac{4\pi\epsilon_0}{e^2}\right)^2 \tag{C.11}$$

The solution of the system of linear algebraic equations (C.3): $\check{A}X = \check{b}$ can be expressed via coefficients of the inverse matrix: $X = \check{A}^{-1}\check{b}$. Let $\check{a}_{\alpha\beta}$ is an element of $\check{A}$ and $\tilde{\check{a}}_{\alpha\beta}$ is an element of $\check{A}^{-1}$.
Then $X_i = \sum_{j=1..2\alpha^{max}} \tilde{\check{a}}_{ij}\check{b}_j$.

It is also convenient to re-normalize a part of the inverted matrix as following:
$\alpha = 1..\alpha^{max}$
$\beta = 1..2\alpha^{max}$

$$\tilde{\check{a}}^{mdf}_{\alpha\beta} = \frac{m_\alpha}{T_{av}}\tilde{\check{a}}_{\alpha+\alpha^{max}\beta} \tag{C.12}$$

The averaged heat flux is:

$$\overline{\mathbf{h}}_\alpha = p_\alpha X_\alpha = p_\alpha \sum_\gamma \tilde{\tilde{a}}_{\alpha\gamma} \frac{5}{2} n_\gamma \frac{\zeta_p}{(Z_{eff} n_e)^2 m_p} \widetilde{\nabla T}_\gamma -$$

$$p_\alpha \sum_\gamma \sum_\beta \left[ \tilde{\tilde{a}}_{\alpha\gamma} \frac{5}{2} \frac{\mu_{\gamma\beta}}{m_\gamma} \check{G}^{(2)}_{\gamma\beta} (\overline{\mathbf{w}}_\gamma - \overline{\mathbf{w}}_\beta) + \tilde{\tilde{a}}_{\alpha\gamma+\alpha^{max}} \frac{35}{2} \left( \frac{\mu_{\gamma\beta}}{m_\gamma} \right)^2 \check{G}^{(8)}_{\gamma\beta} (\overline{\mathbf{w}}_\gamma - \overline{\mathbf{w}}_\beta) \right] =$$

$$\frac{5}{2} p_\alpha \frac{\zeta_p}{(Z_{eff} n_e)^2 m_p} \sum_\gamma \tilde{\tilde{a}}_{\alpha\gamma} n_\gamma \widetilde{\nabla T}_\gamma + p_\alpha \sum_\gamma \sum_\beta c^{(h^A_w *)}_{\alpha\gamma\beta} (\overline{\mathbf{w}}_\gamma - \overline{\mathbf{w}}_\beta) \quad \text{(C.13)}$$

where:

$$c^{(h^A_w *)}_{\alpha\gamma\beta} = -\frac{5}{2} \frac{\mu_{\gamma\beta}}{m_\gamma} \check{G}^{(2)}_{\gamma\beta} \tilde{\tilde{a}}_{\alpha\gamma} - \frac{35}{2} \left( \frac{\mu_{\gamma\beta}}{m_\beta} \right)^2 \check{G}^{(8)}_{\gamma\beta} \tilde{\tilde{a}}_{\alpha\gamma+\alpha^{max}} \quad \text{(C.14)}$$

We combine the $c^{(h^A_w *)}_{\alpha\gamma\beta}$ coefficients in the following way:

$$\sum_\gamma \sum_\beta c^{(h^A_w *)}_{\alpha\gamma\beta} (\overline{\mathbf{w}}_\gamma - \overline{\mathbf{w}}_\beta) = \sum_\gamma \sum_\beta c^{(h^A_w *)}_{\alpha\gamma\beta} (\overline{\mathbf{w}}_\alpha - \overline{\mathbf{w}}_\beta) - \sum_\gamma \sum_\beta c^{(h^A_w *)}_{\alpha\gamma\beta} (\overline{\mathbf{w}}_\alpha - \overline{\mathbf{w}}_\gamma) =$$

$$\sum_\beta \sum_\gamma c^{(h^A_w *)}_{\alpha\gamma\beta} (\overline{\mathbf{w}}_\alpha - \overline{\mathbf{w}}_\beta) - \sum_\beta \sum_\gamma c^{(h^A_w *)}_{\alpha\beta\gamma} (\overline{\mathbf{w}}_\alpha - \overline{\mathbf{w}}_\beta) =$$

$$\sum_\beta (\overline{\mathbf{w}}_\alpha - \overline{\mathbf{w}}_\beta) \left( \sum_\gamma c^{(h^A_w *)}_{\alpha\gamma\beta} - \sum_\gamma c^{(h^A_w *)}_{\alpha\beta\gamma} \right) = \sum_\beta c^{(h^A_w)}_{\beta\alpha} (\overline{\mathbf{w}}_\alpha - \overline{\mathbf{w}}_\beta) \quad \text{(C.15)}$$

where:

$$c^{(h^A_w)}_{\beta\alpha} = \sum_\gamma \left( c^{(h^A_w *)}_{\alpha\gamma\beta} - c^{(h^A_w *)}_{\alpha\beta\gamma} \right) \quad \text{(C.16)}$$

It is convenient to split the heat flux into the $T$- and $\mathbf{w}$-dependent parts. The averaged heat flux is:

$$\overline{\mathbf{h}}_\alpha = \overline{\mathbf{h}}^T_\alpha + \overline{\mathbf{h}}^{\mathbf{w}}_\alpha, \quad \text{(C.17)}$$

where

$$\overline{\mathbf{h}}^T_\alpha = -\sum_\beta \kappa^{(h^A_T)}_{\alpha\beta} \widetilde{\nabla T}_\beta, \quad \overline{\mathbf{h}}^{\mathbf{w}}_\alpha = p_\alpha \sum_\beta c^{(h^A_w)}_{\beta\alpha} (\overline{\mathbf{w}}_\alpha - \overline{\mathbf{w}}_\beta), \quad \text{(C.18)}$$

where

$$\kappa^{(h^A_T)}_{\alpha\beta} = -\frac{5}{2} p_\alpha \frac{\zeta_p}{(Z_{eff} n_e)^2 m_p} \tilde{\tilde{a}}_{\alpha\beta} n_\beta. \quad \text{(C.19)}$$

## C.2 Charge state corrections

Subtracting (4.41) from (4.43) and (4.42) from (4.44) one can obtain:

$$\frac{5}{2}n_\alpha\left(\widetilde{\nabla T_\alpha}-\frac{\overline{Z_\alpha^2}}{Z^2}\nabla T_{\alpha Z}\right)=S_\alpha^{(2)}(\overline{\mathbf{w}}_\alpha-\mathbf{w}_{\alpha Z})+ S_\alpha^{(5)}\left(\frac{\overline{\mathbf{h}}_\alpha}{p_\alpha}-\frac{\mathbf{h}_{\alpha Z}}{p_{\alpha Z}}\right)+\frac{m_\alpha}{T_{av}}S_\alpha^{(9)}\left(\frac{\overline{\mathbf{r}}_\alpha}{p_\alpha}-\frac{\mathbf{r}_{\alpha Z}}{p_{\alpha Z}}\right) \quad \text{(C.20)}$$

$$0=S_\alpha^{(8)}(\overline{\mathbf{w}}_\alpha-\mathbf{w}_{\alpha Z})+7S_{\alpha\beta}^{(9)}\left(\frac{\overline{\mathbf{h}}_\alpha}{p_\alpha}-\frac{\mathbf{h}_{\alpha Z}}{p_{\alpha Z}}\right)+\frac{m_\alpha}{T_{av}}S^{(11)}\left(\frac{\overline{\mathbf{r}}_\alpha}{p_\alpha}-\frac{\mathbf{r}_{\alpha Z}}{p_{\alpha Z}}\right) \quad \text{(C.21)}$$

The system (C.20) and (C.21) has an analytical solution:

$$\frac{\mathbf{h}_{\alpha Z}}{p_{\alpha Z}}-\frac{\overline{\mathbf{h}}_\alpha}{p_\alpha}=\frac{5}{2}n_\alpha\frac{S_\alpha^{(11)}}{S_\alpha^{(5)}S_\alpha^{(11)}-7(S_\alpha^{(9)})^2}\left(\frac{\overline{Z_\alpha^2}}{Z^2}\nabla T_{\alpha Z}-\widetilde{\nabla T_\alpha}\right)+ \frac{S_\alpha^{(9)}S_\alpha^{(8)}-S_\alpha^{(2)}S_\alpha^{(11)}}{S_\alpha^{(5)}S_\alpha^{(11)}-7(S_\alpha^{(9)})^2}(\mathbf{w}_{\alpha Z}-\overline{\mathbf{w}}_\alpha) \quad \text{(C.22)}$$

where S-coefficients are defined in appendix B. One can rewrite:

$$\frac{\mathbf{h}_{\alpha Z}}{p_{\alpha Z}}-\frac{\overline{\mathbf{h}}_\alpha}{p_\alpha}=-\frac{n_\alpha}{\lambda_{\alpha\alpha}}c_\alpha^{(h_T^B)}\left(\frac{\overline{Z_\alpha^2}}{Z^2}\nabla T_{\alpha Z}-\widetilde{\nabla T_\alpha}\right)+c_\alpha^{(h_w^B)}(\mathbf{w}_{\alpha Z}-\overline{\mathbf{w}}_\alpha), \quad \text{(C.23)}$$

where:

$$c_\alpha^{(h_T^B)}=-\frac{5}{2}\frac{S_\alpha^{(11)}\lambda_{\alpha\alpha}}{D_\alpha}=\frac{139750}{53471}\frac{1+\frac{6928\sqrt{2}}{8385}Z_{11\alpha}^s}{D_\alpha^{part}} \quad \text{(C.24)}$$

$$c_\alpha^{(h_w^B)}=\frac{S_\alpha^{(9)}S_\alpha^{(8)}-S_\alpha^{(2)}S_\alpha^{(11)}}{D_\alpha}= \frac{31500}{53471}\frac{1}{D_\alpha^{part}}\Bigg(1-\frac{139\sqrt{2}}{105}Z_{8\alpha}^s-\frac{46\sqrt{2}}{105}Z_{9\alpha}^s+\frac{1732\sqrt{2}}{1575}Z_{11\alpha}^s+ \frac{559\sqrt{2}}{210}Z_{2\alpha}^s-\frac{368}{105}Z_{8\alpha}^sZ_{9\alpha}^s+\frac{6928}{1575}Z_{2\alpha}^sZ_{11\alpha}^s\Bigg) \quad \text{(C.25)}$$

where Z-varibles are defined in appendix B. The heat flux for the each charge state is:

$$\mathbf{h}_{\alpha Z} = \mathbf{h}^{T}_{\alpha Z} + \mathbf{h}^{\mathbf{w}}_{\alpha Z} \tag{C.26}$$

Consequently, the $T$-dependent heat flux for the each charge state is:

$$\mathbf{h}^{T}_{\alpha Z} = -\frac{n_{\alpha Z}}{n_\alpha}\sum_\beta \kappa^{(h^A_T)}_{\alpha\beta}\widetilde{\nabla T_\beta} - \frac{n_{\alpha Z}}{n_\alpha}\kappa^{(h^B_T)}_{\alpha}\left(\frac{\overline{Z^2_\alpha}}{Z^2}\nabla T_{\alpha Z} - \widetilde{\nabla T_\alpha}\right), \tag{C.27}$$

where:

$$\kappa^{(h^B_T)}_{\alpha} = \frac{p_\alpha n_\alpha}{\lambda_{\alpha\alpha}} c^{(h^B_T)}_\alpha. \tag{C.28}$$

The $\mathbf{w}$-dependent heat flux for the each charge state is:

$$\mathbf{h}^{\mathbf{w}}_{\alpha Z} = p_{\alpha Z}\sum_\beta c^{(h^A_w)}_{\beta\alpha}(\overline{\mathbf{w}}_\alpha - \overline{\mathbf{w}}_\beta) + p_{\alpha Z} c^{(h^B_w)}_\alpha(\mathbf{w}_{\alpha Z} - \overline{\mathbf{w}}_\alpha) \tag{C.29}$$

The following combinations are done with a help from A. Stepanenko:

$$\begin{aligned}\frac{\mathbf{h}^{\mathbf{w}}_{\alpha Z}}{p_{\alpha Z}} &= c^{(h^B_w)}_\alpha \mathbf{w}_{\alpha Z} - \overline{\mathbf{w}}_\alpha(c^{(h^B_w)}_\alpha - \sum_\beta c^{(h^A_w)}_{\beta\alpha}) - \sum_\beta c^{(h^A_w)}_{\beta\alpha}\overline{\mathbf{w}}_\beta = \\ &c^{(h^B_w)}_\alpha \mathbf{w}_{\alpha Z} - (\sum_\beta \delta_{\alpha\beta} c^{(6)}_\beta \overline{\mathbf{w}}_\beta - \sum_\beta \delta_{\alpha\beta}\sum_\gamma c^{(h^A_w)}_{\gamma\alpha}\overline{\mathbf{w}}_\beta) - \sum_\beta c^{(h^A_w)}_{\beta\alpha}\overline{\mathbf{w}}_\beta = \\ &c^{(h^B_w)}_\alpha \mathbf{w}_{\alpha Z} - \sum_\beta c^{(h_w)}_{\beta\alpha}\overline{\mathbf{w}}_\beta,\end{aligned} \tag{C.30}$$

where:

$$c^{(h_w)}_{\beta\alpha} = \delta_{\alpha\beta} c^{(h^B_w)}_\beta - \delta_{\alpha\beta}\sum_\gamma c^{(h^A_w)}_{\gamma\alpha} + c^{(h^A_w)}_{\beta\alpha}. \tag{C.31}$$

Using $c^{(h_w)}_{\beta\alpha}$ summation property:

$$\sum_\beta c^{(h_w)}_{\beta\alpha} = c^{(h^B_w)}_\alpha - \sum_\gamma c^{(h^A_w)}_{\gamma\alpha} + \sum_\beta c^{(h^A_w)}_{\beta\alpha} = c^{(h^B_w)}_\alpha, \tag{C.32}$$

one finally can obtain the $\mathbf{w}$-dependent heat flux for the each charge state:

$$\mathbf{h}^{\mathbf{w}}_{\alpha Z} = p_{\alpha Z}\sum_\beta c^{(h_w)}_{\beta\alpha}(\mathbf{w}_{\alpha Z} - \overline{\mathbf{w}}_\beta). \tag{C.33}$$

# D Additional vector moment derivation

## D.1 Averaged over charge states

The solution of the system of linear algebraic equations (C.3) for the additional vector moment:

$$\overline{\mathbf{r}}_\alpha = p_\alpha X_\alpha = p_\alpha \sum_\gamma \tilde{\tilde{a}}_{\alpha+\alpha^{max}\gamma} \frac{5}{2} n_\gamma \frac{\zeta_p}{(Z_{eff} n_e)^2 m_p} \widetilde{\nabla T_\gamma} -$$

$$p_\alpha \sum_\gamma \sum_\beta \left[ \tilde{\tilde{a}}_{\alpha+\alpha^{max}\gamma} \frac{5}{2} \frac{\mu_{\gamma\beta}}{m_\gamma} \check{G}^{(2)}_{\gamma\beta} (\overline{\mathbf{w}}_\gamma - \overline{\mathbf{w}}_\beta) + \tilde{\tilde{a}}_{\alpha+\alpha^{max}\gamma+\alpha^{max}} \frac{35}{2} \left( \frac{\mu_{\gamma\beta}}{m_\gamma} \right)^2 \check{G}^{(8)}_{\gamma\beta} (\overline{\mathbf{w}}_\gamma - \overline{\mathbf{w}}_\beta) \right] =$$

$$\frac{5}{2} p_\alpha \frac{\zeta_p}{(Z_{eff} n_e)^2 m_p} \frac{T_{av}}{m_\alpha} \sum_\gamma \tilde{\tilde{a}}^{mdf}_{\alpha\gamma} n_\gamma \widetilde{\nabla T_\gamma} + p_\alpha \frac{T_{av}}{m_\alpha} \sum_\gamma \sum_\beta c^{(r^A_w *)}_{\alpha\gamma\beta} (\overline{\mathbf{w}}_\gamma - \overline{\mathbf{w}}_\beta) \quad \text{(D.1)}$$

where:

$$c^{(r^A_w *)}_{\alpha\gamma\beta} = -\frac{5}{2} \frac{\mu_{\gamma\beta}}{m_\gamma} \check{G}^{(2)}_{\gamma\beta} \tilde{\tilde{a}}^{mdf}_{\alpha\gamma} - \frac{35}{2} \left( \frac{\mu_{\gamma\beta}}{m_\gamma} \right)^2 \check{G}^{(8)}_{\gamma\beta} \tilde{\tilde{a}}^{mdf}_{\alpha\gamma+\alpha^{max}} \quad \text{(D.2)}$$

Finally, the averaged additional vector moment is:

$$\overline{\mathbf{r}}_\alpha = \overline{\mathbf{r}}^T_\alpha + \overline{\mathbf{r}}^{\mathbf{w}}_\alpha, \quad \text{(D.3)}$$

where:

$$\overline{\mathbf{r}}^T_\alpha = -\frac{T_{av}}{m_\alpha} \sum_\beta \kappa^{(r^A_T)}_{\alpha\beta} \widetilde{\nabla T_\beta}, \quad \overline{\mathbf{r}}^{\mathbf{w}}_\alpha = p_\alpha \frac{T_{av}}{m_\alpha} \sum_\beta c^{(r^A_w)}_{\beta\alpha} (\overline{\mathbf{w}}_\alpha - \overline{\mathbf{w}}_\beta), \quad \text{(D.4)}$$

where, using similar to the heat flux approach (appendix C.1), coefficients are:

$$\kappa^{(r^A_T)}_{\alpha\beta} = -\frac{5}{2} p_\alpha \frac{\zeta_p}{(Z_{eff} n_e)^2 m_p} \tilde{\tilde{a}}^{mdf}_{\alpha\beta} n_\beta. \quad \text{(D.5)}$$

$$c^{(r^A_w)}_{\beta\alpha} = \sum_\gamma \left( c^{(r^A_w *)}_{\alpha\gamma\beta} - c^{(r^A_w *)}_{\alpha\beta\gamma} \right) \quad \text{(D.6)}$$

## D.2 Charge state corrections

The system (C.20) and (C.21) has an analytical solution:

$$\frac{\mathbf{r}_{\alpha Z}}{p_{\alpha Z}} - \frac{\overline{\mathbf{r}}_\alpha}{p_\alpha} = \frac{5}{2} n_\alpha \frac{T_{av}}{m_\alpha} \frac{-7 S_\alpha^{(9)}}{S_\alpha^{(5)} S_\alpha^{(11)} - 7 (S_\alpha^{(9)})^2} \left( \frac{\overline{Z_\alpha^2}}{Z^2} \nabla T_{\alpha Z} - \widetilde{\nabla T_\alpha} \right) + \frac{T_{av}}{m_\alpha} \frac{7 S_\alpha^{(2)} S_\alpha^{(9)} - S_\alpha^{(5)} S_\alpha^{(8)}}{S_\alpha^{(5)} S_\alpha^{(11)} - 7 (S_\alpha^{(9)})^2} (\mathbf{w}_{\alpha Z} - \overline{\mathbf{w}}_\alpha) \quad \text{(D.7)}$$

where S-coefficients are defined in appendix B. One can rewrite:

$$\frac{\mathbf{r}_{\alpha Z}}{p_{\alpha Z}} - \frac{\overline{\mathbf{r}}_\alpha}{p_\alpha} = -\frac{n_\alpha}{\lambda_{\alpha\alpha}} \frac{T_{av}}{m_\alpha} c_\alpha^{(r_T^B)} \left( \frac{\overline{Z_\alpha^2}}{Z^2} \nabla T_{\alpha Z} - \widetilde{\nabla T_\alpha} \right) + \frac{T_{av}}{m_\alpha} c_\alpha^{(r_w^B)} (\mathbf{w}_{\alpha Z} - \overline{\mathbf{w}}_\alpha) \quad \text{(D.8)}$$

where:

$$c_\alpha^{(r_T^B)} = \frac{35}{2} \frac{S_\alpha^{(9)} \lambda_{\alpha\alpha}}{D_\alpha} = \frac{194600}{53471} \frac{1 + \frac{184\sqrt{2}}{139} Z_{9\alpha}^s}{D_\alpha^{part}} \quad \text{(D.9)}$$

$$c_\alpha^{(r_w^B)} = \frac{7 S_\alpha^{(2)} S_\alpha^{(9)} - S_\alpha^{(5)} S_\alpha^{(8)}}{D_\alpha} = \frac{17080}{53471} \frac{1}{D_\alpha^{part}} \left( 1 + \frac{276\sqrt{2}}{61} Z_{9\alpha}^s + \frac{417\sqrt{2}}{61} Z_{2\alpha}^s - \frac{590\sqrt{2}}{61} Z_{8\alpha}^s - \frac{130\sqrt{2}}{61} Z_{5\alpha}^s + \frac{1104}{61} Z_{2\alpha}^s Z_{9\alpha}^s - \frac{1040}{61} Z_{5\alpha}^s Z_{8\alpha}^s \right) \quad \text{(D.10)}$$

where Z-varibles are defined in appendix B. The additional vector moment for the each charge state is:

$$\mathbf{r}_{\alpha Z} = \mathbf{r}_{\alpha Z}^T + \mathbf{r}_{\alpha Z}^{\mathbf{w}} \quad \text{(D.11)}$$

Consequently, the $T$-dependent additional vector moment for the each charge state is:

$$\mathbf{r}_{\alpha Z}^T = -\frac{n_{\alpha Z}}{n_\alpha} \frac{T_{av}}{m_\alpha} \sum_\beta \kappa_{\alpha\beta}^{(r_T^A)} \widetilde{\nabla T_\beta} - \frac{n_{\alpha Z}}{n_\alpha} \frac{T_{av}}{m_\alpha} \kappa_\alpha^{(r_T^B)} \left( \frac{\overline{Z_\alpha^2}}{Z^2} \nabla T_{\alpha Z} - \widetilde{\nabla T_\alpha} \right), \quad \text{(D.12)}$$

where:

$$\kappa_\alpha^{(r_T^B)} = \frac{p_\alpha n_\alpha}{\lambda_{\alpha\alpha}} c_\alpha^{(r_T^B)}. \quad \text{(D.13)}$$

The **w**-dependent additional vector moment for the each charge state is:

$$\mathbf{r}^{\mathbf{w}}_{\alpha Z} = p_{\alpha Z}\frac{T_{av}}{m_\alpha}\sum_\beta c^{(r^A_w)}_{\beta\alpha}(\overline{\mathbf{w}}_\alpha - \overline{\mathbf{w}}_\beta) + p_{\alpha Z}\frac{T_{av}}{m_\alpha}c^{(r^B_w)}_{\alpha}(\mathbf{w}_{\alpha Z} - \overline{\mathbf{w}}_\alpha) = p_{\alpha Z}\frac{T_{av}}{m_\alpha}\sum_\beta c^{(r_w)}_{\beta\alpha}(\mathbf{w}_{\alpha Z} - \overline{\mathbf{w}}_\beta), \quad \text{(D.14)}$$

where, using similar to the heat flux approach (C.30), the corresponding coefficient is:

$$c^{(r_w)}_{\beta\alpha} = \delta_{\alpha\beta}c^{(r^B_w)}_{\beta} - \delta_{\alpha\beta}\sum_\gamma c^{(r^A_w)}_{\gamma\alpha} + c^{(r^A_w)}_{\beta\alpha}. \quad \text{(D.15)}$$

# E Thermal force derivation

## E.1 Summed over charge states

The TF, which is summed over charge states, is:

$$\mathbf{R}_{\alpha}^{T}=\sum_{\beta}\Big[\frac{\mu_{\alpha\beta}}{T_{av}}\overline{G}_{\alpha\beta}^{(2)}\left(\frac{\overline{\mathbf{h}}_{\alpha}^{T}}{m_{\alpha}n_{\alpha}}-\frac{\overline{\mathbf{h}}_{\beta}^{T}}{m_{\beta}n_{\beta}}\right)+\left(\frac{\mu_{\alpha\beta}}{T_{av}}\right)^{2}\overline{G}_{\alpha\beta}^{(8)}\left(\frac{\overline{\mathbf{r}}_{\alpha}^{T}}{m_{\alpha}n_{\alpha}}-\frac{\overline{\mathbf{r}}_{\beta}^{T}}{m_{\beta}n_{\beta}}\right)\Big] \tag{E.1}$$

or:

$$\mathbf{R}_{\alpha}^{T}=\sum_{\beta}\Big[\frac{\mu_{\alpha\beta}}{m_{\alpha}}\overline{G}_{\alpha\beta}^{(2)}\left(\frac{\overline{\mathbf{h}}_{\alpha}^{T}}{p_{\alpha}}-\frac{m_{\alpha}}{m_{\beta}}\frac{\overline{\mathbf{h}}_{\beta}^{T}}{p_{\beta}}\right)+\left(\frac{\mu_{\alpha\beta}}{m_{\alpha}}\right)^{2}\overline{G}_{\alpha\beta}^{(8)}\frac{m_{\alpha}}{T_{av}}\left(\frac{\overline{\mathbf{r}}_{\alpha}^{T}}{p_{\alpha}}-\frac{m_{\alpha}}{m_{\beta}}\frac{\overline{\mathbf{r}}_{\beta}^{T}}{p_{\beta}}\right)\Big] \tag{E.2}$$

where from (C.18) and (D.4):

$$\frac{\overline{\mathbf{h}}_{\alpha}^{T}}{p_{\alpha}}=\frac{5}{2}\frac{\zeta_{p}}{(Z_{eff}n_{e})^{2}m_{p}}\sum_{\gamma}\tilde{\tilde{a}}_{\alpha\gamma}n_{\gamma}\widetilde{\nabla T_{\gamma}},\quad\frac{\overline{\mathbf{h}}_{\beta}^{T}}{p_{\beta}}=\frac{5}{2}\frac{\zeta_{p}}{(Z_{eff}n_{e})^{2}m_{p}}\sum_{\gamma}\tilde{\tilde{a}}_{\beta\gamma}n_{\gamma}\widetilde{\nabla T_{\gamma}}, \tag{E.3}$$

$$\frac{\overline{\mathbf{r}}_{\alpha}^{T}}{p_{\alpha}}=\frac{5}{2}\frac{\zeta_{p}}{(Z_{eff}n_{e})^{2}m_{p}}\frac{T_{av}}{m_{\alpha}}\sum_{\gamma}\tilde{\tilde{a}}_{\alpha\gamma}^{mdf}n_{\gamma}\widetilde{\nabla T_{\gamma}},\quad\frac{\overline{\mathbf{r}}_{\beta}^{T}}{p_{\beta}}=\frac{5}{2}\frac{\zeta_{p}}{(Z_{eff}n_{e})^{2}m_{p}}\frac{T_{av}}{m_{\beta}}\sum_{\gamma}\tilde{\tilde{a}}_{\beta\gamma}^{mdf}n_{\gamma}\widetilde{\nabla T_{\gamma}} \tag{E.4}$$

Thus:

$$\mathbf{R}_{\alpha}^{T}=\frac{5}{2}\frac{\zeta_{p}}{(Z_{eff}n_{e})^{2}m_{p}}\sum_{\beta}\sum_{\gamma}\left[\frac{\mu_{\alpha\beta}}{m_{\alpha}}\overline{G}_{\alpha\beta}^{(2)}\left(\tilde{\tilde{a}}_{\alpha\gamma}-\frac{m_{\alpha}}{m_{\beta}}\tilde{\tilde{a}}_{\beta\gamma}\right)+\left(\frac{\mu_{\alpha\beta}}{m_{\alpha}}\right)^{2}\overline{G}_{\alpha\beta}^{(8)}\left(\tilde{\tilde{a}}_{\alpha\gamma}^{mdf}-\left(\frac{m_{\alpha}}{m_{\beta}}\right)^{2}\tilde{\tilde{a}}_{\beta\gamma}^{mdf}\right)\right]n_{\gamma}\widetilde{\nabla T_{\gamma}}. \tag{E.5}$$

Using (B.2), we obtain:

$$\mathbf{R}_{\alpha}^{T}=\frac{5}{2}\sum_{\beta}\sum_{\gamma}\left[\frac{\mu_{\alpha\beta}}{m_{\alpha}}\check{G}_{\alpha\beta}^{(2)}\left(\tilde{\tilde{a}}_{\alpha\gamma}-\frac{m_{\alpha}}{m_{\beta}}\tilde{\tilde{a}}_{\beta\gamma}\right)+\left(\frac{\mu_{\alpha\beta}}{m_{\alpha}}\right)^{2}\check{G}_{\alpha\beta}^{(8)}\left(\tilde{\tilde{a}}_{\alpha\gamma}^{mdf}-\left(\frac{m_{\alpha}}{m_{\beta}}\right)^{2}\tilde{\tilde{a}}_{\beta\gamma}^{mdf}\right)\right]n_{\gamma}\widetilde{\nabla T_{\gamma}}. \tag{E.6}$$

Replacing the subscripts $\beta \leftrightarrow \gamma$ and the summation order, we get:

$$\mathbf{R}_{\alpha}^{T} = \sum_{\beta} \frac{5}{2} \sum_{\gamma} \left[ \frac{\mu_{\alpha\gamma}}{m_{\alpha}} \check{G}_{\alpha\gamma}^{(2)} \left( \tilde{\check{a}}_{\alpha\beta} - \frac{m_{\alpha}}{m_{\gamma}} \tilde{\check{a}}_{\gamma\beta} \right) + \left( \frac{\mu_{\alpha\gamma}}{m_{\alpha}} \right)^{2} \check{G}_{\alpha\gamma}^{(8)} \left( \tilde{\check{a}}_{\alpha\beta}^{mdf} - \left( \frac{m_{\alpha}}{m_{\gamma}} \right)^{2} \tilde{\check{a}}_{\gamma\beta}^{mdf} \right) \right] n_{\beta} \widetilde{\nabla T_{\beta}} \quad \text{(E.7)}$$

Finally:

$$\mathbf{R}_{\alpha}^{T} = -\sum_{\beta} n_{\beta} \tilde{c}_{\alpha\beta}^{(R_T^A)} \widetilde{\nabla T_{\beta}} \quad \text{(E.8)}$$

where:

$$\tilde{c}_{\alpha\beta}^{(R_T^A)} = -\frac{5}{2} \sum_{\gamma} \left[ \frac{\mu_{\alpha\gamma}}{m_{\alpha}} \check{G}_{\alpha\gamma}^{(2)} \left( \tilde{\check{a}}_{\alpha\beta} - \frac{m_{\alpha}}{m_{\gamma}} \tilde{\check{a}}_{\gamma\beta} \right) + \left( \frac{\mu_{\alpha\gamma}}{m_{\alpha}} \right)^{2} \check{G}_{\alpha\gamma}^{(8)} \left( \tilde{\check{a}}_{\alpha\beta}^{mdf} - \left( \frac{m_{\alpha}}{m_{\gamma}} \right)^{2} \tilde{\check{a}}_{\gamma\beta}^{mdf} \right) \right] \quad \text{(E.9)}$$

## E.2 Charge state corrections

Using (4.57), one can find the TF for the each charge state:

$$\mathbf{R}_{\alpha Z}^{T} = I_{\alpha Z} \mathbf{R}_{\alpha}^{T} + I_{\alpha Z} \sum_{\beta} \left[ \frac{\mu_{\alpha\beta}}{m_{\alpha}} \overline{G}_{\alpha\beta}^{(2)} \left( \frac{\mathbf{h}_{\alpha Z}^{T}}{p_{\alpha Z}} - \frac{\overline{\mathbf{h}}_{\alpha}^{T}}{p_{\alpha}} \right) + \left( \frac{\mu_{\alpha\beta}}{m_{\alpha}} \right)^{2} \frac{m_{\alpha}}{T_{av}} \overline{G}_{\alpha\beta}^{(8)} \left( \frac{\mathbf{r}_{\alpha Z}^{T}}{p_{\alpha Z}} - \frac{\overline{\mathbf{r}}_{\alpha}^{T}}{p_{\alpha}} \right) \right]. \quad \text{(E.10)}$$

Using (B.24) and (B.26), one can get:

$$\mathbf{R}_{\alpha Z}^{T} = I_{\alpha Z} \mathbf{R}_{\alpha}^{T} + I_{\alpha Z} \left[ \frac{2}{5} S_{\alpha}^{(2)} \left( \frac{\mathbf{h}_{\alpha Z}^{T}}{p_{\alpha Z}} - \frac{\overline{\mathbf{h}}_{\alpha}^{T}}{p_{\alpha}} \right) + \frac{2}{35} S_{\alpha}^{(8)} \frac{m_{\alpha}}{T_{av}} \left( \frac{\mathbf{r}_{\alpha Z}^{T}}{p_{\alpha Z}} - \frac{\overline{\mathbf{r}}_{\alpha}^{T}}{p_{\alpha}} \right) \right]. \quad \text{(E.11)}$$

Also, using (C.23) and (D.8), one can get:

$$\mathbf{R}_{\alpha Z}^{T} - I_{\alpha Z} \mathbf{R}_{\alpha}^{T} = -I_{\alpha Z} \left[ \frac{2}{5} \lambda_{\alpha\alpha} \left[ \frac{3}{4} + \frac{3\sqrt{2}}{2} Z_{2\alpha}^{s} \right] \frac{n_{\alpha}}{\lambda_{\alpha\alpha}} c_{\alpha}^{(h_T^B)} \left( \frac{\overline{Z_{\alpha}^{2}}}{Z^{2}} \nabla T_{\alpha Z} - \widetilde{\nabla T_{\alpha}} \right) + \right.$$
$$\left. - \frac{2}{35} \lambda_{\alpha\alpha} \left[ \frac{15}{16} + \frac{15\sqrt{2}}{4} Z_{8\alpha}^{s} \right] \frac{n_{\alpha}}{\lambda_{\alpha\alpha}} c_{\alpha}^{(r_T^B)} \left( \frac{\overline{Z_{\alpha}^{2}}}{Z^{2}} \nabla T_{\alpha Z} - \widetilde{\nabla T_{\alpha}} \right) \right]. \quad \text{(E.12)}$$

Then:

$$\mathbf{R}^T_{\alpha Z} - I_{\alpha Z}\mathbf{R}^T_{\alpha} = -n_{\alpha} I_{\alpha Z} c_{\alpha}^{(R_T^B)} \left( \frac{\overline{Z_{\alpha}^2}}{Z^2} \nabla T_{\alpha Z} - \widetilde{\nabla T_{\alpha}} \right) = -n_{\alpha Z} c_{\alpha}^{(R_T^B)} \left( \nabla T_{\alpha Z} - \frac{Z^2}{\overline{Z_{\alpha}^2}} \widetilde{\nabla T_{\alpha}} \right), \tag{E.13}$$

where:

$$c_{\alpha}^{(R_T^B)} = \frac{3}{5} c_{\alpha}^{(h_T^B)} \left( \frac{1}{2} + \sqrt{2} Z_{2\alpha}^s \right) - \frac{3}{14} c_{\alpha}^{(r_T^B)} \left( \frac{1}{4} + \sqrt{2} Z_{8\alpha}^s \right) = \frac{31500}{53471} \frac{\frac{559}{420} \left( 1 + \frac{6928\sqrt{2}}{8385} Z_{11\alpha}^s \right) \left( 1 + 2\sqrt{2} Z_{2\alpha}^s \right) - \frac{139}{420} \left( 1 + \frac{184\sqrt{2}}{139} Z_{9\alpha}^s \right) \left( 1 + 4\sqrt{2} Z_{8\alpha}^s \right)}{D_{\alpha}^{part}}. \tag{E.14}$$

Finally, one can obtain:

$$\mathbf{R}^T_{\alpha Z} = -I_{\alpha Z} \sum_{\beta} n_{\beta} \tilde{c}_{\alpha\beta}^{(R_T^A)} \widetilde{\nabla T_{\beta}} - n_{\alpha} I_{\alpha Z} c_{\alpha}^{(R_T^B)} \left( \frac{\overline{Z_{\alpha}^2}}{Z^2} \nabla T_{\alpha Z} - \widetilde{\nabla T_{\alpha}} \right) \tag{E.15}$$

# F Friction force derivation

## F.1 Summed over charge states

For derivation, it is convenient to split the friction force into the two parts:

$$\mathbf{R}^{\mathbf{w}}_{\alpha} = \mathbf{R}^{\mathbf{w}1}_{\alpha} + \mathbf{R}^{\mathbf{w}2}_{\alpha}, \quad \mathbf{R}^{\mathbf{w}1}_{\alpha} = \sum_{\beta} \overline{G}^{(1)}_{\alpha\beta}(\overline{\mathbf{w}}_{\alpha} - \overline{\mathbf{w}}_{\beta}), \tag{F.1}$$

$$\mathbf{R}^{\mathbf{w}2}_{\alpha} = \sum_{\beta} \left[ \frac{\mu_{\alpha\beta}}{T_{av}} \overline{G}^{(2)}_{\alpha\beta} \left( \frac{\overline{\mathbf{h}}^{\mathbf{w}}_{\alpha}}{m_{\alpha} n_{\alpha}} - \frac{\overline{\mathbf{h}}^{\mathbf{w}}_{\beta}}{m_{\beta} n_{\beta}} \right) + \left( \frac{\mu_{\alpha\beta}}{T_{av}} \right)^2 \overline{G}^{(8)}_{\alpha\beta} \left( \frac{\overline{\mathbf{r}}^{\mathbf{w}}_{\alpha}}{m_{\alpha} n_{\alpha}} - \frac{\overline{\mathbf{r}}^{\mathbf{w}}_{\beta}}{m_{\beta} n_{\beta}} \right) \right], \tag{F.2}$$

Further, we will focus on the $\mathbf{R}^{\mathbf{w}2}_{\alpha}$ derivation. We should replace $\beta \to \gamma$ to avoid confusion:

$$\mathbf{R}^{\mathbf{w}2}_{\alpha} = \sum_{\gamma} \left[ \frac{\mu_{\alpha\gamma}}{m_{\alpha}} \overline{G}^{(2)}_{\alpha\gamma} \left( \frac{\overline{\mathbf{h}}^{\mathbf{w}}_{\alpha}}{p_{\alpha}} - \frac{m_{\alpha}}{m_{\gamma}} \frac{\overline{\mathbf{h}}^{\mathbf{w}}_{\gamma}}{p_{\gamma}} \right) + \left( \frac{\mu_{\alpha\gamma}}{m_{\alpha}} \right)^2 \overline{G}^{(8)}_{\alpha\gamma} \frac{m_{\alpha}}{T_{av}} \left( \frac{\overline{\mathbf{r}}^{\mathbf{w}}_{\alpha}}{p_{\alpha}} - \frac{m_{\alpha}}{m_{\gamma}} \frac{\overline{\mathbf{r}}^{\mathbf{w}}_{\gamma}}{p_{\gamma}} \right) \right], \tag{F.3}$$

where from (C.18) and (D.4):

$$\frac{\overline{\mathbf{h}}^{\mathbf{w}}_{\alpha}}{p_{\alpha}} = \sum_{\beta} c^{(h^A_w)}_{\beta\alpha} (\overline{\mathbf{w}}_{\alpha} - \overline{\mathbf{w}}_{\beta}), \quad \frac{\overline{\mathbf{h}}^{\mathbf{w}}_{\gamma}}{p_{\gamma}} = \sum_{\beta} c^{(h^A_w)}_{\beta\gamma} (\overline{\mathbf{w}}_{\gamma} - \overline{\mathbf{w}}_{\beta}), \tag{F.4}$$

$$\frac{\overline{\mathbf{r}}^{\mathbf{w}}_{\alpha}}{p_{\alpha}} = \frac{T_{av}}{m_{\alpha}} \sum_{\beta} c^{(r^A_w)}_{\beta\alpha} (\overline{\mathbf{w}}_{\alpha} - \overline{\mathbf{w}}_{\beta}), \quad \frac{\overline{\mathbf{r}}^{\mathbf{w}}_{\gamma}}{p_{\gamma}} = \frac{T_{av}}{m_{\gamma}} \sum_{\beta} c^{(r^A_w)}_{\beta\gamma} (\overline{\mathbf{w}}_{\gamma} - \overline{\mathbf{w}}_{\beta}), \tag{F.5}$$

Thus:

$$\mathbf{R}^{\mathbf{w}2}_{\alpha} = \sum_{\gamma} \Big[ A^{(1)}_{\alpha\gamma} \sum_{\beta} c^{(h^A_w)}_{\beta\alpha} (\overline{\mathbf{w}}_{\alpha} - \overline{\mathbf{w}}_{\beta}) + A^{(2)}_{\alpha\gamma} \sum_{\beta} c^{(r^A_w)}_{\beta\alpha} (\overline{\mathbf{w}}_{\alpha} - \overline{\mathbf{w}}_{\beta}) - A^{(3)}_{\alpha\gamma} \sum_{\beta} c^{(h^A_w)}_{\beta\gamma} (\overline{\mathbf{w}}_{\gamma} - \overline{\mathbf{w}}_{\beta}) - A^{(4)}_{\alpha\gamma} \sum_{\beta} c^{(r^A_w)}_{\beta\gamma} (\overline{\mathbf{w}}_{\gamma} - \overline{\mathbf{w}}_{\beta}) \Big] \tag{F.6}$$

where it is covinient to combine G-objects in the following way:

$$A^{(1)}_{\alpha\gamma} = \frac{\mu_{\alpha\gamma}}{m_\alpha}\overline{G}^{(2)}_{\alpha\gamma} = \frac{3}{5}\frac{\mu_{\alpha\gamma}}{m_\alpha}\lambda_{\alpha\gamma}, \quad A^{(2)}_{\alpha\gamma} = \left(\frac{\mu_{\alpha\gamma}}{m_\alpha}\right)^2 \overline{G}^{(8)}_{\alpha\gamma} = -\frac{3}{14}\left(\frac{\mu_{\alpha\gamma}}{m_\alpha}\right)^2 \lambda_{\alpha\gamma}, \tag{F.7}$$

$$A^{(3)}_{\alpha\gamma} = \frac{\mu_{\alpha\gamma}}{m_\gamma}\overline{G}^{(2)}_{\alpha\gamma} = \frac{3}{5}\frac{\mu_{\alpha\gamma}}{m_\gamma}\lambda_{\alpha\gamma}, \quad A^{(4)}_{\alpha\gamma} = \left(\frac{\mu_{\alpha\gamma}}{m_\gamma}\right)^2 \overline{G}^{(8)}_{\alpha\gamma} = -\frac{3}{14}\left(\frac{\mu_{\alpha\gamma}}{m_\gamma}\right)^2 \lambda_{\alpha\gamma}. \tag{F.8}$$

We want to extract $(\overline{\mathbf{w}}_\alpha - \overline{\mathbf{w}}_\beta)$ terms from (F.6). Note, for any $A^{(*)}_{\alpha\gamma}$ and $c^{(*)}_{\beta\gamma}$ (here $(*)$ can be replaced with any superscript) one can derive:

$$\begin{aligned}
\sum_\gamma A^{(*)}_{\alpha\gamma}\sum_\beta c^{(*)}_{\beta\gamma}(\overline{\mathbf{w}}_\gamma - \overline{\mathbf{w}}_\beta) &= \sum_\gamma A^{(*)}_{\alpha\gamma}\sum_\beta c^{(*)}_{\beta\gamma}(\overline{\mathbf{w}}_\alpha - \overline{\mathbf{w}}_\alpha + \overline{\mathbf{w}}_\gamma - \overline{\mathbf{w}}_\beta) = \\
&\sum_\beta\sum_\gamma A^{(*)}_{\alpha\gamma}c^{(*)}_{\beta\gamma}(\overline{\mathbf{w}}_\alpha - \overline{\mathbf{w}}_\beta) - \sum_\gamma\sum_\beta A^{(*)}_{\alpha\gamma}c^{(*)}_{\beta\gamma}(\overline{\mathbf{w}}_\alpha - \overline{\mathbf{w}}_\gamma) = \\
&\sum_\beta\sum_\gamma A^{(*)}_{\alpha\gamma}c^{(*)}_{\beta\gamma}(\overline{\mathbf{w}}_\alpha - \overline{\mathbf{w}}_\beta) - \sum_\beta\sum_\gamma A^{(*)}_{\alpha\beta}c^{(*)}_{\gamma\beta}(\overline{\mathbf{w}}_\alpha - \overline{\mathbf{w}}_\beta) = \\
&\sum_\beta(\overline{\mathbf{w}}_\alpha - \overline{\mathbf{w}}_\beta)\sum_\gamma\left[A^{(*)}_{\alpha\gamma}c^{(*)}_{\beta\gamma} - A^{(*)}_{\alpha\beta}c^{(*)}_{\gamma\beta}\right]
\end{aligned} \tag{F.9}$$

Therefore (F.6) turns into:

$$\begin{aligned}
&\mathbf{R}^{\mathbf{w}2}_\alpha = \sum_\beta(\overline{\mathbf{w}}_\alpha - \overline{\mathbf{w}}_\beta)\sum_\gamma\left[A^{(1)}_{\alpha\gamma}c^{(h^A_w)}_{\beta\alpha} + A^{(2)}_{\alpha\gamma}c^{(r^A_w)}_{\beta\alpha}\right] - \\
&\sum_\beta(\overline{\mathbf{w}}_\alpha - \overline{\mathbf{w}}_\beta)\sum_\gamma\left[A^{(3)}_{\alpha\gamma}c^{(h^A_w)}_{\beta\gamma} - A^{(3)}_{\alpha\beta}c^{(h^A_w)}_{\gamma\beta}\right] - \sum_\beta(\overline{\mathbf{w}}_\alpha - \overline{\mathbf{w}}_\beta)\sum_\gamma\left[A^{(4)}_{\alpha\gamma}c^{(r^A_w)}_{\beta\gamma} - A^{(4)}_{\alpha\beta}c^{(r^A_w)}_{\gamma\beta}\right] = \\
&\sum_\beta(\overline{\mathbf{w}}_\alpha - \overline{\mathbf{w}}_\beta)\sum_\gamma\Big(\left[A^{(1)}_{\alpha\gamma}c^{(h^A_w)}_{\beta\alpha} + A^{(2)}_{\alpha\gamma}c^{(r^A_w)}_{\beta\alpha}\right] - \left[A^{(3)}_{\alpha\gamma}c^{(h^A_w)}_{\beta\gamma} + A^{(4)}_{\alpha\gamma}c^{(r^A_w)}_{\beta\gamma}\right] + \left[A^{(3)}_{\alpha\beta}c^{(h^A_w)}_{\gamma\beta} + A^{(4)}_{\alpha\beta}c^{(r^A_w)}_{\gamma\beta}\right]\Big) = \\
&\qquad - n_\alpha\sum_\beta\frac{\mu_{\alpha\beta}}{\tau^{(Zh)}_{\alpha\beta}}(\overline{\mathbf{w}}_\alpha - \overline{\mathbf{w}}_\beta)\Big(-\sum_\gamma\frac{1}{\lambda_{\alpha\beta}}\left[A^{(1)}_{\alpha\gamma}c^{(h^A_w)}_{\beta\alpha} + A^{(2)}_{\alpha\gamma}c^{(r^A_w)}_{\beta\alpha}\right] \\
&\qquad + \sum_\gamma\frac{1}{\lambda_{\alpha\beta}}\left[A^{(3)}_{\alpha\gamma}c^{(h^A_w)}_{\beta\gamma} + A^{(4)}_{\alpha\gamma}c^{(r^A_w)}_{\beta\gamma}\right] - \sum_\gamma\frac{1}{\lambda_{\alpha\beta}}\left[A^{(3)}_{\alpha\beta}c^{(h^A_w)}_{\gamma\beta} + A^{(4)}_{\alpha\beta}c^{(r^A_w)}_{\gamma\beta}\right]\Big) = \\
&\qquad\qquad - n_\alpha\sum_\beta\frac{\mu_{\alpha\beta}}{\tau^{(Zh)}_{\alpha\beta}}(\overline{\mathbf{w}}_\alpha - \overline{\mathbf{w}}_\beta)\Big(\tilde{c}^{(R^A_w 1)}_{\beta\alpha} + \tilde{c}^{(R^A_w 2)}_{\beta\alpha} + c^{(R^A_w 3)}_{\beta\alpha}\Big)
\end{aligned} \tag{F.10}$$

where the corresponding coefficients are:

$$\tilde{c}^{(R_w^A 1)}_{\beta\alpha} = -\sum_\gamma \frac{1}{\lambda_{\alpha\beta}}\left[A^{(1)}_{\alpha\gamma} c^{(h_w^A)}_{\beta\alpha} + A^{(2)}_{\alpha\gamma} c^{(r_w^A)}_{\beta\alpha}\right] =$$

$$-\sum_\gamma \Big[\frac{3}{5}\frac{\mu_{\alpha\gamma}}{m_\alpha}\sqrt{\frac{\mu_{\alpha\gamma}}{\mu_{\alpha\beta}}}\frac{\overline{Z^2_\gamma} n_\gamma}{\overline{Z^2_\beta} n_\beta} c^{(h_w^A)}_{\beta\alpha} - \frac{3}{14}\left(\frac{\mu_{\alpha\gamma}}{m_\alpha}\right)^2 \sqrt{\frac{\mu_{\alpha\gamma}}{\mu_{\alpha\beta}}}\frac{\overline{Z^2_\gamma} n_\gamma}{\overline{Z^2_\beta} n_\beta} c^{(r_w^A)}_{\beta\alpha}\Big] =$$

$$-\sum_\gamma \frac{\mu_{\alpha\gamma}}{m_\alpha}\sqrt{\frac{\mu_{\alpha\gamma}}{\mu_{\alpha\beta}}}\frac{\overline{Z^2_\gamma} n_\gamma}{\overline{Z^2_\beta} n_\beta}\Big[\frac{3}{5} c^{(h_w^A)}_{\beta\alpha} - \frac{3}{14}\frac{\mu_{\alpha\gamma}}{m_\alpha} c^{(r_w^A)}_{\beta\alpha}\Big], \quad \text{(F.11)}$$

$$\tilde{c}^{(R_w^A 2)}_{\beta\alpha} = \sum_\gamma \frac{1}{\lambda_{\alpha\beta}}\left[A^{(3)}_{\alpha\gamma} c^{(h_w^A)}_{\beta\gamma} + A^{(4)}_{\alpha\gamma} c^{(r_w^A)}_{\beta\gamma}\right] =$$

$$\sum_\gamma \Big[\frac{3}{5}\frac{\mu_{\alpha\gamma}}{m_\gamma}\sqrt{\frac{\mu_{\alpha\gamma}}{\mu_{\alpha\beta}}}\frac{\overline{Z^2_\gamma} n_\gamma}{\overline{Z^2_\beta} n_\beta} c^{(h_w^A)}_{\beta\gamma} - \frac{3}{14}\left(\frac{\mu_{\alpha\gamma}}{m_\gamma}\right)^2 \sqrt{\frac{\mu_{\alpha\gamma}}{\mu_{\alpha\beta}}}\frac{\overline{Z^2_\gamma} n_\gamma}{\overline{Z^2_\beta} n_\beta} c^{(r_w^A)}_{\beta\gamma}\Big] =$$

$$\sum_\gamma \frac{\mu_{\alpha\gamma}}{m_\gamma}\sqrt{\frac{\mu_{\alpha\gamma}}{\mu_{\alpha\beta}}}\frac{\overline{Z^2_\gamma} n_\gamma}{\overline{Z^2_\beta} n_\beta}\Big[\frac{3}{5} c^{(h_w^A)}_{\beta\gamma} - \frac{3}{14}\frac{\mu_{\alpha\gamma}}{m_\gamma} c^{(r_w^A)}_{\beta\gamma}\Big], \quad \text{(F.12)}$$

$$c^{(R_w^A 3)}_{\beta\alpha} = -\sum_\gamma \frac{1}{\lambda_{\alpha\beta}}\left[A^{(3)}_{\alpha\beta} c^{(h_w^A)}_{\gamma\beta} + A^{(4)}_{\alpha\beta} c^{(r_w^A)}_{\gamma\beta}\right] = -\frac{\mu_{\alpha\beta}}{m_\beta}\sum_\gamma \Big[\frac{3}{5} c^{(h_w^A)}_{\gamma\beta} - \frac{3}{14}\frac{\mu_{\alpha\beta}}{m_\beta} c^{(r_w^A)}_{\gamma\beta}\Big], \quad \text{(F.13)}$$

where the following evident relation (from (2.91)) is used:

$$\frac{\lambda_{\alpha\gamma}}{\lambda_{\alpha\beta}} = \sqrt{\frac{\mu_{\alpha\gamma}}{\mu_{\alpha\beta}}}\frac{\overline{Z^2_\gamma} n_\gamma}{\overline{Z^2_\beta} n_\beta}. \quad \text{(F.14)}$$

Subtracting $\frac{\mu_{\gamma\gamma}}{m_\gamma}\sqrt{\frac{\mu_{\gamma\gamma}}{\mu_{\gamma\beta}}}\frac{\overline{Z^2_\gamma} n_\gamma}{\overline{Z^2_\beta} n_\beta}\Big[\frac{3}{5} c^{(h_w^A)}_{\beta\gamma} - \frac{3}{14}\frac{\mu_{\gamma\gamma}}{m_\gamma} c^{(r_w^A)}_{\beta\gamma}\Big]$ terms from (F.11) and (F.12), because they cancel each other, we finally get:

$$c^{(R_w^A 1)}_{\beta\alpha} = -\sum_{\gamma\neq\alpha} \frac{\mu_{\alpha\gamma}}{m_\alpha}\sqrt{\frac{\mu_{\alpha\gamma}}{\mu_{\alpha\beta}}}\frac{\overline{Z^2_\gamma} n_\gamma}{\overline{Z^2_\beta} n_\beta}\Big[\frac{3}{5} c^{(h_w^A)}_{\beta\alpha} - \frac{3}{14}\frac{\mu_{\alpha\gamma}}{m_\alpha} c^{(r_w^A)}_{\beta\alpha}\Big] \quad \text{(F.15)}$$

$$c^{(R_w^A 2)}_{\beta\alpha} = \sum_{\gamma\neq\alpha} \frac{\mu_{\alpha\gamma}}{m_\gamma}\sqrt{\frac{\mu_{\alpha\gamma}}{\mu_{\alpha\beta}}}\frac{\overline{Z^2_\gamma} n_\gamma}{\overline{Z^2_\beta} n_\beta}\Big[\frac{3}{5} c^{(h_w^A)}_{\beta\gamma} - \frac{3}{14}\frac{\mu_{\alpha\gamma}}{m_\gamma} c^{(r_w^A)}_{\beta\gamma}\Big] \quad \text{(F.16)}$$

$$c^{(R_w^A 3)}_{\beta\alpha} = -\frac{\mu_{\alpha\beta}}{m_\beta}\sum_\gamma \Big[\frac{3}{5} c^{(h_w^A)}_{\gamma\beta} - \frac{3}{14}\frac{\mu_{\alpha\beta}}{m_\beta} c^{(r_w^A)}_{\gamma\beta}\Big] \quad \text{(F.17)}$$

Finally, the FR, which is summed over the charges states, is:

$$\mathbf{R}_{\alpha}^{\mathbf{w}} = -n_{\alpha}\sum_{\beta}\frac{\mu_{\alpha\beta}}{\tau_{\alpha\beta}^{(Zh)}}(\overline{\mathbf{w}}_{\alpha}-\overline{\mathbf{w}}_{\beta})\Big(1+c_{\beta\alpha}^{(R_w^A 1)}+c_{\beta\alpha}^{(R_w^A 2)}+c_{\beta\alpha}^{(R_w^A 3)}\Big) = \\ -n_{\alpha}\sum_{\beta}\frac{\mu_{\alpha\beta}}{\tau_{\alpha\beta}^{(Zh)}}c_{\beta\alpha}^{(R_w^A)}(\overline{\mathbf{w}}_{\alpha}-\overline{\mathbf{w}}_{\beta}), \quad \text{(F.18)}$$

where:

$$c_{\beta\alpha}^{(R_w^A)} = 1+c_{\beta\alpha}^{(R_w^A 1)}+c_{\beta\alpha}^{(R_w^A 2)}+c_{\beta\alpha}^{(R_w^A 3)}. \quad \text{(F.19)}$$

## F.2 Charge state corrections

Using (4.57), one can find the FR for the each charge state:

$$\mathbf{R}_{\alpha Z}^{\mathbf{w}} = I_{\alpha Z}\mathbf{R}_{\alpha}^{\mathbf{w}} + I_{\alpha Z}\sum_{\beta}\Big[\overline{G}_{\alpha\beta}^{(1)}(\mathbf{w}_{\alpha Z}-\overline{\mathbf{w}}_{\alpha})+ \\ \frac{\mu_{\alpha\beta}}{m_{\alpha}}\overline{G}_{\alpha\beta}^{(2)}\left(\frac{\mathbf{h}_{\alpha Z}^{\mathbf{w}}}{p_{\alpha Z}}-\frac{\overline{\mathbf{h}}_{\alpha}^{\mathbf{w}}}{p_{\alpha}}\right)+\left(\frac{\mu_{\alpha\beta}}{m_{\alpha}}\right)^2\frac{m_{\alpha}}{T}\overline{G}_{\alpha\beta}^{(8)}\left(\frac{\mathbf{r}_{\alpha Z}^{\mathbf{w}}}{p_{\alpha Z}}-\frac{\overline{\mathbf{r}}_{\alpha}^{\mathbf{w}}}{p_{\alpha}}\right)\Big], \quad \text{(F.20)}$$

Using (C.23) and (D.8), one can get:

$$\mathbf{R}_{\alpha Z}^{\mathbf{w}} - I_{\alpha Z}\mathbf{R}_{\alpha}^{\mathbf{w}} = I_{\alpha Z}\sum_{\beta}\Big[\frac{-n_{\alpha}\mu_{\alpha\beta}}{\tau_{\alpha\beta}^{(Zh)}}(\mathbf{w}_{\alpha Z}-\overline{\mathbf{w}}_{\alpha})+ \\ \frac{3}{5}\frac{\mu_{\alpha\beta}}{m_{\alpha}}\frac{n_{\alpha}\mu_{\alpha\beta}}{\tau_{\alpha\beta}^{(Zh)}}c_{\alpha}^{(h_w^B)}(\mathbf{w}_{\alpha Z}-\overline{\mathbf{w}}_{\alpha})-\frac{3}{14}\left(\frac{\mu_{\alpha\beta}}{m_{\alpha}}\right)^2\frac{n_{\alpha}\mu_{\alpha\beta}}{\tau_{\alpha\beta}^{(Zh)}}c^{(r_w^B)}(\mathbf{w}_{\alpha Z}-\overline{\mathbf{w}}_{\alpha})\Big], \quad \text{(F.21)}$$

Then:

$$\mathbf{R}_{\alpha Z}^{\mathbf{w}} - I_{\alpha Z}\mathbf{R}_{\alpha}^{\mathbf{w}} = -n_{\alpha}I_{\alpha Z}(\mathbf{w}_{\alpha Z}-\overline{\mathbf{w}}_{\alpha})\sum_{\beta}\frac{\mu_{\alpha\beta}}{\tau_{\alpha\beta}^{(Zh)}}\Big[1-\frac{3}{5}\frac{\mu_{\alpha\beta}}{m_{\alpha}}c_{\alpha}^{(h_w^B)}+\frac{3}{14}\left(\frac{\mu_{\alpha\beta}}{m_{\alpha}}\right)^2 c^{(r_w^B)}\Big] = \\ -n_{\alpha}I_{\alpha Z}(\mathbf{w}_{\alpha Z}-\overline{\mathbf{w}}_{\alpha})\sum_{\beta}\frac{\mu_{\alpha\beta}}{\tau_{\alpha\beta}^{(Zh)}}c_{\beta\alpha}^{(R_w^B)}, \quad \text{(F.22)}$$

where the coefficient $c_{\beta\alpha}^{(R_w^B)}$ is:

$$c_{\beta\alpha}^{(R_w^B)} = 1-\frac{3}{5}\frac{\mu_{\alpha\beta}}{m_{\alpha}}c_{\alpha}^{(h_w^B)}+\frac{3}{14}\left(\frac{\mu_{\alpha\beta}}{m_{\alpha}}\right)^2 c_{\alpha}^{(r_w^B)}, \quad \text{(F.23)}$$

where $c_\alpha^{(h_w^B)}$ and $c_\alpha^{(r_w^B)}$ are found according to (C.25) and (D.10), correspondingly. The FR for the each charge state can be written in the form of:

$$\mathbf{R}^{\mathbf{w}}_{\alpha Z} = -n_\alpha I_{\alpha Z} \sum_\beta \frac{\mu_{\alpha\beta}}{\tau^{(Zh)}_{\alpha\beta}} c^{(R_w^A)}_{\beta\alpha} (\overline{\mathbf{w}}_\alpha - \overline{\mathbf{w}}_\beta) - n_\alpha I_{\alpha Z} (\mathbf{w}_{\alpha Z} - \overline{\mathbf{w}}_\alpha) \sum_\beta \frac{\mu_{\alpha\beta}}{\tau^{(Zh)}_{\alpha\beta}} c^{(R_w^B)}_{\beta\alpha} \quad \text{(F.24)}$$

Then, we apply similar to the heat flux procedure (C.30):

$$\begin{aligned}
\frac{\mathbf{R}^{\mathbf{w}}_{\alpha Z}}{-n_\alpha I_{\alpha Z}} &= \sum_\beta \frac{\mu_{\alpha\beta}}{\tau^{(Zh)}_{\alpha\beta}} c^{(R_w^A)}_{\beta\alpha} (\overline{\mathbf{w}}_\alpha - \overline{\mathbf{w}}_\beta) + \sum_\beta \frac{\mu_{\alpha\beta}}{\tau^{(Zh)}_{\alpha\beta}} c^{(R_w^B)}_{\beta\alpha} (\mathbf{w}_{\alpha Z} - \overline{\mathbf{w}}_\alpha) = \\
&\sum_\beta \frac{\mu_{\alpha\beta}}{\tau^{(Zh)}_{\alpha\beta}} [c^{(R_w^B)}_{\beta\alpha} \mathbf{w}_{\alpha Z} + c^{(R_w^A)}_{\beta\alpha} \overline{\mathbf{w}}_\alpha - c^{(R_w^B)}_{\beta\alpha} \overline{\mathbf{w}}_\alpha - c^{(R_w^A)}_{\beta\alpha} \overline{\mathbf{w}}_\beta] = \\
\mathbf{w}_{\alpha Z} &\sum_\beta \frac{\mu_{\alpha\beta}}{\tau^{(Zh)}_{\alpha\beta}} c^{(R_w^B)}_{\beta\alpha} - \overline{\mathbf{w}}_\alpha \sum_\gamma \frac{\mu_{\alpha\gamma}}{\tau^{(Zh)}_{\alpha\gamma}} [c^{(R_w^B)}_{\gamma\alpha} - c^{(R_w^A)}_{\gamma\alpha}] - \sum_\beta \frac{\mu_{\alpha\beta}}{\tau^{(Zh)}_{\alpha\beta}} c^{(R_w^A)}_{\beta\alpha} \overline{\mathbf{w}}_\beta = \\
\mathbf{w}_{\alpha Z} &\sum_\beta \frac{\mu_{\alpha\beta}}{\tau^{(Zh)}_{\alpha\beta}} c^{(R_w^B)}_{\beta\alpha} - \sum_\beta \delta_{\alpha\beta} \overline{\mathbf{w}}_\beta \sum_\gamma \frac{\mu_{\alpha\gamma}}{\tau^{(Zh)}_{\alpha\gamma}} [c^{(R_w^B)}_{\gamma\alpha} - c^{(R_w^A)}_{\gamma\alpha}] - \sum_\beta \frac{\mu_{\alpha\beta}}{\tau^{(Zh)}_{\alpha\beta}} c^{(R_w^A)}_{\beta\alpha} \overline{\mathbf{w}}_\beta = \\
\mathbf{w}_{\alpha Z} &\sum_\beta \frac{\mu_{\alpha\beta}}{\tau^{(Zh)}_{\alpha\beta}} c^{(R_w^B)}_{\beta\alpha} - \sum_\beta \frac{\mu_{\alpha\beta}}{\tau^{(Zh)}_{\alpha\beta}} \overline{\mathbf{w}}_\beta (\delta_{\alpha\beta} \sum_\gamma \frac{\mu_{\alpha\gamma} \tau^{(Zh)}_{\alpha\beta}}{\mu_{\alpha\beta} \tau^{(Zh)}_{\alpha\gamma}} [c^{(R_w^B)}_{\gamma\alpha} - c^{(R_w^A)}_{\gamma\alpha}] + c^{(R_w^A)}_{\beta\alpha}) = \\
&\mathbf{w}_{\alpha Z} \sum_\beta \frac{\mu_{\alpha\beta}}{\tau^{(Zh)}_{\alpha\beta}} c^{(R_w^B)}_{\beta\alpha} - \sum_\beta \frac{\mu_{\alpha\beta}}{\tau^{(Zh)}_{\alpha\beta}} c^{(R_w)}_{\beta\alpha} \overline{\mathbf{w}}_\beta, \quad \text{(F.25)}
\end{aligned}$$

where:

$$c^{(R_w)}_{\beta\alpha} = \delta_{\alpha\beta} \sum_\gamma \frac{\mu_{\alpha\gamma} \tau^{(Zh)}_{\alpha\beta}}{\mu_{\alpha\beta} \tau^{(Zh)}_{\alpha\gamma}} [c^{(R_w^B)}_{\gamma\alpha} - c^{(R_w^A)}_{\gamma\alpha}] + c^{(R_w^A)}_{\beta\alpha}, \quad \text{(F.26)}$$

and finally one can get:

$$c^{(R_w)}_{\beta\alpha} = \delta_{\alpha\beta} \sum_\gamma \sqrt{\frac{\mu_{\alpha\gamma}}{\mu_{\alpha\beta}}} \frac{\overline{Z^2_\gamma} n_\gamma}{\overline{Z^2_\beta} n_\beta} [c^{(R_w^B)}_{\gamma\alpha} - c^{(R_w^A)}_{\gamma\alpha}] + c^{(R_w^A)}_{\beta\alpha}. \quad \text{(F.27)}$$

Using $c^{(R_w)}_{\beta\alpha}$ summation property:

$$\begin{aligned}
\sum_\beta \frac{\mu_{\alpha\beta}}{\tau^{(Zh)}_{\alpha\beta}} c^{(R_w)}_{\beta\alpha} &= \sum_\beta \frac{\mu_{\alpha\beta}}{\tau^{(Zh)}_{\alpha\beta}} (\delta_{\alpha\beta} \sum_\gamma \frac{\mu_{\alpha\gamma} \tau^{(Zh)}_{\alpha\beta}}{\mu_{\alpha\beta} \tau^{(Zh)}_{\alpha\gamma}} [c^{(R_w^B)}_{\gamma\alpha} - c^{(R_w^A)}_{\gamma\alpha}] + c^{(R_w^A)}_{\beta\alpha}) = \\
&\sum_\gamma \frac{\mu_{\alpha\gamma}}{\tau^{(Zh)}_{\alpha\gamma}} c^{(R_w^B)}_{\gamma\alpha} - \sum_\gamma \frac{\mu_{\alpha\gamma}}{\tau^{(Zh)}_{\alpha\gamma}} c^{(R_w^A)}_{\gamma\alpha} + \sum_\beta \frac{\mu_{\alpha\beta}}{\tau^{(Zh)}_{\alpha\beta}} c^{(R_w^A)}_{\beta\alpha} = \sum_\beta \frac{\mu_{\alpha\beta}}{\tau^{(Zh)}_{\alpha\beta}} c^{(R_w^B)}_{\beta\alpha}, \quad \text{(F.28)}
\end{aligned}$$

one finally can obtain the FR for the each charge state:

$$\mathbf{R}^{\mathbf{w}}_{\alpha Z} = -n_\alpha I_{\alpha Z} \sum_\beta \frac{\mu_{\alpha\beta}}{\tau^{(Zh)}_{\alpha\beta}} c^{(R_w)}_{\beta\alpha} (\mathbf{w}_{\alpha Z} - \overline{\mathbf{w}}_\beta) \tag{F.29}$$

# G Viscous-stress tensor derivation

## G.1 Averaged over charge states

The system of linear algebraic equations for rank-2 moments (4.66) and (4.67) using (B.4), (B.5) and (B.6) turns into:

$$\sum_{\beta}\left[\frac{\check{G}^{(3)}_{\alpha\beta}\overline{\pi}_{\alpha rs}}{p_\alpha}+\frac{\check{G}^{(4)}_{\alpha\beta}\overline{\pi}_{\beta rs}}{p_\beta}+\frac{m_\alpha}{T_{av}}\frac{\check{G}^{(13)}_{\alpha\beta}\overline{\sigma}_{\alpha rs}}{p_\alpha}+\frac{m_\beta}{T_{av}}\frac{\check{G}^{(14)}_{\alpha\beta}\overline{\sigma}_{\beta rs}}{p_\beta}\right]= \frac{\zeta_p}{(Z_{eff}n_e)^2T_{av}}W^{\overline{h}_\alpha}_{rs}+p_\alpha\frac{\zeta_p}{(Z_{eff}n_e)^2T_{av}}\widetilde{W^{u_\alpha}_{rs}}, \quad \text{(G.1)}$$

$$\sum_{\beta}\left[\frac{7}{2}\frac{\check{G}^{(13)}_{\alpha\beta}\overline{\pi}_{\alpha rs}}{p_\alpha}+\frac{7}{2}\frac{m_\alpha}{m_\beta}\frac{\check{G}^{(14)}_{\alpha\beta}\overline{\pi}_{\beta rs}}{p_\beta}+\frac{m_\alpha}{T_{av}}\frac{\check{G}^{(15)}_{\alpha\beta}\overline{\sigma}_{\alpha rs}}{p_\alpha}+\frac{m_\alpha}{T_{av}}\frac{\check{G}^{(16)}_{\alpha\beta}\overline{\sigma}_{\beta rs}}{p_\beta}\right]= \frac{7}{2}\frac{\zeta_p}{(Z_{eff}n_e)^2T_{av}}W^{\overline{h}_\alpha}_{rs}, \quad \text{(G.2)}$$

The (G.1) and (G.2) is a system of equation $2\alpha^{max}\times 2\alpha^{max}$, which can be written in the form of:

$$\sum_{\beta=1..2\alpha^{max}}\check{c}_{\alpha\beta}Y_\beta=\check{d}_\alpha \quad \text{(G.3)}$$

where:

$$Y_\beta=\begin{cases}\frac{\overline{\pi}_{\beta rs}}{p_\beta}, & \beta=1..\alpha^{max}\\ \frac{\overline{\sigma}_{\beta rs}}{p_\beta}, & \beta=\alpha^{max}+1..2\alpha^{max}\end{cases} \quad \text{(G.4)}$$

and the l.h.s. coefficients are:
$\alpha=1..\alpha^{max}$
$\beta=1..\alpha^{max}$

$$\check{c}_{\alpha\beta}=\check{G}^{(4)}_{\alpha\beta}, \quad \check{c}_{\alpha+\alpha^{max}\beta}=\frac{7}{2}\frac{m_\alpha}{m_\beta}\check{G}^{(14)}_{\alpha\beta} \quad \text{(G.5)}$$

$$\check{c}_{\alpha\beta+\alpha^{max}} = \frac{m_\alpha}{T_{av}}\frac{m_\beta}{m_\alpha}\check{G}^{(14)}_{\alpha\beta}, \quad \check{c}_{\alpha+\alpha^{max}\beta+\alpha^{max}} = \frac{m_\alpha}{T_{av}}\check{G}^{(16)}_{\alpha\beta} \tag{G.6}$$

Addition for diagonal elements:
$\beta = 1..\alpha^{max}$

$$\check{c}_{\beta\beta} = \check{c}_{\beta\beta} + \sum_\gamma \check{G}^{(3)}_{\beta\gamma}, \quad \check{c}_{\beta+\alpha^{max}\beta} = \check{c}_{\beta+\alpha^{max}\beta} + \frac{7}{2}\sum_\gamma \check{G}^{(13)}_{\beta\gamma} \tag{G.7}$$

$$\check{c}_{\beta\beta+\alpha^{max}} = \check{c}_{\beta\beta+\alpha^{max}} + \frac{m_\alpha}{T_{av}}\sum_\gamma \check{G}^{(13)}_{\beta\gamma}, \quad \check{c}_{\beta+\alpha^{max}\beta+\alpha^{max}} = \check{c}_{\beta+\alpha^{max}\beta+\alpha^{max}} + \frac{m_\alpha}{T_{av}}\sum_\gamma \check{G}^{(15)}_{\beta\gamma} \tag{G.8}$$

and the r.h.s. terms are:
$\alpha = 1..\alpha^{max}$

$$\check{d}_\alpha = \frac{\zeta_p}{(Z_{eff}n_e)^2 T_{av}} W^{\overline{h}_\alpha}_{rs} + p_\alpha \frac{\zeta_p}{(Z_{eff}n_e)^2 T_{av}} \widetilde{W^{u_\alpha}_{rs}}, \tag{G.9}$$

$$\check{d}_{\alpha+\alpha^{max}} = \frac{7}{2}\frac{\zeta_p}{(Z_{eff}n_e)^2 T_{av}} W^{\overline{h}_\alpha}_{rs} \tag{G.10}$$

The solution of the system of linear algebraic equations (4.70): $\check{C}Y = \check{d}$ can be espressed via coefficients of the inverse matrix: $Y = \check{C}^{-1}\check{d}$. Let $\check{c}_{\alpha\beta}$ is an element of $\check{C}$ and $\tilde{\check{c}}_{\alpha\beta}$ is an element of $\check{C}^{-1}$.
Then $Y_i = \sum_{j=1..2\alpha^{max}} \tilde{\check{c}}_{ij}\check{d}_j$.
In $\alpha\beta$ terms:

$$\begin{aligned}\overline{\pi}_{\alpha rs} = p_\alpha \sum_\beta \tilde{\check{c}}_{\alpha\beta}\check{d}_\beta = p_\alpha \frac{\zeta_p}{(Z_{eff}n_e)^2 T_{av}} \sum_\beta \tilde{\check{c}}_{\alpha\beta} p_\beta \widetilde{W^{u_\beta}_{rs}} \\ + p_\alpha \frac{\zeta_p}{(Z_{eff}n_e)^2 T_{av}} \sum_\beta \tilde{\check{c}}_{\alpha\beta} W^{\overline{h}_\beta}_{rs} + p_\alpha \frac{7}{2}\frac{\zeta_p}{(Z_{eff}n_e)^2 T_{av}} \sum_\beta \tilde{\check{c}}_{\alpha\beta+\alpha^{max}} W^{\overline{h}_\beta}_{rs} = \\ p_\alpha \frac{\zeta_p}{(Z_{eff}n_e)^2 T_{av}} \left[ \sum_\beta \tilde{\check{c}}_{\alpha\beta} p_\beta \widetilde{W^{u_\beta}_{rs}} + \sum_\beta (\tilde{\check{c}}_{\alpha\beta} + \frac{7}{2}\tilde{\check{c}}_{\alpha\beta+\alpha^{max}}) W^{\overline{h}_\beta}_{rs} \right]\end{aligned} \tag{G.11}$$

It is convenient to split the viscous-stress tensor into the $u$- and $h$-dependent parts. The averaged viscous-stress tensor is:

$$\overline{\pi}_{\alpha rs} = \overline{\pi}^u_{\alpha rs} + \overline{\pi}^h_{\alpha rs}, \tag{G.12}$$

where

$$\frac{\overline{\pi}^{u}_{\alpha rs}}{p_\alpha} = -\sum_\beta \check{c}^{(\pi^A_u)}_{\alpha\beta}\tau^{(Zh)}_{\alpha\beta}\frac{n_\beta}{n_\alpha}\widetilde{W^{u_\beta}_{rs}}, \quad \frac{\overline{\pi}^{h}_{\alpha rs}}{p_\alpha} = -\sum_\beta \check{c}^{(\pi^A_h)}_{\alpha\beta}\tau^{(Zh)}_{\alpha\beta}\frac{1}{p_\alpha}W^{\bar{h}_\beta}_{rs} \tag{G.13}$$

where:

$$\check{c}^{(\pi^A_u)}_{\alpha\beta} = -\frac{\overline{Z^2_\alpha}n_\alpha}{Z_{eff}n_e}\frac{\overline{Z^2_\beta}n_\beta}{Z_{eff}n_e}\frac{\tilde{\check{c}}_{\alpha\beta}}{\sqrt{\mu_{\alpha\beta}/m_p}}, \quad \check{c}^{(\pi^A_h)}_{\alpha\beta} = -\frac{\overline{Z^2_\alpha}n_\alpha}{Z_{eff}n_e}\frac{\overline{Z^2_\beta}n_\beta}{Z_{eff}n_e}\frac{\tilde{\check{c}}_{\alpha\beta}+\frac{7}{2}\tilde{\check{c}}_{\alpha\beta+\alpha^{max}}}{\sqrt{\mu_{\alpha\beta}/m_p}} \tag{G.14}$$

## G.2 Charge state corrections

Subtracting (4.64) from (4.66) and (4.65) from (4.67) one can obtain:

$$p_\alpha\widetilde{W^{u_\alpha}_{rs}} - \frac{\overline{Z^2_\alpha}}{Z^2}p_\alpha W^{u_{\alpha Z}}_{rs} + W^{\bar{h}_\alpha}_{rs} - \frac{\overline{Z^2_\alpha}n_\alpha}{Z^2 n_{\alpha Z}}W^{h_{\alpha Z}}_{rs} = \frac{T_{av}}{m_\alpha}S^{(3)}_\alpha\left(\frac{\overline{\pi}_{\alpha rs}}{p_\alpha} - \frac{\pi_{\alpha Zrs}}{p_{\alpha Z}}\right) + S^{(13)}_\alpha\left(\frac{\overline{\sigma}_{\alpha rs}}{p_\alpha} - \frac{\sigma_{\alpha Zrs}}{p_{\alpha Z}}\right) \tag{G.15}$$

$$\frac{7}{2}W^{\bar{h}_\alpha}_{rs} - \frac{7}{2}\frac{\overline{Z^2_\alpha}n_\alpha}{Z^2 n_{\alpha Z}}W^{h_{\alpha Z}}_{rs} = \frac{7}{2}\frac{T_{av}}{m_\alpha}S^{(13)}_\alpha\left(\frac{\overline{\pi}_{\alpha rs}}{p_\alpha} - \frac{\pi_{\alpha Zrs}}{p_{\alpha Z}}\right) + S^{(15)}_\alpha\left(\frac{\overline{\sigma}_{\alpha rs}}{p_\alpha} - \frac{\sigma_{\alpha Zrs}}{p_{\alpha Z}}\right) \tag{G.16}$$

The system (G.15) and (G.16) has an analytical solution:

$$\frac{\pi_{\alpha Zrs}}{p_{\alpha Z}} - \frac{\overline{\pi}_{\alpha rs}}{p_\alpha} = \frac{m_\alpha}{T_{av}}\frac{S^{(15)}_\alpha}{S^{(3)}_\alpha S^{(15)}_\alpha - \frac{7}{2}\left(S^{(13)}_\alpha\right)^2}p_\alpha\left(\frac{\overline{Z^2_\alpha}}{Z^2}W^{u_{\alpha Z}}_{rs} - \widetilde{W^{u_\alpha}_{rs}}\right) + \frac{m_\alpha}{T_{av}}\frac{S^{(15)}_\alpha - \frac{7}{2}S^{(13)}_\alpha}{S^{(3)}_\alpha S^{(15)}_\alpha - \frac{7}{2}\left(S^{(13)}_\alpha\right)^2}\left(\frac{\overline{Z^2_\alpha}n_\alpha}{Z^2 n_{\alpha Z}}W^{h_{\alpha Z}}_{rs} - W^{\bar{h}_\alpha}_{rs}\right) \tag{G.17}$$

where S-coefficients are defined in appendix B. One can rewrite:

$$\frac{\pi_{\alpha Zrs}}{p_{\alpha Z}} - \frac{\overline{\pi}_{\alpha rs}}{p_\alpha} = -2c^{(\pi^B_u)}_\alpha\tau^{(Zh)}_{\alpha\alpha}\left(\frac{\overline{Z^2_\alpha}}{Z^2}W^{u_{\alpha Z}}_{rs} - \widetilde{W^{u_\alpha}_{rs}}\right) - 2c^{(\pi^B_h)}_\alpha\tau^{(Zh)}_{\alpha\alpha}\left(\frac{\overline{Z^2_\alpha}}{Z^2}\frac{1}{p_{\alpha Z}}W^{h_{\alpha Z}}_{rs} - \frac{1}{p_\alpha}W^{\bar{h}_\alpha}_{rs}\right) \tag{G.18}$$

where:

$$c_{\alpha}^{(\pi_u^B)} = -\lambda_{\alpha\alpha}\frac{S_{\alpha}^{(15)}}{D_{\alpha}^{\pi}} = \frac{265}{334}\frac{1+\frac{204\sqrt{2}}{265}Z_{22\alpha}^{\pi}}{D_{\alpha}^{\pi part}} \tag{G.19}$$

$$c_{\alpha}^{(\pi_h^B)} = -\lambda_{\alpha\alpha}\frac{S_{\alpha}^{(15)}-\frac{7}{2}S_{\alpha}^{(13)}}{D_{\alpha}^{\pi}} = \frac{475}{334}\frac{1+\frac{252\sqrt{2}}{475}Z_{12\alpha}^{\pi}+\frac{204\sqrt{2}}{475}Z_{22\alpha}^{\pi}}{D_{\alpha}^{\pi part}} \tag{G.20}$$

where Z-varibles are defined in appendix B. The viscous-stress tensor for the each charge state is:

$$\pi_{\alpha Zrs} = \pi_{\alpha Zrs}^{u} + \pi_{\alpha Zrs}^{h} \tag{G.21}$$

$$\pi_{\alpha Zrs}^{u} = -p_{\alpha Z}\sum_{\beta}\check{c}_{\alpha\beta}^{(\pi_u^A)}\tau_{\alpha\beta}^{(Zh)}\frac{n_{\beta}}{n_{\alpha}}\widetilde{W_{rs}^{u_{\beta}}} - 2p_{\alpha Z}c_{\alpha}^{(\pi_u^B)}\tau_{\alpha\alpha}^{(Zh)}\left(\frac{\overline{Z_{\alpha}^2}}{\overline{Z^2}}W_{rs}^{u_{\alpha Z}} - \widetilde{W_{rs}^{u_{\alpha}}}\right) \tag{G.22}$$

$$\pi_{\alpha Zrs}^{h} = -p_{\alpha Z}\sum_{\beta}\check{c}_{\alpha\beta}^{(\pi_h^A)}\tau_{\alpha\beta}^{(Zh)}\frac{1}{p_{\alpha}}W_{rs}^{\overline{h}_{\beta}} - 2p_{\alpha Z}c_{\alpha}^{(\pi_h^B)}\tau_{\alpha\alpha}^{(Zh)}\left(\frac{\overline{Z_{\alpha}^2}}{\overline{Z^2}}\frac{1}{p_{\alpha Z}}W_{rs}^{h_{\alpha Z}} - \frac{1}{p_{\alpha}}W_{rs}^{\overline{h}_{\alpha}}\right) \tag{G.23}$$

# H Improved analytical method for the additional vector moment, the thermal and friction forces

## H.1 Additional vector moment

The (4.89)-(4.90) solution for $\overline{\mathbf{r}}_\alpha$ is:

$$\overline{\mathbf{r}}_\alpha = \frac{5}{2}\frac{T_{av}}{m_\alpha}\frac{p_\alpha n_\alpha}{\lambda_{\alpha\alpha}}\frac{\tilde{\alpha}_{21\alpha}}{\tilde{\alpha}_{12\alpha}\tilde{\alpha}_{21\alpha}-\tilde{\alpha}_{11\alpha}\tilde{\alpha}_{22\alpha}}\widetilde{\nabla T_\alpha}+ \\ \frac{p_\alpha}{\lambda_{\alpha\alpha}}\frac{T_{av}}{m_\alpha}\sum_\beta\left[\frac{\frac{15}{4}\left(\frac{\mu_{\alpha\beta}}{m_\alpha}\right)^2\tilde{\alpha}_{11\alpha}-\frac{3}{2}\frac{\mu_{\alpha\beta}}{m_\alpha}\tilde{\alpha}_{21\alpha}}{\tilde{\alpha}_{12\alpha}\tilde{\alpha}_{21\alpha}-\tilde{\alpha}_{11\alpha}\tilde{\alpha}_{22\alpha}}\lambda_{\alpha\beta}(\overline{\mathbf{w}}_\alpha-\overline{\mathbf{w}}_\beta)\right]. \quad \text{(H.1)}$$

Using (4.91) one can write:

$$\overline{\mathbf{r}}_\alpha = -\frac{175}{48}\frac{p_\alpha n_\alpha}{\lambda_{\alpha\alpha}}\frac{T_{av}}{m_\alpha}\frac{1}{\tilde{\Delta}_\alpha}\left(1+\frac{23\sqrt{2}}{8}Z^s_{9\alpha}\right)\widetilde{\nabla T_\alpha}+ \\ \frac{35}{24}\frac{p_\alpha}{\lambda_{\alpha\alpha}}\frac{T_{av}}{m_\alpha}\frac{1}{\tilde{\Delta}_\alpha}\sum_\beta\left[\frac{\mu_{\alpha\beta}}{m_\alpha}\Big(\frac{3}{2}-\frac{5}{2}\frac{\mu_{\alpha\beta}}{m_\alpha}+\frac{69\sqrt{2}}{16}Z^s_{9\alpha}-\frac{65\sqrt{2}}{16}\frac{\mu_{\alpha\beta}}{m_\alpha}Z^s_{5\alpha}\Big)\lambda_{\alpha\beta}(\overline{\mathbf{w}}_\alpha-\overline{\mathbf{w}}_\beta)\right] \quad \text{(H.2)}$$

Combining the transport coefficients, one can obtain the final form of the additional vector moment:

$$\overline{\mathbf{r}}_\alpha = -\frac{p_\alpha n_\alpha}{\lambda_{\alpha\alpha}}c_\alpha^{(r_T^A)}\frac{T_{av}}{m_\alpha}\widetilde{\nabla T_\alpha}+p_\alpha\frac{T_{av}}{m_\alpha}\sum_\beta c_{\beta\alpha}^{(r_w^A)}(\overline{\mathbf{w}}_\alpha-\overline{\mathbf{w}}_\beta) \quad \text{(H.3)}$$

where:

$$c_\alpha^{(r_T^A)} = \frac{175}{48}\frac{1}{\tilde{\Delta}_\alpha}\left(1+\frac{23\sqrt{2}}{8}Z^s_{9\alpha}\right) \quad \text{(H.4)}$$

$$c_{\beta\alpha}^{(r_w^A)} = -\frac{35}{24}\frac{\mu_{\alpha\beta}}{m_\alpha}\frac{1}{\tilde{\Delta}_\alpha}\sqrt{2}\sqrt{\frac{\mu_{\alpha\beta}}{m_\alpha}\frac{\overline{Z^2_\beta}n_\beta}{\overline{Z^2_\alpha}n_\alpha}}\Big(\frac{5}{2}\frac{\mu_{\alpha\beta}}{m_\alpha}-\frac{3}{2}+\frac{65\sqrt{2}}{16}\frac{\mu_{\alpha\beta}}{m_\alpha}Z^s_{5\alpha}-\frac{69\sqrt{2}}{16}Z^s_{9\alpha}\Big) \quad \text{(H.5)}$$

## H.2 Thermal and Friction forces

Using (E.2) one can obtain:

$$\mathbf{R}_{\alpha}^{T} = \mathbf{R}_{\alpha}^{T1} + \mathbf{R}_{\alpha}^{T2}, \tag{H.6}$$

$$\mathbf{R}_{\alpha}^{T1} = \sum_{\beta\neq\alpha}\Big[\frac{\mu_{\alpha\beta}}{m_{\alpha}}\overline{G}_{\alpha\beta}^{(2)}\frac{\overline{\mathbf{h}}_{\alpha}^{T}}{p_{\alpha}} + \left(\frac{\mu_{\alpha\beta}}{m_{\alpha}}\right)^{2}\overline{G}_{\alpha\beta}^{(8)}\frac{m_{\alpha}}{T_{av}}\frac{\overline{\mathbf{r}}_{\alpha}^{T}}{p_{\alpha}}\Big], \tag{H.7}$$

$$\mathbf{R}_{\alpha}^{T2} = -\sum_{\beta\neq\alpha}\frac{m_{\alpha}}{m_{\beta}}\Big[\frac{\mu_{\alpha\beta}}{m_{\alpha}}\overline{G}_{\alpha\beta}^{(2)}\frac{\overline{\mathbf{h}}_{\beta}^{T}}{p_{\beta}} + \left(\frac{\mu_{\alpha\beta}}{m_{\alpha}}\right)^{2}\overline{G}_{\alpha\beta}^{(8)}\frac{m_{\alpha}}{T_{av}}\frac{\overline{\mathbf{r}}_{\beta}^{T}}{p_{\beta}}\Big], \tag{H.8}$$

With a help from (4.93) and (H.2) the first part of TF can be written as:

$$\mathbf{R}_{\alpha}^{T1} = -\frac{n_{\alpha}}{\tilde{\Delta}_{\alpha}}\sum_{\beta\neq\alpha}\Bigg[\frac{75}{32}\frac{\mu_{\alpha\beta}}{m_{\alpha}}\frac{\lambda_{\alpha\beta}}{\lambda_{\alpha\alpha}}\left(1+\frac{433\sqrt{2}}{360}Z_{11\alpha}^{s}\right) - \frac{25}{32}\left(\frac{\mu_{\alpha\beta}}{m_{\alpha}}\right)^{2}\frac{\lambda_{\alpha\beta}}{\lambda_{\alpha\alpha}}\left(1+\frac{23\sqrt{2}}{8}Z_{9\alpha}^{s}\right)\Bigg]\widetilde{\nabla T_{\alpha}} \tag{H.9}$$

Combining the transport coefficients, one can obtain the first part of the TF:

$$\mathbf{R}_{\alpha}^{T1} = -\sum_{\beta\neq\alpha}n_{\alpha}c_{\alpha\beta}^{(R_{T}^{A})}\frac{\overline{Z_{\beta}^{2}}n_{\beta}}{\overline{Z_{\alpha}^{2}}n_{\alpha}}\widetilde{\nabla T_{\alpha}} \tag{H.10}$$

where:

$$c_{\alpha\beta}^{(R_{T}^{A})} = \frac{1}{\tilde{\Delta}_{\alpha}}\frac{25\sqrt{2}}{16}\left(\frac{\mu_{\alpha\beta}}{m_{\alpha}}\right)^{3/2}\left[\frac{3}{2}\left(1+\frac{433\sqrt{2}}{360}Z_{11\alpha}^{s}\right) - \frac{1}{2}\frac{\mu_{\alpha\beta}}{m_{\alpha}}\left(1+\frac{23\sqrt{2}}{8}Z_{9\alpha}^{s}\right)\right] \tag{H.11}$$

Similarly, the second part of the TF is:

$$\mathbf{R}_{\alpha}^{T2} = \sum_{\beta\neq\alpha}\frac{n_{\beta}}{\tilde{\Delta}_{\beta}}\Bigg[\frac{75}{32}\frac{\mu_{\alpha\beta}}{m_{\beta}}\frac{\lambda_{\alpha\beta}}{\lambda_{\beta\beta}}\left(1+\frac{433\sqrt{2}}{360}Z_{11\beta}^{s}\right) - \frac{25}{32}\left(\frac{\mu_{\alpha\beta}}{m_{\beta}}\right)^{2}\frac{\lambda_{\alpha\beta}}{\lambda_{\beta\beta}}\left(1+\frac{23\sqrt{2}}{8}Z_{9\beta}^{s}\right)\Bigg]\widetilde{\nabla T_{\beta}} \tag{H.12}$$

Combining the transport coefficients, one can obtain the second part of the TF:

$$\mathbf{R}_{\alpha}^{T2} = \sum_{\beta \neq \alpha} n_{\beta} c_{\beta\alpha}^{(R_T^A)} \frac{\overline{Z_{\alpha}^2} n_{\alpha}}{\overline{Z_{\beta}^2} n_{\beta}} \widetilde{\nabla T_{\beta}} \tag{H.13}$$

The total TF is:

$$\mathbf{R}_{\alpha}^{T} = -\sum_{\beta \neq \alpha} \left[ n_{\alpha} c_{\alpha\beta}^{(R_T^A)} \frac{\overline{Z_{\beta}^2} n_{\beta}}{\overline{Z_{\alpha}^2} n_{\alpha}} \widetilde{\nabla T_{\alpha}} - n_{\beta} c_{\beta\alpha}^{(R_T^A)} \frac{\overline{Z_{\alpha}^2} n_{\alpha}}{\overline{Z_{\beta}^2} n_{\beta}} \widetilde{\nabla T_{\beta}} \right]. \tag{H.14}$$

The (H.14) is equivalent to:

$$\mathbf{R}_{\alpha}^{T} = -\sum_{\beta} \left[ n_{\alpha} c_{\alpha\beta}^{(R_T^A)} \frac{\overline{Z_{\beta}^2} n_{\beta}}{\overline{Z_{\alpha}^2} n_{\alpha}} \widetilde{\nabla T_{\alpha}} - n_{\beta} c_{\beta\alpha}^{(R_T^A)} \frac{\overline{Z_{\alpha}^2} n_{\alpha}}{\overline{Z_{\beta}^2} n_{\beta}} \widetilde{\nabla T_{\beta}} \right]. \tag{H.15}$$

The (H.15) can be written in the form of (4.59):

$$\mathbf{R}_{\alpha}^{T} = -\sum_{\beta} n_{\beta} \tilde{c}_{\alpha\beta}^{(R_T^A)} \widetilde{\nabla T_{\beta}}, \tag{H.16}$$

where:

$$\tilde{c}_{\alpha\beta}^{(R_T^A)} = \delta_{\alpha\beta} \sum_{\gamma} c_{\alpha\gamma}^{(R_T^A)} \frac{\overline{Z_{\gamma}^2} n_{\gamma}}{\overline{Z_{\alpha}^2} n_{\alpha}} - c_{\beta\alpha}^{(R_T^A)} \frac{\overline{Z_{\alpha}^2} n_{\alpha}}{\overline{Z_{\beta}^2} n_{\beta}} \tag{H.17}$$

The FR is derived identically as in appendix F.1, where the coefficients $c_{\beta\alpha}^{(h_w^A)}$ and $c_{\beta\alpha}^{(r_w^A)}$ in (F.15), (F.16) and (F.17) are chosen according to (4.96) and (H.5).

# I Improved analytical method for the viscous-stress tensor

We neglect the cross terms, which depend on the $\overline{\pi}_{\beta rs}$ and $\overline{\sigma}_{\beta rs}$ for $\beta \neq \alpha$, in the rank-2 equations (4.66) and (4.67):

$$\sum_{\beta\neq\alpha} \frac{T_{av}}{m_\alpha + m_\beta}\left[\frac{\overline{G}^{(3)}_{\alpha\beta}\overline{\pi}_{\alpha rs}}{p_\alpha} + \frac{\mu_{\alpha\beta}}{T_{av}}\frac{\overline{G}^{(13)}_{\alpha\beta}\overline{\sigma}_{\alpha rs}}{p_\alpha}\right] + \frac{T_{av}}{2m_\alpha}\left[\frac{\overline{G}^{(3)}_{\alpha\alpha}\overline{\pi}_{\alpha rs}}{p_\alpha} + \frac{\overline{G}^{(4)}_{\alpha\alpha}\overline{\pi}_{\alpha rs}}{p_\alpha} + \frac{\mu_{\alpha\alpha}}{T_{av}}\left(\frac{\overline{G}^{(13)}_{\alpha\alpha}\overline{\sigma}_{\alpha rs}}{p_\alpha} + \frac{\overline{G}^{(14)}_{\alpha\alpha}\overline{\sigma}_{\alpha rs}}{p_\alpha}\right)\right] = W^{\overline{h}_\alpha}_{rs} + p_\alpha\widetilde{W^{u_\alpha}_{rs}} \quad \text{(I.1)}$$

$$\sum_{\beta\neq\alpha} \frac{T_{av}}{m_\alpha + m_\beta}\left[\frac{7}{2}T_{av}\mu_{\alpha\beta}\frac{\overline{G}^{(13)}_{\alpha\beta}\overline{\pi}_{\alpha rs}}{m_\alpha^2 p_\alpha} + \frac{\overline{G}^{(15)}_{\alpha\beta}\overline{\sigma}_{\alpha rs}}{p_\alpha} + \frac{\overline{G}^{(16)}_{\alpha\beta}\overline{\sigma}_{\beta rs}}{p_\beta}\right] + \frac{T_{av}}{2m_\alpha}\left[\frac{7}{2}T_{av}\frac{m_\alpha}{2}\left(\frac{\overline{G}^{(13)}_{\alpha\alpha}\overline{\pi}_{\alpha rs}}{m_\alpha^2 p_\alpha} + \frac{\overline{G}^{(14)}_{\alpha\alpha}\overline{\pi}_{\alpha rs}}{m_\alpha^2 p_\alpha}\right) + \frac{\overline{G}^{(15)}_{\alpha\alpha}\overline{\sigma}_{\alpha rs}}{p_\alpha} + \frac{\overline{G}^{(16)}_{\alpha\alpha}\overline{\sigma}_{\alpha rs}}{p_\alpha}\right] = \frac{7}{2}\frac{T_{av}}{m_\alpha}W^{\overline{h}_\alpha}_{rs} \quad \text{(I.2)}$$

Combining G-objects into the coefficients and using Z-variables (appendix B), one can get:

$$\frac{T_{av}}{m_\alpha}\tilde{\gamma}_{11\alpha}\lambda_{\alpha\alpha}\frac{\overline{\pi}_{\alpha rs}}{p_\alpha} + \tilde{\gamma}_{12\alpha}\lambda_{\alpha\alpha}\frac{\overline{\sigma}_{\alpha rs}}{p_\alpha} = W^{\overline{h}_\alpha}_{rs} + p_\alpha\widetilde{W^{u_\alpha}_{rs}} \quad \text{(I.3)}$$

$$\frac{T_{av}}{m_\alpha}\tilde{\gamma}_{21\alpha}\lambda_{\alpha\alpha}\frac{\overline{\pi}_{\alpha rs}}{p_\alpha} + \tilde{\gamma}_{22\alpha}\lambda_{\alpha\alpha}\frac{\overline{\sigma}_{\alpha rs}}{p_\alpha} = \frac{7}{2}\frac{T_{av}}{m_\alpha}W^{\overline{h}_\alpha}_{rs}, \quad \text{(I.4)}$$

where $\lambda_{\alpha\beta}$ is defined according to (2.91) and the $\tilde{\gamma}_{**\alpha}$ coefficients are:

$$\tilde{\gamma}_{11\alpha} \overset{\text{def}}{=} -\frac{6}{5} - \frac{6\sqrt{2}}{5}Z^{\pi}_{11\alpha}, \quad \tilde{\gamma}_{21\alpha} \overset{\text{def}}{=} \frac{7}{2}\tilde{\gamma}_{12\alpha} \overset{\text{def}}{=} \frac{9}{10} + \frac{9\sqrt{2}}{5}Z^{\pi}_{12\alpha}, \quad \tilde{\gamma}_{22\alpha} \overset{\text{def}}{=} -\frac{41}{28} - \frac{51\sqrt{2}}{35}Z^{\pi}_{22\alpha}. \quad \text{(I.5)}$$

The viscous-stress tensorsolution of the (I.3) and (I.4) is:

$$\frac{\overline{\pi}_{\alpha rs}}{p_\alpha} = \frac{1}{\lambda_{\alpha\alpha}}\frac{m_\alpha}{T_{av}}\frac{\tilde{\gamma}_{22\alpha}}{\tilde{\gamma}_{11\alpha}\tilde{\gamma}_{22\alpha}+\tilde{\gamma}_{12\alpha}\tilde{\gamma}_{21\alpha}}p_\alpha\widetilde{W_{rs}^{u_\alpha}} + \frac{1}{\lambda_{\alpha\alpha}}\frac{m_\alpha}{T_{av}}\frac{\tilde{\gamma}_{22\alpha}-\frac{7}{2}\tilde{\gamma}_{12\alpha}}{\tilde{\gamma}_{11\alpha}\tilde{\gamma}_{22\alpha}+\tilde{\gamma}_{12\alpha}\tilde{\gamma}_{21\alpha}}W_{rs}^{\overline{h}_\alpha}. \quad \text{(I.6)}$$

It is convenient to define:

$$\Delta_\alpha^\pi \stackrel{\text{def}}{=} \frac{204}{89}Z_{11\alpha}^\pi Z_{22\alpha}^\pi - \frac{108}{89}{Z_{12\alpha}^\pi}^2 + \frac{205\sqrt{2}}{178}Z_{11\alpha}^\pi + \frac{102\sqrt{2}}{89}Z_{22\alpha}^\pi - \frac{54\sqrt{2}}{89}Z_{12\alpha}^\pi + 1, \quad \text{(I.7)}$$

then:

$$\tilde{\gamma}_{11\alpha}\tilde{\gamma}_{22\alpha}+\tilde{\gamma}_{12\alpha}\tilde{\gamma}_{21\alpha} = \frac{267}{175}\Delta_\alpha^\pi. \quad \text{(I.8)}$$

Combining the transport coefficients, one can obtain the final form of the viscous-stress tensor:

$$\frac{\overline{\pi}_{\alpha rs}}{p_\alpha} = -\frac{1}{\lambda_{\alpha\alpha}}\frac{m_\alpha}{T_{av}}c_\alpha^{(\pi_u^A)}p_\alpha\widetilde{W_{rs}^{u_\alpha}} - \frac{1}{\lambda_{\alpha\alpha}}\frac{m_\alpha}{T_{av}}c_\alpha^{(\pi_h^A)}W_{rs}^{\overline{h}_\alpha}, \quad \text{(I.9)}$$

where coefficients are:

$$c_\alpha^{(\pi_u^A)} \stackrel{\text{def}}{=} -\frac{\tilde{\gamma}_{22\alpha}}{\tilde{\gamma}_{11\alpha}\tilde{\gamma}_{22\alpha}+\tilde{\gamma}_{12\alpha}\tilde{\gamma}_{21\alpha}} = \frac{1025}{1068}\frac{1}{\Delta_\alpha^\pi}\left(1+\frac{204\sqrt{2}}{205}Z_{22\alpha}^\pi\right), \quad \text{(I.10)}$$

$$c_\alpha^{(\pi_h^A)} \stackrel{\text{def}}{=} -\frac{\tilde{\gamma}_{22\alpha}-\frac{7}{2}\tilde{\gamma}_{12\alpha}}{\tilde{\gamma}_{11\alpha}\tilde{\gamma}_{22\alpha}+\tilde{\gamma}_{12\alpha}\tilde{\gamma}_{21\alpha}} = \frac{1655}{1068}\frac{1}{\Delta_\alpha^\pi}\left(1+\frac{204\sqrt{2}}{331}Z_{22\alpha}^\pi+\frac{252\sqrt{2}}{331}Z_{12\alpha}^\pi\right). \quad \text{(I.11)}$$

The viscous-stress tensor (I.9) can be written in the form of (4.72):

$$\overline{\pi}_{\alpha rs} = -\sum_\beta \check{c}_{\alpha\beta}^{(\pi_u^A)}\tau_{\alpha\beta}^{(Zh)}p_\beta\widetilde{W_{rs}^{u_\beta}} - \sum_\beta \check{c}_{\alpha\beta}^{(\pi_h^A)}\tau_{\alpha\beta}^{(Zh)}W_{rs}^{\overline{h}_\beta}, \quad \text{(I.12)}$$

if the transport coefficients are written as:

$$\check{c}_{\alpha\beta}^{(\pi_u^A)} = 2c_\alpha^{(\pi_u^A)}\delta_{\alpha\beta}, \quad \check{c}_{\alpha\beta}^{(\pi_h^A)} = 2c_\alpha^{(\pi_h^A)}\delta_{\alpha\beta}. \quad \text{(I.13)}$$

# J Zhdanov closure for SOLPS-ITER (additional content)

## J.1 Electron transport coefficients

The relation between the SOLPS-ITER electron transport coefficients and the Eq. (8.2.8) in [18] are considered.

The $c_e^{(1)}$ is used in the electron conductivity $\sigma_{\parallel}^{(CL)}$ (3.27), which is then used in the electron-ion FR (3.24) and in the Ohm's law (3.63). The relation between $c_e^{(1)}$ and $\alpha_{\parallel}$ in Eq. (8.2.8) in [18] is:

$$c_e^{(1)} = \frac{(1+0.24Z_{eff})(1+0.93Z_{eff})}{(1+2.56Z_{eff})(1+0.29Z_{eff})} \approx 1 - \frac{0.22+0.73/Z_{eff}}{0.31+1.20/Z_{eff}+0.41/Z_{eff}^2} = \alpha_{\parallel} \quad \text{(J.1)}$$

The $c_e^{(2)} z_{eff}/\left(z_{eff}+\sqrt{2}/2\right)$ (3.35) is used in the electron TF coefficient $\alpha_x^{(CL)}$ (3.27), which is then used in the electron-ion TF (3.23) and in the Ohm's law (3.63). Besides, the $c_e^{(2)} z_{eff}/\left(z_{eff}+\sqrt{2}/2\right)$ used in $c_{071}$ (3.47), which is then used in the electron **w**-dependent part of the heat flux (3.38). The relation between $c_e^{(2)} z_{eff}/\left(z_{eff}+\sqrt{2}/2\right)$ and $\beta_{\parallel}$ in Eq. (8.2.8) in [18] is:

$$c_e^{(2)} \frac{Z_{eff}}{(\sqrt{2}/2+Z_{eff})} = 1.56 \frac{(1+1.4Z_{eff})(1+0.52Z_{eff})}{(1+2.56Z_{eff})(1+0.29Z_{eff})} \frac{\sqrt{2}Z_{eff}}{(1+\sqrt{2}Z_{eff})} \approx \frac{0.47+0.94/Z_{eff}}{0.31+1.20/Z_{eff}+0.41/Z_{eff}^2} = \beta_{\parallel} \quad \text{(J.2)}$$

The $f_{k_e}(z_{eff})$ is used in the electron heat conductivity $\kappa_{ex}^{(CL)}$ (3.46), which than used in the electron $T$-dependent part of the heat flux (3.38). The relation between $f_{k_e}(z_{eff})$ and $\gamma_{\parallel}$ in Eq. (8.2.8) in [18] is:

$$f_{k_e}(z_{eff}) = \frac{3.9+2.3/Z_{eff}}{0.31+1.20/Z_{eff}+0.41/Z_{eff}^2} = \gamma_{\parallel} \quad \text{(J.3)}$$

## J.2 Electron and ion heat sources

Using (4.20) one can re-write the corresponding heat sources in collisions (3.58) and (3.50) as following:

$$Q_{F_{ab}} = -\sum_{\alpha Z} w_{\alpha Z\|}\left(R_{\alpha Z} + R^e_{\alpha Z}\right) = \\ -\left(\sum_a V_{a\|}\left(S^m_{fr,a} + S^m_{Therm,a}\right) - V_\|\sum_a\left(S^m_{fr,ea} + S^m_{Therm,ea}\right)\right), \quad \text{(J.4)}$$

$$Q_{F_{ei}} = w_{e\|}\sum_{\alpha Z}\sum_Z R^e_{\alpha Z} = \\ V_{e\|}\left(\sum_a\left(S^m_{fr,ea} + S^m_{Therm,ea}\right) - \frac{V_\|}{V_{e\|}}\sum_a\left(S^m_{fr,ea} + S^m_{Therm,ea}\right)\right), \quad \text{(J.5)}$$

where:

$$w_{a\|} = V_{a\|} - V_\|, \quad V_\| = \frac{1}{\rho}\sum_a \rho_a V_{a\|}, \quad \rho = \sum_a \rho_a, \quad \rho_a = m_a n_a. \quad \text{(J.6)}$$

## J.3 Viscous-stress tensor divergence

Using (5.9), we extract the $u_{\alpha Z\|}$ dependence as following:

$$(\nabla\cdot\overleftrightarrow{\pi}^u_{\alpha Z})_\| = -\frac{4}{3}b_x B^{3/2}\frac{\partial}{h_x\partial x}\left[\frac{b_x}{B^2}\frac{n_{\alpha Z}}{n_\alpha}\left[\check{c}^{(\pi^A_u)}_{\alpha\alpha}\tau^{(Zh)}_{\alpha\alpha}p_{\alpha Z}\frac{\partial}{h_x\partial x}\left(\sqrt{B}u_{\alpha Z\|}\right) + \right.\right. \\ \check{c}^{(\pi^A_u)}_{\alpha\alpha}\tau^{(Zh)}_{\alpha\alpha}\sum_{\zeta\neq Z}p_{\alpha\zeta}\frac{\partial}{h_x\partial x}\left(\sqrt{B}u_{\alpha\zeta\|}\right) + \sum_{\beta\neq\alpha}\check{c}^{(\pi^A_u)}_{\alpha\beta}\tau^{(Zh)}_{\alpha\beta}\sum_\zeta p_{\beta\zeta}\frac{\partial}{h_x\partial x}\left(\sqrt{B}u_{\beta\zeta\|}\right) + \\ 2c^{(\pi^B_u)}_\alpha\tau^{(Zh)}_{\alpha\alpha}p_{\alpha Z}\left(\frac{1}{I_{\alpha Z}} - 1\right)\frac{\partial}{h_x\partial x}\left(\sqrt{B}u_{\alpha Z\|}\right) \\ \left.\left. - 2c^{(\pi^B_u)}_\alpha\tau^{(Zh)}_{\alpha\alpha}\sum_{\zeta\neq Z}p_{\alpha\zeta}\frac{\partial}{h_x\partial x}\left(\sqrt{B}u_{\alpha\zeta\|}\right)\right]\right]. \quad \text{(J.7)}$$

Then, the terms are combined as:

$$(\nabla\cdot\overleftrightarrow{\pi}^u_{\alpha Z})_\| = (\nabla\cdot\overleftrightarrow{\pi}^u_{\alpha Z})^{\alpha Z}_\| + (\nabla\cdot\overleftrightarrow{\pi}^u_{\alpha Z})^{ai}_\| \quad \text{(J.8)}$$

$$(\nabla\cdot\overleftrightarrow{\pi}^u_{\alpha Z})^{\alpha Z}_\| = \\ -\frac{4}{3}b_x B^{3/2}\frac{\partial}{h_x\partial x}\left[\frac{b_x}{B^2}\frac{n_{\alpha Z}}{n_\alpha}\left[\check{c}^{(\pi^A_u)}_{\alpha\alpha} + 2c^{(\pi^B_u)}_\alpha\left(\frac{1}{I_{\alpha Z}} - 1\right)\right]\tau^{(Zh)}_{\alpha\alpha}p_{\alpha Z}\frac{\partial}{h_x\partial x}\left(\sqrt{B}u_{\alpha Z\|}\right)\right] \quad \text{(J.9)}$$

$$(\nabla \cdot \overleftrightarrow{\pi}^{u}_{\alpha Z})^{ai}_{\parallel} =$$
$$-\frac{4}{3} b_x B^{3/2} \frac{\partial}{h_x \partial x} \left[ \frac{b_x}{B^2} \frac{n_{\alpha Z}}{n_\alpha} \left[ \sum_{\beta \neq \alpha} \check{c}^{(\pi^A_u)}_{\alpha\beta} \tau^{(Zh)}_{\alpha\beta} \sum_{\zeta} p_{\beta\zeta} \frac{\partial}{h_x \partial x} \left( \sqrt{B} u_{\beta\zeta\parallel} \right) + \right. \right.$$
$$\left. \left. (\check{c}^{(\pi^A_u)}_{\alpha\alpha} - 2c^{(\pi^B_u)}_{\alpha}) \tau^{(Zh)}_{\alpha\alpha} \sum_{\zeta \neq Z} p_{\alpha\zeta} \frac{\partial}{h_x \partial x} \left( \sqrt{B} u_{\alpha\zeta\parallel} \right) \right] \right] \quad \text{(J.10)}$$

The (J.9) can be written in the form of:

$$(\nabla \cdot \overleftrightarrow{\pi}^{u}_{\alpha Z})^{\alpha Z}_{\parallel} = -\frac{4}{3} b_x B^{3/2} \frac{\partial}{h_x \partial x} \left[ \eta^{(CL)}_{\alpha Z x} \frac{1}{B^2 b_x} \frac{\partial}{h_x \partial x} \left( \sqrt{B} u_{\alpha Z\parallel} \right) \right] \quad \text{(J.11)}$$

where the coefficient $\eta^{(CL)}_{\alpha Z x}$ is defined as following:

$$\eta^{(CL)}_{ax} = [a \to \alpha Z] = \eta^{(CL)}_{\alpha Z x} = \left[ \frac{\eta^{(u_i A)}_{\alpha\alpha x}}{p_\alpha} + \frac{\eta^{(u_i B)}_{\alpha x}}{p_\alpha} \left( \frac{1}{I_{\alpha Z}} - 1 \right) \right] \frac{n_{\alpha Z}}{n_\alpha} p_{\alpha Z}, \quad \text{(J.12)}$$

where $\frac{\eta^{(u_i A)}_{\alpha\beta x}}{p_\alpha}$ and $\frac{\eta^{(u_i B)}_{\alpha x}}{p_\alpha}$ are defined as following:

$$\frac{\eta^{(u_i A)}_{\alpha\beta x}}{p_\alpha} = b_x^2 \frac{\eta^{(u_i A)}_{\alpha\beta}}{p_\alpha}; \quad \frac{\eta^{(u_i A)}_{\alpha\beta}}{p_\alpha} = \check{c}^{(\pi^A_u)}_{\alpha\beta} \tau^{(Zh)}_{\alpha\beta}; \quad \frac{\eta^{(u_i B)}_{\alpha x}}{p_\alpha} = b_x^2 \frac{\eta^{(u_i B)}_{\alpha}}{p_\alpha}; \quad \frac{\eta^{(u_i B)}_{\alpha}}{p_\alpha} = 2c^{(\pi^B_u)}_{\alpha} \tau^{(Zh)}_{\alpha\alpha}, \quad \text{(J.13)}$$

Using $\nabla \cdot \mathbf{B} = 0$ and $\frac{\partial B_z h_z}{\partial x} = \frac{\partial B_z h_z}{\partial y} = 0$ the (J.11) can be split into the diffusive and convective terms in the divergent part of the $(\nabla \cdot \overleftrightarrow{\pi}^{u}_{\alpha Z})^{\alpha Z}_{\parallel}$ and the remaining part, which is implemented as a source.

$$(\nabla \cdot \overleftrightarrow{\pi}^{u}_{\alpha Z})^{\alpha Z}_{\parallel} = (\nabla \cdot \overleftrightarrow{\pi}^{u}_{\alpha Z})^{div}_{\parallel} + (\nabla \cdot \overleftrightarrow{\pi}^{u}_{\alpha Z})^{res}_{\parallel} \quad \text{(J.14)}$$

$$(\nabla \cdot \overleftrightarrow{\pi}^{u}_{\alpha Z})^{div}_{\parallel} = -\frac{1}{h_z \sqrt{g}} \frac{\partial}{\partial x} \left( \frac{h_z \sqrt{g}}{h_x} \frac{4}{3} \eta^{(CL)}_{\alpha Z x} \frac{\partial \ln h_z}{h_x \partial x} u_{\alpha Z\parallel} - \frac{h_z \sqrt{g}}{h_x} \frac{4}{3} \eta^{(CL)}_{\alpha Z x} \frac{\partial u_{\alpha Z\parallel}}{h_x \partial x} \right) \quad \text{(J.15)}$$

$$(\nabla \cdot \overleftrightarrow{\pi}^{u}_{\alpha Z})^{res}_{\parallel} = -\frac{1}{h_z \sqrt{g}} \frac{\partial}{\partial x} \left( \frac{h_z \sqrt{g}}{h_x} \frac{4}{3} \eta^{(CL)}_{\alpha Z x} \frac{\partial \ln \left( h_z B^{\frac{1}{2}} \right)}{B^{\frac{1}{2}} h_x \partial x} \right) B^{\frac{1}{2}} u_{\alpha Z\parallel} \quad \text{(J.16)}$$

Thus, the momentum flux is:

$$\Gamma^m_{ax} = \begin{cases} m_a V_{\parallel a}\Gamma^{Cor}_{ax} + \frac{4}{3}\eta^{(CL)}_{ax}\frac{\partial \ln h_z}{h_x \partial x}V_{\parallel a} - \eta_{ax}\frac{\partial V_{\parallel a}}{h_x \partial x}, & z_a \neq 0 \\ m_a V_{\parallel a}\Gamma^{Cor}_{ax} - \eta_{ax}\frac{\partial V_{\parallel a}}{h_x \partial x}, & z_a = 0 \end{cases} \tag{J.17}$$

$$S^m_{a\parallel} = -\left(\nabla \cdot \overset{\leftrightarrow}{\pi}{}^{\parallel}_a\right)_{\parallel} = \begin{cases} -\left(\nabla \cdot \overset{\leftrightarrow}{\pi}{}^{V_\parallel}_a\right)^{res}_{\parallel} - \left(\nabla \cdot \overset{\leftrightarrow}{\pi}{}^{V_\parallel}_a\right)^{ai}_{\parallel} - \left(\nabla \cdot \overset{\leftrightarrow}{\pi}{}^{h_i}_a\right)_{\parallel}, & z_a \neq 0 \\ 0, & z_a = 0 \end{cases} \tag{J.18}$$

$$\left(\nabla \cdot \overset{\leftrightarrow}{\pi}{}^{V_\parallel}_a\right)^{res}_{\parallel} = -\frac{1}{h_z\sqrt{g}}\frac{\partial}{\partial x}\left(\frac{h_z\sqrt{g}}{h_x}\frac{4}{3}\eta^{(CL)}_{ax}\frac{\partial \ln\left(h_z B^{\frac{1}{2}}\right)}{B^{\frac{1}{2}}h_x \partial x}\right) B^{\frac{1}{2}}V_{\parallel a} \tag{J.19}$$

$$\left(\nabla \cdot \overset{\leftrightarrow}{\pi}{}^{V_\parallel}_a\right)^{ai}_{\parallel} = [a \to \alpha Z] = -\frac{4}{3}b_x B^{3/2}\frac{\partial}{h_x \partial x}\left[\frac{1}{B^2 b_x}\frac{n_{\alpha Z}}{n_\alpha}\left[\sum_{\beta\neq\alpha}\frac{\eta^{(u_i A)}_{\alpha\beta x}}{p_\alpha}\sum_\zeta p_{\beta\zeta}\frac{\partial}{h_x\partial x}\left(\sqrt{B}u_{\beta\zeta\parallel}\right) + \left(\frac{\eta^{(u_i A)}_{\alpha\alpha x}}{p_\alpha} - \frac{\eta^{(u_i B)}_{\alpha x}}{p_\alpha}\right)\sum_{\zeta\neq Z} p_{\alpha\zeta}\frac{\partial}{h_x\partial x}\left(\sqrt{B}u_{\alpha\zeta\parallel}\right)\right]\right]. \tag{J.20}$$

The $\left(\nabla \cdot \overset{\leftrightarrow}{\pi}{}^{h_i}_a\right)_{\parallel}$ is derived in subsection 5.1.4.

## J.4 Viscous-drift currents

Following [88, 83], the drift currents, which depend on the velocity-dependent part of the viscous-stress tensor, which previously were written only for the main ion species (3.69) and (3.70), are written in this thesis for any ion species $a$ for $z_a \neq 0$:

$$\widetilde{j}^{(vis\parallel)}_{ax} = [a \to \alpha Z] = -\frac{B_z\sqrt{B}}{3B_x}\frac{\partial}{h_y\partial y}\left(\frac{1}{B^2}\right)\frac{\partial}{h_x\partial x}\left[\eta^{(CL)}_{\alpha Z x}\left(\sqrt{B}u_{\alpha Z\parallel}\right) + \frac{n_{\alpha Z}}{n_\alpha}\left[\sum_{\beta\neq\alpha}\frac{\eta^{(u_i A)}_{\alpha\beta x}}{p_\alpha}\sum_\zeta p_{\beta\zeta}\frac{\partial}{h_x\partial x}\left(\sqrt{B}u_{\beta\zeta\parallel}\right) + \left(\frac{\eta^{(u_i A)}_{\alpha\alpha x}}{p_\alpha} - \frac{\eta^{(u_i B)}_{\alpha x}}{p_\alpha}\right)\sum_{\zeta\neq Z} p_{\alpha\zeta}\frac{\partial}{h_x\partial x}\left(\sqrt{B}u_{\alpha\zeta\parallel}\right)\right]\right], \tag{J.21}$$

$$\widetilde{j}_{ay}^{(vis\|)} = [a \to \alpha Z] = \frac{B_z\sqrt{B}}{3B_x}\frac{\partial}{h_x\partial x}\left(\frac{1}{B^2}\right)\frac{\partial}{h_x\partial x}\left[\eta_{\alpha Z x}^{(CL)}\left(\sqrt{B}u_{\alpha Z\|}\right)+\right.$$
$$\left.\frac{n_{\alpha Z}}{n_\alpha}\left[\sum_{\beta\neq\alpha}\frac{\eta_{\alpha\beta x}^{(u_iA)}}{p_\alpha}\sum_\zeta p_{\beta\zeta}\frac{\partial}{h_x\partial x}\left(\sqrt{B}u_{\beta\zeta\|}\right)+\left(\frac{\eta_{\alpha\alpha x}^{(u_iA)}}{p_\alpha}-\frac{\eta_{\alpha x}^{(u_iB)}}{p_\alpha}\right)\sum_{\zeta\neq Z}p_{\alpha\zeta}\frac{\partial}{h_x\partial x}\left(\sqrt{B}u_{\alpha\zeta\|}\right)\right]\right]. \tag{J.22}$$

Following [88, 83], the drift currents, which depend on the heat-flux-dependent part of the viscous-stress tensor, which previously were written only for the main ion species (3.75) and (3.76), are written in this thesis for any ion species $a$ for $z_a \neq 0$:

$$\widetilde{j}_{ax}^{(visq)} = [a \to \alpha Z] =$$
$$-\frac{2}{5}\frac{B_z\sqrt{B}}{3B_x}\frac{\partial}{h_y\partial y}\left(\frac{1}{B^2}\right)\frac{\partial}{h_x\partial x}\left[\frac{n_{\alpha Z}}{n_\alpha}\left[\sum_\beta\frac{\eta_{\alpha\beta x}^{(h_iA)}}{p_\alpha}\frac{\partial}{h_x\partial x}\left(\sqrt{B}\frac{\overline{h}_{\beta x}^{*(0)}}{b_x}\right)+\right.\right.$$
$$\left.\left.\frac{\eta_{\alpha x}^{(h_iB)}}{p_\alpha}\left(\frac{1}{I_{\alpha Z}}\frac{\partial}{h_x\partial x}\left(\sqrt{B}\frac{h_{\alpha Z x}^{(0)}}{b_x}\right)-\frac{\partial}{h_x\partial x}\left(\sqrt{B}\frac{\overline{h}_{\alpha x}^{*(0)}}{b_x}\right)\right)\right]\right], \tag{J.23}$$

$$\widetilde{j}_{ay}^{(visq)} = [a \to \alpha Z] =$$
$$\frac{2}{5}\frac{B_z\sqrt{B}}{3B_x}\frac{\partial}{h_x\partial x}\left(\frac{1}{B^2}\right)\frac{\partial}{h_x\partial x}\left[\frac{n_{\alpha Z}}{n_\alpha}\left[\sum_\beta\frac{\eta_{\alpha\beta x}^{(h_iA)}}{p_\alpha}\frac{\partial}{h_x\partial x}\left(\sqrt{B}\frac{\overline{h}_{\beta x}^{*(0)}}{b_x}\right)+\right.\right.$$
$$\left.\left.\frac{\eta_{\alpha x}^{(h_iB)}}{p_\alpha}\left(\frac{1}{I_{\alpha Z}}\frac{\partial}{h_x\partial x}\left(\sqrt{B}\frac{h_{\alpha Z x}^{(0)}}{b_x}\right)-\frac{\partial}{h_x\partial x}\left(\sqrt{B}\frac{\overline{h}_{\alpha x}^{*(0)}}{b_x}\right)\right)\right]\right], \tag{J.24}$$

where in the poloidal heat fluxes, the parallel heat conductivity and the diamagnetic contributions are taken into account according to (5.19) and (5.20).

# K Acknowledgments

This work would not have been possible without the invaluable help and unwavering support of numerous people. I would like to express them my deep gratitude.

I want to thank Dr. David Coster for the wise supervision of my PhD project. Many fresh ideas came to us during our fruitful discussions at lunch and at the white board. I would like to express special gratitude for the freedom and trust in choosing my doctoral path that David has given me. I want to thank him also for his many valuable practical advises and patience in reading my hopeless English texts. Many thanks to my second supervisor Dr. Andreas Stegmeir for help with the GRILLIX project and introduction into thoughtful way of code development. His outstanding professional and personal qualities allow him to effectively manage the entire GRILLIX team (even when it comes to carpets). I would like to thank my academic supervisor prof. Dr. Frank Jenko for the efficient strategic guidance of my PhD project.

I want to thank the team of St. Petersburg Polytechnic University for their help in the theory and code application of the multi-ion model. I would like to thank prof. Dr. Vladimir Rozhansky for great support of the theoretical part of my project. I thank Dr. Elizaveta Kaveeva for her help in developing a wide range of models, from simple yet powerful analytics to complex geometric representations. A significant role in the generalization and practical implementation of the model was played by Dr. Ilya Senichenkov. I thank him for this help. I deeply gratitude Dr. Sergey Voskoboynikov for the invaluable help with numerical implementation of the generalized multi-ion model into the SOLPS-ITER code. I aslo thank Dr. Irina Veselova for the guidance in preforming DT runs.

I would like to gratitude Dr. Alexander Stepanenko for the comprehensive assistance on the very deep level of the multi-ion collisional theory. I would like to express my heartfelt gratitude to the late prof. Dr. Vladimir Zhdanov, the author of the famous closure, for his invaluable help and support. His sudden death was a great loss for the whole science community. I also want to thank Dr. Madhusudan Raghunathan for the frutful disscussion about multi-species closure.

I thank my colleagues from ITER for the huge contribution to my PhD project. Dr. Xavier Bonnin has made great efforts to make the multi-ion closure part of the SOLPS-ITER code. I am very grateful for this. I want to thank Dr. Richard Pitts with the help of our DT project.

I want to express my large gratitude for Dr. Francesco Sciortino for our memorable discussions, which always bring me both deep thoughts and a lot of inspiration. I also thank Dr. Wladimir Zholobenko for the interesting and fruitful scientific discussions. I would like to thank the ASDEX Upgrade experimental team for their great support. I especially want to thank Tabea Gleiter, who is open to efficient collaboration and spends

a lot of time providing me with valuable experimental data. Many thanks for the Dr. Ralph Dux for the comprehensive help with understanding spectroscopy theory. I am very grateful for the fruitful collaboration with Antonello Zito, who is not only helping me with experimental data but also teaching me how to calibrate diagnostics myself. I want to thank Dr. Dominik Brida for helping me with Langmuir probe data analyzing. I express my gratitude to Dr. Pierre David for his significant help in the analysis of the Bolometer data.

I wish that all the support that I received from people close to me will not be forgotten. I want to thank my old friend Aleksander Ryabov, who supported me in all happy and difficult situations. I thank my old buddy Valentin Mylnikov for being close even when far away. I am very grateful for all the warmth that I received from the wonderful Agnieszka Bebinek-Bielanska. It is impossible to forget our ASTRAnomical adventure which we performed together with incomparable Dr. Marco Muraca. It doesn't matter what you do with this guy, it will be fun anyways! Let's not forget our amazing discussions with Brando Rettino during jogging and drinking together! I thank Dr. Francesco Vannini for all advetures togeter: ITER, There and Back Again, and for our wonderful discussions (including my favorite religious ones). I am very grateful for the fun time together with Daniel Hachmeister and his warm welcome in Lisbon (cannot forget this delicious Bacalhau à Brás). I want to thank Dr. Oleg Samoylov for all he has brought to me on the scientific and personal levels. I am very grateful for the time spent together with Aleksandr Mustonen (especially our adventures in Spain). It is always unforgettable spending time with Dr. Teobaldo Luda di Cortemiglia (that what she said)! Even staying in queue with you is fun! I thank Dr. Felipe Nathan de Oliveira Lopes for amazing parties that you organized and helped me feeling alive. Many thanks to Constantin Gahr for our bouldering and talks (sometimes in German) together. I am very grateful to all my friends, who helped me went though this PhD: Dr. Tautvydas Jeronimas, Daniel Fajardo, Dr. Davide Silvagni, Dr. Antonio Magnanimo, Dr. Nicola Isernia, Melanie Bolle, Dr. Maximilian Reisner, Dr. Pedro Molina Cabrera, Dr. Andres Cathey, Natalia Logvinova, Elisey Strelnikov, Danila Lapko, Albir Kipot, Aleksandra Rykachevskaia, Ekaterina Makarova, Dr. Oleksii Girka, Dr. Serhiy Mochalskyy and many other people who have been around.

I want to thank my German teacher Alexander Pagin who brought me to a decent level and beyond.

Last but definitely not least I desire to express my deepest gratitude to my family. It's impossible to say how important you are to me. I thank my mother Anna Makarova for all the love and support that helped me overcome all difficulties. I admire my father, Oleg Makarov, who awakened my interest in science and made a lot of efforts to bring me to this level. I am very grateful to my sister Vera Makarova, who has been always near and physically for the last year, when I especially needed it.